Summer 8-13-2019

Clay Mineralogy and Porosity Estimates of the Lower Permian Wolfcamp Shale

Morgan Garner

Recommended Citation

Garner, Morgan, "Clay Mineralogy and Porosity Estimates of the Lower Permian Wolfcamp Shale." Thesis, Georgia State University, 2019.

doi: https://doi.org/10.57709/14969773

CLAY MINERALOGY AND POROSITY ESTIMATES OF THE LOWER PERMIAN WOLFCAMP SHALE

by

MORGAN KENNEDY GARNER

Under the Direction of W. CRAWFORD ELLIOTT, Ph.D.

ABSTRACT

Diagenetic controls (pressure, temperature, and time) altered petrophysical properties in black shale petroleum source rocks. Several samples of the lower Permian Wolfcamp Shale, a prominent tight gas oil play from the mid-continent US, were collected from a range of thermal maturity values (0.8-1.07% VRo) to test this hypothesized relation among the formation of diagenetic illite, over-pressuring, and porosity generation. Microporosity was observed between clay aggregates, organic material, and cementing materials. Moldic porosity was seen within POM. Microporosity measured 5.5% for the most thermally mature sample and 7.1% for the least mature sample. Based on preliminary measurements on partially reduced small angle scattering data (SAXS), packets of particles 30 Å, consistent with fundamental particles were visible. These preliminary results suggest that both micro- and possibly nano-porosity decreased with thermal maturity. Lithification, diagenetic mineral formation/pore fill, as well as organic matter migration have been attributed to disaggregating porosity at increased thermal maturities.

INDEX WORDS: Diagenesis, Shale, Thermal maturity, Illitization, Porosity, Clay mineralogy, SAXS, XRD, SEM, Midcontinent.

CLAY MINERALOGY AND POROSITY ESTIMATES OF THE LOWER PERMIAN WOLFCAMP SHALE

by

MORGAN KENNEDY GARNER

A Thesis Submitted in Partial Fulfillment of the Requirements for the Degree of

Master of Science

in the College of Arts and Sciences

Georgia State University

2019

CLAY MINERALOGY AND POROSITY ESTIMATES OF THE LOWER PERMIAN WOLFCAMP SHALE

by

Morgan Kennedy Garner

Committee Chair: W. Crawford Elliott

Committee: Brian K. Meyer

Hassan A. Babaie

Electronic Version Approved:

Office of Graduate Studies

College of Arts and Sciences

Georgia State University

July 2019

DEDICATION

I want to dedicate this scientific achievement to the best landlord I could ever have. Thank you to my Sissy Bird for creating such a warm, supportive, and loving environment. This document would not be possible without that yellow house on Berkeley Road. I will never forget those wonderful two years spent together. You inspire me every day to be a better person.

This thesis is also dedicated to my mama, Suzianne Garner. Thank you for teaching me to dance in the rain even when I forget my umbrella. I can never thank you enough for inspiring my love of sciences. You taught me to care for things that are bigger than myself. You are my hero.

Thank you to my mini mojo, my beautiful sister. I am so proud to be your big sis. If I could write this thesis, you accomplish anything… starting with cleaning your room. Thank you to my (not so) baby brother for teaching me patience and unconditional love. A special thank you to my dad for reminding me not to sweat the small things and all the other tidbits of life advice hidden underneath an off-key singing voice. The last thank you is for the other Christopher in my life. I now see life in hues of yellow, purple, and orange I never saw before. Our pack has nestled into a place in my heart I never knew existed. Cheers to the next adventure, may it contain many more sunrises and frozen grapes.

ACKNOWLEDGEMENTS

This thesis would not be possible without the support of Georgia State University, Geosciences Department. Geosciences provided a teaching assistantship and stipend for the duration of this study. This research used resources of the Advanced Photon Source, a U.S. Department of Energy (DOE) Office of Science User Facility operated for the DOE Office of Science by Argonne National Laboratory under Contract No. DE-AC02-6CH11357. Lawrence Anovitz, Jan Ilavsky provided commentary and advice when needed which was appreciated. The Panalytical Xpert Pro X-ray diffractometer was purchased with funds from NSF to D.M. Deocampo and W.C. Elliott (NSF Award 1029020). Thanks to Richard Whittington and Mark Longman from QEP, and Prof. R. Douglas Elmore (Oklahoma University) for providing these samples. Thank you to Katie Garrett for being extremely helpful and insightful with all FE-SEM measurements. Thank you to Dr. Elmore for all your help and allowing me to borrow one of your brilliant graduate students. Thanks to John Tougas for always coming to the rescue for the many technical difficulties.

A giant thank you to my committee for being instrumental in my undergraduate and graduate success. Dr. Meyer and Dr. Babaie are both uniquely brilliant and I will always cherish all of our thoughtful conversations. The knowledge and skills taught to me by my advisor, Dr. Elliott, are absolutely priceless. Thank you for your patience, your unwavering support, and cat photos.

TABLE OF CONTENTS

LIST OF TABLES

LIST OF FIGURES

LIST OF ABBREVIATIONS

Å	Ångstrom
Ar	argon
CaCl	calcium chloride
CBD	sodium citrate, dosium bicarbonate, and sodium dithionate
Cm	Centimeter
ºC	degree Celsius
DI	deionized
EG	ethylene glycol
G	gram
>	greater than
I-S	illite-smectite
I	illite
K	potassium
K-Ar	potassium-argon
km	kilometer
<	less than
Ma	million years
m	meter
mm	millimeter
ml	milliliter
mg	milligram
µm	micrometer
M	molarity
Na	sodium
NaOAc	sodium acetate
NaAc-HAc	sodium acetate-acetic acid buffer
O	Oxygen
OM	organic matter
%	percent
RPM	rotations per minute
R	Reichweite
S	smectite
SST	solid state transformation
TOC	total organic carbon
TTI	Time Temperature Index
Θ	theta
VR_o	Vitrinite Reflectance
λ	wavelength of X-rays (Ångstrom)
XRD	X-ray diffraction

1 INTRODUCTION

1.1 Focus of Study

Advances in unconventional drilling techniques, i.e., shale hydraulic fracturing and horizontal drilling, have increased the productivity and the secondary recovery of crude oil and natural gas from formerly inaccessible fine-grained source rocks. Black shales in the eastern and midwestern United States (US), in particular, have been targeted for promising untapped natural gas exploration via horizontal drilling and hydrofracturing. The Lower Permian Wolfcamp Shale has become a significant site of hydrocarbon exploration in the US due to hydrofracturing and related secondary recovery of crude oil and natural gas. The US Geological Survey assessed technically recoverable mean resources of 20 billion barrels of oil and 16 trillion cubic feet of gas in the Wolfcamp Shale in the Midland Basin, the largest estimate of continuous oil that USGS has ever assessed in the United States (Gaswirth et al., 2016). All of the Wolfcamp shale is profitable for oil and gas exploitation due to the predictable VRo content throughout the Permian Basin. The Wolfcamp shale was chosen for its regional extent and stacked pay zones ideal for horizontal drilling endeavors (Blomquist, 2016). This unit has been referred to as fine-grained ‘tight’ source rock due to their low permeability, and low porosity (porosities ranging from 4-12%) which are now viewed as reservoir rocks (Blomquist, 2016). The US has recently exported natural gas for the first time in many decades. The exportationexploration of natural gas reflects the impact of the use of hydraulic fracturing of Paleozoic black shale and related shale source rocks.

Geologic studies of black shales have become increasingly important due to our nation’s domestic oil and gas production. The exploration of sedimentary basins has been guided by knowledge of thermal maturity and by petrophysical features of both source and reservoir rocks. Clay mineral transformations (such as conversion from smectite to illite), and select organic indices (e.g., vitrinite reflectance, VRo) have provided useful information on the thermal maturity of source rocks generating crude oil and natural gas. Clay mineral transformations (smectite to illite) at diagenetic conditions have promoted over-pressuring among these shales in the Gulf Coast (Magara, 1975; Burst, 1969; Bruce, 1984). Shale overpressure has led to the expulsion of crude oil and natural gas from otherwise very tight source rocks to more porous and permeable reservoir rocks. Overpressuring has also lead to the alteration of pore structures in these shales. New secondary minerals precipitated in these newly developed pores (Roberts and Elmore, 2018). The stacking order of illite layers in illite-smectite has been utilized in many studies as a semi-quantitative geothermometer to study the thermal histories of sedimentary basins (Hower et al., 1976; Pollastro, 1989; 1993). This semiquantitative thermometer is used in a way comparable to vitrinite reflectance (VRo) and to time-temperature index (TTI) values (Waples, 1980). The age of the illite-smectite as measured by K-Ar geochronology has been integrated with other index values to understand further the thermal maturation of sedimentary basins, generation, and trapping of hydrocarbons (Pevear, 1999). However, the role of mineral transformation (illitization), and its role in the development of microporosity/fracturing and over-pressuring of hydrocarbon source rocks requires further research.

Many issues arose in relating the thermal maturity to the creation and deformation of porosity. While results have been concluded (Clarkston et al., 2013; Jin et al., 2013; Mastalerz et al., 2013; Ruppert et al., 2013; Anovitz et al., 2015) none have yet correlated the amount, size, and distribution and connectedness of pores to a timing of thermal maturation generating crude oil and natural gas. Additional data are needed to understand the development of porosity and permeability of these rocks as they become thermally mature.

The Paleozoic basins in the mid-continent US are ideal locations for continued diagenetic studies due to the range of mineralogy, thermal maturities, and existing wells within the region. The focus of this study was to evaluate the petrophysical changes of black shale source rocks at the nanometric scale. The measurement of nanoporosity by way of beam-line techniques is relatively new (Anovitz et al., 2017). This research was conducted to assess the evolution and connectedness of porosity within black shale source rocks at various thermal maturities. This research goes beyond former works by examining micrometer (µm) and angstrom (Å) scales of porosity. This comprehensive thesis will likely challenge previous knowledge of the formation of petrophysical characteristics with progressive burial depth.

The ages of diagenetic events and authigenic mineral formation are vital in understanding thermal histories of sedimentary basins. Multiscale pore structure evaluation is needed to describe the porosity and its possible roles in hydrocarbon migration, diagenetic development, and overall reservoir quality of US midcontinent black shales. This study intended to answer the following questions (1) How do diagenetic controls (T, time) alter the reservoir quality of black shales? (2) What pore networks are evident in this shale? (3) What is the development of nano and micro-porosity in thermally mature systems?

1.2 Geologic History

Black shale samples were collected from Midland Basin (TX) for this study by Prof. Elmore (Oklahoma University) and Richard Whittington, QEP Resources (Figure 1). This basin has been actively explored for crude oil and vertical plays of shale gas since the 1950s (Baumgardner et al., 2014). This unit is economically feasible to exploit due to its susceptibility to brittle deformation and high TOC (Nygård et al., 2004; Wickard, 2016; Blomquist, 2016; Cardott, 2012).

The US Energy Information Administration referred to this region as containing some of the most profitable liquid-rich shale plays in North America (U.S. Energy Information Administration, 2017). Extensive seismic and drilling data obtained during the exploration for US midcontinent hydrocarbon resources have provided increased understanding of sedimentary basins in context to the overall geology of the Texas region (e.g., Johnson and Cardott, 1992; Whittington, 2009). The stratigraphic development and basin geometry of midcontinent US Paleozoic basins, such as the Midland, was influenced by depositional processes and uplift events. Areas of low elevation, formed by regional tectonic activity, allowed for the accumulation of terrestrial and marine sediments within the basin. Thick carbonates, turbidites, shales, sandstones were deposited in during periods of prolonged crustal subsidence during the late Paleozoic Era. The combined effects of tectonic activity and the overall climate of the region determined the nature of sediment, the rate of sediment supply, total organic content (TOC), and vertical succession of different sedimentary rocks. These depositional factors controlled the occurrence, thickness, and composition of the Wolfcamp Shale. Structural and stratigraphic data provided useful information in determining which units will be oil-producing (Giles, 1997).

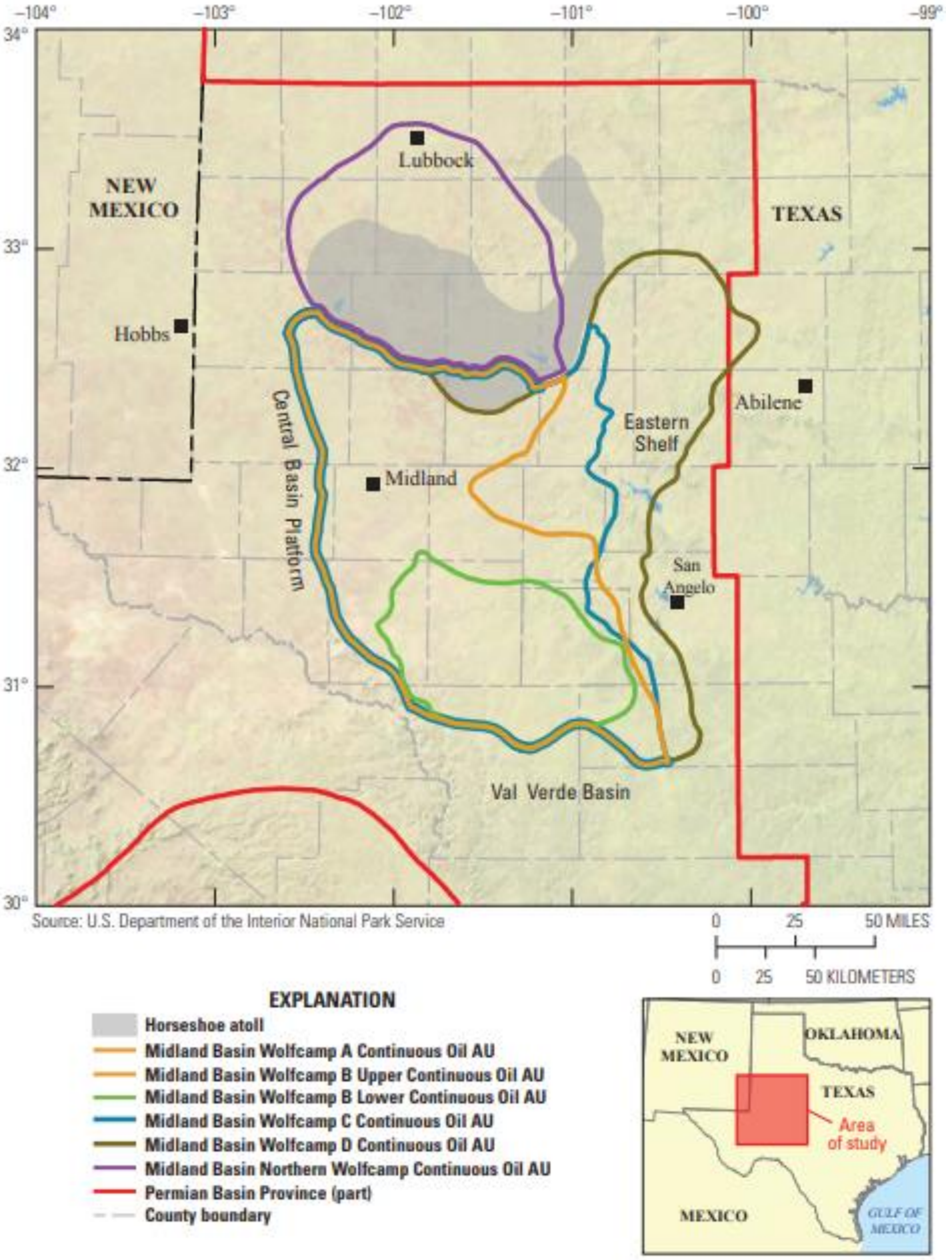

Figure 1: Map adapted from USGS National and Global Petroleum Assessment. This figure shows the location of the midland basin and the extent of the Wolfcamp Shale.

The Greater Permian Basin was one of the largest sedimentary basins in the continental US. This basin was located throughout west Texas and southeast New Mexico (Frenzel et al., 1988). The Marathon Ouachita thrust belt borders this basin to the south and is responsible for tectonic uplift in this and other basins in the Midwest (Figure 2). This thrust belt was activated during the assembly of the Pangea supercontinent (Sinclair, 2007). Movement along this thrust belt caused tectonic uplift and the rotation of two hanging-wall fault blocks of the frontal Wichita fault system at the southern margin of the Anadarko basin (Yang and Dorobeck, 1995). This progression created the central basin platform that segmented the Greater Permian into three sub-basins, Delaware, Central and the Midland Basin (Yang and Dorobeck, 1995). The cores of the Wolfcamp Shale, whose shale samples were examined in this study, were drilled near the eastern shelf of the Midland Basin. The region was bounded to the north by the Matador Arch. The Diablo Platform and Pedernal Uplift were found directly west of this basin (Ball, 1995). A north trending en echelon fault system, Fort Chadbourne fault zone, lies to the east and served as the eastern border of the basin (Ewing, 1990).

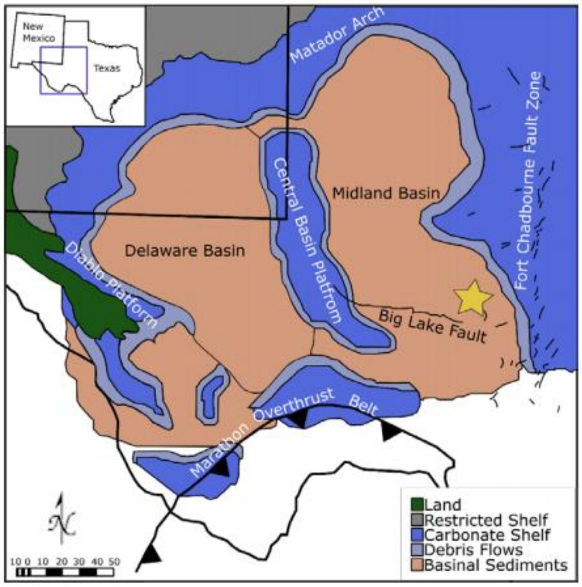

Figure 2: Map adapted from Wickard (2016) to show the Permian basin and surrounding structural provinces. The star approximates the location of samples collected. Base map modified from Stoudt (1998) and structural map modified from Ewing (1990).

Rifting opened the proto Atlantic ocean during the late to Precambrian to Cambrian period (Denison et al., 1984). This rifting produced a broad shallow marine shelf, later covered by the

Cretaceous seaway, on the continental US from the late Cambrian to early Mississippian time (Johnson, 1989). This broad shelf, which later was the site of the Cretaceous Western Interior Seaway, experienced a long period of subsidence (Johnson, 1989). Shales, limestones, siltstones, and sandstones were deposited as these basins experienced rapid subsidence (Denison et al., 1984; Johnson, 1989). The late lower Permian deposits of an organic-rich mudstone, now known as the Wolfcamp Shale, was deposited during these conditions (Frenzel et al., 1988).

1.3 Lithology of Wolfcamp Shale

The dominant grain size within this shale ranged from fine grained clays (< 5 μm) to fine sand (< 75 μm). Sedimentation of mineral grains in this basin was controlled by rapid subsidence and sea level fluctuations also associated with the initiation of the late Paleozoic icehouse (Brown, 1972; Montgomery, 1996; Mazzullo, 1997; Sarg et al., 1999; Golonka and Kiessling, 2002). Post-rift subsidence influenced the stratigraphy and allowed for the accumulation and redistribution of hemipelagic sediments throughout the midcontinental US region. Oceanic currents delivered grains as suspended sediments. As the energy of currents deceased sedimentation occurred allowing clay sized particles to flocculate (forming flocculants) within the water column and the seafloor. Continental margin sediments (approx. >60%, clay minerals) were buried among marine sources of organic carbon. The prevailing redox conditions showed that this epicontinental seaway was euxinic (anoxic and sulfide-rich) allowing high preservation rates of organic matter (OM) and sulfur (Connant and Swanson, 1961; Kirkland et al., 1992; Whittington, 2009). The bulk rock volume is altered by effective stress that occurred during sediment loading. This change causes a reduction in porosity and spaces between grain boundaries. The Wolfcamp Shale was lithified as an organic-rich marine mudstone preserved within the Midland Basin. The predominant facies of this units consisted of siliceous mudstone, carbonate mudstone, carbonate debris flow, and carbonate turbidites (Wickard et al., 2016). An in-depth look at the four dominant facies was created by Wickard (2016) using images of core slabs and thin sections. This shale exhibited heterogeneity in terms of its mineral composition and structural feature. However, the primary constituents that make up an average shale are quartz, clays, carbonates, feldspars, albite, apatite, pyrite and organic material was present throughout this shale. This formation has been classified as a black to dark grey, fissile to blocky mudrock. The amount of TOC has been attributed to slow sedimentation rate and marine conditions (Kennedy et al., 2014).

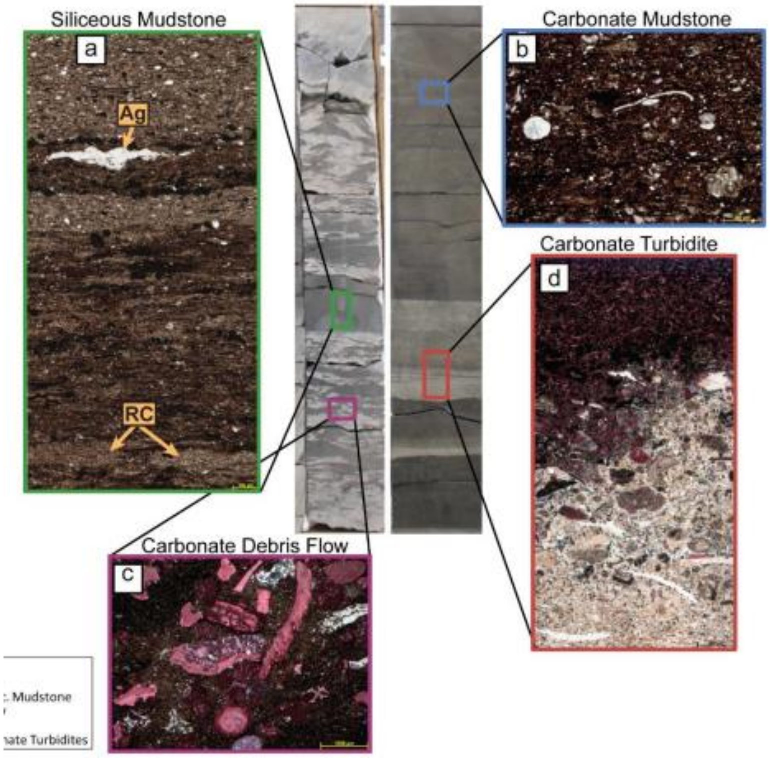

Figure 3: This figure adapted by Wickard et al. (2016) provided an in-depth description of the core and facies of the Wolfcamp Shale. The four main facies can be seen to the right and left of the core. This paragenetic sequence provides evidence of the spatial relationships of each facies.

In addition to the well-known suite of minerals in shales, hydrothermal minerals have been shown in fractures through which hydrothermal fluids migrated (Wickard et al., 2016; Roberts and Elmore, 2018). Samples of the hydrothermal mineralization features were examined petrographically in directions perpendicular to the bedding plane (Figure 4). Mineralized fractures were abundant, contain hydrocarbons, calcite, and celestine-barite, and some contain porosity within Paleozoic black shales (Figure 6) (Roberts and Elmore, 2018). These hydrothermal minerals (assumed to be dolomite, quartz and pyrite) were formed by the infiltration of high salinity fluids during diagenesis (Roberts and Elmore, 2018). Early diagenesis included precompactional veins of ferrous minerals (Figure 5) as well as mineral precipitationprecipitation of calcite/phosphate concretions, sphalerite, barite, quartz, dolomite, and ferroan dolomite. Horizontal and vertical fractures were likely the result of overpressuring (Roberts and Elmore, 2018). The mineralized fractures contained secondary porosity, dolomite, albite, chlorite, and quartz (along bedding) perpendicular to fracture walls (Figure 5; Roberts and Elmore, 2018). The appearance of (detrital, overgrowth) quartz, a mineral defined by its conchoidal fracture, increased the tendency of the formation towards brittle deformation. This brittle behavior increases susceptibility to hydraulic fracturing, a large factor influencing the viability of these shales (Nygård et al., 2004; Wickard et al., 2016).

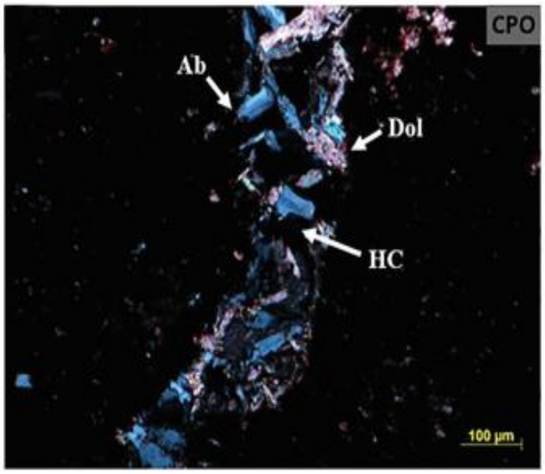

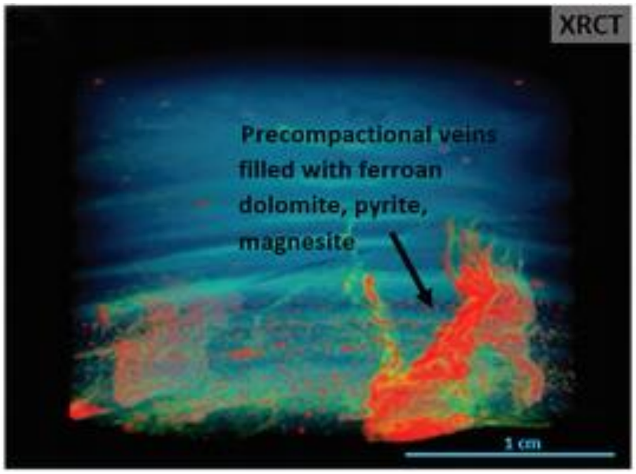

Figure 4 (left): This image adapted from Roberts and Elmore (2018) showed the appearance of hydrocarbons, albite and dolomite within the Woodford shale under cross polarized light. Figure 5 (right): This X-ray computer tomography (XRCT) image was adapted from Roberts (2018) to demonstrate the pathway(s) of hydrothermal fluids (bright red) within brine-filled veins (darker red). These images were taken of Woodford shale samples but can be readily applicable to other mid-continental black shales, such as the Wolfcamp Shale.

The presence of hydrothermal minerals suggested that warm high salinity fluids migrated throughout the Woodford, and assuming Wolfcamp, shale within fluid conduits sometime during its burial history. Fluid inclusion analysis showed that mineralized fractures were conduits for warm, high salinity brines that were observed to be externally derived (Wickard et al., 2016; Roberts and Elmore, 2018). It was likely the conduits of fluid migration of hydrocarbons occluded mesopores during middle to late diagenesis (Wickard et al., 2016; Roberts and Elmore, 2018). Hydrothermal alterations started other diagenetic reactions during the middle to late diagenesis (Wickard et al., 2016; Kennedy et al., 2014). Fracture and fluid inclusions caused complex development of secondary pore systems within the organic and inorganic constituents. These alterations and their distributions in the shale matrix affected the predictability of reservoir quality.

1.4 Diagenetic Features

The mechanical properties of black shales were directly influenced by the grain size, sorting, and mineralogy. However, the original depositional texture was also altered by mechanisms of diagenesis. Compaction, cementation, recrystallization, and neoformation occurred in conjunction with diagenesis (Hester, 1992). The boundary conditions of this diagenetic process are temperatures less than 200 °C and pressures between 1 and 1000 bar (Chapmin, 1983). These mechanisms formed a range of diagenetic features within these boundary conditions.

This mudstone exhibited early, middle, and late diagenetic features such as pyrite framboids, phosphatic concretions, calcareous concretions, and neoformation (Wickard et al, 2016; Roberts and Elmore, 2018). Structural features (such as porosity) were altered by the intrusion of fluids (formation waters, connate brines or external fluids) (Wickard at al., 2016; Roberts and Elmore, 2018). These fluids migrated into the matrix via pore spaces (and fractures).

Secondary or diagenetic minerals precipitated from these fluids. Authigenic mineral precipitation (chlorite, kaolinite, and dolomite) occurred through the segmentation of pore spaces reducing the extent and connectedness of primary porosity.

Diagenesis influenced porosity, permeability, tendency to fracture, fluid-flow pathways, and ultimately the capacity of a unit to maintain a sufficient amount of natural gas (Wickard et al., 2016; Giles, 1997; Stroker et al., 2013). Through the use of scanning electron microscopy, Roberts and Elmore (2018) observed the presence of meso-scale porosity in this Paleozoic black shale. They captured images of meso- and microporosity that had occurred within pyrite framboids (Figure 6), vugs in fractures and allochems, and between clay sheets (Figure 7). Similarly, in the Wolfcamp Shale porosity was recorded to exist in pyrite framboids and between sheets of chlorite (Wickard et al., 2016). Intercrystalline and moldic porosity is present in dolomitized intervals (Figure 8). Overpressuring, hydrothermal alteration, and authigenic mineral formation destroyed primary porosity during early diagenetic phases of these shales.

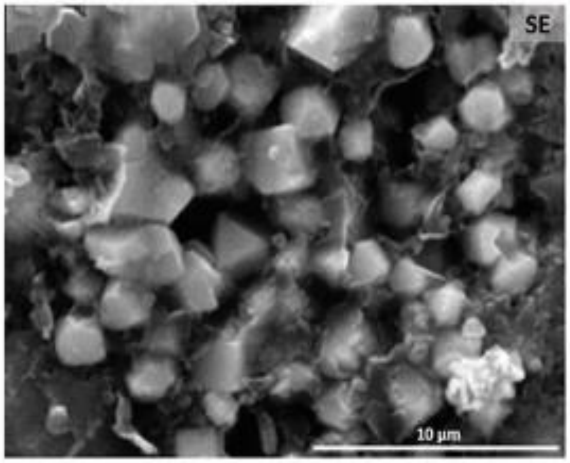

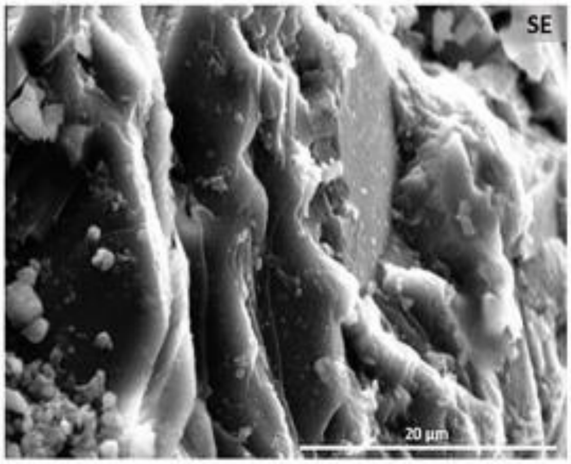

Figure 6: Two FE SEM images adapted from Roberts and Elmore (2018) showing high-resolution imagery of porosity. This image depicts porosity between pyrite framboids. Figure 7: FE SEM images with porosity shown between clay sheets.

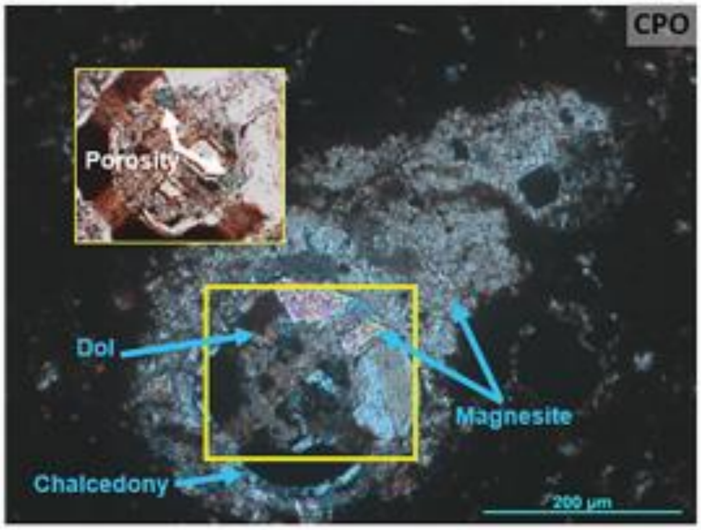

Figure 8: SEM images adapted from Wickard et al., (2016) to show intercrystalline and moldic porosity present in dolomitized intervals. This image was taken under cross-polarized light.

1.4.1 Illitization

It has been widely accepted that the progressive burial of argillaceous marine sediments will prompt the formation of diagenetic illite from expandable smectite (Moore and Reynolds, 1997). Illitization has been used as a term to denote the growth of illite grains from smectite during siliciclastic diagenesis. This reaction has been characterized by a number of distinct processes: tetrahedral substitution of Al for Si in the tetrahedral sheet, dehydration (removal of water from the smectite interlayer sites), collapse of layers after incorporation of K^+ in the interlayer, and loss of internal surface area (Equation 1; Moore and Reynolds, 1997). Layers of smectite are converted to illite, once thought to occur as a conversion of an intact smectite layer to an illite layer. The conversion of smectite to illite led to the formation of an interstratification of I-S where illite layers are stacked on smectite layers parallel to the c-axis (turbostratic stacking). I-S was seen first at temperatures as low as 50°C. The conversion of smectite layers to illite layers proceeded to an I-S with the majority of layers formed as illite layers. The endpoint of this process typically occurred at 200°C (Waples, 1980; Hoffman and Hower, 1979; Velde et al., 1986). Although this reaction has limiting factors in which it will form (time, temperature, and availability of K^+ (Elliott and Matisoff, 1996)), I-S clay has been seen as the most commonly observed phyllosilicate mineral in Phanerozoic argillaceous rocks than either smectite or diagenetic illite (Moore and Reynolds, 1997). The presence and availability of pore fluids has been an important parameter in the rate and extent of the conversion mechanism of smectite to illite. Smectite has been thought to have been converted to illite by one of three processes. These processes included: solid state conversion of layers, dissolution of smectite (or illite) and precipitation illite, or Ostwaldt Ripening) (Altaner and Ylagan, 1997; Eberl and Środoń, 1988).

$$\text{K-feldspar} + \text{smectite} \rightarrow \text{smectite/illite} + \text{quartz} + H_2O$$

Equation 1: This expression showed the direct gain of illite from smectite, adapted from Moore and Reynolds (1977) where H_2O and quartz are expelled as products. Of note, K-feldspar was the source of K+ forming diagenetic illite in Gulf Coast shales (Hower et al., 1976).

1.4.1 Smectite

The presence of smectite has been essential to the preservation and burial of organic carbon (OC) (Kennedy et al., 2014). Smectite species possessed layer charge between 0.2 – 0.6 identified by (00*l*) d-spacing values, from 12.5 - 17 Angstroms (Å) (Moore and Reynolds, 1977). The commonly observed smectite species (montmorillonite, beidellite and nontronite) are characterized by their interlayer cation and the type of octahedral cations (Figure 9). When compared with other phyllosilicates, smectite has a comparatively large mineral surface area and expandable interlayer space due to its arrangement of tetrahedral and octahedral (TO) sheets (Środoń, 1990). The presence of relatively weak bonds between layers and the low (and deep positioned) layer charge in part originating from the octahedral sheet contributedto its expandable nature. The expanded interlayer site stored and protected OM, ions or water from microbial degradation (Kennedy et al., 2014). Interlayer ions were expelled to accommodate the growth of illite. This transformation also reduced the available mineral surface area for geochemical reactions. K^+ is fixed strongly in diagenetically formed illite. Diagentically formed illite has been considered a useful phase for K-Ar geochronology at diagenetic temperatures (e.g., Elliott et al., 1991).

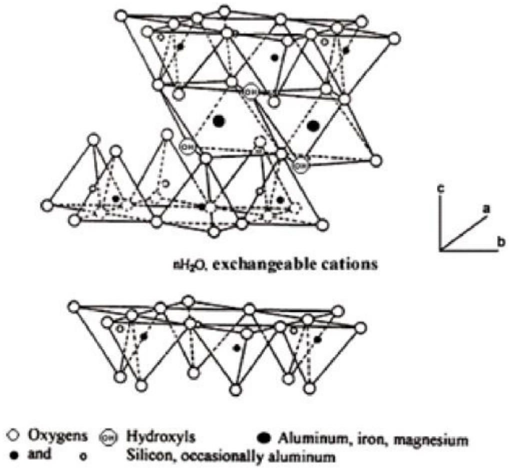

Figure 9: This figure is adapted from Moore and Reynolds (1997). This schematic diagram shows the internal crystal structure of the expandable phyllosilicate mineral, smectite.

1.4.2 Illite

Illite has been known to have been formed as a weathering byproduct of detrital muscovite. In the 1970s, illite was begun to be considered to have formed through the conversion of smectite to illite in the presence of K^+ rich pore fluids in marine diagenetic systems. The formula for illite is shown in Equation 2 below. Illite, a dioctahedral phyllosilicate mineral, is distinguished by the presence of interlayer potassium fixed to siloxane surfaces between the 2:1 layers (Moore and Reynolds, 1997). This micaceous clay possessed a slightly higher layer charge ($0.6 < z < 0.9$) and smaller (00*l*) d-spacing value, 10 Å (Moore and Reynolds, 1997). The higher layer charge of illite restricted its expandability (Osborn, 2006). The neoformation of illite layers between expandable smectite grains was highly sensitive to temperature and therefore can provide useful information regarding the thermal history of a sedimentary basin (Elliott et al., 1991).

$$K_{.9}\ Al_2\ Si_{3.1}\ Al_{.9}\ O_{10}\ (OH)_2$$

Equation 2: General chemical formula for illite adapted from Nadeau and Bain (1986).

The extent and arrangement of illite (i.e. illite crystallinity) were probed via optical properties (SEM) and through X-ray diffraction (XRD). The end-member illite has been identified in straightforward manner via X-ray diffraction. The diffraction peaks for the mixed layer I-S were depicted as asymmetrical peaks whose d-spacing values were between the pure illite or pure smectite (Osborne, 2006; Moore and Reynolds, 1997). Characteristic I-S diffraction patterns were used to distinguish illite polytype and stacking order. The illite polytype (1Md, 1M, and $2M_1$) typically has corresponded with its petrogenetic origin. Illite polytypes are distinguished by stacking arrangements through the study of random mounts. In shales, the smallest size fraction (approximately <0.2 μm) typically contained the highest fraction of the 1M*d* polytype. This polytype is that of diagenetic illite, as observed by Weaver and Wampler (1970) and Pevear (1999). The coarser fractions in shale contained more $2M_1$ illite polytype. This polytype corresponded to detrital illite or muscovite mica. Consequently, shale are considered binary mixtures of diagenetic illite (1M*d* polytype) and detrital illite ($2M_1$) polytype.

More typically, the classification of interstratified clays was based on the percentage of illite layers in an I-S and the stacking order of illite layers with smectite Three stacking orders have been observed (random, ordered and Kalkberg-ordered). The *Reichweite* (R) term is used to express the stacking order seen in I-S. The *Reichweite* (German for reach back) descriptor is the number of illite layers following smectite. For the random order of I-S (R=0, SSISSIS, no I followed by I), smectite layers are followed by smectite layers such that illite was not observed in two consecutive layers. This fraction of illite layers in this stacking order is typically 0% to 50% illite in I-S. As illite increases to 50% of the I-S, the stacking order of illite and smectite evolved to a “short-range” (R=1 ISISIS..) (Hoffman and Hower, 1979). In this stacking order, a smectite layer is followed by one or more illite layers. The fraction of illite layers ranged from 50%- 80% illite layers in I-S. With progressive burial conditions, I-S approaches the solid end member illite and a “long range” stacking order was referred to as Kalkberg ordering, R=3 (SIIISIII) (Hoffman and Hower, 1979). In this last stacking order, three or more illite layers followed one smectite layer. The stacking layer of I-S can be determined by the change in diffraction peaks (Figure 10). The stacking order has been used as a semi quantitative geothermometer for the study of the thermal histories of sedimentary basins (Pollatro, 1989; Hoffman and Hower, 1979).

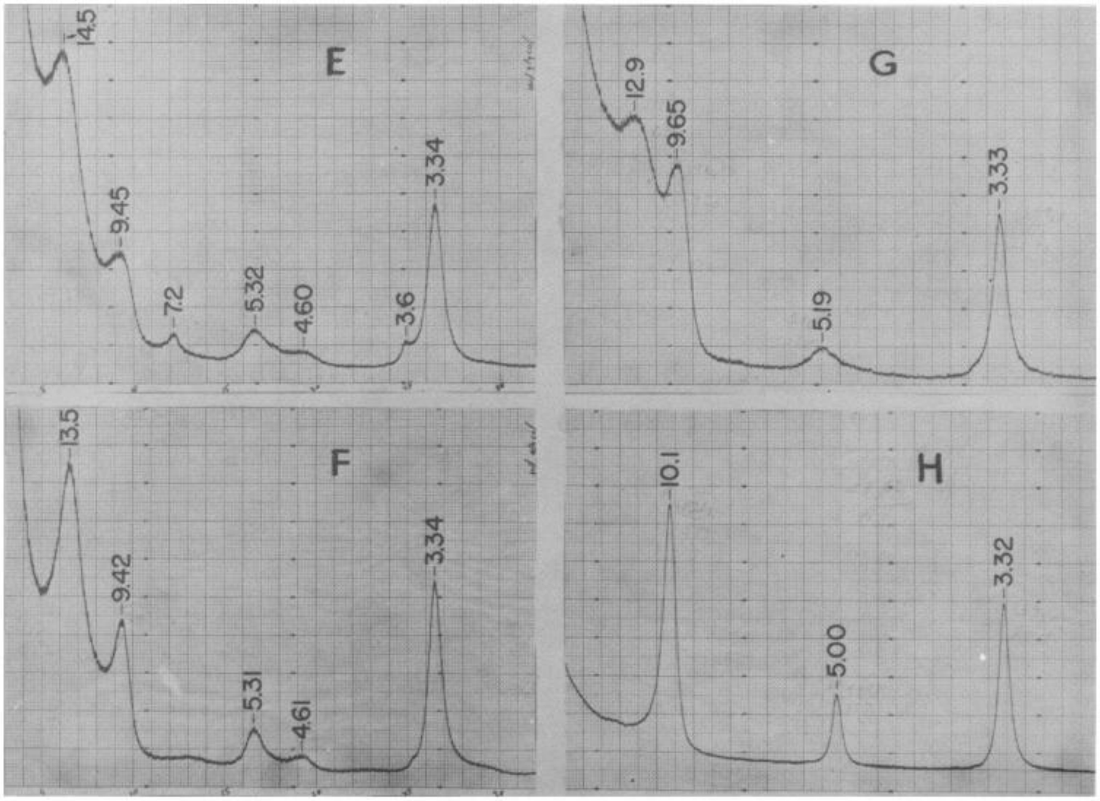

Figure 10: Ethylene glycol diffraction patterns adapted from Reynolds and Hower (1970). The diffraction patterns show to conversion of interlayered I-S 70% (E) to end member illite (H).

1.4.3 Kinetics

The diagenetic growth of illite in black shales has corresponded to the time and temperature conditions needed to generate crude oil and natural gas (i.e. oil generating window, Schieber, 2010; Waples, 1980). Mature hydrocarbons were generated when 80% of the clay minerals are illite (R=3) (Waples, 1980). The extent of illitization was limited also by cation (K+) availability, time, and temperature. The rate of reactions across mineral faces can be shown through mathematical modeling i.e. kinetics (duration of the reaction; Elliott and Matisoff, 1996). The theory of kinetics determined the duration of a reaction as a system approached equilibrium (Giles, 1997). The loss of smectite to form illite layers has been modeled with an Arrhenius type kinetic expression (Elliott and Matisoff, 1996). Time and temperature in this reaction are independent parameters (Waples, 1980). At low temperatures, illite precipitated slowly. Conversely, rapid illitization occurred as an instantaneous alteration of pore-water chemistry at higher burial temperatures.

Kinetic models of diagenetic evolution were used to derive a time and temperature history to predict thermal maturation. These kinetic expressions (Equation 3 and Equation 4) can be computed at a range of geologic setting using a time-depth burial curve, geothermal gradients, and availability of K^+ ions (Elliott and Matisoff, 1996). In this equation, S represents the amount of smectite lost to form an ordered I-S (M). Time is represented by t and the variable k is the rate constant (time -1).

$$dS/dt = -k1S \qquad (3)$$

Equation 3: This equation was adapted from Huang et al. (1992).

$$k1 = A\, e^{(-Ea/RT)} \qquad (4)$$

Equation 4: The parameter k1 is the illitization rate constant described in Equation 4. Where A is a pre-exponential rate constant (sec-1). Ea is the activation energy of this process. R and T are the gas constant and absolute temperature, respectively.

1.4.4 Illite and Petroleum

Illite has been successfully employed by the petroleum industry as a semi-quantitative geothermometer (Figure 11). Additionally, since K^+ is fixed strongly within the interlayer, diagenetic illite has been found to be a suitable for K-Ar geochronologic methods at diagenetic temperatures. Consequently, the timing of thermal maturation in shales leading to the expulsion of crude oil and natural gas can be estimated via a K-Ar age of diagenetic illite in shales. This geothermometer is based on the tightly held ^{40}K within the interlayer between two illite layers. K-Ar methods have been used extensively to determine the approximate age of heating or timing of diagenetic events (e.g., Weaver and Wampler, 1970; Hower and Aronson, 1976; Elliott and Haynes, 2002). Pevear (1999) combined illite polytype data with K-Ar ages of illite to estimate the ages of diagenetic illite in shales (Illite Age Analysis, Pevear, 1999). IAA is a technique to derive the age of diagenetic illite in the presence of detrital illite.

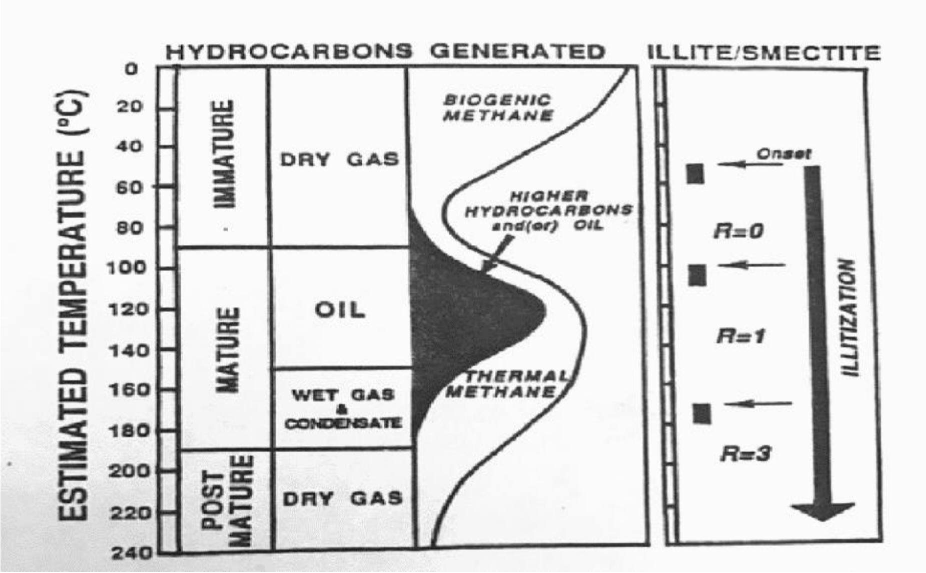

Figure 11: This table was adapted from Pollastro (1993). It is shown that the time and temperature needed to created natural gas coincides with increasing illitization.

1.5 Thermal Maturity Estimates of the Wolfcamp Shale

The distribution and effectiveness of hydrocarbon maturation has been a function of sedimentation (deposition and preservation of organic carbon), subsidence (temperature from burial), and time. Carter et al. (1998) used burial history models to deduce that oil generation began in basins (containing the Wolfcamp Shale) as early as late Mississippian Period. Per these models, this formation has reached thermal maturity generating crude oil and natural gas by the end of the late Cretaceous (Engle et al., 2016).

These determinations were based on assumptions that the reservoirs associated were associated with these source rocks. In these tight gas plays, it was also assumed that there was little to no appreciable lateral migration of mature organic matter and expulsed crude oil and natural gas. Thermal maturity measurements were essential parameters to determine the viability of source rocks as producers of hydrocarbons. The degree of thermal maturity can be evaluated by changes in petrographic, clay mineral, and/or organic indices (Osborn, 2006). Examples of thermal maturity indicators relevant to this study were described in the following paragraphs.

Many diagenetic reactions occurred at the approximate temperature and pressure regime needed to transform organic matter in shales or petroleum source rocks (OM) into crude oil and natural gas (Velde and Lanson, 1993; Pevear, 1999; Velde and Vasseur, 1992). Time and temperature both exerted considerable control in the generation of crude oils and natural gas from OM in source rocks. Diagenetic parameters (temperature, time) lithostatic pressure, rate of subsidence typically drive the extent and rate of the conversion of kerogen and related materials (proteins, lipids, amino acids) to crude oil and natural gas. This shale was deposited in both deep water and continental in the Midland Basin. The amounts of total organic carbon (TOC) measured and recorded from well data varied laterally and vertically. TOC within the Wolfcamp Shale ranged from 0.8 to 17 wt. % (Higley et al., 2014; Cardott and Lambert, 1985; Kirkland et al., 1992).

The organic material fractions of black shales are composed of type-II kerogen and bitumen (which forms from the thermal maturation of kerogen; Kirkland et al., 1992). The source of type-II kerogen has been traced to marine phytoplankton, zooplankton, and remains of some of the first terrestrial herbaceous plants (Kirkland et al., 1992; Sullivan, 1985). Immature kerogen accumulated as micrometer pockets along with siliciclastic grains, in turn, created petroleum source rocks. Covalent-bonded compounds composed alkanes and aromatic compounds of carbon and hydrogen were converted to crude oil and natural gas. Biogenic natural gas formed typically at temperatures well below the oil-generating window. Through the decay of this material during diagenesis and thermal maturation, carbon-bearing compounds (alkanes, aromatic) became incorporated in marine sediments so that global crude oil production 85 million barrels each day or 31 billion barrels each year (Ryan, 2014). OM within this Paleozoic shale was highly preserved due to anoxic burial conditions, found in pores that would otherwise contain water, ions, or mineral cavities, and bonded within clay sheets.

The maximum temperature reached in a basin can be used to predict whether the shale will produce, oil, wet-gas, or dry gas in addition to the characterization of the organic matter itself. With increased temperature due to increased burial, the solubility of OM is increased. This change in behavior allowed for the release of organic acids (such as acetate and bicarbonate), CH_4, and CO_2 (Palandri and Reed, 2001; Harrison and Thyne, 1992). As the temperature was increased, CO_2 was formed through the thermal breakdown of OM. The migration of these organic acids enhanced the dissolution of feldspar thus providing a source of K^+ and Al^{+3} to form diagenetic illite in shales (Hower et al., 1976; MacGowan and Surdam, 1990). The dissolution of feldspar also provided Si and Al for the precipitation of other minerals such as kaolinite. As the organic matter was maturing, the stability of the silicate minerals were controlled by temperature, pore fluid chemistry, accessory minerals, and the effects of organic acids.

In addition to the increase in temperature, the burial of sediment increased the effective stress (σ_e) on underlying units. Wickard et al. (2016) noted the presence of relict hydrocarbons within horizontal fractures of the Wolfcamp Shale. Overpressuring, a function of σ_e, occurred during hydrocarbon migration (Marshall, 1982) common in sedimentary basins with high levels of subsidence. Hydrocarbon migration was interpreted as occurring after secondary porosity due to its location within the matrix. It was not uncommon for a Paleozoic oil shale to contain vertical fractures when the maximum principle stress was vertical (Eseme et al., 2007). Hydraulically-induced fracture propagated in the same direction during the search for natural gas (Eseme et al., 2007). Horizontal fractures occurred in relative shallow shales where there is a smaller discrepancy between vertical and horizontal stress (Eseme et al., 2007). These fractures were propagated by overpressuring.

Lastly, the time-temperature index (TTI) was formulated to evaluate thermal maturity and related geochemical reactions. Organic petrologists correlated measured values of the vitrinite reflectance (VRo) against the depth of burial to derive burial temperature. Vitrinite was formed from the lignin in cell walls of vascular plants (Waples, 1980). This technique measured the amount of incident light reflected from the surface of the organic material at a magnification of 500 x (Waples, 1980). Thermal maturity can be estimated knowing the maximum temperature (T_{max}; (Jarvie et al., 2001; Equation 5). The oil and gas generating window was correlated at a range of vitrinite reflectance values from 0.55%-1.15%, reaching optimal maturity at 0.90% (Waples, 1980). The earth's crustal geothermal gradient, 25^{o}C/km, paired with the estimated depth, can be used to derive the maximum temperatures (T_{max}) corresponding to specific depths of burial in the absence of knowing a burial curve.

$$\%R_o = 0.0180 \times \mathrm{Tmax} - 7.16$$

Equation 5: This equation, adapted from Jarvie et al. (2001) provides the calculation of %VRo from maximum temperature (Tmax).

Estimates of organic parameters of thermal maturity have been useful to prevent the cost and environmental disturbances associated with an unsuccessful well. The extraction of hydrocarbons trapped in black shales was based on knowledge of a source rocks' thermal maturity. The continuous burial of hemipelagic sediments advanced the biogeochemical and thermal processes producing hydrocarbons. It is assumed and typically observed that thermal maturity increased with depth. Along with increased thermal maturation with increased depth, uniaxial strain caused compaction of previously unconsolidated sediments with increased burial depth. During burial, a shale's low permeability prevented the lateral migration of generated oil and natural gas and precursion organic compounds to adjacent reservoir rocks. Although the thermal maturities of these basins are well known from extensive petroleum studies, there are fewer studies addressing the effects of porosity and permeability of stored gas (Clarkston et al., 2013; Jin et al., 2013; Masterlez et al., 2013; Ruppert et al., 2013; Anovitz and Cole, 2015). The performance of a reservoir or well is dependent on the storage capacity (porosity), pathways of carbon migration through accessible and connected pores (permeability) as well as knowing the presence of trapping mechanism (Pevear, 1999). Increasing knowledge of the timing of hydrocarbon generation reduced the risk of drilling inefficient wells due to the lack of a trapping mechanism (Pevear, 1999). It is critical to establish a time-temperature history that correlates the formation of porosity and trapping mechanism to the cracking of organic material into oil or natural gas.

1.6 Effects of Thermal Maturity on Porosity

Although the thermal maturity of black shales has been studied extensively for oil exploration, there have been fewer number of studies addressing the effects of microporosity and micropermeability on the migration and expulsion of crude oil from source rocks. The effect of microstructure on transport and fluid production had renewed interest in petrophysical studies (Nagaraj et al., 1990; Anovitz et al., 2017). Due to the existence of complex pore networks and heterogeneous nature of shales, their complex pore morphology have not been well understood. These discrepancies within shales required a range of field and lab techniques to characterize the overall transmissivity of rock fabric. Methodologies for probing microstructures has improved with time including innovative methods such as well logs, seismic data, ion beam milling, gas adsorption, SEM, backscattering neutron/electron imaging, and X-ray scattering. Increased knowledge and ability to recognize structural patterns in thermally mature source rocks will improve performance and control production during the synthesis of natural gas. These studies are important to denote conduits for fluid and gas migration are formed from micropores and fracturesin nonporous rocks.

Black shales are relatively impermeable and nonporous. Shale has an extremely high range (0-30%) of average porosity (Anovitz and Cole, 2018). Pores present in shales are known to have been distributed heterogeneously, most on the nanometer scale. This micro and nano-porosity has been attributed to organic content, mineral content and diagenetic processes alike. In turn, the permeability of shales have also been recorded as very low due to the presence of micro and nano-pore sizes. The effective porosity has been measured in the range of somewhere between 8-29% although most are less than 15% (Anovitz and Cole, 2018). Variations of microstructures have been attributed to diagenetic responses (interlayer ion expulsion) to discrepancies in texture, chemistry, thermal maturity (Hester et al., 1990).

Porosity is defined by the total amount of void space divided by the volume of the entire rock, including those pores that are not accessible for fluids or gas exchange (Equation 6). Porosity can either be effective, allowing the migration of fluids or closed (Anovitz and Cole, 2015). Hierarchies of pore structures are assessed by size, shape, and connectivity. Pores are typically classified into three categories based on diameter, largest to smallest respectably: Macroporosity (>10 μm), mesoporosity (Ashman and Puri, 2002), micropores (10- 75um) and nanopores (< 75 um) (Loucks et al., 2012) according to the IUPAC classification scheme. Micropores may connect larger pores perpetuating the migration of organic material.

$$\Phi = Vp/ Vt$$

Where: Φ is the effective porosity

Vp is the volume of interconnected pores

Vb is the total volume

Equation 6: Mathematical expression for total effective rock porosity (Ashman and Puri, 2002).

The development of primary porosity has been seen as a function of arrangement of clastic grains, presence of cements and C-org, and tectonic forces. Pore systems have been determined by grain size distribution at deposition, lithostatic and effective stress, geothermal gradient, and mineralogy. The accessibility and connectedness of microstructures are determined by mechanical compaction as well as pore fluid reactions (precipitation, cementation, and dissolution; Anovitz, 2017). Compaction, cementation, and diagenetic mineral formation are attributed to a decrease in porosity and permeability (Hester, 1980). Gravity anomaly increases thermal maturity due to increase in sedimentary thickness/sedimentary load.

Lithification has been often associated with a decrease in porosity and permeability, thus reducing the economic viability of a formation (Giles, 1997). Mechanical compaction during burial directly controlled the reduction of pore space (Figure 12). Initial porosity has been diminished by compaction with depth. The effective stress of these units can be calculated with each depth interval. The lateral compression of sediment loading alters volume and pore space. Porosity volume alteration also occurs during oil generation, chemical compaction, and clay mineral transformations. The thermal expansion of minerals also affected the structure and properties of these shales. The plasticity of kerogen deformation alters porosity by generating fluids and migrating through the matrix (Eseme et al., 2007)

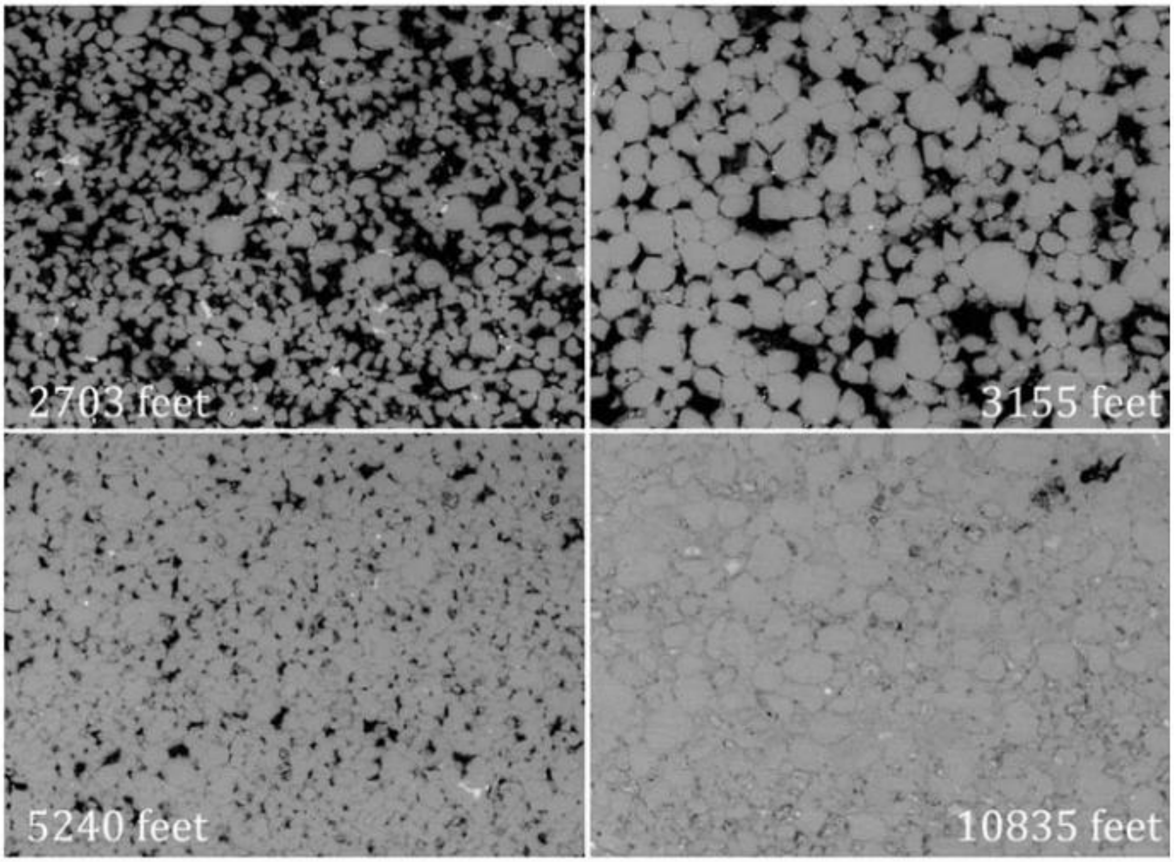

Figure 12: BSE images from Anovtiz et al. (2017) demonstrating the effect of cementation and decrease in porosity with depth with the St. Peters sandstone.

Neoformation of minerals may disaggregate larger pores into smaller pores during formation. An increase in micropores with depth is attributed to the disaggregation of preexisting macropores (Anovitz et al., 2017). Modifications to pore geometry affect storage capacity as well as sorption inclinations. Elongated pore structures in organic-rich shales allow higher rates of sorption across pores, such as the sorption of potassium to form illite. Geochemical reactions may even modify existing pores to accommodate gas expansion (Anovitz et al., 2017; Anovitz and Cole, 2018).

Nagaraj et al. (1990) described various locations of types of pore spaces within clay-sized fractions. Open porosity in phyllosilicates often occurred intraparticle and interparticle mineral grains (Schieber, 2010), between edges of minerals, and/or between mineral faces. Porosity can be found between the edge-face and edge-edge boundary of clay particles. Porosity can also be found between groups of clay minerals, also known as floccs. Pores have been found between grains or minerals or clay aggregates or exist within organic matter (high internal surface area- affect gas sorption). Porosity might be present with the inorganic or organic constituents of these shales. These pockets of porosity impacted the mechanical strength, yield stress of pores. For instance, the elastic moduli of shale is decreased with the compaction of pores and matrix minerals. Kerogen, a more ductile material, has been seen to infiltrate pores during compaction more so than siliciclastic matrix materials (Berger et al., 1997; Harrison and Thyne, 1992; Eseme et al., 2007, Pommer and Milliken, 2015).

The Wolfcamp Shale demonstrated complex intra-organic microstructural features throughout the evolution to complete thermal maturation (Wickard et al., 2016). Time-temperature burial influenced the mineral matrix and organic matter composition by inhibiting the mobility/storage of natural gas within a source rock. Immature kerogen was weaker than inorganic constituents of the matrix; therefore, organic porosity was more susceptible to deformation. Kerogen will more readily integrate into pore spaces when stress is applied. Shales with higher amounts of organic material will experience a decrease in overall porosity.

Pores either contained moisture or air (Eseme et al., 2007). During heating, these fluids (water or hydrocarbons) became more volatile, and deformed plastically (Eseme et al., 2007). Upon increased heating, water stored within mineral structures (such as smectite) was expelled, and kerogen continued to deform and decay (Eseme et al., 2007). The heating of pore fluids/water during heating has led to the cracking of bitumen. Thermally mature hydrocarbon chains may flow into or migrate across pores. The development of hydrogen chains to mature natural gas has shown to decrease overall matrix porosity (Mohnhoff et al., 2016). Additionally the precipitation of minerals during diagenesis may impede fluid and vapor migration throughout a source/reservoir rock. Cementing minerals and flocculation of clay minerals may segment or completely destroy primary porosity, often referred to as pore throating (Mohnhoff et al., 2016). Illite and mature TOC occupied space that would otherwise have been void. This textural change was referred to as 'pore throating' or 'pore plugging' (Mohnhoff et al., 2016).

Knowledge of particle distribution and configuration played an important role in determining reservoir vitality and further sedimentary basin modeling. The dispersion of micron-size particles affected material performance; such as mature natural gas generation. Nagaraj et al. (1990) noticed a bimodal distribution of porosity within shales that coincided with Anovitz's et al. (2017) observations of bimodal porosity in an Ordovician sandstone. However, there was an observed considerable difference in the location and geometry of porosity between Paleozoic black shale samples at different resolutions and grain sizes. Understanding porosity development was crucial in predicting hydrocarbon production and storage (Nagaraj et al, 1990). The ability to predict porosity trends is crucial to successful well placement and efficient resource extraction. To better understand the qualitative characteristics of this basin, high-resolution techniques were used. Pore networks carry fundamental information able to improve reservoir modeling and petrophysical exploration.

2 METHODS

The existence of micrometer structures has been investigated through various methods. Increased knowledge has improved technology and computing in-lab capabilities. These radiological methods include SEM, TEM, Ct computer tomography, Neutron scattering, and X-ray scattering. Each of these methods used in conjunction would provide accurate estimates of nanometer structures. High-resolution images can be used to probe samples with unprecedented clarity. The analysis techniques were chosen based on their ability to accurately probe porosity size, shape, and surface area and produce accurate representations when abetted with mineralogical data.

Most laboratory-based techniques used in this study were conducted at Georgia State University. These analytical approaches were purposefully designed to study the thermal history of a black shale source rock. The techniques used in this research to study the thermal history of the Wolfcamp Shales included X-ray diffraction, petrography of thin sections, scanning electron microscopy (SEM), and preliminary data on small-angle X-ray scattering (SAXS)/ultra-small-angle X-ray scattering (WAXS). These data were designed to provide new insights as to the thermal history and the evolution of porosity in these shales. Isotope dating of samples at the sub-micron level can also be used to date the timing of diagenetic processes, particularly a proxy for the timing of the maturation of kerogen to crude oil and natural gas. The sample register can be found in Table 1. K-Ar geochronology of clay fractions was planned for this study. The argon vacuum extraction line is being brought back to operation after the move to Sparks Hall from Kell Hall.

2.1 Sample Preparation

Nine samples of the Wolfcamp Shale from various depths in the Midland Basin. Six Wolfcamp samples were provided by Dr. Elmore's group (ConocoPhillips School of Geology and Geophysics, Univ. of Oklahoma). The Wolfcamp Shale samples were collected by Devon Energy from the eastern shelf of the Midland Basin from the Cortes (WC), Pizzaro (WP), and Pioneer (WI) cores. Richard Whittington (QEP Research) provided the samples from the Wolfcamp D/Cline formation from the University 7-27 #9 Well (UN). It is assumed these samples were cut parallel to bedding. Accompanying well data provides depths and location of samples are shown in Table 1. These samples were chosen for their varied thermal maturities (0.8 to 1.07% VRo). The highest thermal maturity (1.07% VRo) occurred in the deepest Wolfcamp sample. The observed maximum temperature estimated from VRo was 210 ^{o}C (Roberts and Elmore, 2018).

After collection, samples of this blocky shale were manually disaggregated. Approximately 25 grams of each sample was soaked in deionized water for three weeks. This soaking encouraged further disaggregation needed to separate the clay from the sand and silt materials. After soaking, the shale was lightly crushed to sizes <1 mm by eye. Several treatments described in Section 3.2 were employed to remove cements and gross organic matter from soaked and lightly crushed samples of the whole shale rock (Jackson, 1985). These treatments aided the disaggregation of clay from these samples. Removal of these compounds promotes the parallel orientation of clay minerals aiding in successful X-ray diffraction analyses. The following treatments were developed for phyllosilicate treatment by M.L. Jackson (1985).

Sample ID	SAXS ID	Period/Formation	Depth (ft)	VRo (%)
WP15-4	9TO-004	Mississippian Wolfcamp	5949.1	0.8
WP42-1	9TO-005	Mississippian Wolfcamp	6136.7	0.8
WP60-1	9TO-006	Mississippian Wolfcamp	6305.9	0.8
WC 9-3	9TO-001	Mississippian Wolfcamp	6433.35	0.9
WC 50-3	9TO-003	Mississippian Wolfcamp	6843.45	0.9
WI 27-2	N/A	Mississippian Wolfcamp	9704.8	1.07
UN 9-01	9UL -001	Mississippian Wolfcamp	10637.5	0.95
UN 9-02	9UL -002	Mississippian Wolfcamp	10705.8	0.98
UN 9-03	N/A	Mississippian Wolfcamp	10791	0.99

Table 1: In this sample ID depth, geologic formation, and thermal maturity are shown.

2.1.1 Sample Pretreatment

Each sample was treated to remove carbonate and iron (III) oxide cementing materials that have sorbed to the faces of the phyllosilicate minerals and inhibit size separation. Additionally, the presence of cementing materials obstructed the preferential alignment of phyllosilicates for X-ray diffractometry. One normal sodium acetate-acetic acid buffer (pH=5, NaAc-HAc) was used at 50 C to remove carbonate cements. These treatments were run overnight at 50°C. These treated samples were washed in this NaAc-HAc to remove any soluble divalent ions and to leave the sample material wetted in the buffer solution. Organic matter was removed in part by reacting these carbonated-treated samples with 30% hydrogen peroxide at 50°C overnight. This treatment was only partially successful in removing all organic matter as judged by the dark color of the treated samples. The heterogeneity of samples became apparent during this treatment (Figure 13)

Other treatments such as methylene chloride or heating were not used because some or all of these samples would be analyzed for their ages by K-Ar geochronologic methods. Iron (III) oxides were removed by the citrate-dithionate-bicarbonate method at 50°C (Jackson, 1979). These samples were washed in buffer several times to remove soluble alkali and alkaline earth metals. The samples were washed in methanol (absolute) to prevent the development of microbial communities.

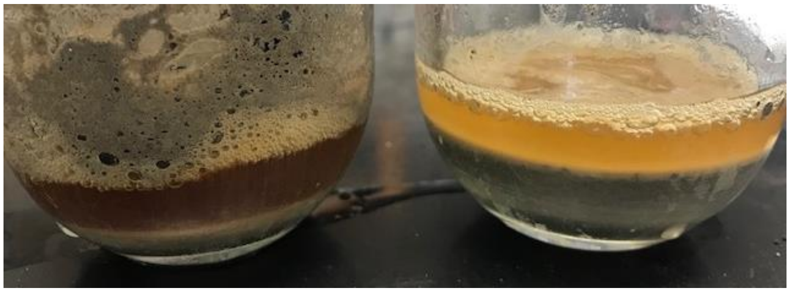

.

Figure 13: The heterogenous nature of shales was apparent during sample preparation.

2.2 Size Separation

Following the chemical treatment, sediments were separated by size into sand, silt, and clay fractions. The sand (> 50 µm), silt (2-50 µm) and clay (< 2 µm) fractions were separated by timed settling (Jackson, 1985). Settling time is dependent on the suspension of grain size. Centrifugation time was determined by using a formula by Jackson (1979) (Equation 7). The clay fraction was separated into three clay subfractions (1-2 µm, 0.25-1.0 µm, and < 0.25 µm) to concentrate the diagenetic illite clay (e.g., Pevear, 1999). The settling rates are those given in Jackson (1979). Sand was settled in a column of 10 cm in 40 seconds. Silt was settled in a 10 cm column of the solution in 4 minutes. The fine silt (2-20 µm) fraction was obtained by settling the < 20 µm eight hours for every 10 cm of solution. The clay fraction was then settled using 1*M* $CaCl_2$, washed by repetitive centrifugation in deionized water and suspended. The resultant clay fraction was centrifuged to obtain the 1-2µm. 0.25-1 µm, and < 0.25 µm clay fractions. These samples were centrifuged at various speeds in a Baxter Varifuge 3.0 Centrifuge. The time for centrifugation was calculated given a distance from the axis to the top of the sediment in the centrifuge tube (R) and the length of the axis of rotation (S) per the Equation 7 below (Jackson, 1979). Centrifugation effectively separates sediment and supernatant according to differences in densities. Samples of the clay fraction less than 1 µm were centrifuged in Nalgene plastic bottles for high-speed centrifugation.

$$t_{(minutes)} = \frac{\left[63.0 \times 10^{8}\, \eta \, \log_{10}\left(\frac{R}{S}\right)\right]}{\left[(N_m)^2 \left(D_{\mu m}\right)^2 (\Delta s)\right]}$$

Equation 7: Various size fraction settling times (Jackson 1979).

The <0.25 µm fractions were settled in 1*M* $CaCl_2$. A sufficient amount of clay was seen in two of the xx <0.25 µm fractions. It was thought that Na citrate might have been used by mistake to settle these <0.25 µm fractions. 1*M* $CaCl_2$ was added again and not clay settled in those fractions. We have five <0.25 µm fractions for this study (UN 9-01, UN 9-03, WP60-1, WC 9-3, and WI 27-2).

2.3 X-ray Diffraction

X-ray diffraction (XRD) is the interaction of X-rays through the internal crystalline structure of a solid, resulting in a coherent and constructive scattering of X-rays waves. The d-spacing values of minerals can be derived from the diffraction X-rays by use of Bragg’s law (Equation 8; Moore and Reynolds 1997). This nondestructive technique was used to identify the clay minerals present in these samples. X-ray diffraction of mineral samples yielded a set of d-spacing values characteristic of minerals present in these samples. The d-spacing is the distance between two parallel plans of atoms in the mineral’s internal atomic structure. Each mineral or compound has a unique set of d-spacing values, a fingerprint of the mineral. The clay fractions were prepared by dropping liquid clay onto a petrographic slide. The clay dried in away such that the h-k or a-b plane of phyllosilicate minerals laid flat on the petrographic slide. X-ray diffraction of that oriented mount diffracted only the 00l planes of the phyllosilicate mineral present.

$$2d \sin\theta = n\lambda$$

Equation 8: Bragg’s law (Moore and Reynolds 1997).

The oriented mounts were scanned from 2° to 32° 2-Θ using Ni-filtered Cu (Cu radiation: λ =1.54059Å) radiation (45 kV, 40 mA) at a speed of 2° 2-Θ per minute. The oriented mounts were treated in three ways prior to scanning: air-dried, glycol saturated, and heat-treated (500◦°C, 1 hour). The d-spacing values of each diffraction peak were measured using the PANalytical EXPERT PRO diffractometer software. Corresponding diffraction patterns were evaluated to identify the presence of mixed-layered illite smectite (I-S), the I-S stacking order and the percentage of illite layers in I-S per tables in Moore and Reynolds (1997). The stacking order the percentage of illite layers in I-S have been correlated to burial temperatures to study the thermal histories of sedimentary basins (Waples, 1980; Moore and Reynolds, 1997; Pollastro, 1989). The R-descriptor (*Reicheweite*, or reach back) has been used to express the stacking order of illite or smectite in mixed layered I-S. The I-S having a stacking order of R=0 has been called random ordered I-S. This stacking order did not have consecutive illite layers stacked on each other. Random ordered I-S typically has <50% illite or ≥ 50 % smectite layers. The R ≥ 1 I-S signified the presence of illite and smectite layers stacked in alternation along the c-axis. This order is called “short range”. R≥3 (also known as long-range) is the nomenclature for mixed-layer clay containing over 80% illite. This stacking order features no less than three illite layers stacked after every smectite layer. The stacking order of I-S has been used in the study of the thermal histories of sedimentary basins. Waples (1980) correlated the stacking order and/ or the fraction of expandable layers with the integrated TTI. The timing of the decrease in expandable clay (i.e., conversion to illite) coincided with the TTI needed to generate mature hydrocarbons (Waples, 1980). The window for oil and wet gas appear at the beginning of the R≥1 stacking order. Isotope dating of samples at the sub-micron level can also be used to date the timing of diagenetic processes, particularly a proxy for the timing of the maturation of kerogen to crude oil and natural gas.

2.4 Porosity Determination

The interaction of X-rays through a medium can lead to refraction, diffraction, absorption, and scattering. Dependent on the angle of the incident X-ray beam, X-ray scattering (also known as small-angle scattering SAXS) can occur at small angle of the X-ray beam and the sample. Variants of small-angle X-ray scattering include Small/Ultra small angle/Wide-angle X-ray scattering (SAXS, USAXS andand WAXS). This technique has been proven to be a useful tool for structural characterization of materials (Nirschl and Guo, 2018). This advanced technological approach uses small monochromatic X-rays to quantify the geometry and size of submicron pore structures. Thin sections of the Wolfcamp Shales were analyzed with X-ray scattering at the Argonne National Laboratory APS Beamline (9-ID; 10-24 keV) to permit the visualization of nano and microporosity in these shales. The datasets generated were viewed in Igor Nika and Irena plugins (Ilavsky and Jemian, 2009). The Igor software was navigated with the help of Dr. Anovitz and the online web manual as a comprehensive guide for processing data.

Five polished thin sections (approx. 0.30 mm thick) were prepared by Spectrum Petrographics Inc. These thin sections were probed with an incident X-ray beam along the sample surface normal (Anovitz et al., 2017; Anovitz and Cole, 2018). These incident X-rays were scattered at various angles and detected. The SAXS analysis was performed at Argonne National Laboratory by Dr. Lawrence Anovitz, Dr. Elliott, and colleagues in the October 2016. The corresponding sample IDs for this experiment can be found in Table 1.

For the actual scattering experiment, the thin section was situated normal to the X-ray beam. This incident beam was directed at areas of these thin sections preselected as representative areas of shale-rich matrix (Figure 14). The synchrotron beamline created a high scattering intensity used to assess the variation in densities between the sample and its surroundings; also known as excess electron density (Nirschl and Guo, 2018). This technique is powerful when used on nonporous materials, like shale, to observe pores or void spaces. High-resolution measurements were created from the assemblage of SAXS experiments; probing structures as small sub-micron in diameter. Observations in this experiment were made at the Å scale. The presence of pores and minerals determined the scattering length density. The amount and length of scattering were determined by the detector that is placed at a distance from the sample. The pore (or particle) diameter can be approximated. Small pores scatter X-rays at larger angles and therefore have higher q values. While larger pores scatter X-rays at small angles therefore having lower q values (Leu et al., 2016).

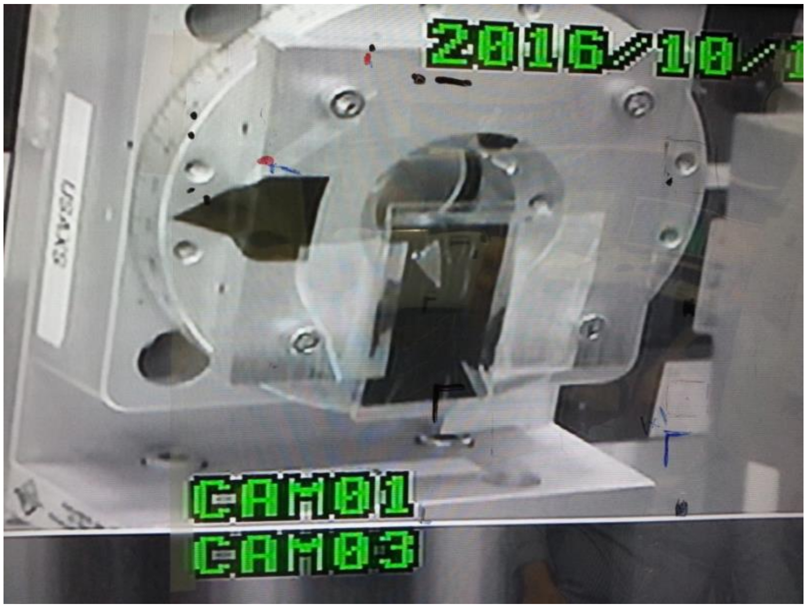

Figure 14: The approximate location of SAXS measurements is shown in this image. Measurements were taken between the two pieces of metal tape.

WAXS provided complementary scattering data through the use of wide angle scattering. The WAXS scattering pattern included the scattering and diffraction by micron-sized particles. The WAXS pattern is in effect an X-ray diffraction pattern. Data was interpreted to confirm mineral identification from diffraction patterns. The data analysis software Igor Pro with Nika and Irena plugins were used to produce scattering curves that illustrates the distribution of porosity in theis shale. The derived porosity distributions was compared to their thermal maturity levels for each sample.

The raw data was uploaded into Igor. Samples were desmeared until all errors sat at zero (Figure 15). Data was then manipulated to combined SAXS and USAXS datasets into a single scattering curve using the ‘data merging panel’ in Irena (Figure 16). The data was then evaluated in the scattering contrast calculator. Samples were calculated assuming that all pores were spherical. For this experiment it was assumed that the samples only contain two phase, empty pore was evaluated against a illite. Illite was used as the comparator as it is the most prevalent clay mineral in these shales. Comparing these scattering length densities gave an approximate contrast value. This value was calculated by using the mineral formula and density of illite. The change in density between these phases allowed for the computation of an accurate scattering contrast (X-ray delta rho = 519). The amount of scattering is a function of mineral composition or atomic number.

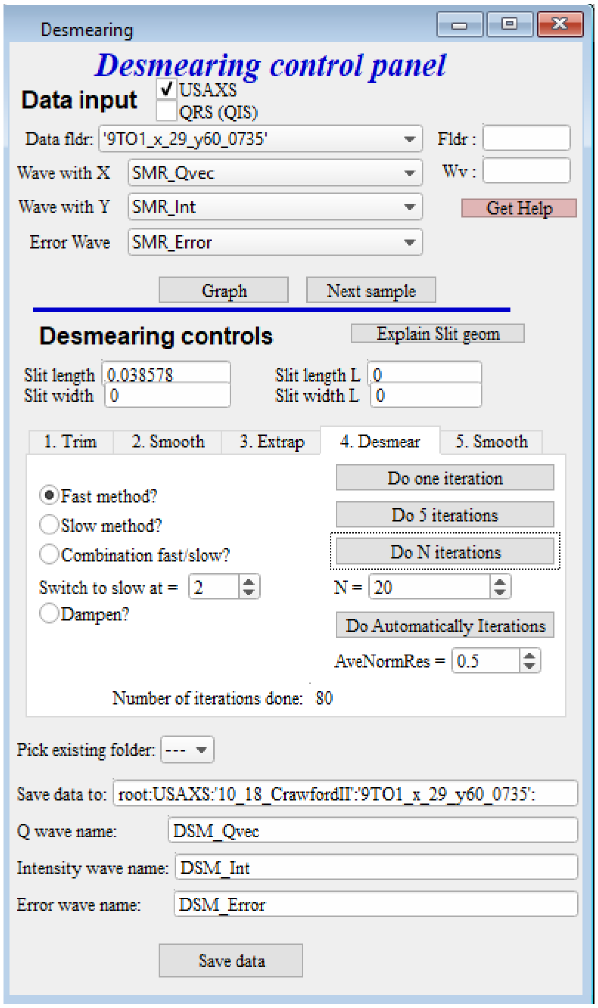

☑ USAXS
☐ QRS (QIS)

Data fldr: '9TO1_x_29_y60_0735'
Fldr :
Wave with X: SMR_Qvec
Wv :
Wave with Y: SMR_Int
Error Wave: SMR_Error

Slit length: 0.038578
Slit width: 0
Slit length L: 0
Slit width L: 0

● Fast method?
○ Slow method?
○ Combination fast/slow?
Switch to slow at = 2
○ Dampen?
N = 20
AveNormRes = 0.5
Number of iterations done: 80

Pick existing folder: ---
Save data to: root:USAXS:'10_18_CrawfordII':'9TO1_x_29_y60_0735':
Q wave name: DSM_Qvec
Intensity wave name: DSM_Int
Error wave name: DSM_Error

Figure 15: Desmearing control panel found in Irena plug in for Igor. Each sample was desmeared until all errors nromalized to 0.0.

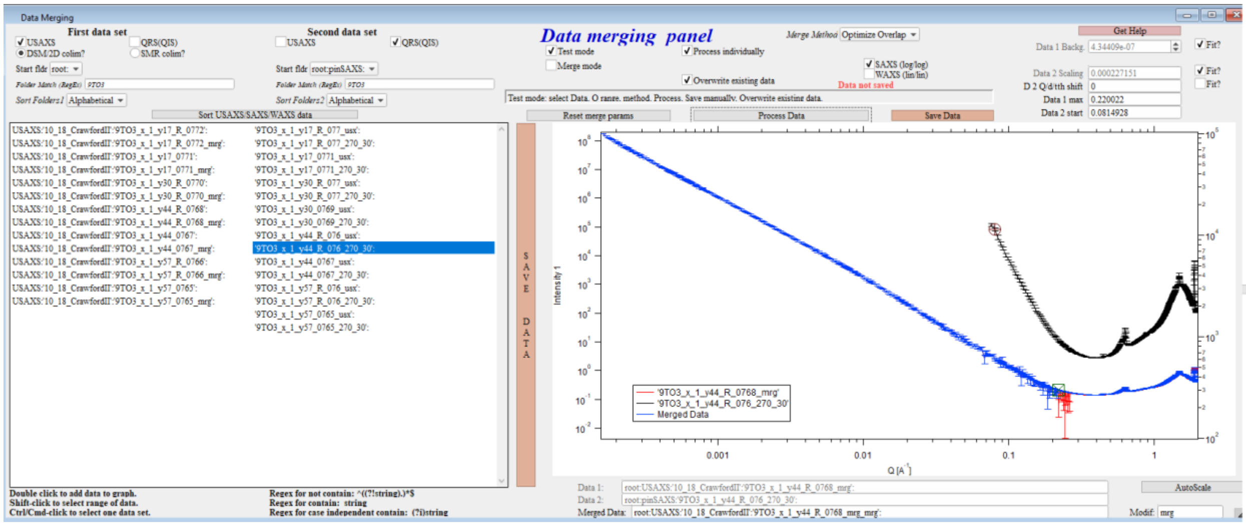

First data set
☑ USAXS ☐ QRS(QIS)
● DSM/2D colim? ○ SMR colim?
Start fldr root:
Folder Match (RegEx) 9TO3
Sort Folders1 Alphabetical

Second data set
☐ USAXS ☑ QRS(QIS)
Start fldr root:pinSAXS:
Folder Match (RegEx) 9TO3
Sort Folders2 Alphabetical

Merge Method Optimize Overlap
☑ Test mode
☐ Merge mode
☑ Process individually
☑ Overwrite existing data
☑ SAXS (log/log)
☐ WAXS (lin/lin)
Data not saved
Test mode: select Data. Q range. method. Process. Save manually. Overwrite existing data.

Data 1 Backg. 4.34409e-07 ☑ Fit?
Data 2 Scaling 0.000227151 ☑ Fit?
D 2 Q/d/tth shift 0 ☐ Fit?
Data 1 max 0.220022
Data 2 start 0.0814928

USAXS:'10_18_CrawfordII':'9TO3_x_1_y17_R_0772':	'9TO3_x_1_y17_R_077_usx':
USAXS:'10_18_CrawfordII':'9TO3_x_1_y17_R_0772_mrg':	'9TO3_x_1_y17_R_077_270_30':
USAXS:'10_18_CrawfordII':'9TO3_x_1_y17_0771':	'9TO3_x_1_y17_0771_usx':
USAXS:'10_18_CrawfordII':'9TO3_x_1_y17_0771_mrg':	'9TO3_x_1_y17_0771_270_30':
USAXS:'10_18_CrawfordII':'9TO3_x_1_y30_R_0770':	'9TO3_x_1_y30_R_077_usx':
USAXS:'10_18_CrawfordII':'9TO3_x_1_y30_R_0770_mrg':	'9TO3_x_1_y30_R_077_270_30':
USAXS:'10_18_CrawfordII':'9TO3_x_1_y44_R_0768':	'9TO3_x_1_y30_0769_usx':
USAXS:'10_18_CrawfordII':'9TO3_x_1_y44_R_0768_mrg':	'9TO3_x_1_y30_0769_270_30':
USAXS:'10_18_CrawfordII':'9TO3_x_1_y44_0767':	'9TO3_x_1_y44_R_076_usx':
USAXS:'10_18_CrawfordII':'9TO3_x_1_y44_0767_mrg':	'9TO3_x_1_y44_R_076_270_30':
USAXS:'10_18_CrawfordII':'9TO3_x_1_y57_R_0766':	'9TO3_x_1_y44_0767_usx':
USAXS:'10_18_CrawfordII':'9TO3_x_1_y57_R_0766_mrg':	'9TO3_x_1_y44_0767_270_30':
USAXS:'10_18_CrawfordII':'9TO3_x_1_y57_0765':	'9TO3_x_1_y57_R_076_usx':
USAXS:'10_18_CrawfordII':'9TO3_x_1_y57_0765_mrg':	'9TO3_x_1_y57_R_076_270_30':
	'9TO3_x_1_y57_0765_usx':
	'9TO3_x_1_y57_0765_270_30':

Double click to add data to graph.
Shift-click to select range of data.
Ctrl/Cmd-click to select one data set.

Regex for not contain: ^((?!string).)*$
Regex for contain: string
Regex for case independent contain: (?i)string

Data 1: root:USAXS:'10_18_CrawfordII':'9TO3_x_1_y44_R_0768_mrg':
Data 2: root:pinSAXS:'9TO3_x_1_y44_R_076_270_30':
Merged Data: root:USAXS:'10_18_CrawfordII':'9TO3_x_1_y44_R_0768_mrg_mrg':
Modif: mrg

Figure 16: Corresponding USAXS and SAXS datasets were merged using the 'data merging panel'.

Each sample was processed through the size distribution panel 500 times to estimate the uncertainties (Figure 17). All shale thin sections were scanned under the same conditions at the beamline. These thin sections exhibited similar flat backgrounds, so that the background counts could later be removed (Figure 17). Each sample provided between 2-10 patterns due to various location of beam interaction on each thin section.

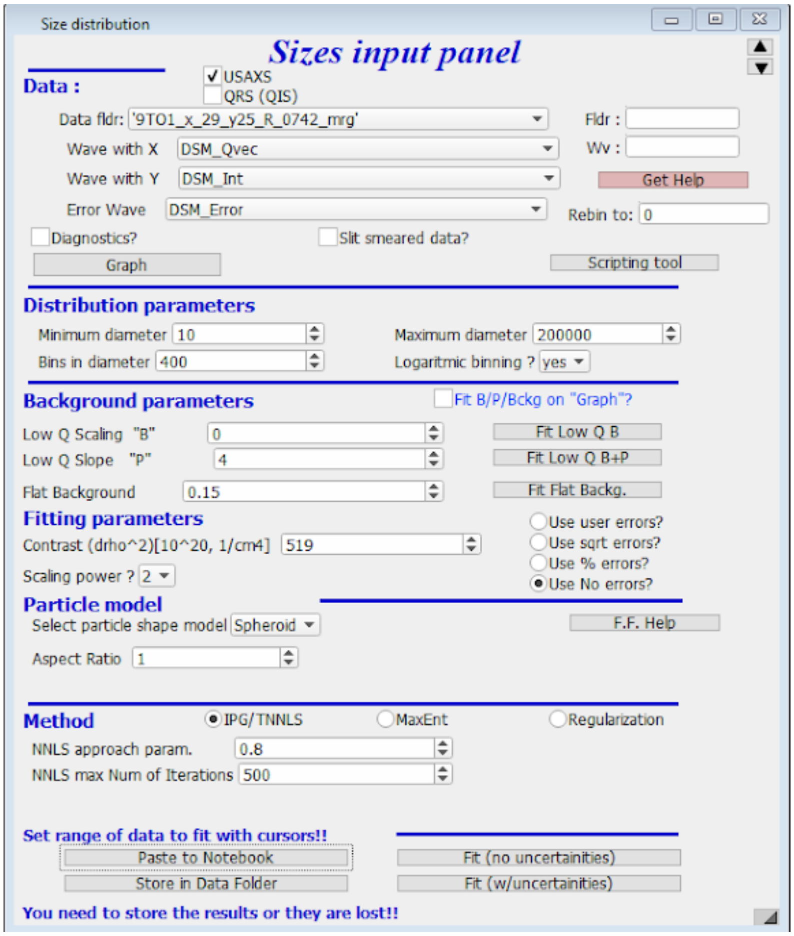

Data :
☑ USAXS
☐ QRS (QIS)
Data fldr: '9TO1_x_29_y25_R_0742_mrg'
Fldr :
Wave with X: DSM_Qvec
Wv :
Wave with Y: DSM_Int
Error Wave: DSM_Error
Rebin to: 0
☐ Diagnostics?
☐ Slit smeared data?

Distribution parameters
Minimum diameter: 10
Maximum diameter: 200000
Bins in diameter: 400
Logaritmic binning ?: yes

Background parameters
☐ Fit B/P/Bckg on "Graph"?
Low Q Scaling "B": 0
Low Q Slope "P": 4
Flat Background: 0.15

Fitting parameters
Contrast (drho^2)[10^20, 1/cm4]: 519
Scaling power ?: 2
○ Use user errors?
○ Use sqrt errors?
○ Use % errors?
● Use No errors?

Particle model
Select particle shape model: Spheroid
Aspect Ratio: 1

Method
● IPG/TNNLS
○ MaxEnt
○ Regularization
NNLS approach param.: 0.8
NNLS max Num of Iterations: 500

Set range of data to fit with cursors!!
You need to store the results or they are lost!!

Figure 17: This is the command panel seen in Igor in the size distribution function. The values entered were consistent for every sample run except for the occasional variation in the 'flat background'. This value varied based on the dataset, ranged from 0.9-0.17.

The USAXS, SAXS, and WAXS datasets were collected from six samples from the Wolfcamp Shale. These data were plotted to create scattering curves, each scattering dataset can be found in Appendix C. Information about the sample’s microscopic pore structure geometry and connectivity were determined. Multiple datasets of USAXS and SAXS were produced by each thin section. When this data was plugged into the ‘evaluate size distribution’ function three scattering curves were produced: 1) size volume distribution; 2) cumulative size distribution; and 3) cumulative surface area distribution.

Pore volume distribution was determined by the size distribution function within Irena. These curves can be read as scatterer diameters (Å) along the top x-axis. Average porosity values can be read from the ‘Scatterers diameter’ or ‘Particle diameter’ axis. The volume of particles (i.e. pores) can be read from the y-axis reading ‘particle vol. distribution’. The volume of pores provided by the Irena function were given on a linear scale. The y-axis was manipulated to a log scale so that the amount of pores were read from a log-scaled curves. The axis of particle distribution was manipulated to a log scale to view other larger scale structures or discrepancies. A linear axis with a minimum value set to 10^{-8}m was displayed for further interpretations of larger scaled pores. SEM measurements were recorded in nm (10^{-9} m). Therefore, the pores measured via SEM were not able to be seen via SAXS studies.

2.5 SEM Imaging

Scanning electron microscope (SEM) and field emission scanning electron microscope (FE SEM) analysis were conducted at Oklahoma University by Katie Garrett and Morgan Garner. SEM generated an electron beam from a heated tungsten filament (cathode). A narrow electron beam was emitted towards the sample in a vacuum. The interaction between the incident beam, electromagnetic lens, and sample can create multiple signals depending on what detectors were attached. The FEI Quanta 250 SEM was fitted with two detectors. A Bruker XFlash 61100 energy dispersive spectroscopy (EDS), used to identify various crystalline components and chemical variation in samples. Energy dispersive X-ray spectroscopy (EDX) was used for mineral/particle identification. Chemical compositions were confirmed by referring to Energy Dispersive Spectrometry of Common Rock Forming Minerals (Severin, 2004). Also, a secondary electron detector (SE2), was used to observe texture and topographic changes. The system was operated at an acceleration voltage between 20 kV with a spot size of 5 µm, and a working distance between 5 mm and 10 mm. The Zeiss NEON 40 EsB FE SEM was operated at an accelerating voltage 0.1-

30 kV. The FE SEM produced an electron beam over a smaller area. This smaller area beam increased spatial resolution while reducing charging and electrostatic background noise.

FE SEM sample locations were aimed to evaluate the approximate position of corresponding to SAXS measurements. The random sampling was assumed to be representative of the bulk average of each thin section. Each sample was viewed through three machine magnifications (5X, 10X, 50X). Through SEM and EDX systems analyst can identify mineral grains and measure pores within the rock fabric. This high spatial resolution allows the observation of mineral and pore distribution.

Manual trace measurements were taken of imaged pores to measure their sizes. Pores were traced on randomly selected locations (Figure 18). Measurements were annotated along the longest axis (La). Trace measurements provided length of pores in nm and bidirectional degrees of the La. The short axis and area was calculated post-analysis with the Fiji software. Pores were measured on the scales of nanometers and, occasionally, on microns. No vector orientation was denoted on the thin sections. No geographical coordinates could successfully be applied to these values. The direction of pore elongation was measured along an arbitrary 0 value. A pore stretched horizontally reads either 0/360 degrees. Pores appearing vertical gave measurements of 90/180. No correlation to the direction of bedding could be made.

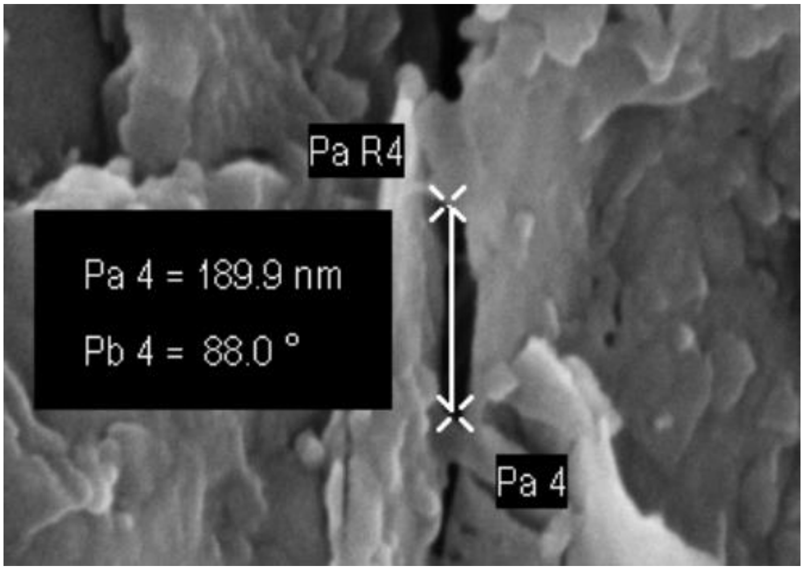

Figure 18: A FESEM image with manually traced pore data. The top number indicates the length (in nm) of the La. The second number (in degrees) indicates the amount the line is rotated from the horizontal (0).

Since the SEM did not measure volume, the area of pores was approximated with the software Fiji (Schindelinet al., 2012). Each image at 50,000 machine magnification was individually uploaded into the program. The scale was adjusted based on the number of pixels found in the scale bar at the bottom right corner of the image. The photos were then duplicated, and the threshold was adjusted. This feature highlights (in red) all the darkest areas of the photo that most likely correlate to pores (Figure 19). The threshold was manually adjusted until all the pores were highlighted. Once this feature was applied, the percent of pores, total pore area, and average pore area was calculated. This preliminary data were used to approximate bulk area found via SEM measurements and provide supplemental information to SAXS data.

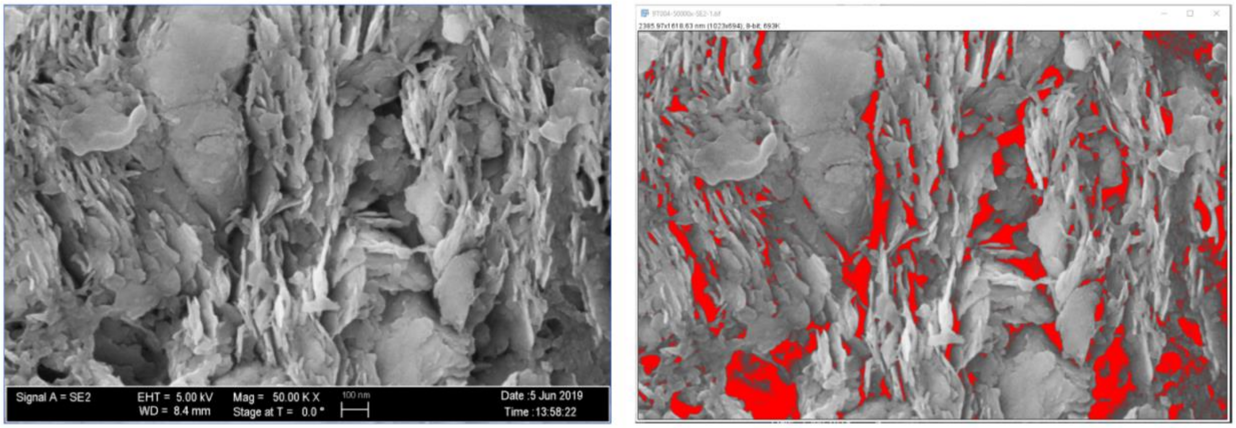

Figure 19: A FESEM image of 9TO-04 highlighted by the threshold feature in Fiji (Rueden et al., 2017). The pore spaces were highlighted and then the bulk pore area was calculated.

3 RESULTS

3.1 Clay Fraction Mineralogy

The minerals were identified in the clay fractions from their measured d-spacing values from the diffracted peaks measured from air-dried, glycol-solvated and heat-treated oriented mounts of the clay fractions. The initial diffraction analysis was conducted on air-dried oriented slides for each sample. Solvating samples in EG was needed to identify smectite and the mixed layer I-S phase. Expandable smectite swelled in the EG solution altering the diffraction peaks of interlayered clays (Moore and Reynolds, 1997). Heat-treated mounts (500^{o}C, 1 hour) were necessary to identify chlorite. These d-spacing values were compared to the known d-spacing values for minerals typically observed in the clay fraction (Moore and Reynolds, 1997). Diffraction patterns for all three analysis are attached as Appendix B. These results are summarized for each size fractions (1-2 µm, 0.25-1.0 µm, and <0.25 µm) in Table 3.

				Clay Mineralogy by Size Fraction		
Sample ID	Period/Formation	Depth (ft)	VRo (%)	1-2 µm	0.25-1 µm	<0.25 µm
WP15-4	Mississippian Wolfcamp	5949.1	0.8	I-S, Quartz, Albite	I/S & Quartz	N/A
WP42-1	Mississippian Wolfcamp	6136.7	0.8	I-S, Kaolinite, Quartz, Albite, Dolomite	I-S, Kaolinite, Quartz, Albite	N/A
WP60-1	Mississippian Wolfcamp	6305.9	0.8	I-S, Quartz, Albite	I-S, Quartz	Illite
WC 9-3	Mississippian Wolfcamp	6433.35	0.9	I-S, Quartz, Albite	I-S, Quartz	I-S
WC 50-3	Mississippian Wolfcamp	6843.45	0.9	Chlorite, I-S, Kaolinite, Albite, Quartz	Chlorite, I-S, Kaolinite, Quartz	N/A
WI 27-2	Mississippian Wolfcamp	9704.8	1.07	Chlorite, I-S, Kaolinite, Quartz, Albite	Chlorite, I-S, Kaolinite, Quartz, Albite	I-S

UN 9-1	Mississippian Wolfcamp	10637.5	0.95	Chlorite, I-S, Kaolinite, Quartz, Albite	Chlorite, I-S, Quartz	I-S, Quartz
UN 9-2	Mississippian Wolfcamp	10705.8	0.98	I-S, Quartz, Albite, Dolomite	I-S, Quartz, Dolomite	N/A
UN 9-3	Mississippian Wolfcamp	10791	0.99	Chlorite, I-S, Kaolinite, Quartz, Albite	Chlorite, I-S, Kaolinite, Quartz, Albite	Chlorite, I-S

Table 2: Observed minerals found in the clay fractions. N/A not enough for XRD analysis.

Results of XRD analyses demonstrated the presence of illite (mixed layered, chlorite, and kaolinite) and carbonate minerals for this sample suite. The main mineral constituents within these samples were illite (mixed layered illite-smectite $R \geq 3$), chlorite (d_{001}=14.2Å), kaolinite (d_{001}=7.14Å), and quartz (d_{001}=4.25Å) at all size fractions. The presence of kaolinite was confirmed by heating at 550 °C for one hour prior to the scan. Smectite was verified by the expanded peaks within glycol saturated slides.

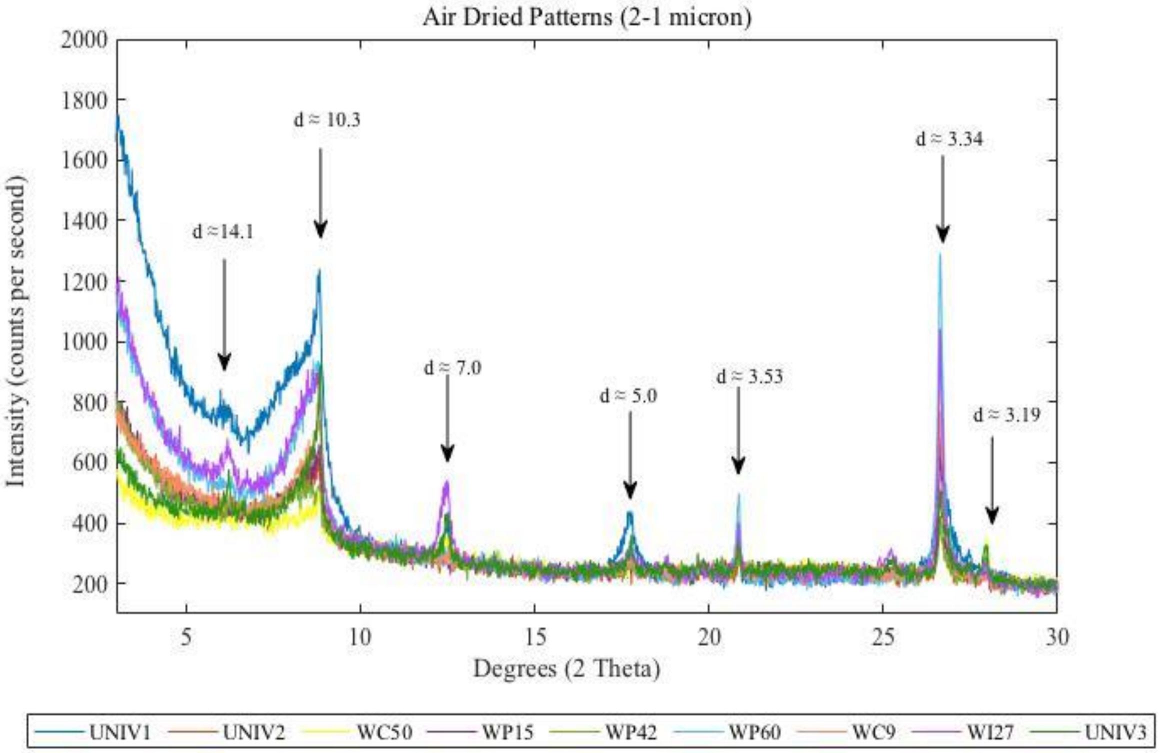

Figure 20: The combined air dried diffraction patterns of all samples at the 1-2 um scale.

All samples in the 1-2 μm sized fraction contained R≥3 I-S, likely > 90% illite, with trace amounts of quartz and albite (d_{001}=3.18Å) (Figure 20). Chlorite was found in the deepest (UN 9-1, UN 9-3, WC 50-3 and WI 27-2). This mineral persisted in these samples at the 0.25-1 μm size fraction as well. Kaolinite was present in five samples (WP 42-1, WC 50-3, and WI 27-2, UN 9-1, and UN 9-3). Although these samples were treated to remove all carbonate minerals, trace amounts of dolomite (d_{001}=2.9Å) were found in two samples (WP-42-1 and UN 9-2) in this size fraction and persisted into those 0.25-1 μm samples (Figure 21). A decrease in grain size corresponded with an overall decrease in the presence of kaolinite, dolomite, and albite among samples based on peak intensity.

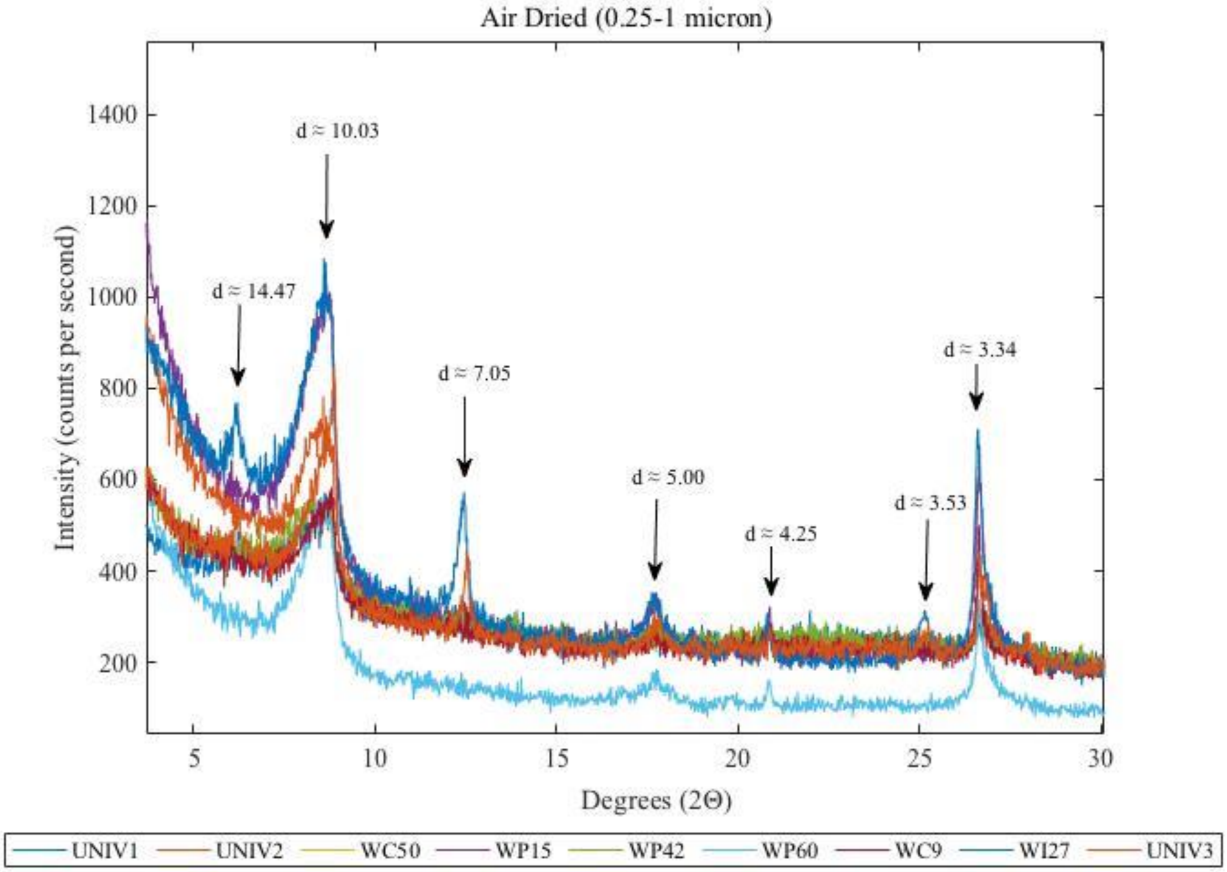

Figure 21:The combined air dried diffraction patterns of all samples at the 0.25-1 µm scale.

The following five samples provided identifiable mineralogical data for the < 0.25 µm size fraction: UN 9-1, UN 9-3, WP60-1, WC 9-3, and WI 27-2 (Figure 22). A combined XRD pattern of these five samples can be seen in Figure 18. An asymmetric peak was seen in all clay fractions of all shale at 10Å. This asymmetry permitted the identification as an illite-smectite. The <0.25 µm fractions of other four samples not included in this figure displayed diffraction patterns with an amorphous hump. This amorphous pattern could not be interpreted further.

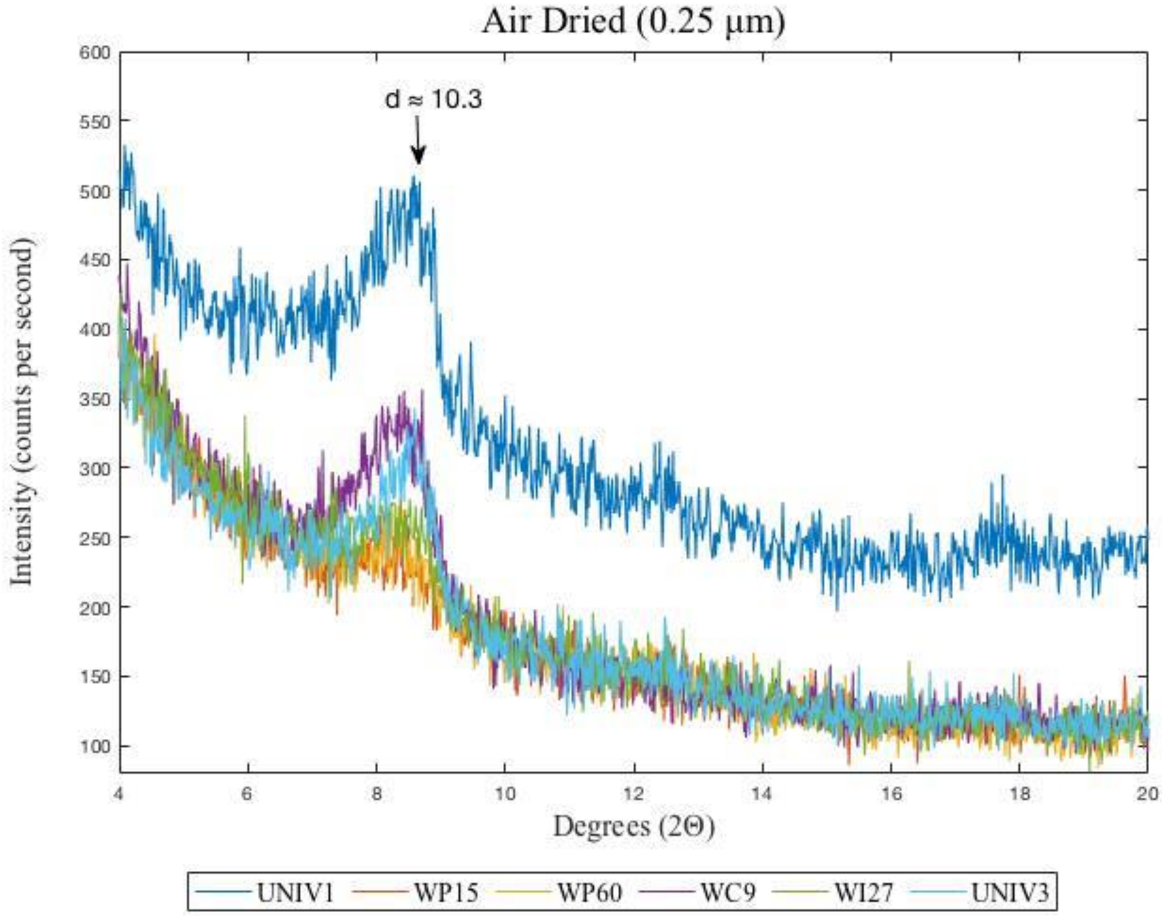

Figure 22: The combined air dried diffraction patterns of all samples at the 0.25 μm scale.

3.2 Porosity Measurements

The SAXS patterns showed variability in the amounts and locations of scattering peaks. The variability in the locations and numbers of scattering peaks are showed for a representative scattering curve from each sample (Figures 23-27). Based on preliminary data, the observed volumes of pore spaces were likewise variable (Table 3). The sizes of the nanopores (i.e. nanoporosity) derived from these scattering curves (refer to section method where the IRINA plugin was used to estimate these pore sizes/volumes) was likewise variable in size

These patterns resembled a positively skewed log-normal distributions. Typically, three to five individual groups of scattering were shown by prominent peaks in each scattering curve. The largest sizes of scattering peaks were located at approximately 30 Å in each sample. The next distinct pocket occurred at approximately 60 Å with another peak following at 90-80 Å with additional broad peaks at ranging from 120 Å and 180 Å. All curves can be found in Appendix C. The uncertainties of the measurements were shown as red error bars in the following five figures. The length of the error bars denoted the amount of uncertainty at each point. The uncertainties of many of the larger pores (approaching 10^5 Å) are relatively large (within the WAXS data).

		Avg. Obs. Peak Scatternings (Å)				
Sample	**VRo %**	**Low**				**High**
9TO1	0.9	35	60	83	120	150 B
9TO3	0.9	40	60	90	120	180
9TO4	0.8	37.5	60	80	108	142
9TO5	0.8	25	47.5	90	165	
9UL1	0.95	50	80	110	180	

Table 3: Each thin section provided various scattering curves. Each curve was compared and averaged. This table represents the observed pore sizes seen via SAXS experiments. 'B' denotes broad peaks.

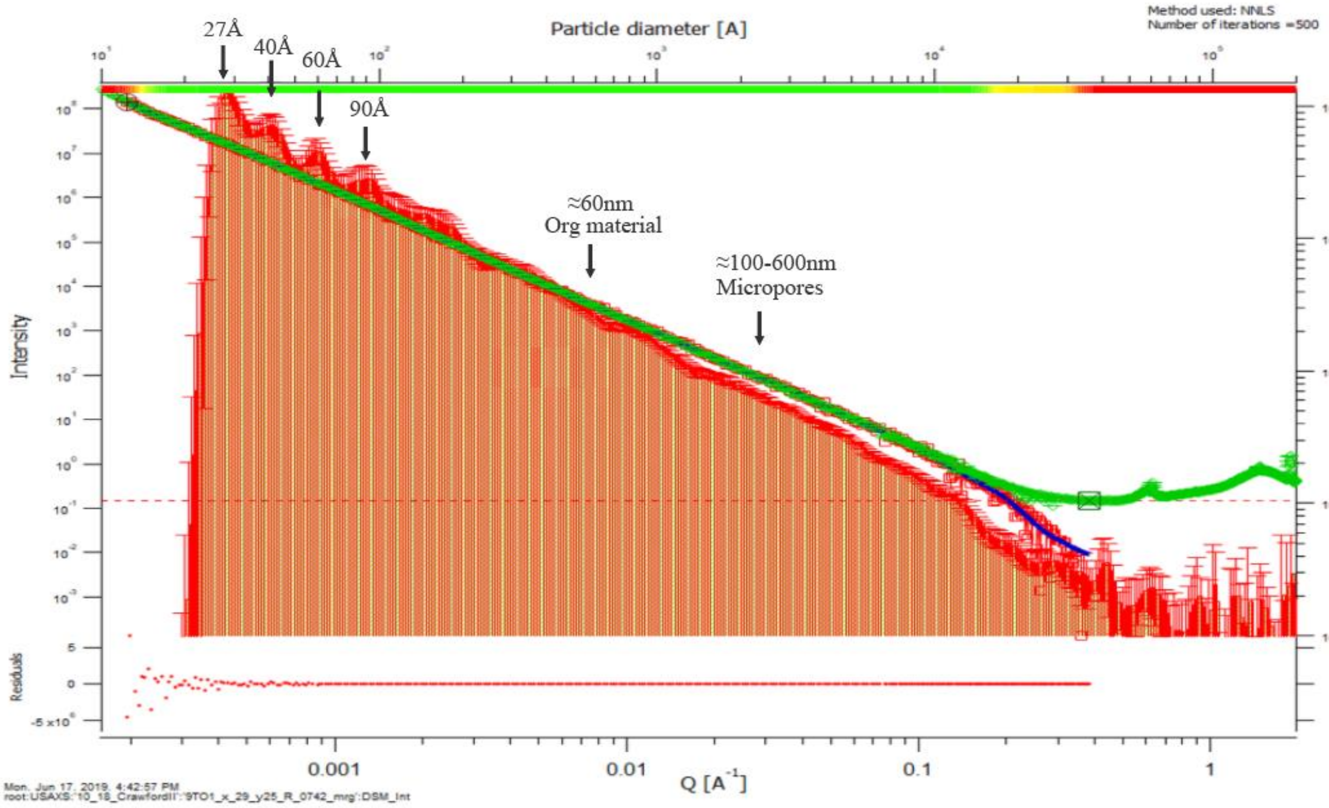

Figure 23: SAXS data processed using Igor with the Irena plugin. This processed data created size distribution curve where intensity versus scattering sizes (Q) for sample 9TO-1 (9TO1_x_29_y25_R_0742) was plotted. Large volumes of pores are seen at 37 Å, 40 Å, 60 Å and 90 Å. The green line indicates the measured data. The fitted curve is drawn with red error bars and filled in with green and red vertical stripes. The horizontal dashed red line indicates the background (Anovitz et al., 2017). WAXS diffraction peak can be seen on the right in green.

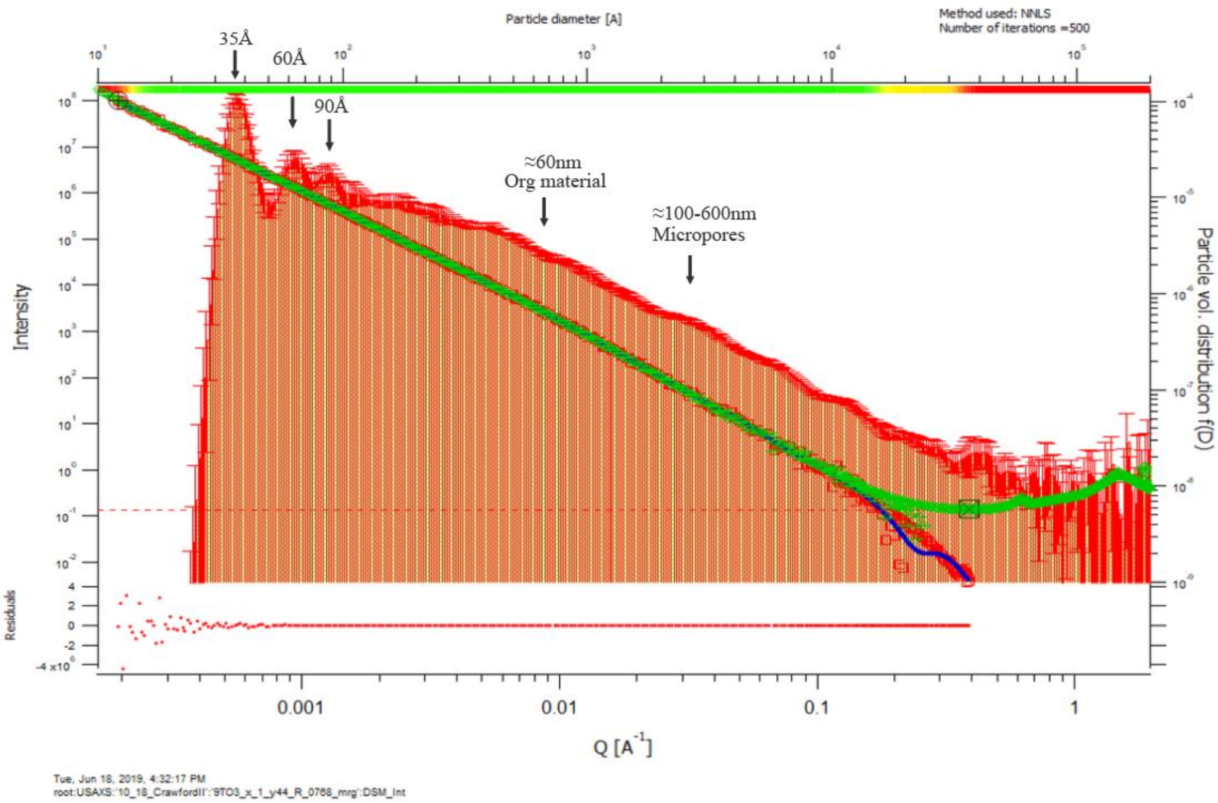

Figure 24: SAXS data processed using Igor with the Irena plugin created size distribution curve where intensity versus scattering sizes (Q) for sample 9TO3 (9TO3_x_1_y52_R_0766) was plotted. Large volumes of pores are seen at 35 Å, 60 Å, and 90 Å. The green line indicates the measured data. The fitted curve is drawn with red error bars and filled in with green and red vertical stripes. The horizontal dashed red line indicates the background (Anovitz et al., 2017). WAXS diffraction peak can be seen on the right in green.

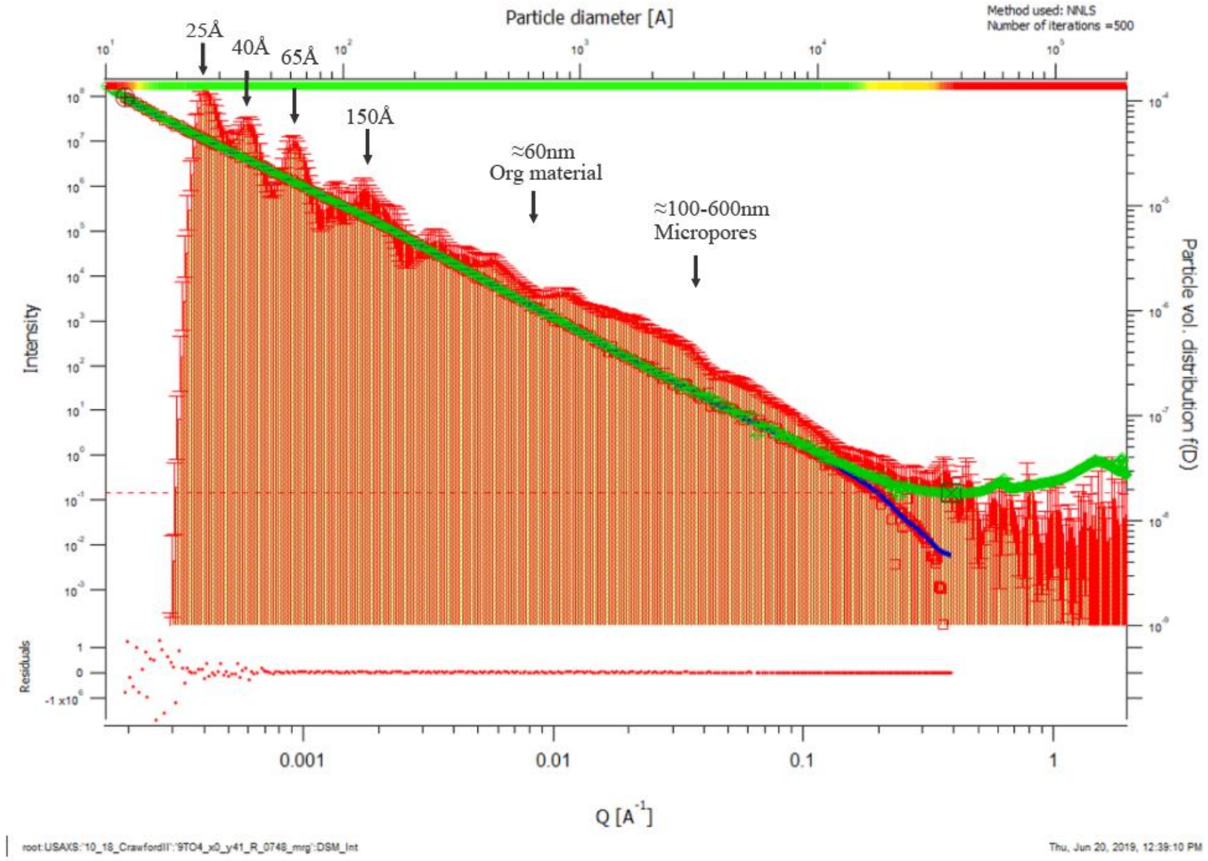

Figure 25: SAXS data processed using Igor with the Irena plugin created size distribution curve where intensity versus scattering sizes (Q) for sample 9TO4 (9TO4_x0_y41_R_0748) was plotted. Large volumes of pores were seen at 25 Å, 40 Å, 65 Å, and 150 Å. The green line indicates the measured data. The fitted curve is drawn with red error bars and filled in with green and red vertical stripes. The horizontal dashed red line indicates the background (Anovitz et al., 2017). WAXS diffraction peak can be seen on the right in green.

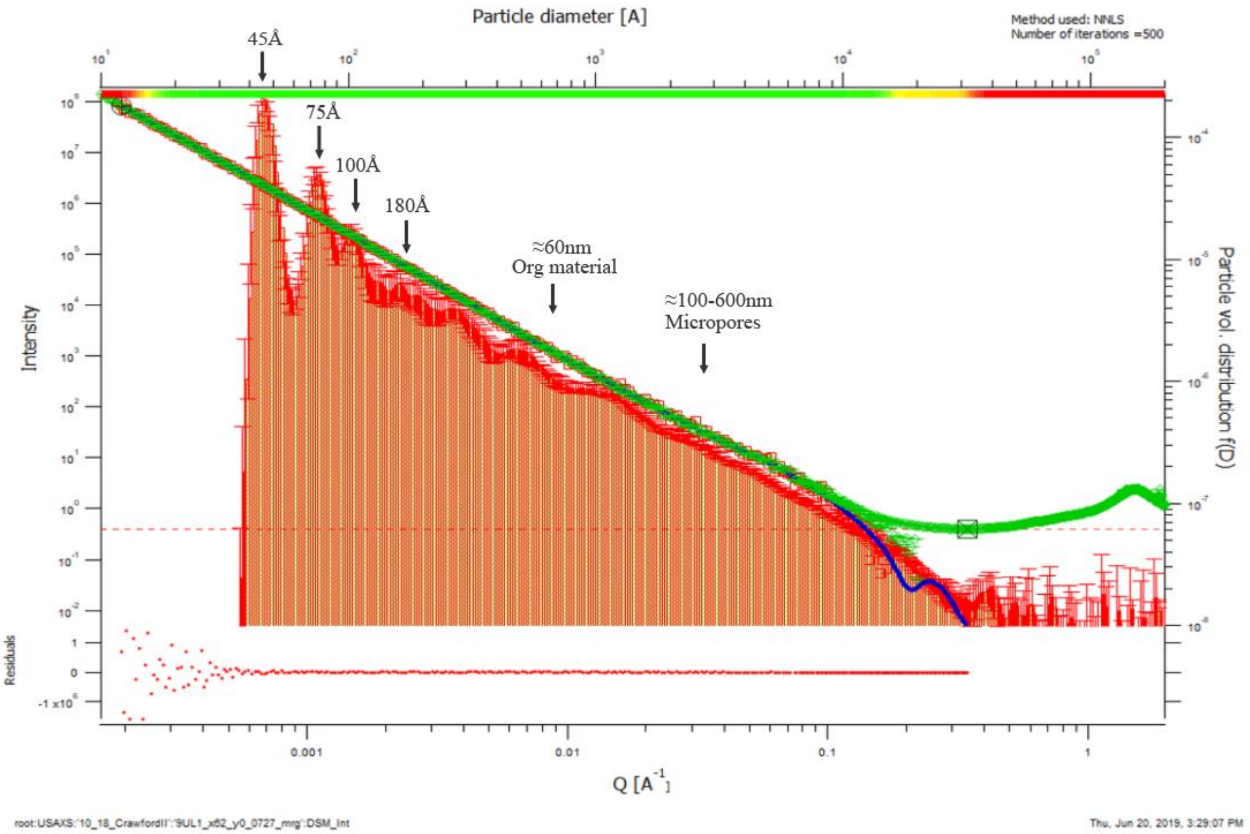

Figure 26: SAXS data processed using Igor with the Irena plugin showing the intensity versus scattering sizes (Q) for sample 9UL (9UL_x62_y0_0727) was plotted. Large volumes of pores are seen as 45 Å, 75 Å, 100 Å, and 180 Å. The green line indicates the measured data. The fitted curve is drawn with red error bars and filled in with green and red vertical stripes. The horizontal dashed red line indicates the background (Anovitz et al., 2017). WAXS diffraction peak can be seen on the right in green.

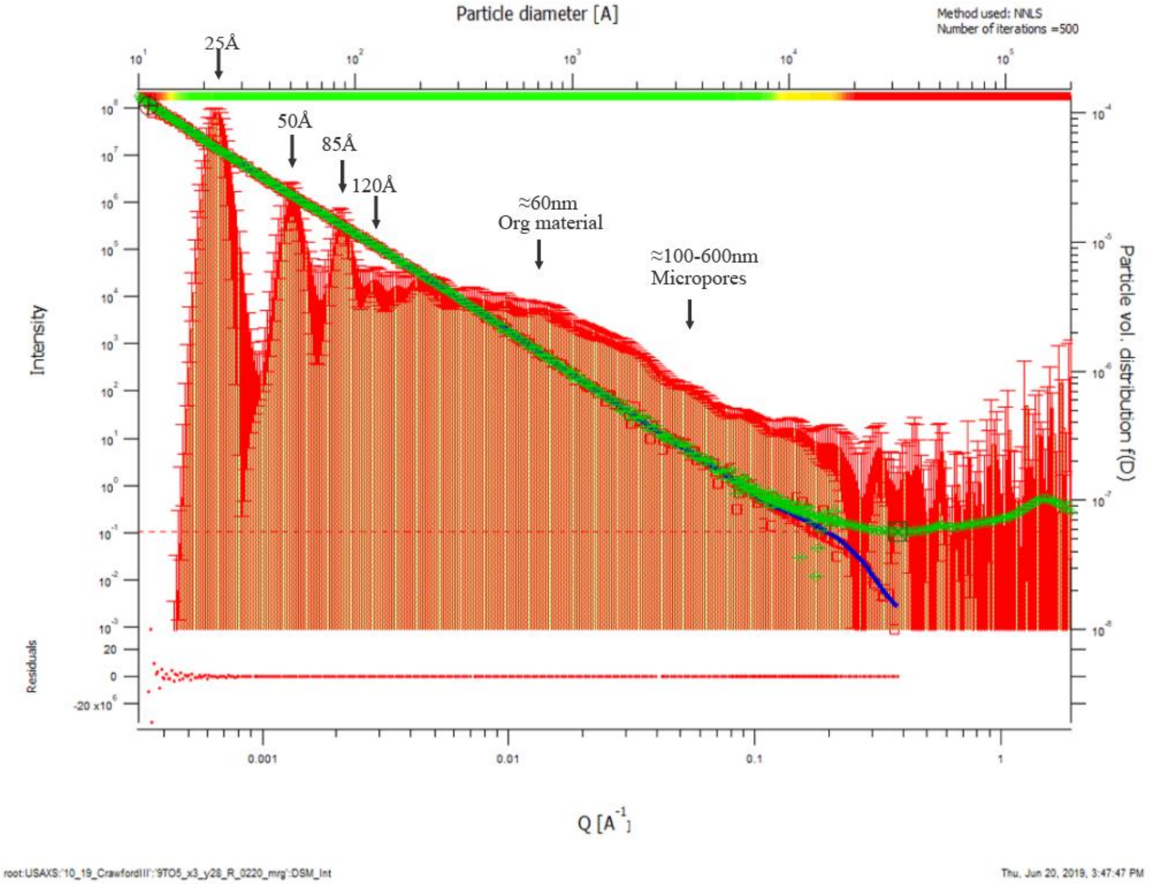

Figure 27: SAXS data processed using Igor with the Irena plugin showing intensity versus scattering sizes (Q) for sample 9TO5 (9TO5_x3_y28_R_0220) was plotted. Large volumes of pores are seen at 25 Å, 50 Å, 85 Å, and 120 Å. The green line indicates the measured data. The fitted curve is drawn with red error bars and filled in with green and red vertical stripes. The horizontal dashed red line indicates the background (Anovitz et al., 2017). WAXS diffraction peak can be seen on the right in green.

The cumulative size distribution and the surface area remained constant throughout most samples. The cumulative surface area curve looked like the positive side of a basic cubic function (X^3) curve. The cumulative size distribution curve resembles a gradual sloping linear function. This curve is almost a straight like from the bottom left corner of the graph to the top right corner. Both of these two curvesgently veered off to the top right corner of the graph (Figure 28).

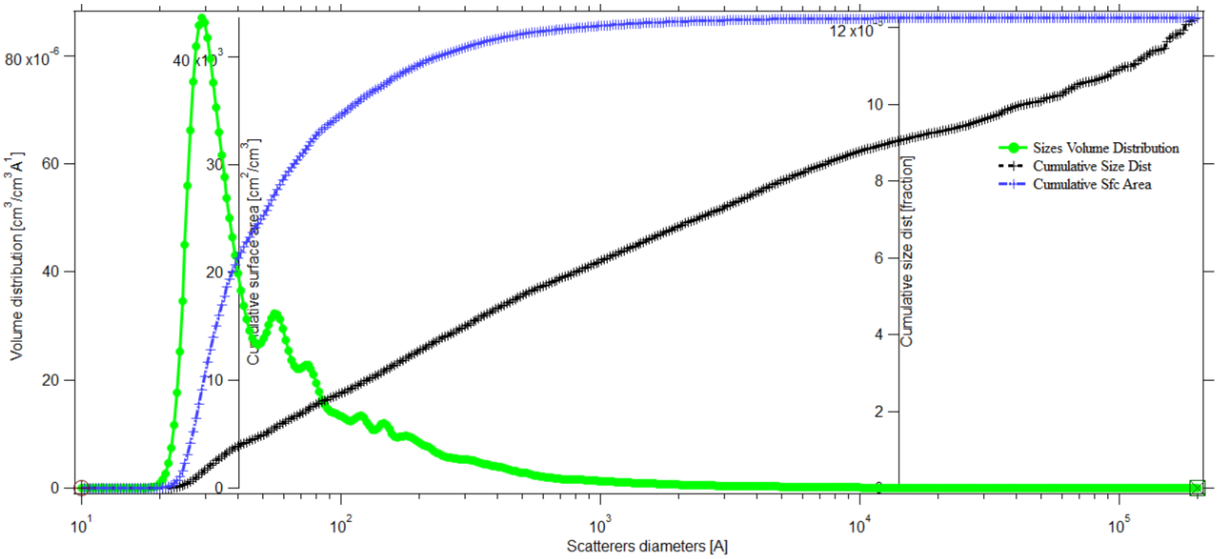

Figure 28: This curve has shown volume distribution plotted versus scattering particles (in angstrom) for sample 9TO1 (9TO1_x_29_y52_R_0738).The green curve shows where the large volumes of pore sizes are. The blue curve shows where the majority of the surface area of pores were found. The black curve shows the cumulative size distribution.

3.3 FE SEM Examination

The samples displayed heterogeneity in size, shape, and location of pores at this low magnification. The pore systems geometries varied significantly ranging from simple (circular/ovid/elliptical) shapes to complex shapes (composite pores). The measured pores were found between 1) clastic or carbonate grain boundaries, 2) within phyllosilicate cleavage planes (001 surfaces) or between clay flocs, 3) within organic material and adjacent to inorganic grains, and 4) hosted within organic material (Pommer and Miliken, 2005). The largest pores were found between silicate/carbonate grain boundaries or between clay partings (Figure 29)

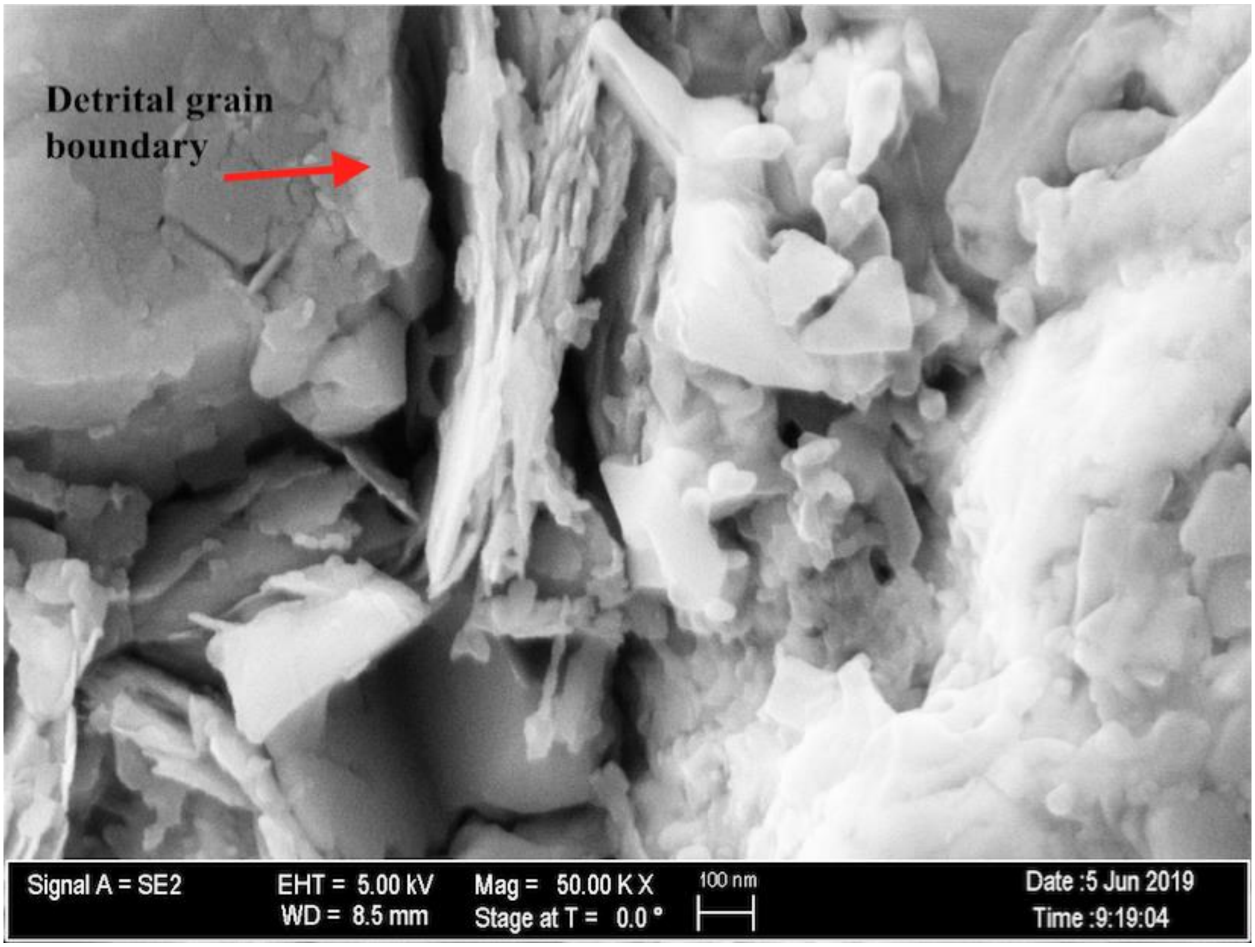

Figure 29: This is a FE SEM photo of sample 9TO-1 taken as 50X machine magnification. The largest pores were categorized as intraparticle. This large pore can be seen between a detrital grain and clay aggregates.

After the survey at low magnification, the shale sections were examined for their porosity at higher machine magnifications (5,000-50,000X). The lengths of the pores were measured at each magnification. Larger pores were seen at lower magnification. Their lengths varied from 715-939 nm. The smallest pores were seen at the highest magnification. Their lengths varied from 109-143 nm (Table 4). The total areas of pores in the three slides measured was 9.0 mm^2. The shale sections were viewed first 50X machine magnification.

Formation	ID	Mag	Average observed Pore Length (nm)	% VRo	Depth (ft)
Wolfcamp	9TO4	5,000	939.90	0.8	5949.1
	9TO4	10,000	529.54	0.8	5949.1
	9TO4	50,000	132.50	0.8	5949.1
Wolfcamp	9TO1	5,000	792.51	0.9	6433.35
	9TO1	10,000	376.36	0.9	6433.35
	9TO1	50,000	109.15	0.9	6433.35
Wolfcamp*	9UL1	5,000	715.88	0.95	10637.5
	9UL1	10,000	344.80	0.95	10637.5
	9UL1	50,000	142.75	0.95	10637.5

Table 4: Representatives of the average observed porosity at each sample site with three different machine magnifications. *Insufficient sample size refer to the discussion section.

The trends in the pore lengths showed decrease in the sizes of the pores as the spatial resolution increased. The increased resolution at high magnification permitted more precise pore measurements with this FE-SEM. The diameter of micropores changed with thermal maturity. No correlation to pore length and thermal maturity was made. However, when calculating the ranges of pore sizes, values collected from 9UL varied the least throughout various magnifications. 9UL was the sample with the highest thermal maturity in this experiment. There was a smaller range of pore sizes with increased thermal maturity (Table 4).

The nanometer (Submicron)-sized pores were located most frequently between grains and within clay aggregates. Large amounts of illitic clays were observed at every machine magnification. Most pores demonstrated an elongated shape with pore throats that separated them from surrounding pores. Pores were seen as ellipses rather than spheres. Elongated pores were formed between individual clay sheets as well as between groups of clays flocs. Evidence of diagenetic clay growth was apparent due to the shape of growth patterns i.e. illite grains growth around and into pre-existing grains (Figure 31). Diagenetic clay sheets are seen growing perpendicular to the clay fabric and therefore disaggregated the previous space of macropores (Figure 30). Diagenetic (1Md) and detrital (2M1) illite were identified based on characteristic shapes for each illite polytype (Pevear, 1999). Fibrous laths are interpreted to be 1M illite. Hexagonal platy textures are interpreted to be 2M1 illites (mica). Illite nucleated from a pre-existing detrital clay, smectite or 2M1 illite, can be seen in Figure 30. These illite grains grew into and around pore spaces. The sizes of pores were modified by precipitation and resulting orientation of illite laths. Illite was identified as the dominant clay mineral based on shapes and EDS analyses (Figure 32).

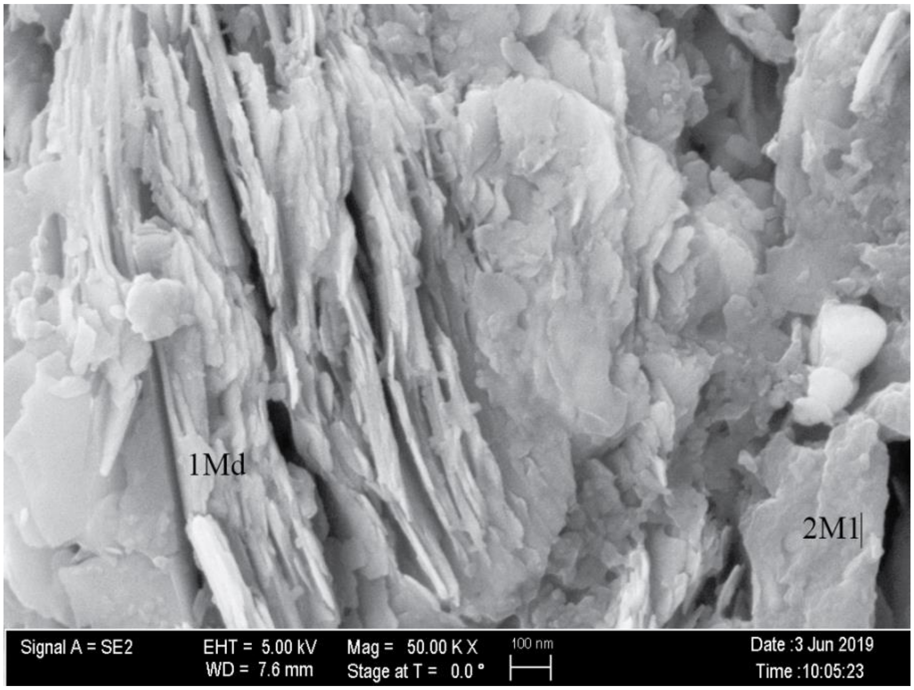

Figure 30: FE SEM image of 9TO-01 depicting diagenetic (1Md) from a detrital (2M1) grain.

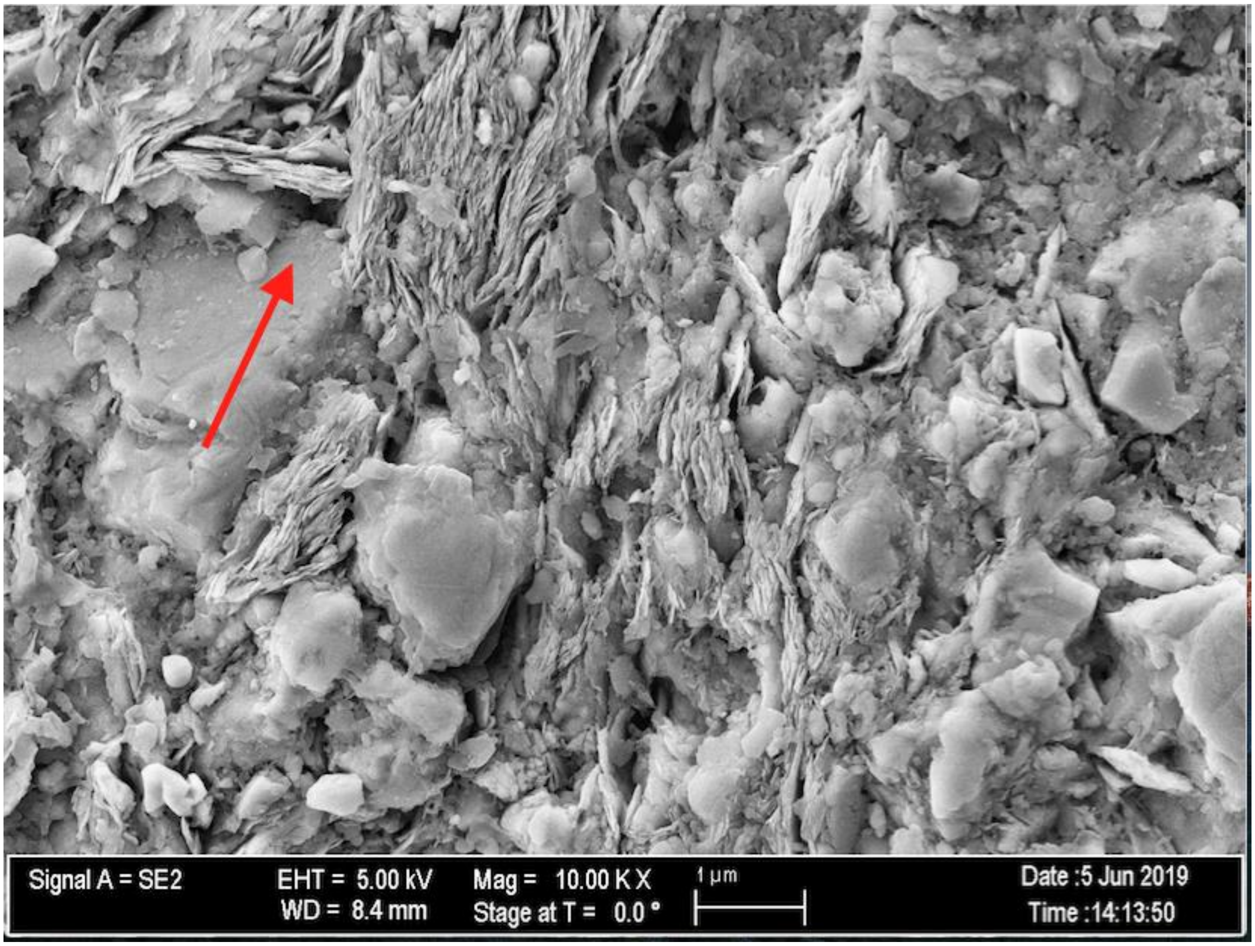

Figure 31: This is an FE SEM image of sample 9TO-04. The red arrow shows the growth of diagenetic clay sheets. These sheets have grown perpendicular to the clay matrix fabric. This image shows phyllosilicates growing around and into pre-existing pore spaces.

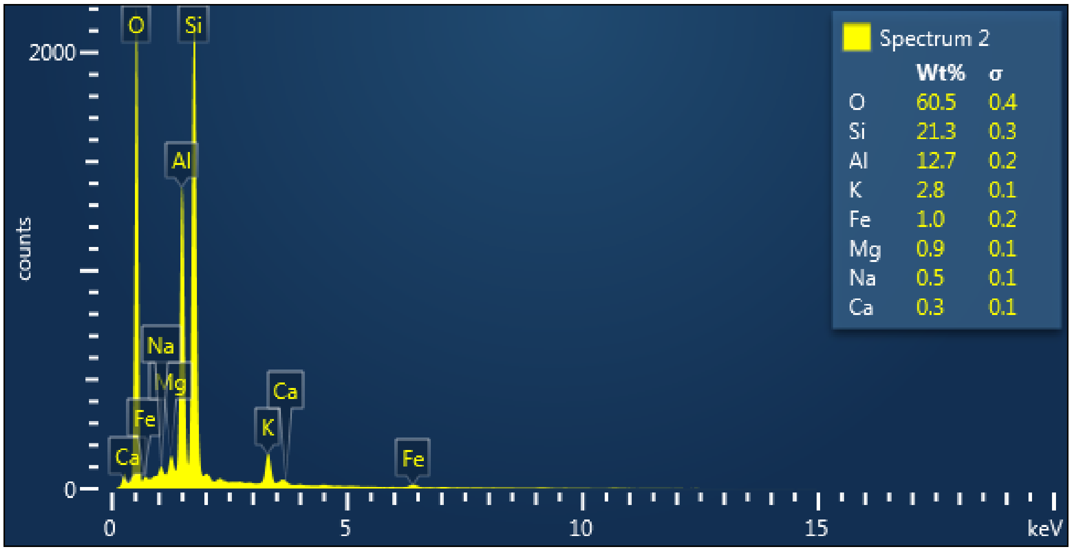

Figure 32: EDS provided the chemical composition confirming the dominant phyllosilicate as illite. This spectrum shows the presence of Si, Al, K and lesser amounts of Ca, Na and Fe. That elemental analysis is consistent with the presence of illite phyllosilicates.

Particulate organic matter (POM) was observed in the three shales examined by SEM and FE SEM. POM was more frequently seen in 9UL, the most mature sample. All POM appeared to contain pores as seen with SEM. In the shallowest sample, organic matter (OM) had a more jagged boundary based on FE-SEM imagery. Smooth edges were observed in OM from the more thermally mature sample (Figure 33). POM contained sponge-like pores that were subangular in shape. Complex pores within POM, separate portioned chambers within this material. Moldic pores in OM did not appear to be connected. POM was often located between 1Md and 2M1 (Figure 33). Through random sampling, more OM was seen in the more thermally mature samplesof the Wolfcamp. The average size of OM measured within pores was 5 µm based on our preliminary number of measurements.

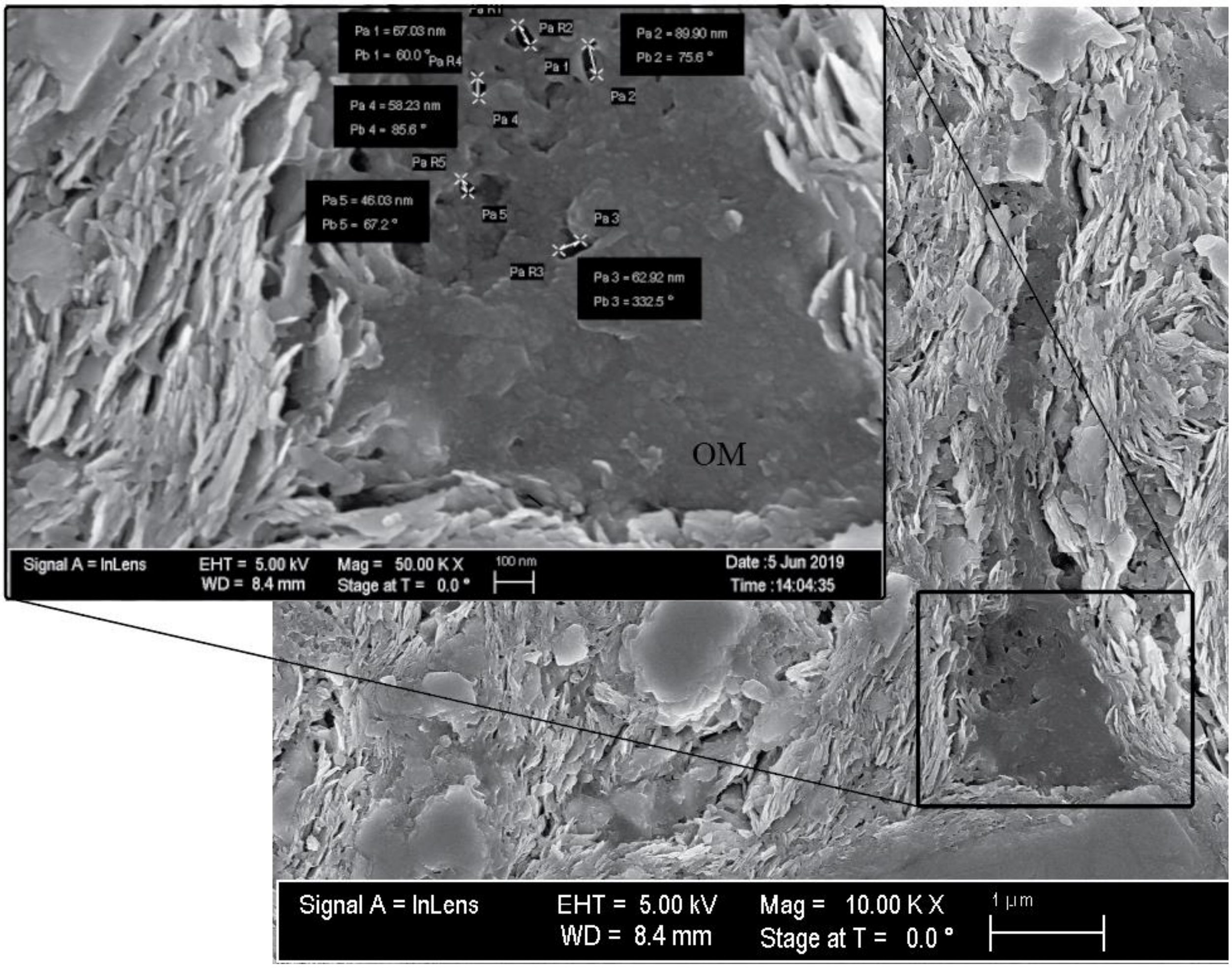

Figure 33: Sponge-like pores observed with FE SEM.

In addition to sizes of pores, variability was noted in shapes and mineral phases. Authigenic phases present were evidence of rock-fluid interactions. This alteration was likely during diagenesis. In particular, sharp edges of minerals were evidence of post-depositional mineral nucleation. Figure 34 showed the alteration of pore space-filling with fibers and quartz. Preexisting pores allowed for interstitial fluid migration bringing opportunities for mineral dissolution and precipitation. Pore spaces were created in smaller pores by mineral precipitation. Cementing minerals such as quartz and carbonates occluded pore spaces within the matrix (Figure 34). Dolomite often contained a ferroan rim, identified characteristic Fe X-rays (SEM-EDX).

Dolomite and pyrite were seen replacing other minerals, pore spaces, and fossils. The fossil constituents include tasmanites, radiolarian, and conodonts. The two types of pyrites, framboids, and cubic, confirmed that these marine shales had undergone middle to late diagenesis. Additional trace minerals seen within this analysis were: rutile (Ti oxide), sphalerite (Zn sulfide), and a Fe oxide (possibly hematite or magnetite).

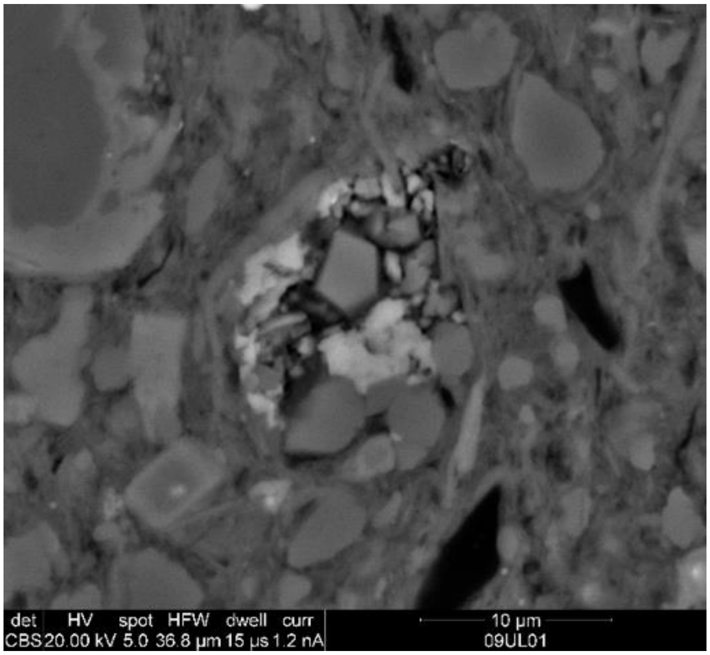

Figure 34: Authigenic pore fill with hexagonal crystal shape quartz and clay laths captured with SEM.

Compaction of grains was evident due to the elliptical pore structure. It was common to see pores surrounding clay minerals elongated between 50-70 degrees from an arbitrary 0 horizon line. However, a cluster analysis was performed, and no meaningful orientation across all samples can be noted. There is was not one consistent direction of elongation of pores. Pores are elongated in multiple directions, as shown by Figure 31. There were multiple (or no) preferred orientation of porosity deformation.

The average bulk area of pores was modeled with Fiji. The data can be found in Table 5. The percent porosity calculated ranged from 5.5-7.1%. The most immature sample contained the highest percentage of porosity (7.1%) and the largest average size pores (340.9 nm). The median sample had porosity values in between the other two samples. The standard deviation (2.14) of this data must be considered during this analysis. The most mature sample 9UL-01 (VRo = .95) contained the lowest percentage of porosity at 5.52%. This sample also measured the smallest average pore sizes. The frequency of average measured pore sizes seen in 50X FE SEM can be viewed in the histogram below (Figure 36). The data provides preliminary evidence that the average size and average percent of porosity decreased with increased thermal maturity.

Depth (ft)	**Porosity (%)**	**Std Dev.**	**Av. Pore Size (nm^2)**
5949.10	7.13	0.75	356.60
6433.35	6.98	2.14	279.96
10637.50	5.52	N/A	226.04

Table 5: Porosity estimates created by Fiji software (Schindelin et al., 2012).

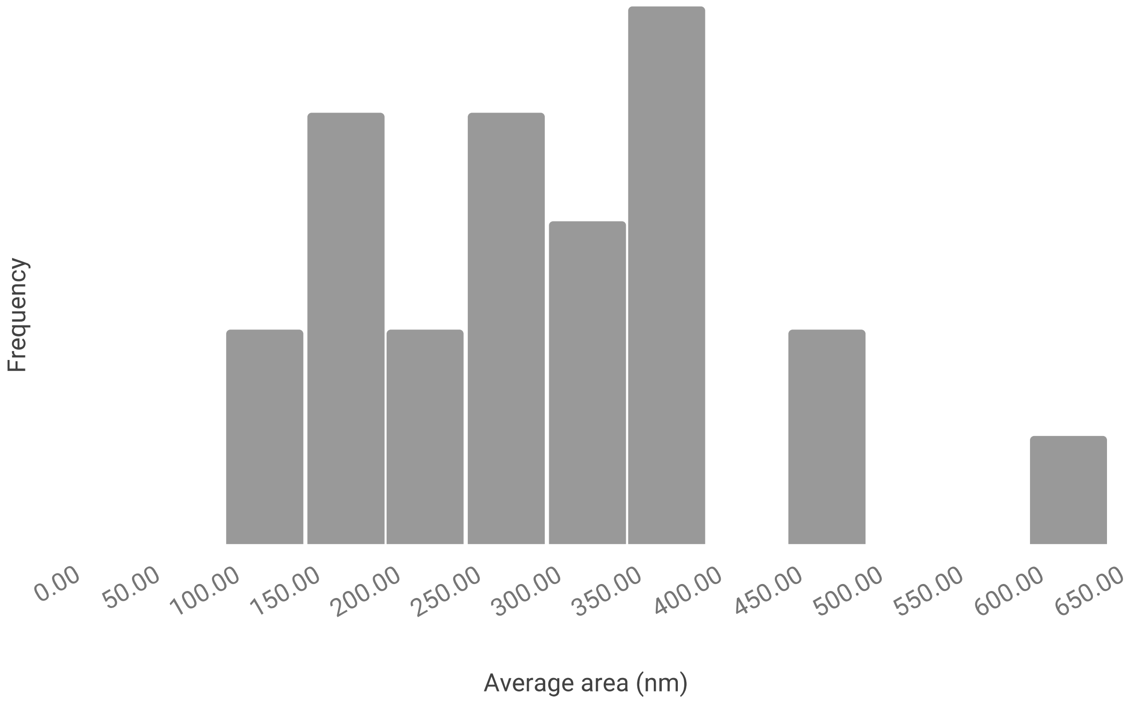

Figure 35: This histogram shows the distribution of pore areas of FE SEM images (50X).

Pores seen within SEM and SAXS data are at an order of magnitude in size differences. SAXS experiments were excellent at observing nanopores. The micro-sized pores were seen well with the FE SEM. Pores seen in SAXS experiments cannot be seen in SEM even at the highest resolution. Pores seen in SEM analysis can be viewed in SAXS data when the particle size has been manipulated to the log scale (Figure 37). SAXS experiments confirm the presence of these size pores. There are no dramatic peaks in this range that would signify an exceptional number of pores in this area.

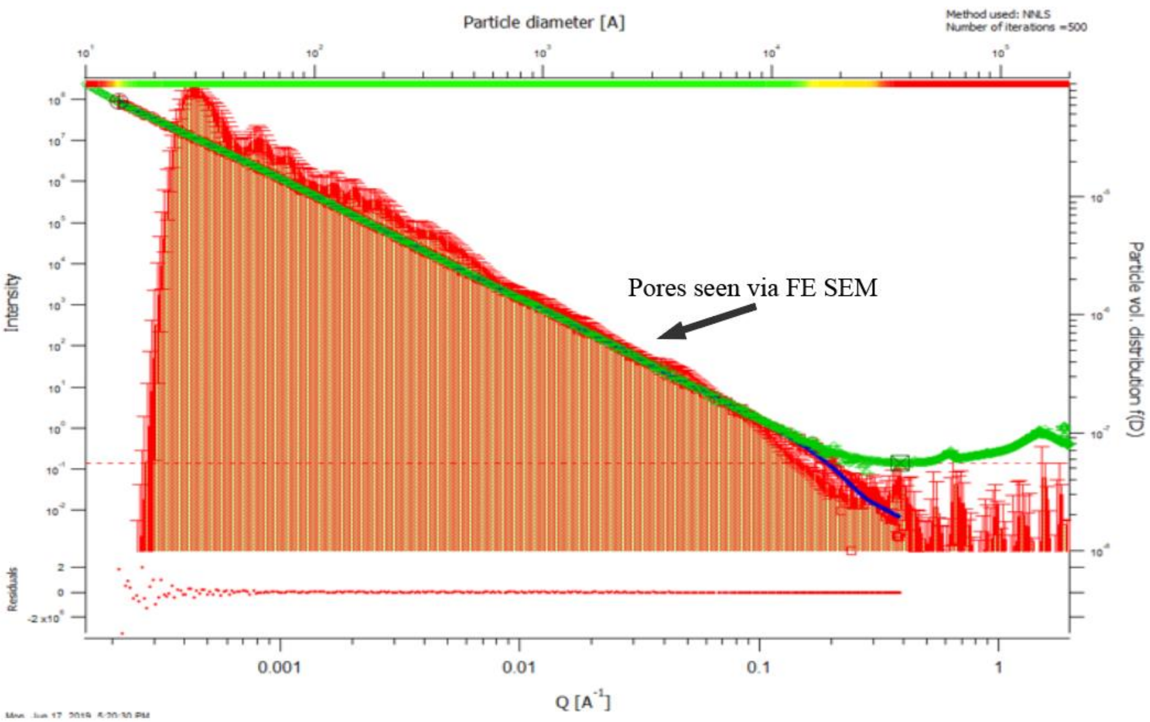

Figure 36: SAXS curve showing the approximate location of pores seen via FE SEM analysis. (Sample ID: 9TO1_x_29_y52_R_0738).

4 DISCUSSION

The increase in temperature and pressure during diagenesis led to the formation of pore-filling minerals and changes in the illite clay mineralogy of this Paleozoic shale (Wolfcamp Shale) in the mid-Continent USA (Blomquist, 2016; Cardott, 2012; Kennedy, 2014; Nagaraj et al., 1990; Wickard et al., 2016; Roberts and Elmore, 2018). The interpretation of the illite clay mineralogy from these samples suggested the presence of diagenetic transformations forming the illitic I-S clays. Evidence of post-depositional clay diagenesis included: 1) presence of illitic I-S via X-ray diffraction data and 2) SEM images of 1Md illite laths. It can be assumed that detrital smectite was transformed into I-S with high amounts of illite by increased time, and temperature in the presence of sufficient potassium as pore-water solution. Although this study regarded the illitization as a completely abiotic process, preliminary research by Kim et al. (2019) suggested the formation of illite without abiotic conditions. Further research is needed to conclude the influence of biotic processes on the formation of illite in these Paleozoic sedimentary basins and other sedimentary basins.

4.1 Mineralogy Comparisons

Despite the vastly heterogeneous nature of shales, some commonalities were noted among all samples in this study. The mineralogy of the clay fractions in both units was composed of illite (I-S with high percentage 90% of illite layers), smectite, quartz, kaolinite, chlorite, quartz as well as trace amounts of dolomite and albite. I-S was found in the clay fraction (of this sequence at all size fractions for all shale studied). The observed Kalkberg stacking orders of illite in all samples (i.e., over 90% illite layers in I-S) indicated that this basin reached middle to late diagenetic parameters (approx. 100-200 °C). The observed illite mineralogy is consistent with crude oil generation and Vitrinite reflectance values ranging from 0.5 to 1.5% VRo (Waples, 1980). The clay mineralogy was constant throughout the samples despite the large scale mineralogic heterogeneity of shales (Wickard et al., 2016).

Some heterogeneity, however, was noted in terms of other minerals present in the clay fractions of these shales. Chlorite was not found in every shale despite the high level of thermal maturation. Given the lack of uniform occurrence, chlorite might have precipitated during the movement of hydrothermal fluids which were detected in some of the pore-filling mineral (Wickard et al., 2016). Dolomite was another mineral that was not found in all shales studied. The samples contain minerals dolomite, albite, chlorite that may be interpreted as hydrothermal origin (Roberts and Elmore, 2017). Roberts suggested this mineralogy as evidence that the Paleozoic black shales, such as the lower Permian Wolfcamp, was an open system at some point during the burial history. The varied mineral suite (chlorite, albite, quartz, and dolomite) might have precipitated from externally derived fluids. Dolomite was seen via SEM with a ferroan rim. The growth of this rim from a preexisting dolomite grain was confirmed with EDX. This feature was further evidence of hydrothermal alterations. It is uncertain if all carbonate minerals detected by XRD analysis formed in sedimentary conditions as cementing materials or precipitated from interstitial fluids. Further analysis is needed to confirm the origin of these trace minerals. Additional authigenic clay cementing materials (quartz overgrowths and clay/dolomite cement) were seen via SEM. Pyrite, as well as other minerals commonly identified with EDX, were not seen in XRD. The absence of pyrite patterns can be attributed to successful lab treatment as well as the fine-grained focus of this research.

4.2 Porosity

Insights on pore type abundance and pore size distributions were provided by SAXS and FE SEM analyses. Pores found in this study extended over a magnitude of scales. Pores found in this study were grouped into two categories micropores (> 75µm) and nanopores (< 75 µm) (Loucks et al., 2012). FE SEM measurements allowed the quantification of microporosity. The fully reduced small-angle scattering data permitted an unprecedented resolution of pores as small as 20 Å in diameter, known as nanoporosity. Small-angle X-ray scattering was the ideal nondestructive method to successfully characterize the size, distribution, and surface area of nanopores (Anovitz and Cole, 2015; Nirschl and Guo, 2018). All SAXS data were generated with the assumption that the samples are made of two constituents, illite, and pores.

Scattering intensity profiles obtained from combined SAXS measurements revealed a broad pore size distribution (meso- to nano-porosity). As expected there were variations in pore size distribution from sample-to-sample. These local variations among samples may be due to locations of porosity, i.e. between clay aggregates or within organic material. Due to the heterogeneity of shales and hierarchy of pores, the pore networks within shales are extremely complex.

A preliminary observed decrease in pore size volume (in FE SEM) might be due to changes in the lithostratigraphy across samples. One might speculate the discrepancies described may be attributed to the presence of porosity in organic material. Additionally, the local variability in microporosity might be explained by the dewatering of the smectite structure and creation of an "overpressure" condition. Packets of illite precipitating as small as 30 Å, were observed with SAXS. The sizes of these packets coincided with previous observations made by Nadeau et al., (1984). Nadeau's work show packets of illite up to 50 angstroms thick (even up to 160 angsrom thick) per SEM and transmission electron microscopy. Less illitic I-S have thinner packets < 50 Å. We have concluded that roughly the same thickness of aggregated illite packets analyses were seen via SAXS. Speculatively, the occurrence of Nano porosity might have been a function of the S-to-I process where the sizes of nanopores are likely constrained by the sizes of clay packets (Nadeau et al., 1984).

4.2.1 Microporosity

Pore size populations within these shales were broad. The range of imageable pores could not be viewed effectively through one single experiment, technique, or magnification. X-ray scattering paired with SEM measurements allowed unprecedented resolution and clarity of qualitative and quantitative insights of the pore network in these shales. For example, pores ranging in size from 500 to 100 nm were also observed via SEM. These pores, when analyzed with IGOR software associated with SAXS imaging, did not display distinct populations within the scattering curves (Figure 23-27). The analyses of these pores were beyond the scope of what was seen via SAXS. These shales were imaged using field emission SEM to permit the identification of populations of micro pores in these shales.

From FE-SEM imaging, the pores and pore throats were visible at even the lowest machine magnification. It was expected to see pores within the organic material. Pores within the OM were noted to be approx. 60 nm in size while the organic macerals were estimated at 5 µm (Figure 33). The pores within this spongy material were most likely generated during the cracking and migration of hydrocarbons (Monhoff et al., 2016). Further maturation might have prompted the development of further pores/pore networks in the organic material and the surrounding matrix. Therefore, the organic pores are interpreted as secondary pores. The larger pores (approx. 200 nm) were observed surrounding detrital grains and packets of clays (Figure 31). These larger pores were filled and altered by the migration of ductile kerogen and secondary mineral precipitation during thermal maturation. Burial conditions paired with the amount and type of OM influenced the OM hosted pore network evolution.

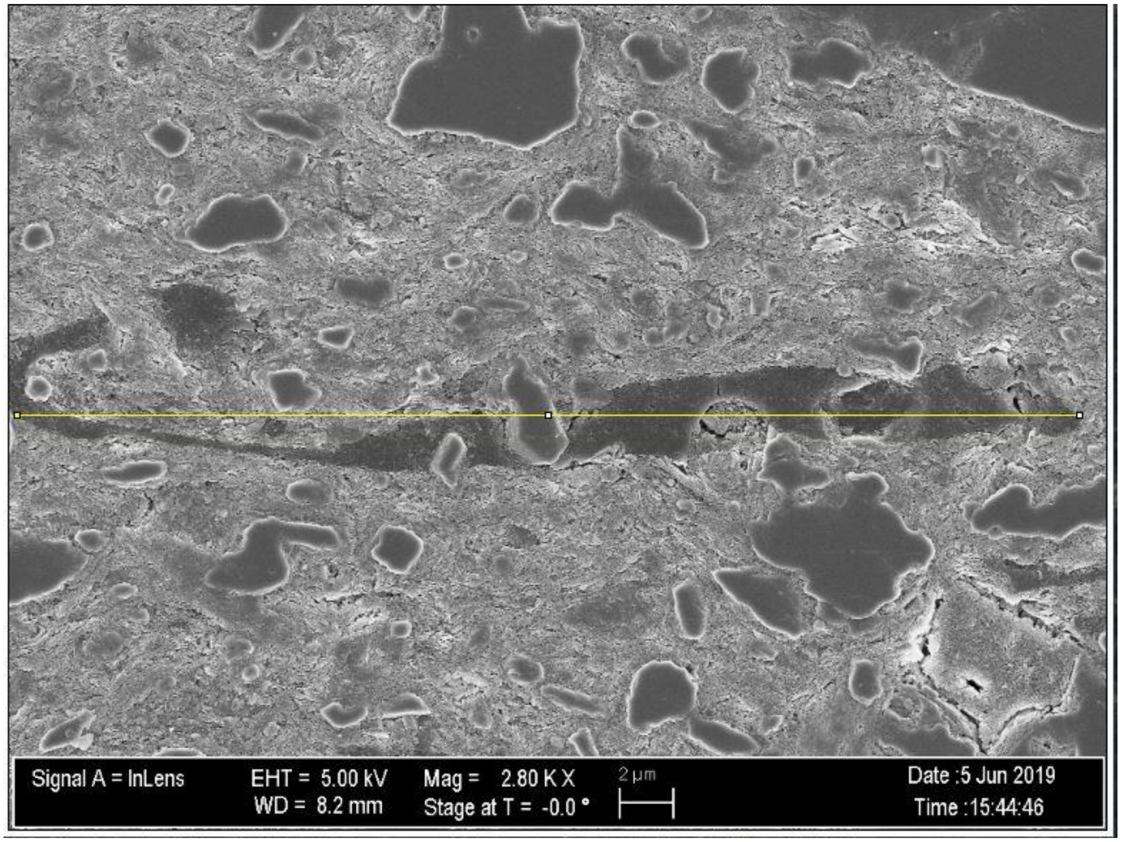

Figure 37: FE SEM image of 9UL at 2.8X magnification. This shows the estimates length of organic macerals within these shales. Length was drawn with Fiji (Schindelinet al., 2012).

From the SEM examination, pores were found throughout the matrix. These pores were prominent between and around phyllosilicates. The morphology of pore sizes was influenced by the flocculation of clays and their thin diffuse layer. Larger pores seen between grain boundaries were likely a function of the original arrangement of siliciclastic grains. The existence of those pores not appreciably changed by diagenesis, S-to-I reaction or other burial/diagenetic processes. SEM and SAXS examinations were helpful for differentiating pores formed through deposition from those pores that formed by other diagenetic processes.

Pockets of porosity (200-600 nm) were imaged between either clay sheets, aggregates of clay minerals, or within organic material (Figure 33). The general shape of pores were ellipses. About half of the pores were observed surrounding clay particles (Figure 31). The alignment of clay sheets is thought to be a function of preferential growth habitat combined with post-burial compaction. Elongated pores were seen in between clay sheets and between aggregates of clays. The elongated shapes of these pores suggested mechanical compaction soon after deposition. Compaction was apparent due to the elongated shape of pores. OM showed elongated shapes and thus was thought to result as well from compaction. The elongated organic matter was more common due to the relative more ductile behavior when compared to minerals (Eseme et al., 2007). However, this elongation cannot be correlated to the direction of primary bedding. There was not one direction of parallel alignment of pores and clay laths.

Porosity was influenced by burial (subsurface geochemical reactions) and arrangement of detrital grains. Porosity (nano and micro) was highest for the less mature shales (Table 3 and Table 4). These low values can be attributed/interpreted as a consequence of hydrocarbon chains blocking pore throats during an imperative phase of oil generation. The geometric size, orientation, and tortuosity of fluid pathways directly influenced permeability. The sub-parallel alignment of pores due to preferred mineral alignment affects migration pathways throughout a reservoir rock. The lack of preferably aligned pores also inhibits permeability and therefore limits extensive hydrocarbon generation and migration (Burnham, 2017; Monhoff et al., 2016; Schieber, 2010).

The discrepancies of microporosity may be attributed to the changing facies within the cores. Both Wolfcamp samples were taken from different cores. 9TO-01 was extracted from the Cortes core where the lithology was described by Wickard et al. (2016) as siliceous mudstone. Sample 9TO-04 was extracted from the Pizarro core categorized as a siliceous/calcareous mudstone (Wickard et al., 2017). Sample 9UL, the UN sample probed with FE SEM did not have an in-depth description of the facies. When calculating the ranges of pore sizes, values collected from 9UL varied the least throughout various magnifications. There is a smaller range of pore sizes as thermal maturity increases. This could be a true correlation or a function of sample size.

The nature and connection of pores will continue to be probed due to their importance in petroleum research. To predict/understand the behavior of the average shale, the composite minerals must be studied individually. For future studies, other diagenetic minerals may be used with Igor to generate a slightly contrasting contrast value, possibly changing the location of scattering. We have utilized Igor Pro and Fiji to create models that correlate the timing of thermal maturity and pore networks evolutions. However, it difficult to measure the natural aspects of pore systems in heterogeneous microscopic samples due to whole rock variations.

4.3 Limitations of Data

Porosity seen in FE-SEM analysis could have been created during sample preparation. When thin sections are created and polished cracks or holes may be induced. Porosity may change during wet/dry measurements. High-pressure laboratory techniques may potentially damage nature structure of fragile pore systems during sample collection or preparation. This effect is an important parameter to consider when discussing the connectivity or throats of pores. The effect of sample preparation on organic petrographic studies. One must pose the question of the possibility of drying or disaggregation lead to pore shrinkage. Artificial pores may have also been propagated by beam interaction. Pores that appeared to be artificially induced were not included in pore quantifications. No pores smaller than 15 A were seen within these analyses. This could be a function of incident beam size. No preferred orientation of elongation may be due to sample preparation. No correlation could be made between pores and stress/strain because the samples were cut parrelllel to bedding. A correlation between stress/strain and elongation direction may be made in samples cut perpendicular to bedding.

A consistent number of datasets were not collected for all FE SEM measurements. Note that 10 sample locations were observed at each magnification for 9TO1 and 9TO4 however only 3 sample locations were probed on 9UL due to time constraints. Therefore, more data must be collected to confirm preliminary speculations among pore size relationship across samples. Additionally, the standard deviation for sample 9TO-01 was higher than the others at 2. This must be considered when making assumptions during data interpretation.

SAXS date processed using Igor provided values of Φ(1- Φ). The actual value of Φ was calculated by evaluating the lowest Q value (approx. 60,000 Ǻ) and finding the corresponding value of 'size dist. diameter' (0.013 Ǻ), found in the data browser. Due to shales nonporous nature, the dataset only needs to be corrected by 1.01%, The pore surface area and cumulative size distribution values all must be multiplied by 1.01 for corrected pore values. The data in this study was not corrected by the Φ value, due to time constraints. Therefore all the nanoporosity data is skewed by 1.01%. For future studies this data should be corrected by the appropriate Φ value. This refinement will permit the precise determination of the sizes of nano-pores in these shales.

.

4.4 Potential Future Research

The data derived in this thesis aims to improve the understanding of the network of pore spaces that control fluid flow in tight reservoir rocks. This, in turn, will increase the efficiency of well placement and drilling in reservoir rocks. These results can be directly applied to further petroleum exploration and the understanding of geomechanical and geochemical behaviors within sedimentary basins. Although the search continues for alternative fuels, advances in technology have assured that fossil fuels will continue to meet the world's energy demand (US. Energy Information Administration, 2017). Natural gas has become the most highly consumed fossil fuel due to its relatively lower emissions rate and increased efficiency compared to oil and coal (US. Energy Information Administration, 2017). When burned, natural gas emits less carbon dioxide than any other fossil fuel (US. Energy Information Administration, 2017). By 2040, shale is expected to supply 70% of the nation's natural gas reserves (US. Energy Information Administration, 2017). Fossil fuels extracted from tight gas plays are a vital energy source needed to meet the fuel demands of increasing populations. An estimate of the microstructural evolution and behavior of fine-grained source rocks will enable maximal recovery rates of thermally mature hydrocarbons.

Isotopic data of diagenetic illites can be integrated with this research to further the prediction of the timing of structural features, the role of porosity network, authigenic mineral distribution on porosity. Although no isotopic data were corresponding to these samples as of yet, it would be an interesting supplemental data. It can be assumed that the apparent diagenetic age of I-S does not differ appreciably throughout these samples. This assumption is based on the locality of samples found, the common mineralogy, pore network, and small range of VRo across samples. Further studies must be conducted to confirm this theory. This research aims to provide the foundation for furthering knowledge and scientific literature to understanding pore pressure, oil and gas production, and diagenetic reactions. The results of this experiment may be used as preliminary data to further interpretations of thermal maturity and migration pathways of hydrocarbons in black shale source rocks. Horizontal drilling may sometimes be inefficient due to gaps in knowledge regarding the extent of fracturing, porosity, and permeability. A continued understanding of the mechanisms of diagenesis permits successful resource prediction and modeling.

5 CONCLUSION

The following conclusions were derived from the data gathered in this study.

1. The illite clay mineralogy displayed the presence of I-S with >90% illite layers with a Kalkberg stacking order (R>3). This stacking order and percentage of illite layers in I-S pointed to diagenetic conditions favorable for the generation of crude oil and natural gas based on the samples examined in this study. Chlorite, suspected to be of hydrothermal origin, was found within the deeper cores (UN 9-01, UN 9-03, WC 50-3 and WI 7-2). As grain size decreased, there was an overall decrease in the amount of kaolinite, dolomite, and albite based on the intensity of diffraction peaks.
2. Images from SEM showed the presence of detrital illite and diagenetic illite (I-S) based on the comparison of shapes with known the known literature. Large amounts of illitic clay was seen at every machine magnification.
3. Porosity was observed at the micro- and nano-scale. Microporosity was observed best with scanning electron microscopy and field-emission scanning electron microscopy (FE-SEM). The FE-SEM analyses showed elongated micropores between mineral grains and pores within organic matter. Due to the orientation of the samples, it was not possible to determine whether the direction of elongation corresponded to known bedding or other directions of stress/strain in these rocks. The moldic porosity seen within POM was separated from other pores by pore throats.
4. The calculated percent porosity calculated ranged from 5.5-7.1% from FE-SEM measurements. The most immature Wolfcamp sample contained the highest percentage of porosity (7.1%) and the largest average size pores (340.9 nm). The most mature sample

9UL-01 contained the lowest percentage of porosity at 5.52%. This sample also measured the smallest average pore sizes.

5. Scattering intensity profiles obtained from combined SAXS-USAXS-WAXS measurements revealed a broad pore size distribution (micro- to nano-porosity). As expected there were variations in pore size distribution from sample-to-sample. The more precise nanopore distribution will be known after the SAXS data is reduced fully.
6. Based on preliminary findings, where VRo increased, the largest volumes of nanoporosity occurred at larger pore sizes. Shale with the lowest VRo (0.8%) had either broad or sharp peaks indicating the sizes of pores that first appeared around 30 Å. Samples with 0.9% VRo had porosity peak first appearing slightly higher at 37 Å. The most thermally mature samples (0.95 % VRo) showed initial peaks closer to 50 Å. As thermal maturity increased, the largest amount of pores were found at slightly higher particle diameters (Figures 18-22 and Table 3).
7. These preliminary results suggest pore sizes decreased with increased maturity. Subsurface geochemistry, such as organic material migration and diagenetic mineral precipitation, can be attributed to disaggregated and occluded porosity at increased thermal maturities.

REFERENCES

Altaner, S.P. and Ylagan, R.F. (1997) Comparison of Structural Models of Mixed-Layer Illite/Smectite and Reaction Mechanisms of Smectite Illitization. Clays and Clay Minerals, v. 45, p. 517-533.

Anovitz, L. M., and Cole, D. R. (2015) Characterization and Analysis of Porosity and Pore Structures. *Reviews in Mineralogy and Geochemistry*, *80*(1), 61–164. https://doi.org/10.2138/rmg.2015.80.04

Anovitz, L.M., Frieburg, J.T., Wasbrough, M., Mildner, D.F.R., Littrell, K.C., Pipich, V., and Ilavsky, J., (2017) The effects of burial diagenesis on multiscale porosity in the St. Peter Sandstone: An imaging, small-angle, and ultra-small-angle neutron scattering analysis, *Marine and Petroleum Geology* doi: 10.1016/j.marpetgeo.2017.11.004

Anovitz, L. M., and Cole, D. R. (2018) Analysis of the Pore Structures of Shale Using Neutron and X-Ray Small Angle Scattering. 71-118. DOI: 10.1002/9781119118657.ch4.

Ashman, M.R., and Puri, G, (2002) Essential Soil Science. Hoboken, NJ: Wiley-Blackwell

Ball, M. (1995) Permian Basin Province (044), in Gautier, D.L., Dolton, G.I., Takahashi, K.T., and Varnes, K.L., eds., 1995 National assessment of United States oil and gas resources—Results, methodology, and supporting data: U.S. Geological Survey Digital Data Series DDS-30.

Baumgardner, Robert W., Jr , Hamlin1, Scott H., and Rowe1, Harry D. (2014) High-Resolution Core Studies of Wolfcamp/Leonard Basinal Facies, Southern Midland Basin, Texas. 1 The Bureau of Economic Geology, Jackson School of Geosciences, The University of Texas at Austin, Austin, TX

Berger, G., Lacharpagne, J.C., Velde, B., Beaufort, D., and Lanson, B. (1997) Kinetic constraints on illitization reactions and the effects of organic diagenesis in sandstone/shale sequences: Applied Geochemistry 12(1): 23-35.

Blomquist, P.K. (2016) Wolfcamp Horizontal Play, Midland Basin, West Texas. Oral presentation given at the AAPG Pacific Section and Rocky Mountain Section Joint Meeting, Las Vegas, Nevada, 2-5 October.

Brown, L. F. Jr., (1972) Virgil and Lower Wolfcamp Repetitive Environments and the Depositional Model, NorthCentral Texas. Cyclic sedimentation in the Permian Basin, ed. 2. West Texas Geological Society, 115–134.

Bruce, CH. (1984) Smectite dehydration—Its relation to structural development and hydrocarbon accumulation in northern Gulf of Mexico basin. AAPG Bull 68:673–683.

Burnham, Alan K. (2017) Porosity and permeability of Green River oil shale and their changes during retorting, Volume 203, pp. 208-213 ISSN 0016-2361

Burst, JF Jr. (1969) Diagenesis of Gulf Coast clayey sediments and its possible relation to petroleum migration. AAPG Bull 68:73–93.

Cardott, B.J., and Lambert, M.W. (1985) Thermal maturation by vitrinite reflectance of Woodford Shale, Anadarko basin, Oklahoma: AAPG Bulletin, v. 69, p. 1982-1998.

Cardott, Brian J. (2012) Thermal Maturity of Woodford Shale Gas and Oil Plays, Oklahoma, USA." International Journal of Coal Geology, vol. 103, pp. 109-119. EBSCO host, doi:10.1016/j.coal.2012.06.004.

Carter, L.S., Kelley, S.A., Blackwell, D.D., and Naeser, N.D. (1998) Heat flow and thermal history of the Anadarko basin, Oklahoma: AAPG Bulletin, v. 82, p. 291-316.

Chapmin, R. (Ed.). (1983) Chapter 2 Early Deformation of Sedimentary Basins: Growth Structures. *Petroleum Geology*. Elsevier. https://doi.org/https://doi.org/10.1016/S0376-7361(08)70086-4

Clarkston, C.R., Solano, N., Bustin, R.M., Bustin, A.M.M., Chalmers, G.R.L., He, L., Melnichenko, Y.B., Radlinski, A.P., Black, T.P., (2013) Pore structure charachterization of North American shale gas reservoirs using USANS/SANS, gas adsorption, and mercury intrusions: Fuel, v. 103 ©, p.606-616.

Conant, L. C. and Swanson, V. E. (1961) Chattanooga Shale and related rocks of central Tennessee and nearby areas. U. S. Geological Survey Professional Paper. United States, U. S. Geological Survey: Reston, VA, United States.

Denison, R.E.,. Lidiak E.G, Bickford, M.E., and Kisvarsanyi E.B., (1984) Geology and geochronology of Precambrian rocks in the central interior region of the United States, in J. E. Harrison and Z. E. Peterman, eds., Correlation of Precambrian rocks of the United States and Mexico: U.S. Geological Survey Professional Paper 1241–C, 20 p.

Eberl, D. D. and Środoń, J. (1988) Ostwald ripening and interparticle-diffraction effects for illite crystals: American Mineralogist 73: 1345-1335.

Elliott, W.C., Aronson, J.L., Matisoff, G., and Gautier, D.L. (1991) Kinetics of the Smectite to Illite Transformation in the Denver Basin: Clay Mineral, K-Ar Data, and Mathematical

Model Results. The American Association of Petroleum Geologists Bulletin, v. 75, no. 4, p. 436-462.

Elliott, W.C. and Matisoff, G. (1996) Evaluation of Kinetic Models for the Smectite to Illite Transformation. Clays and Clay Minerals, v. 44, no. 1, p. 77-87.

Elliott, W.C. and Haynes, J. (2002) The Chemical Character of Fluids Forming Diagenetic Illite in the Southern Appalachian Basin. American Mineralogist, v. 87, p. 1519-1527.

Engle, M. A., Reyes, F. R., Varonka, M. S., Orem, W. H., Ma, L., Ianno, A. J., Carroll, K. C. (2016) Geochemistry of formation waters from the Wolfcamp and "Cline" shales: Insights into brine origin, reservoir connectivity, and fluid flow in the Permian Basin, USA. Chemical Geology, 425, 76–92.

Eseme, J.L., Urai, B.M., Krooss, R. Littke(2007) Review of mechanical properties of oil shales: implications for exploitation and basin modeling. Oil Shale, 24 (2)

Eslinger, E., and Pevear, D. R. (1988) *Clay minerals for petroleum geologists and engineers*. SEPM. Retrieved from https://books.google.com/books?id=LFTwAAAAMAAJ

Ewing, T.E., (1990) Tectonic map of Texas: The University of Texas at Austin, Bureau of Economic Geology.

Frenzel, H. N., Bloomer, R. R., Cline, R. B., Cys, J. M., Galley, J. E., Gibson, W. R., ... & Thompson III, S. (1988). The Permian basin region. Sedimentary cover—North American craton: US: Boulder, Colorado, Geological Society of America, The Geology of North America, 2, 261-306.

Gaswirth, S.B., Marra, K.R., Lillis, P.G., Mercier, T.J., Leathers-Miller, H.M., Schenk, C.J., Klett, T.R., Phuong, A.L., Tennyson, M.E., Hawkins, S.J., Brownfield, M.E., Pitman, J.K., Finn, T.M., 2018 Assessment of undiscovered continuous oil resources in the Wolfcamp shale of the Midland Basin, Permian Basin Province, Texas, 2016; USGS Fact Sheet 2016-3092

Giles, M. R. (1997) Diagenesis: A Quantitative Perspective. Implications for Basin Modelling and Rock Property Prediction.

Golonka, J., & Kiessling, W. (2002) Phanerozoic time scale and definition of time slices. In Kiessling, W.; Flugel, E.; and Golonka, J., eds. Phanerozoic reef patterns. SEPM Special Publication, 72, 11–20.

Harrison, W. J. and G. D. Thyne (1992) Predictions of diagenetic reactions in the presence of organic acids. Geochimica et Cosmochimica Acta 56(2): 565-586.

Hester, T.C., Schmoker, J.W., and Sahl, H.L. (1990) Log-derived regional source-rock characteristics of the Woodford Shale, Anadarko basin, Oklahoma: U.S. Geological Survey Bulletin 1866-D, 38 p.

Hester, T.C., Schmoker, J.W., and Sahl, H.L., (1992) Structural controls on sediment distribution and thermal maturation of the Woodford Shale, Anadarko basin, Oklahoma, in K.S. Johnson and B.J. Cardott, eds., Source rocks in the southern Midcontinent, 1990 symposium: OGS Circular 93, p. 321-326.

Higley, D.,Cook A., Troy & J Pawlewicz, Mark. (2014) Chapter 6 Petroleum Systems and Assessment of Undiscovered Oil and Gas in the Anadarko Basin Province, Colorado, Kansas, Oklahoma, and Texas—Woodford Shale Assessment Units.

Hoffman, J. and Hower, J. (1979) Clay Mineral Assemblages as Low Grade Metamorphic Geothermometers: Application to the Thrust Faulted Disturbed Belt of Montana, U.S.A.. Society of Economic Paleontologists and Mineralogists, Special Publication no. 26, p. 55-79.

Hower, J., Eslinger, E., Hower, M., and Perry, E., (1976) The mechanism of burial diagenetic reactions in argillaceous sediments: 1. Mineralogical and chemical evidence. Geological Society of America Bulletin, 87, 725-'737

Hower, J. and Aronson, J.L. (1976) Mechanism of Burial Metamorphism of Argillaceous Sediment: 2. Radiogenic Argon Evidence. Geological Society of America Bulletin, v. 87, p 738-74.

Jackson, M.L. (1979) Soil Chemical Analysis-Advanced Course, A Manual of Methods Useful for Instruction and Research in Soil Chemistry, Physical Chemistry of Soils, Soil Fertility, and Soil Genesis. Second Edition, Revised from original edition of 1956, Published by the Author.

Ilavsky, Jan and Jemian, Peter R., "Irena: tool suite for modeling and analysis of small-angle scattering", Journal of Applied Crystallography, vol. 42 (2009).

Jarvie, D.M., Claxton, B.L., Henk, F., Breyer, J.T. (2001) Oil and shale gas from the Barnett Shale, Ft. Worth Basin, Texas AAPG National Convention, June 3–6, 2001, Denver, CO, AAPG Bull., 85, p. A100

Jin, L., Mathur, R., Rother, G., Cole, D., Bazilevskaya, E., Williams, J., … Brantley, S. (2013). Evolution of porosity and geochemistry in Marcellus Formation black shale during weathering. Chemical Geology, 356, 50–63. https://doi.org/10.1016/J.CHEMGEO.2013.07.012

Johnson, K. S. (1989) Geologic evolution of the Anadarko Basin, in K.S. Johnson ed., Anadarko basin symposium, 1988: OGS Circular 90

Johnson, K.S., and Cardott, B.J. (1992) Geologic framework and hydrocarbon source rocks of Oklahoma, in K.S. Johnson and B.J. Cardott, eds., Source rocks in the southern Midcontinent, 1990 symposium: OGS Circular 93, p. 21-37.

Kennedy, M., Löhr, S., Fraser, S., and Baruch, E.,(2014) Direct evidence for organic carbon preservation as clay-organic nanocomposites in a Devonian black shale; from deposition to diagenesis. Earth and Planetary Science Letters. 388. 59–70. 10.1016/j.epsl.2013.11.044.

Kim, J., Dong, H., Yang, K., Park, H., Elliott W.C., Spivack, A., Koo, T., Kim, G., Morono, Y., Henkel, S., Inagaki, F., Zeng, Q., Hoshino, T., Heuer, V.B. (2019) Naturally occurring, microbially induced smectite-to-illite reaction. *Geology* ; 47 (6): 535–539. doi: https://doi.org/10.1130/G46122.1

Kirkland, D.W., Denison, R.E., Summers, D.M., and Gormly, J.R. (1992) Geology and organic geochemistry of the Woodford Shale in the Criner Hills and western Arbuckle Mountains, in K.S. Johnson and B.J. Cardott, eds., Source rocks in the southern Midcontinent, 1990 symposium: OGS Circular 93, p. 38-69.

Leu, L., Georgiadis, A., Blunt, M. J., Busch, A., Bertier, P., Schweinar, K., Liebi, M., Menzel, A. & Ott, H. (2016) Multiscale Description of Shale Pore Systems by Scanning SAXS and WAXS Microscopy. Energy Fuels, 30, 10282–10297.

Loucks, R. G., Reed, R. M., Ruppel, S. C., and Hammes, U. (2012) Spectrum of pore types and networks in mudrocks and a descriptive classification for matrix-related mudrock pores: AAPG Bulletin, v. 96, no. 6, p. 1071–1098, doi: 10.1306 /08171111061

MacGowan, D. B. and Surdam, R.C. (1990) Carboxylic acid anions in formation waters, San Joaquin Basin and Louisiana Gulf Coast, U.S.A.--Implications for clastic diagenesis: Applied Geochemistry 5(5-6): 687-701.

Magara, K. (1975) Reevaluation of montmorillonite dehydration as a cause of abnormal pressure. AAPG Bull 59:292–302.

Marshall, J.D., (1982) Isotopic composition of displacive fibrous calcite veins: reversals in pore-water composition trends during burial diagenesis, Journal of Sedimentary Petrology, v. 52, p. 615-630.

Mastalerz, Maria, Schimmelmann, Arndt, Drobniak, Agnieszka, and Chen, Yanyan (2013) Porosity of Devonian and Mississippian New Albany Shale across a maturation gradient: Insights from organic petrology, gas adsorption, and mercury intrusion. *AAPG Bulletin* ; 97 (10): 1621–1643. doi: https://doi.org/10.1306/04011312194

Mazzullo, S. J. (1997) Stratigraphic exploration plays in Ordovician to Lower Permian strata in the Midland Basin and on the Eastern Shelf. Publications-West Texas Geological Society, 1-38.

Mohnhoff, D.l, Littke, R., Krooss, B.M., Weniger, P.(2016) Flow-through Extraction of Oil and Gas Shales under Controlled Stress Using Organic Solvents: Implications for Organic Matter-Related Porosity and Permeability Changes with Thermal Maturity. *International Journal of Coal Geology*, vol. 157, pp. 84–99. *EBSCOhost*, doi:10.1016/j.coal.2015.09.010.

Montgomery, S. L. (1996) Permian "Wolfcamp" Limestone Reservoirs: Powell Ranch Field, Eastern Midland Basin. AAPG Bulletin, 80(9), 1349-1365.

Moore, D. M. and Reynolds, R. C., Jr. (1997.) X-Ray Diffraction and the Identification and Analysis of Clay Minerals, 2nd ed. xviii + 378 pp. Oxford, New York: Oxford University Press.

Nadeau P.H., and Bain, D.C. (1986) Composition of some smectites and diagenetic illitic clays \and implications for their origin. Clays and Clay Minerals, 34.

Nadeau, P. H., Wilson, M. J., McHardy, W. J., and Tait, J. M. (1984) Interstratified clays as fundamental particles: Science 225: 923-925.

Nagaraj, N.S. Pandian, P.S.R. Narasimha Raju (1993) Stress state-permeability relationships for fine-grained soil. Géotechnique, 43, pp.

Nagaraj, T.S., Griffiths, F.J., Joshi, R.C., Vatsala, A., and Murthy, B.R.S. (1990) Change in pore-size distribution due to consolidation of clays – discussion. Geotechnique, 40, 303– 309.

Nirschl, H. and Guo, X. (2018) Characterisation of structured and functionalized particles by small-angle X-ray scattering (SAXS). Chemical Engineering Research and Design, ISSN: 0263-8762, Vol: 136, Page: 431-446.

Nygård, R.M., Gutierriez, M., Guatim, R., Hoeg, K., 2004, Compaction behavior of argillaceous sediments as a function of diagenesis: Marine and Petroleum Geology, v. 21, p. 349-362.

Osborn, S.G. (2006) The timing and causes of illite formation in the Cretaceous Marias River Shale, Disturbed Belt, Montana M.S. Thesis, Georgia State University, Atlanta Georgia, USA, 117 pp.

Palandri, J. L. and Reed, M. H. (2001) Reconstruction of in situ composition of sedimentary formation waters: Geochimica et Cosmochimica Acta 65(11): 1741-1767.

Pevear, D. R. (1999) Illite and hydrocarbon exploration. *Proceedings of the National Academy of Sciences*, *96*(7), 3440 LP-3446. https://doi.org/10.1073/pnas.96.7.3440

Pollastro, R.M. (1989) Clay minerals as geothermometers and indicators of thermal maturity - Application to basin history and hydrocarbon generation. United States

Pollastro, R. M., (1993) Considerations and applications of the illite/smectite geothermometer in hydrocarbon-bearing rocks of Miocene to Mississippian age, Clays and Clay Minerals, vol. 41, p. 119-119.

Pommer, M., and Milliken, K. L. (2015) Pore types and pore-size distributions across thermal maturity, Eagle Ford Formation, southern Texas. *AAPG Bulletin*, *99*(9), 1713-1744. https://doi.org/10.1306/03051514151

Reynolds Jr., R. C. and Hower, J. (1970) The nature of interlayering in mixed-layer illite-montmorillonites: *Clays & Clay Minerals* **18**, 25–26.

Roberts, Jennifer M., and Elmore, R. D. (2018) A diagenetic study of the Woodford Shale in the southeastern Anadarko Basin, Oklahoma, USA: Evidence for hydrothermal alteration in mineralized fractures.

Ruppert L.F., Sakurovs R. , Blach T.P., He L., Melnichenko Y.B., Mildner D.F.R. , Alcantar–Lopez L., (2013) A USANS/SANS study of the accessibility of pores in the Barnett Shale to methane and water Energy Fuel, 27, pp. 772-779

Ryan, Peter. (2014) Environmental and Low Temperature Geochemistry. Wiley Blackwell.

Sarg, J.F., Markello, J.R. and Weber, L.J. (1999) The second-order cycle, carbonate-platform growth, and reservoir, source, and trap prediction. In: Harris, P.M., Simo, J.A. and Saller, A.H., Editors, 1999. Advances in Carbonate Sequence Stratigraphy: Application to Reservoirs, Outcrops, and Models. SEPM Special Publication, 62, 1-24.

Schieber, J. (2010) Common Themes in the Formation and Preservation of Intrinsic Porosity in Shales and Mudstones - Illustrated with Examples Across the Phanerozoic. Society of Petroleum Engineers. doi:10.2118/132370-MS

Schindelin, J.; Arganda-Carreras, I. and Frise, E. (2012) "Fiji: an open-source platform for biological-image analysis", *Nature methods* 9(7): 676-682, PMID 22743772, doi: 10.1038/nmeth.2019

Severin, Kenneth P. (2004) Energy Dispersive Spectrometry of Common Rock Forming Minerals. Springer.

Sinclair, T. D. (2007) The generation and continued existence of overpressure in the Delaware Basin, Texas. [Doctoral dissertation]. Durham University.

Środoń, J. (1990) Illite-Smectite in the rock cycle: Lectures 6th Meet. European Clay Groups. Seville: 137-150.

Stroker, T.M., Harris, N.B., Elliott, W.C., and Wampler, J.M., (2013) Diagenesis of a tight gas reservoir: Upper Cretaceous Mesaverde Group, Piceance, Basin: Journal of Marine and Petroleum Geology, **40**, p 48-68. http://dx.doi.org/10.1016/j.marpetgeo.2012.08.003

Sullivan, K.L. (1985) Organic facies variation of the Woodford Shale in western Oklahoma: Shale Shaker, v. 35, p. 76-89.

U.S. Energy Information Administration (2017) International Energy Outlook 2017 https://www.eia.gov/outlooks/ieo/pdf/0484(2017).pdf

Velde, B., Suzuki, T., and Nicot, E. (1986) Pressure-Temperature-Composition of Illite/Smectite Mixed Layer Minerals: Niger Delta Mudstones and Other Examples. Clays and Clay Minerals, v. 34, no. 4, p. 435-441.

Velde B. and Vasseur G. (1992) Estimation of the diagenetic smectite-to-illite transformation in time-temperature space. Am. Mineral 77:967-976.

Velde, B. and Lanson, B. (1993) Comparison of I/S Transformation and Maturity of Organic Matter at Elevated Temperatures. Clays and Clay Minerals, v. 41, no. 2, p. 178-183.

Waples, D.W. (1980) Time and Temperature in Petroleum Formation: application of Lopatin’s method to Petroleum exploration: AAPG Bull., 64, p. 916-926.

Weaver, C.E. and Wampler, J.M. (1970) K, Ar, Illite Burial. Geological Society of America Bulletin, v. 81, p. 3423-3430.

Whittington II, Richard Allen, (2009) "Clay Mineralogy and Illite Crystallinity in the Late Devonian to Early Mississippian Woodford Shale in the Arbuckle Mountains, Oklahoma, USA." Thesis, Georgia State University http://scholarworks.gsu.edu/geosciences_theses/13

Wickard, Alyssa K, Elmore R. D. and Gerhard H.. (2016) A Diagenetic Study of the Wolfcamp Shale, Midland Basin, West Texas. 10.15530/urtec-2016-2460784.

Yang, K. M., and Dorobek, S. L. (1995) The Permian basin of west Texas and New Mexico: tectonic history of a" composite" foreland basin and its effects on stratigraphic development. Stratigraphic evolution of foreland basins: SEPM Special Publication, 52, 149-174.

APPENDICES

Appendix A: XRD Pattern Key

Appendix B: Air Dry, Ethylene Glycol Solvated and Heated Sample Patterns

Appendix C: Combined SAXS, USAXS and WAXS Curves

Appendix D: FE SEM Images

Appendix A

Below is the XRD pattern key used to label these samples.

XRD Patterns Key:

Ab:	albite
Chl:	chlorite
Dol:	dolomite
I:	illite
I/S:	illite-smectite
K:	kaolinite
Qtz:	quartz
S:	smectite
Tr:	trace mineral

Appendix B

Air gry, ethylene glycol solvated and heated sample patterns are shown below.

WC 9-3 (1-2 µm)

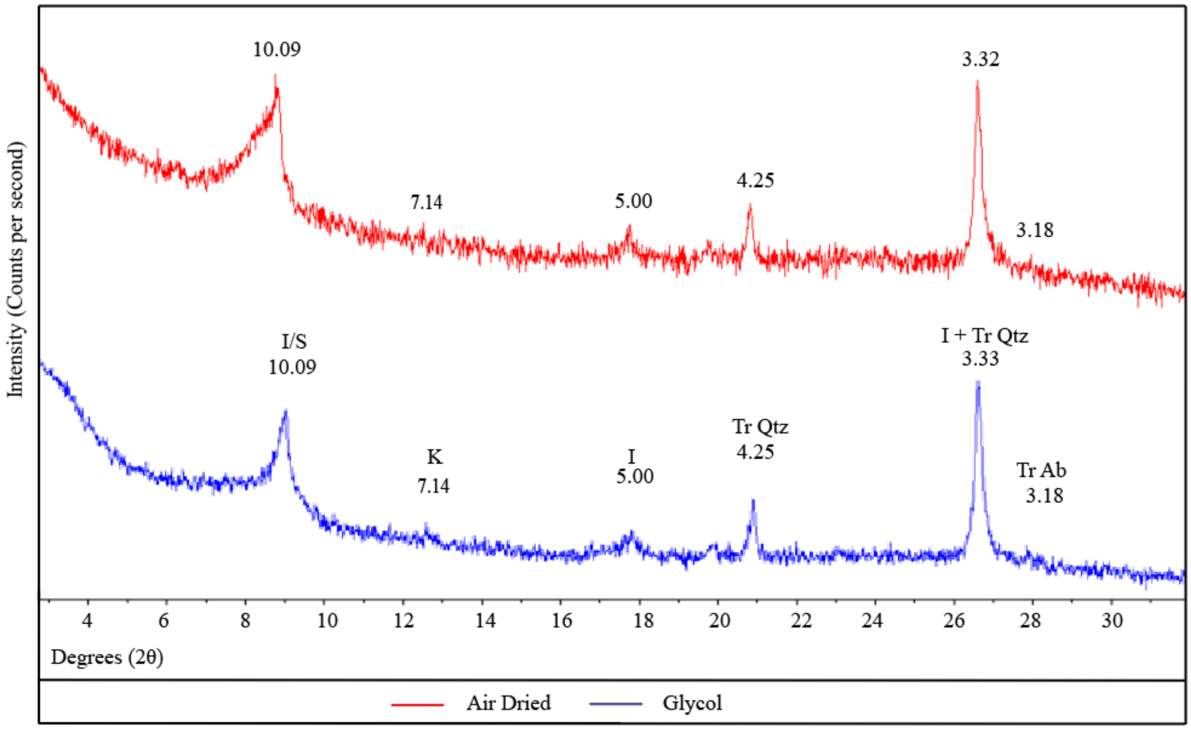

WP 60-1 (1-2 µm)

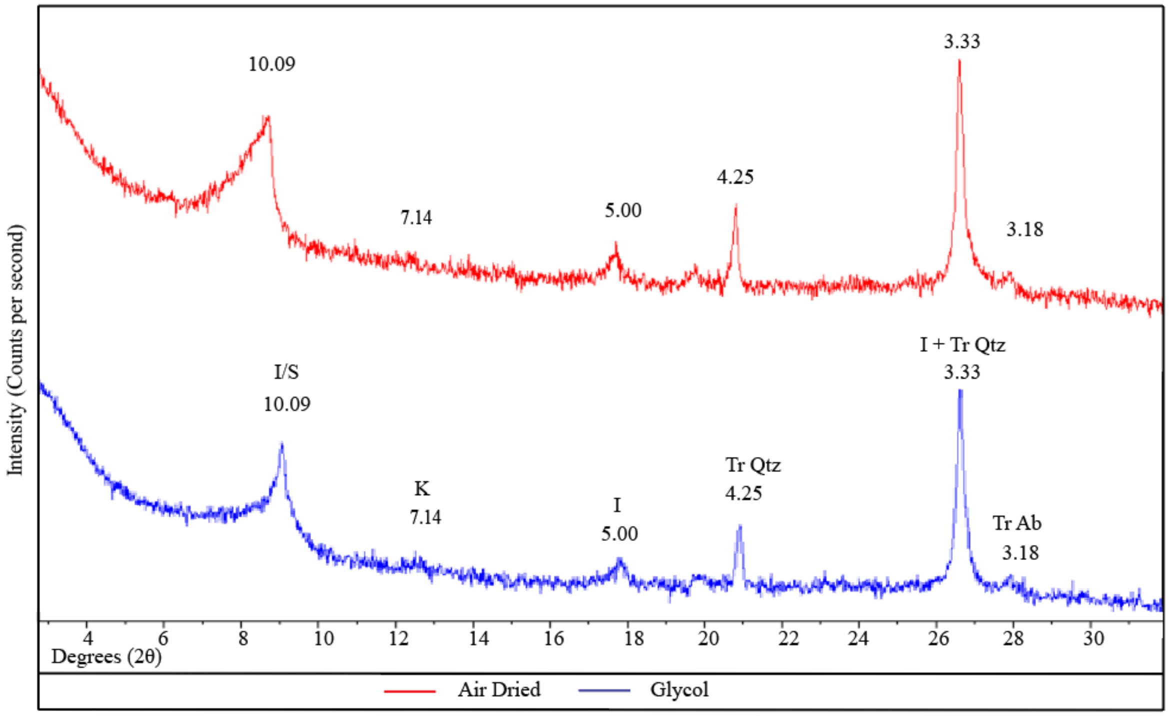

WP15-4 (1-2 μm)

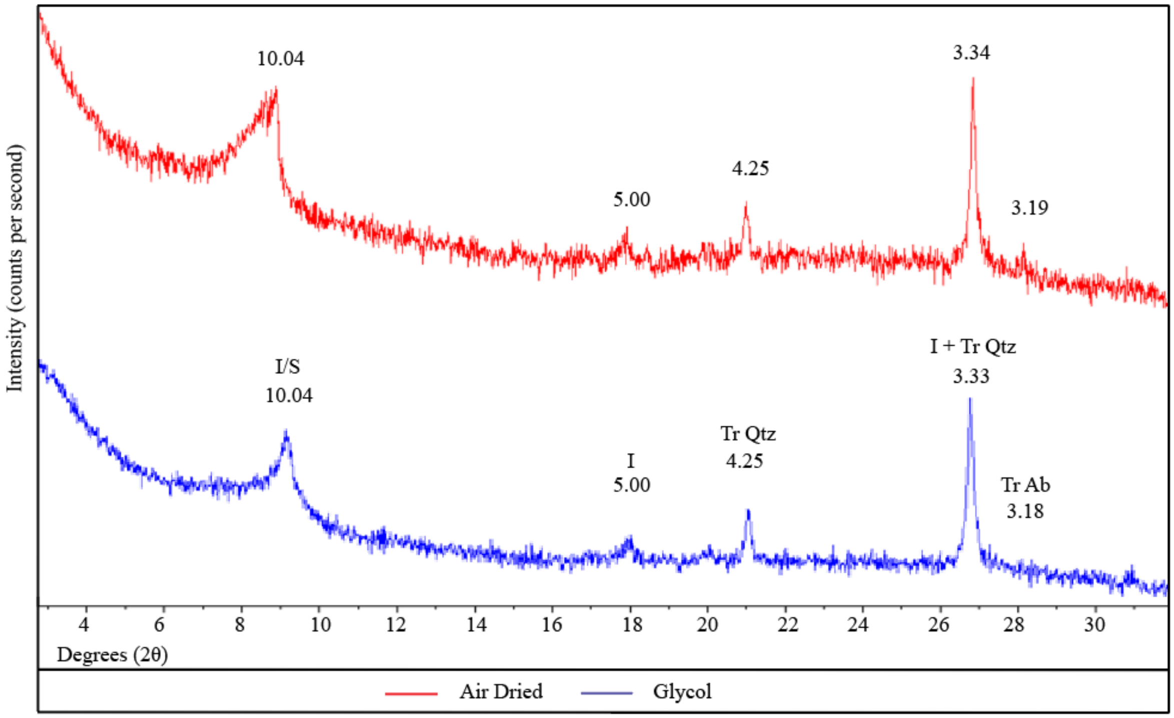

WP42-1 (1-2 μm)

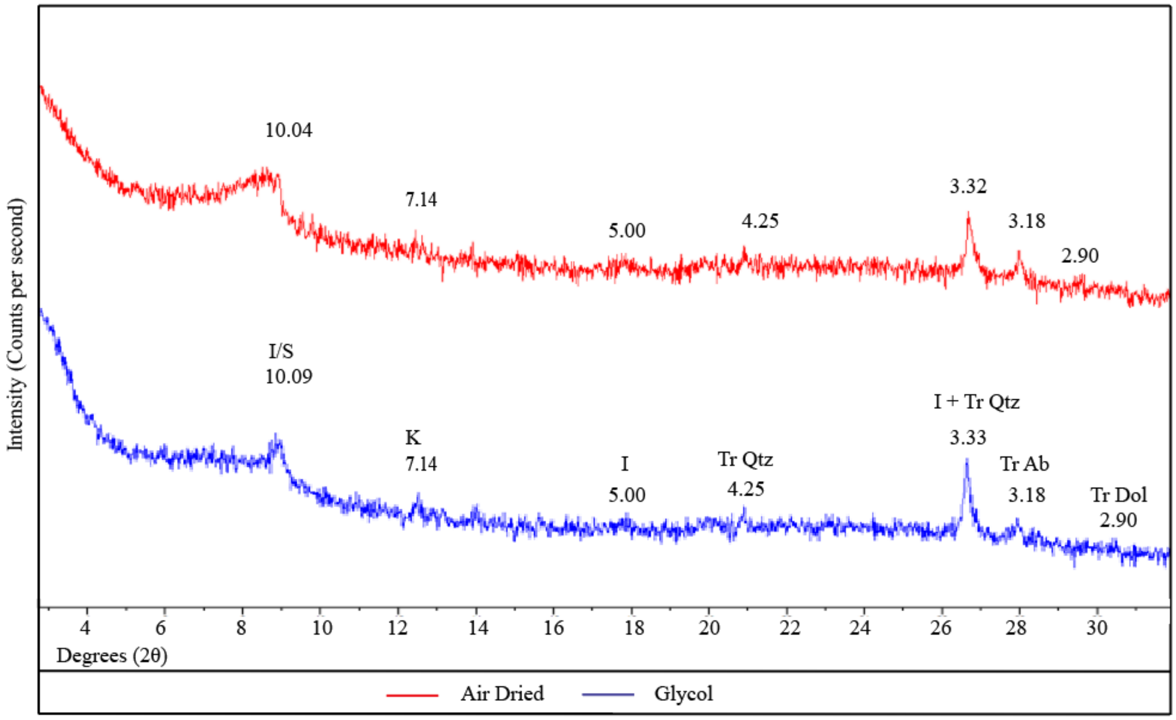

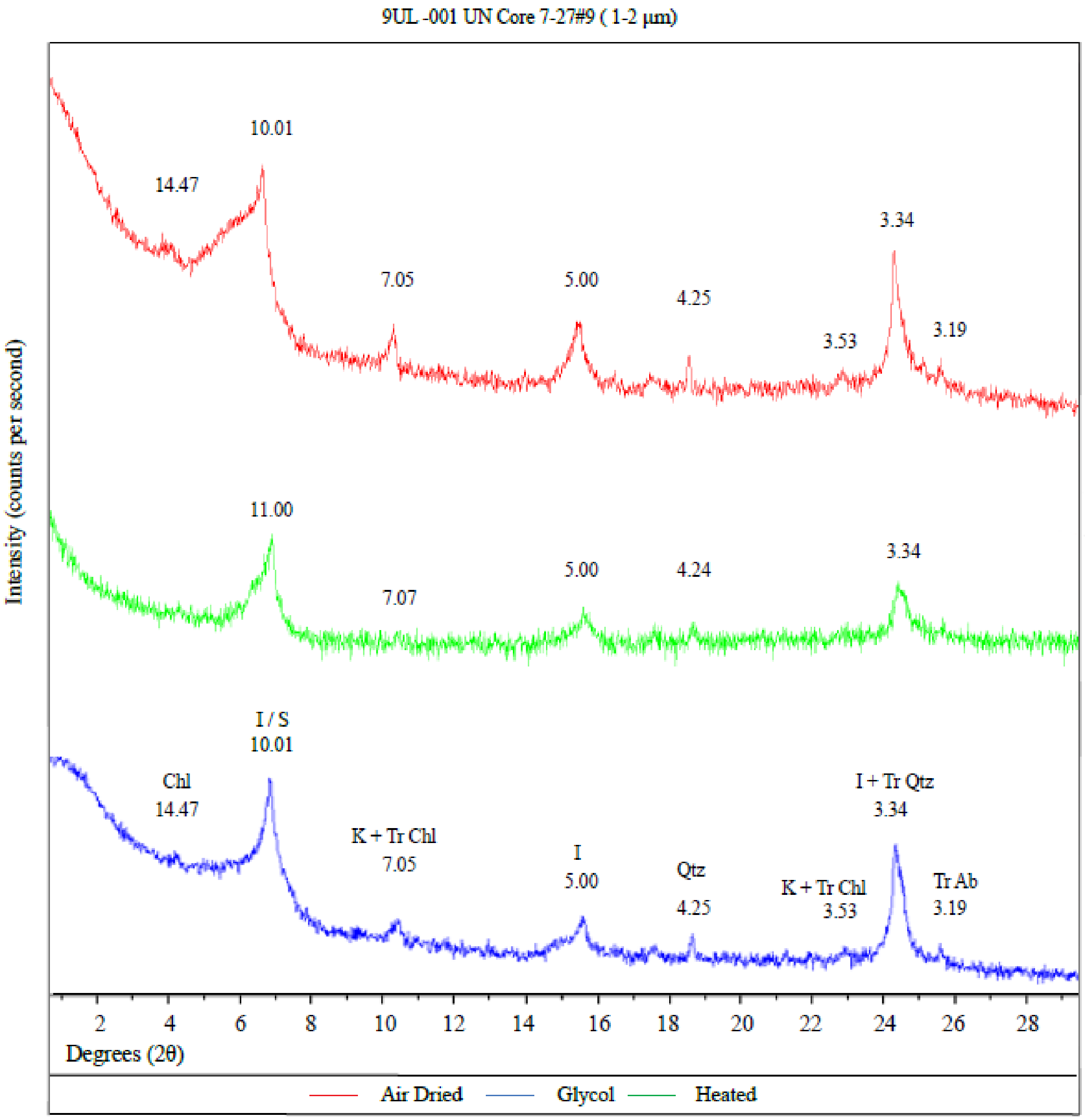
9UL -001 UN Core 7-27#9 (1-2 µm)
Intensity (counts per second)
14.47
10.01
7.05
5.00
4.25
3.53
3.34
3.19
11.00
7.07
5.00
4.24
3.34
I / S
10.01
Chl
14.47
K + Tr Chl
7.05
I
5.00
Qtz
4.25
K + Tr Chl
3.53
I + Tr Qtz
3.34
Tr Ab
3.19
2
4
6
8
10
12
14
16
18
20
22
24
26
28
Degrees (2θ)
Air Dried
Glycol
Heated

UN Core 7-27 #9-02 (1-2 µm)

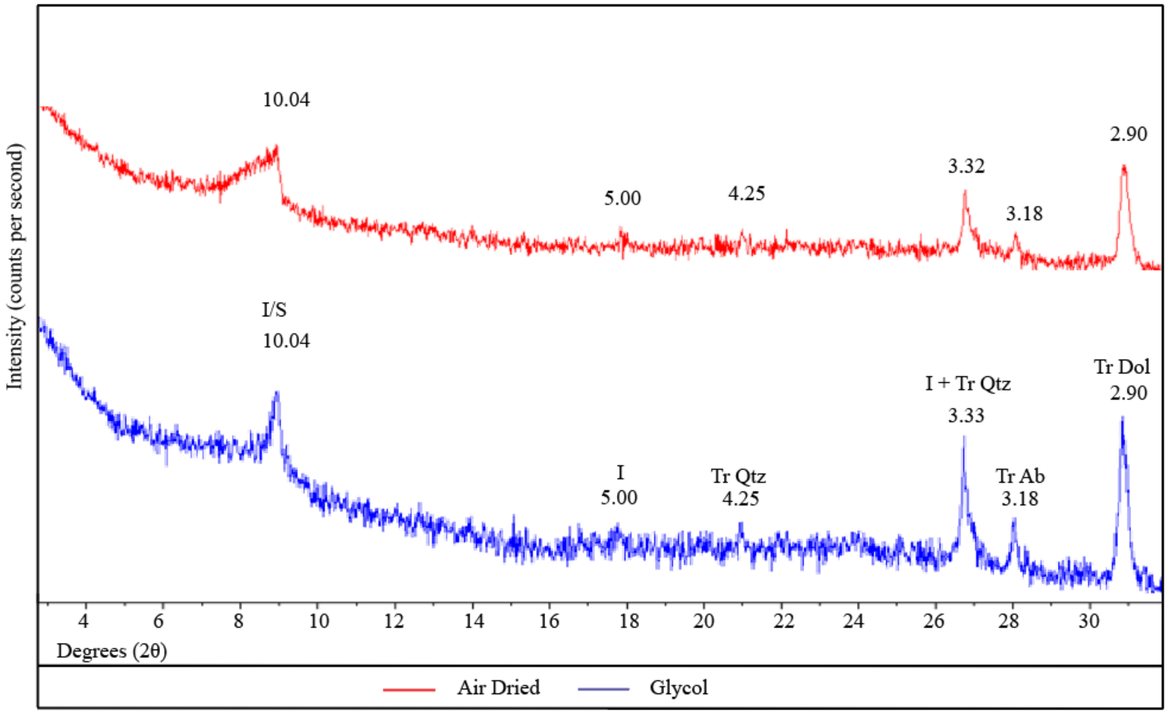

WC 9-3 (0.25 - 1 µm)

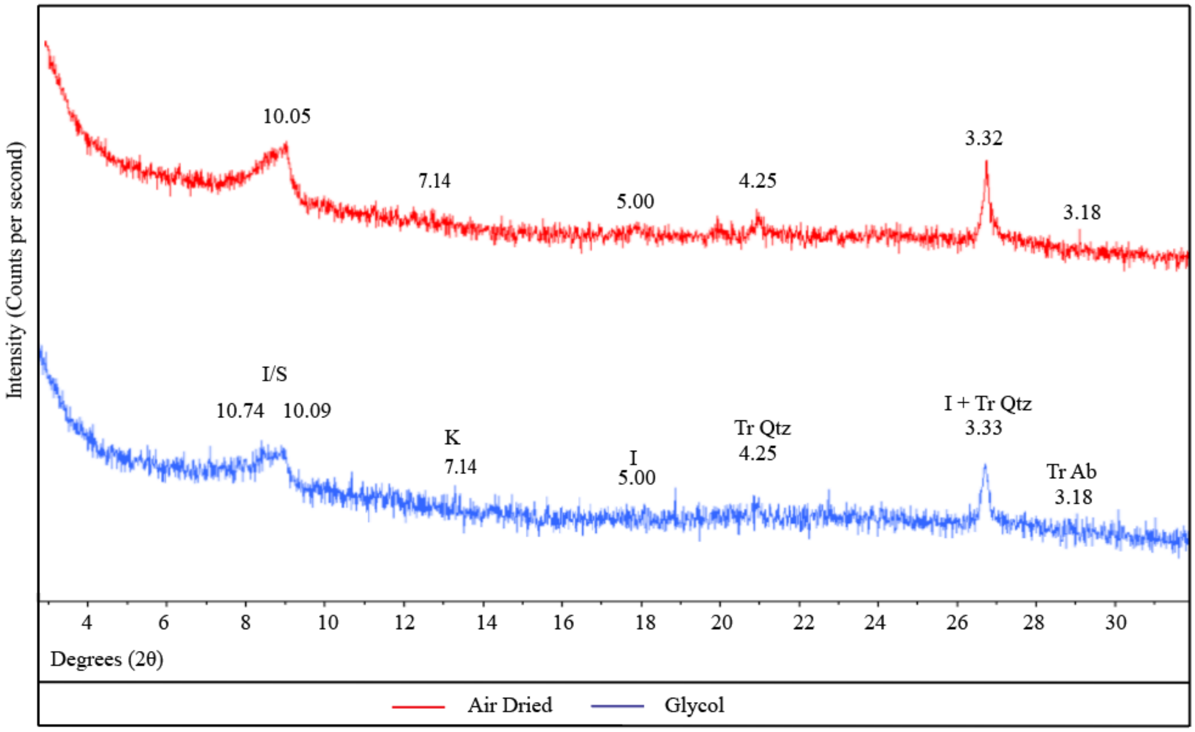

WP15-4 (0.25 - 1 μm)

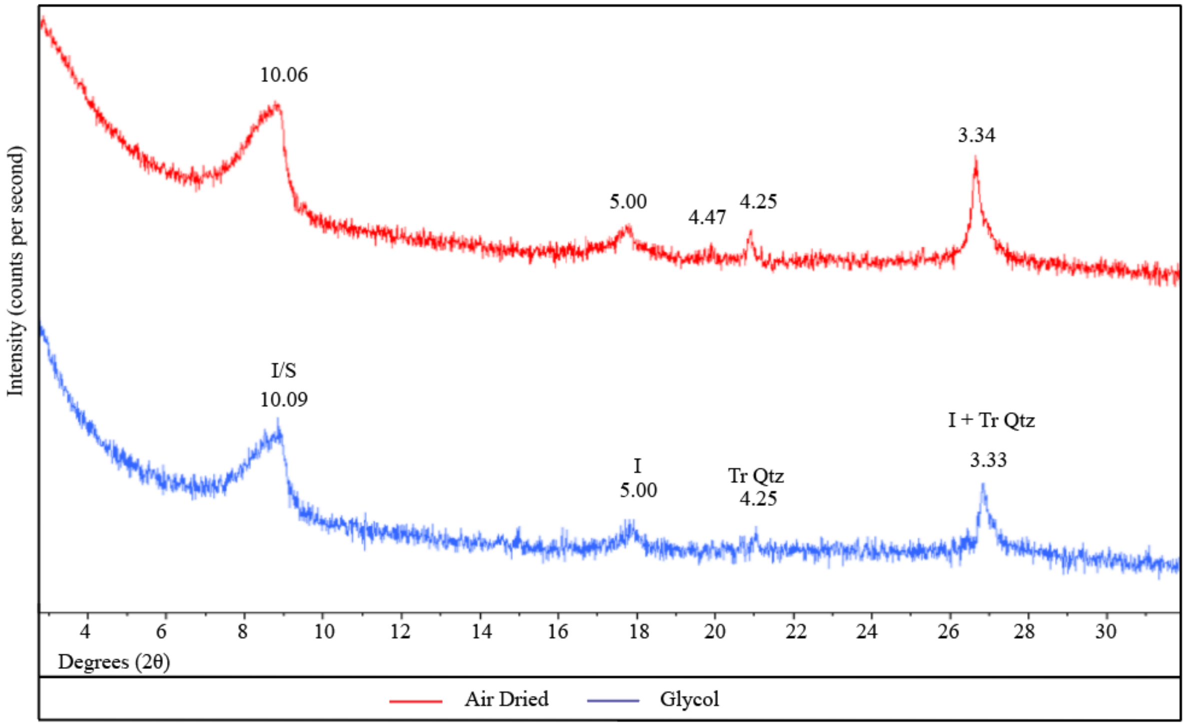

WP42-1 (0.25 - 1 μm)

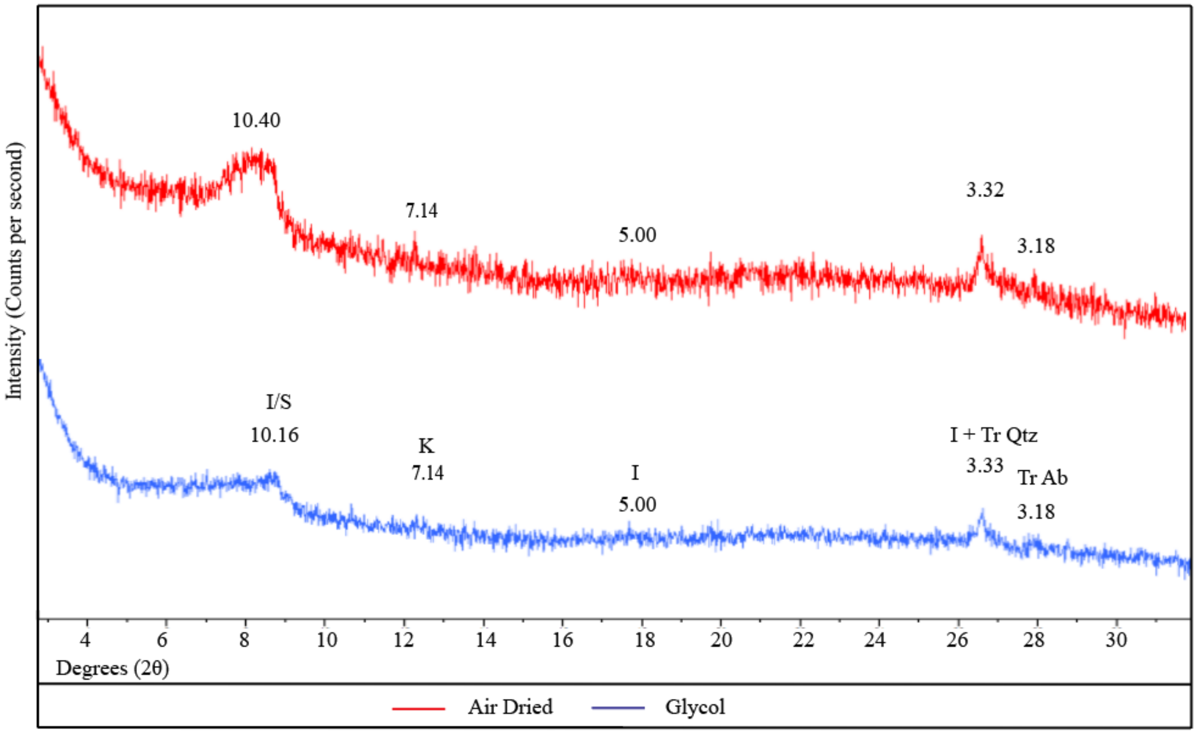

WP42-1 (0.25 - 1 μm)

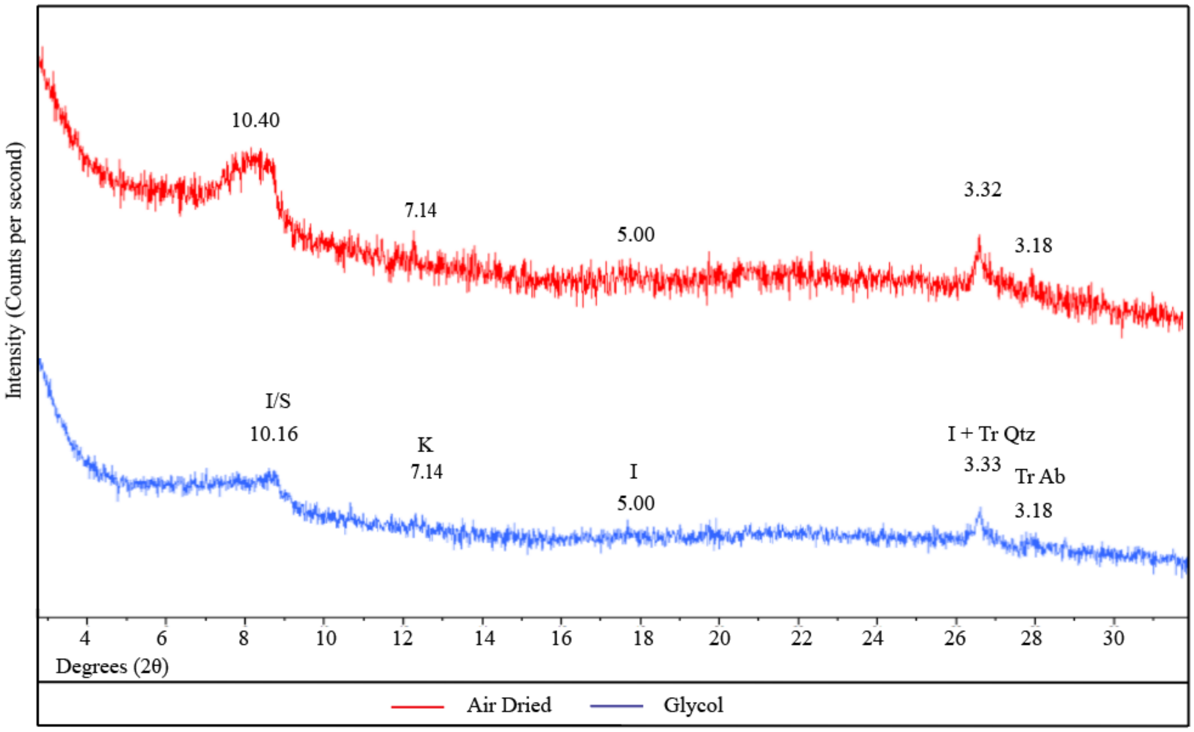

WP60-1 (0.25 - 1 μm)

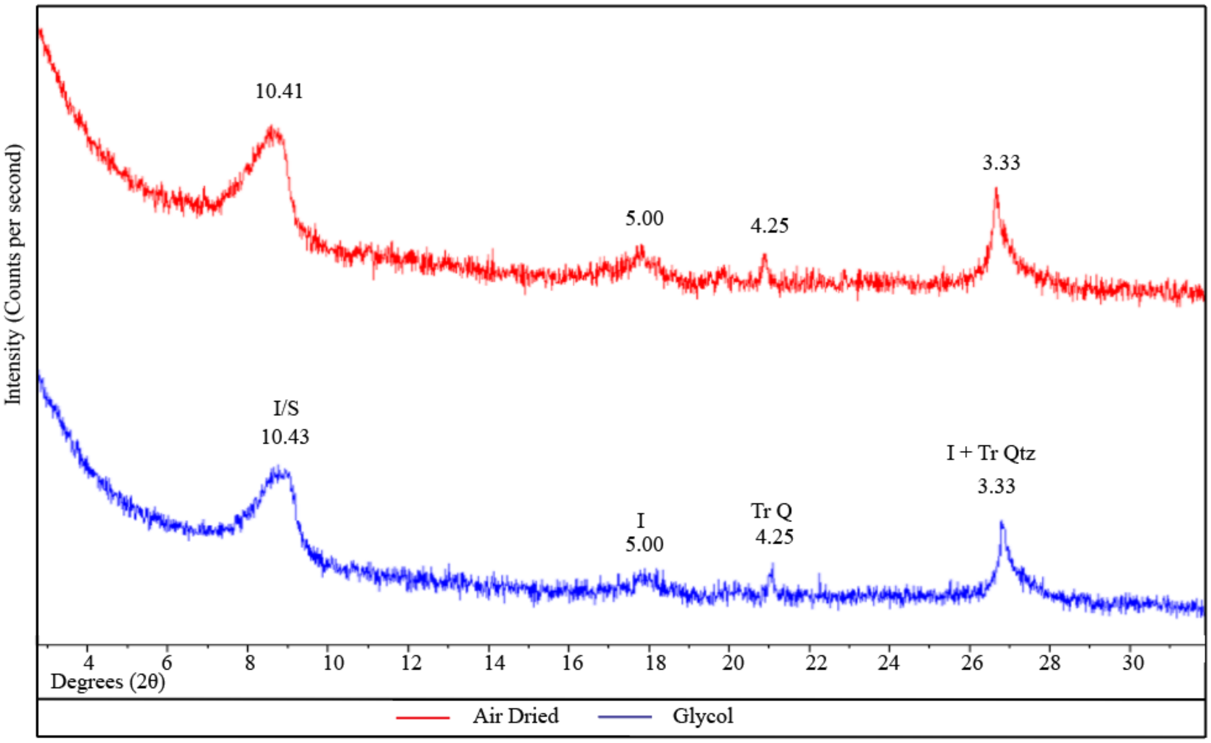

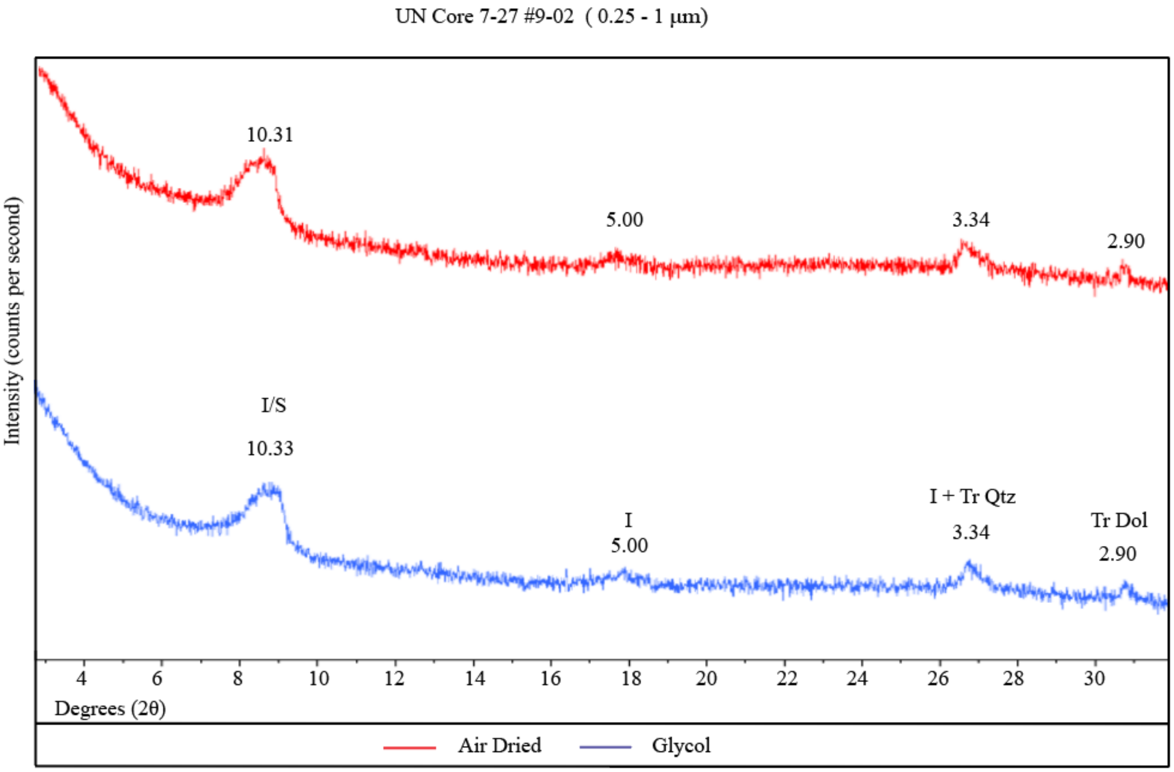
UN Core 7-27 #9-02 (0.25 - 1 µm)
Intensity (counts per second)
10.31
5.00
3.34
2.90
I/S
10.33
I + Tr Qtz
I
5.00
3.34
Tr Dol
2.90
4
6
8
10
12
14
16
18
20
22
24
26
28
30
Degrees (2θ)
Air Dried
Glycol

Appendix C

All scattering curves created by Igor are shown below. These curves were created with combines SAXS and USAXS data. Each sample has two corresponding patterns.

1. 9TO1_x_29_y14_R_0744

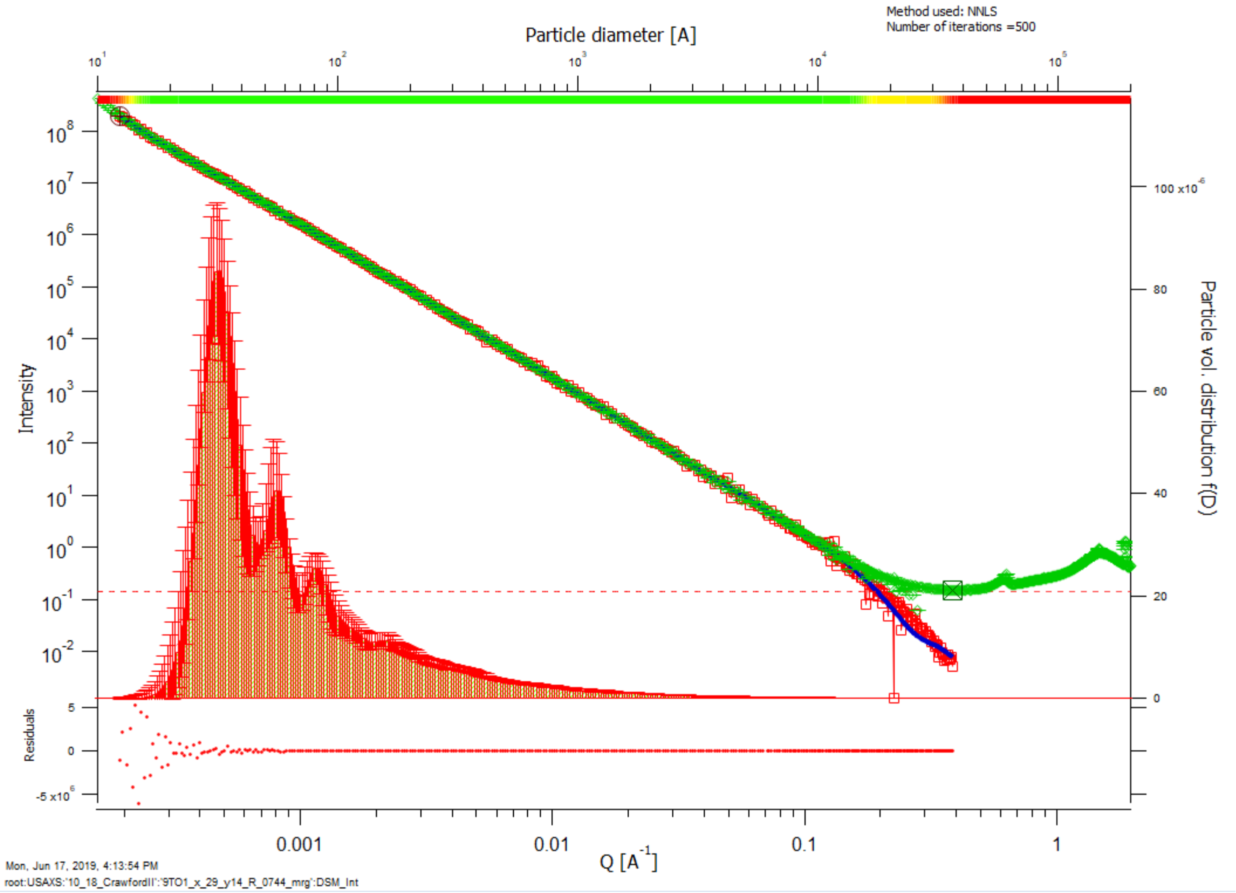

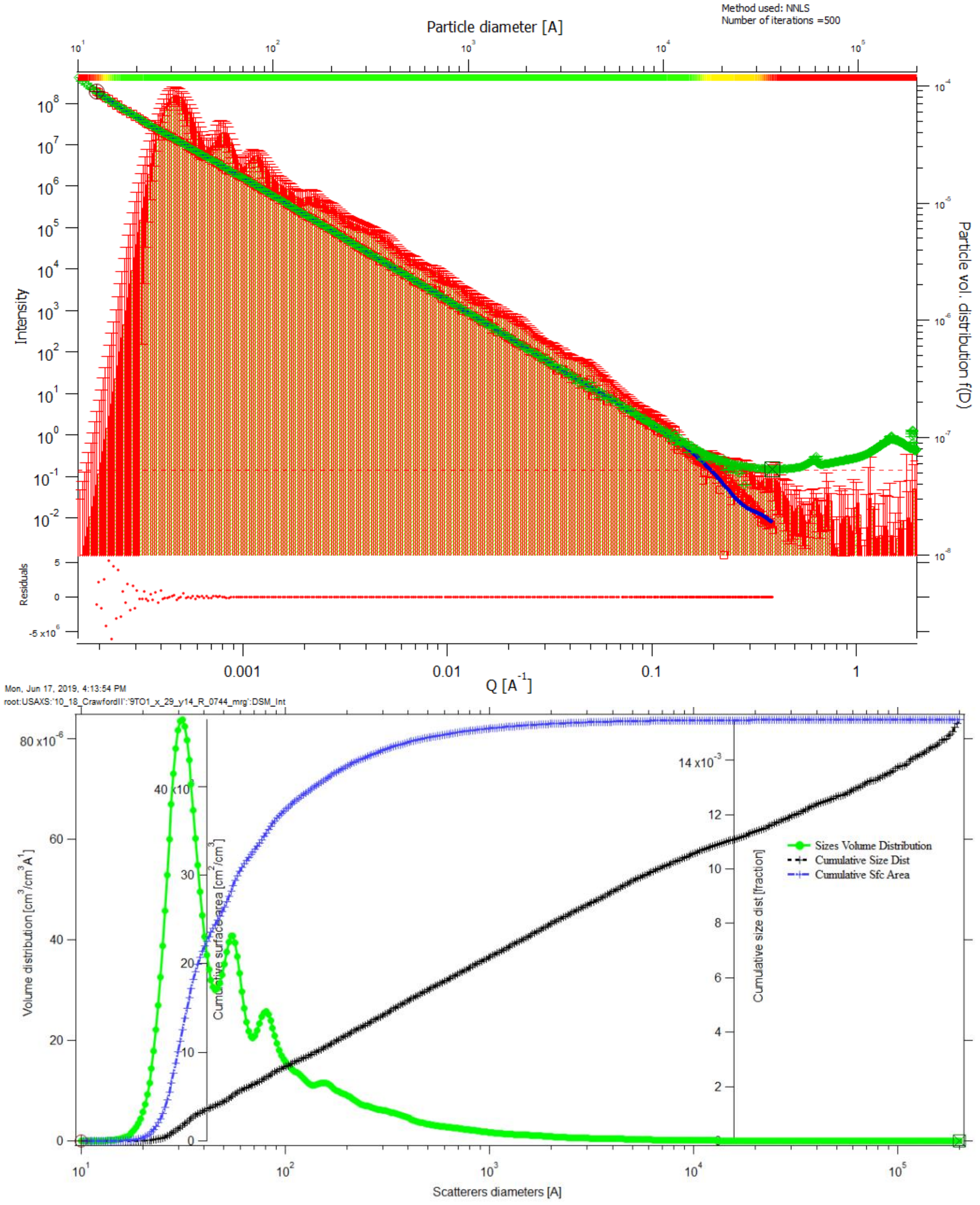
Method used: NNLS
Number of iterations =500
Particle diameter [A]
10^1
10^2
10^3
10^4
10^5
Intensity
10^8
10^7
10^6
10^5
10^4
10^3
10^2
10^1
10^0
10^-1
10^-2
Particle vol. distribution f(D)
10^-4
10^-5
10^-6
10^-7
10^-8
Residuals
5
0
-5 x10^6
0.001
0.01
0.1
1
Q [A^-1]
Mon, Jun 17, 2019, 4:13:54 PM
root:USAXS:'10_18_CrawfordII':'9TO1_x_29_y14_R_0744_mrg':DSM_Int
80 x10^-6
60
40
20
0
Volume distribution [cm^3/cm^3A^1]
40 x10^3
30
20
10
0
Cumulative surface area [cm^2/cm^3]
14 x10^-3
12
10
8
6
4
2
0
Cumulative size dist [fraction]
Sizes Volume Distribution
Cumulative Size Dist
Cumulative Sfc Area
10^1
10^2
10^3
10^4
10^5
Scatterers diameters [A]

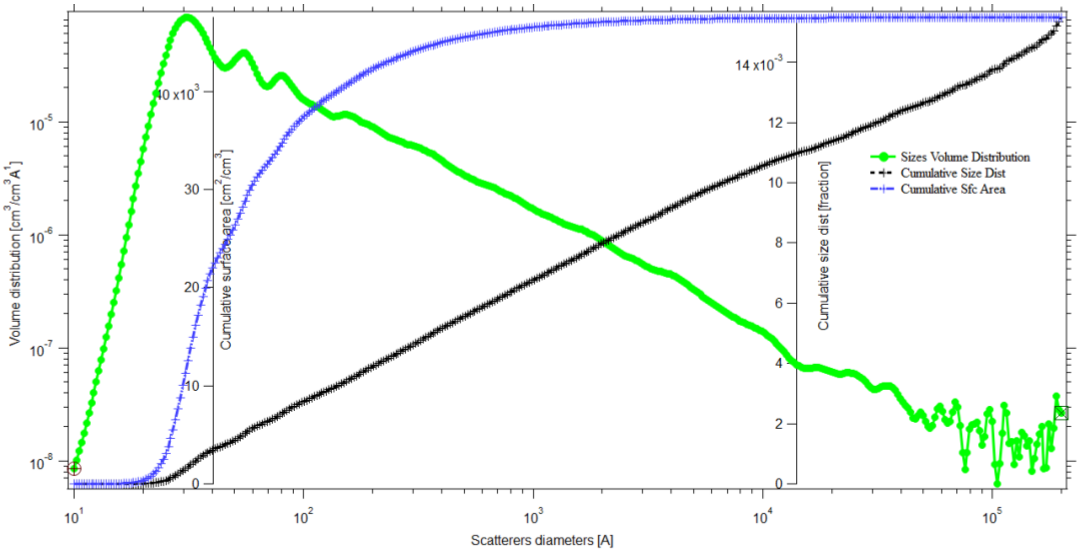

2. 9TO1_x_29_y_12_R_0746

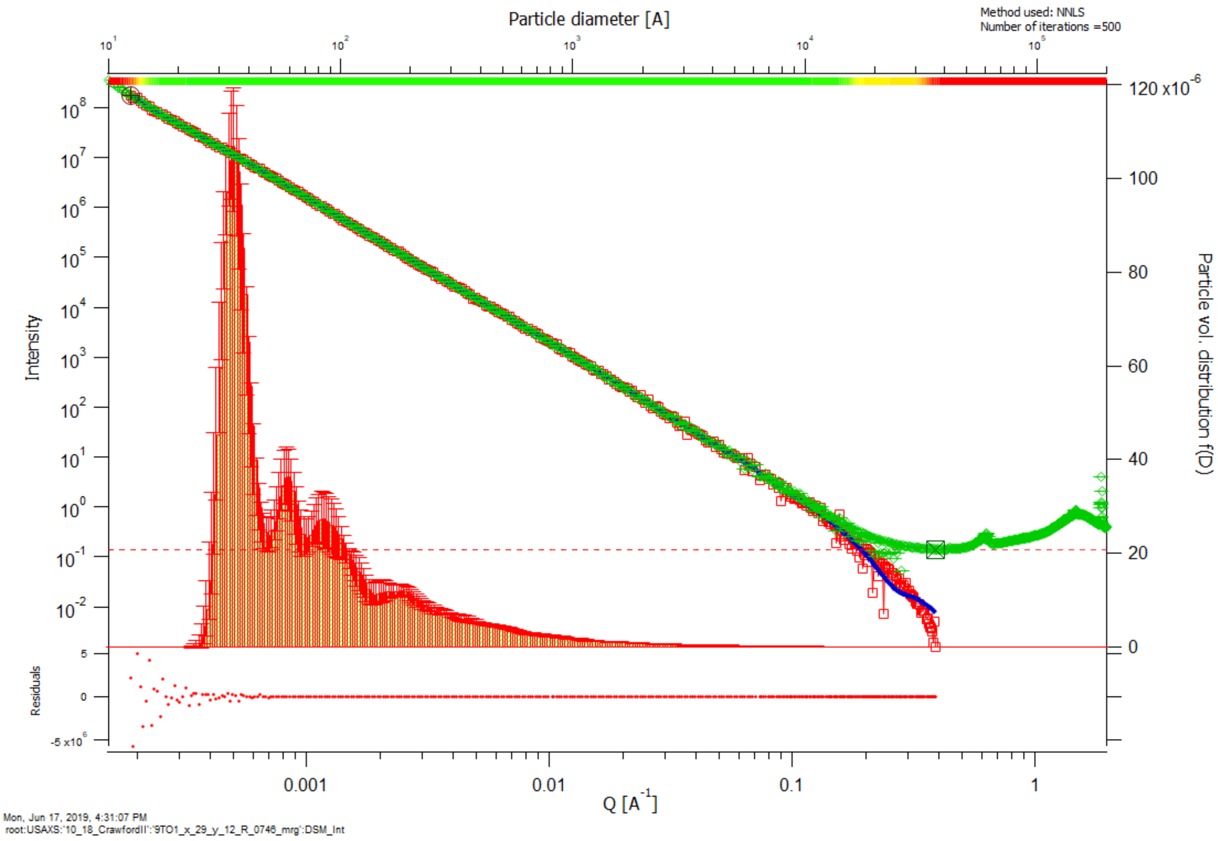

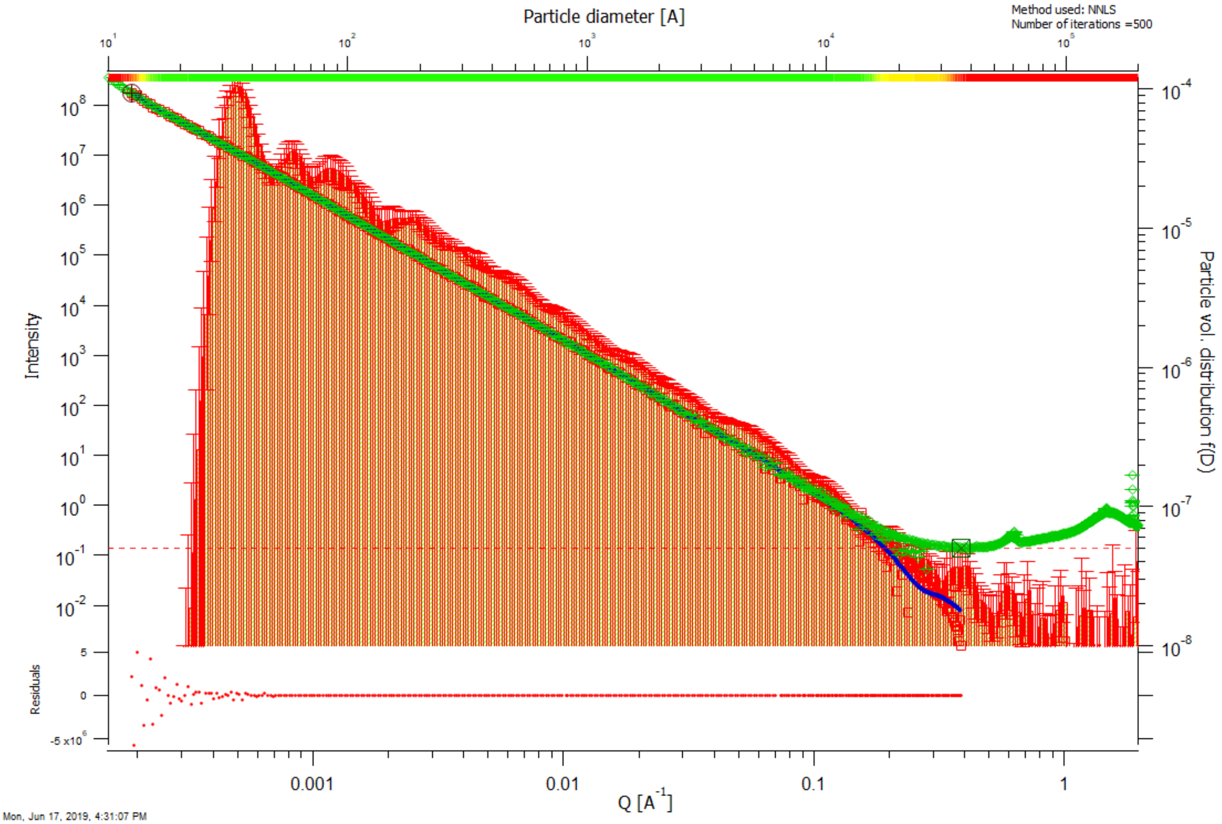

Mon, Jun 17, 2019, 4:31:07 PM
root:USAXS:'10_18_CrawfordII':'9TO1_x_29_y_12_R_0746_mrg':DSM_Int

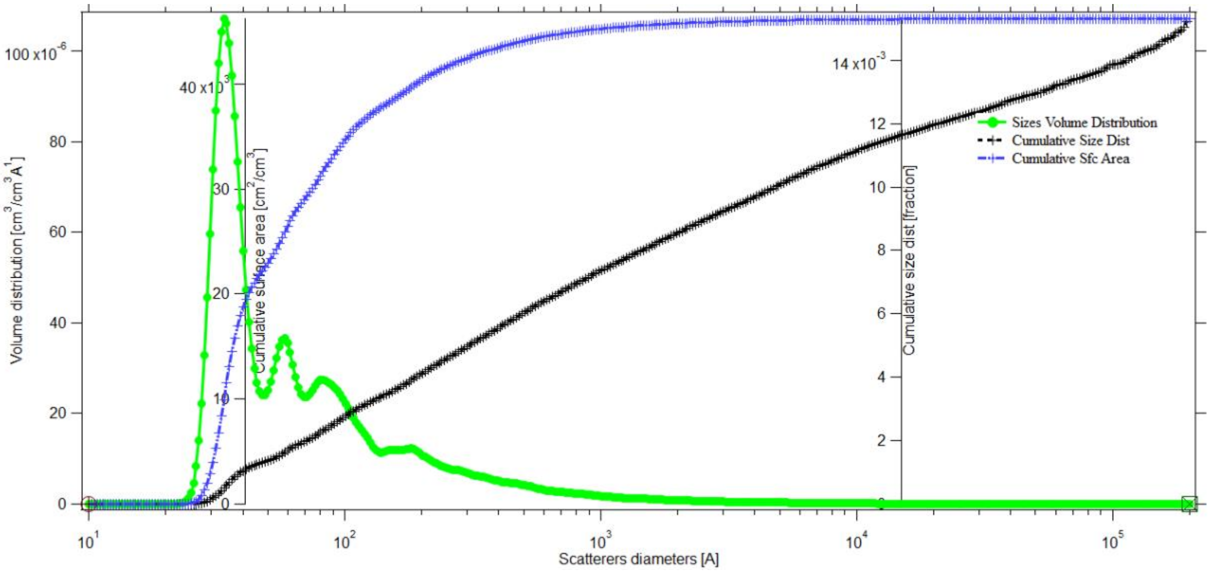

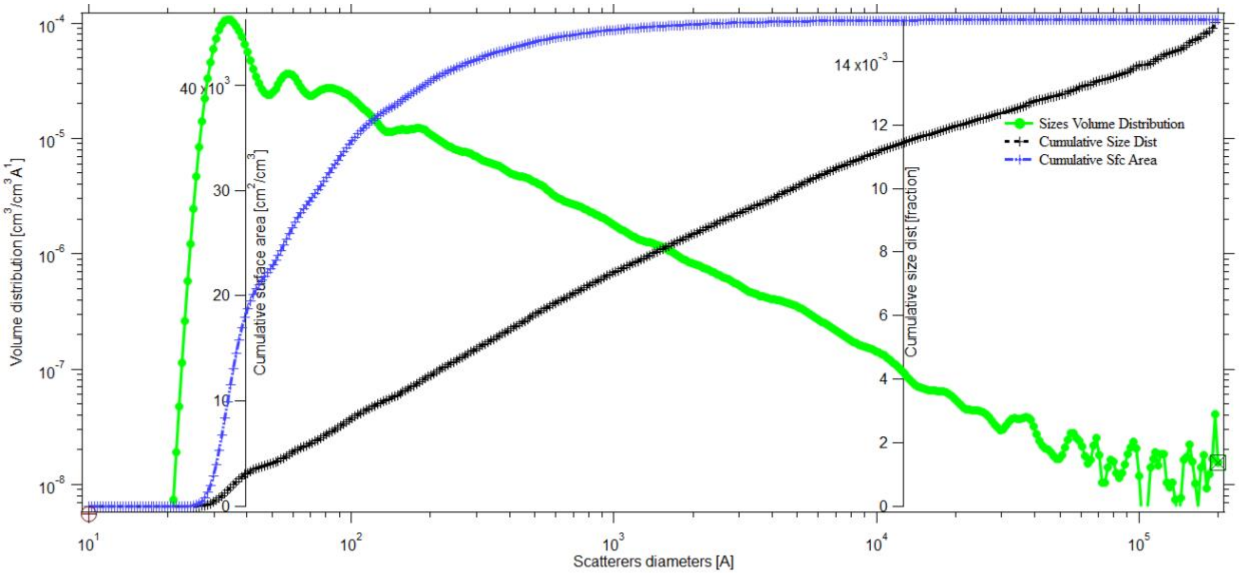

3. 9TO1_x_29_y25_R_0742

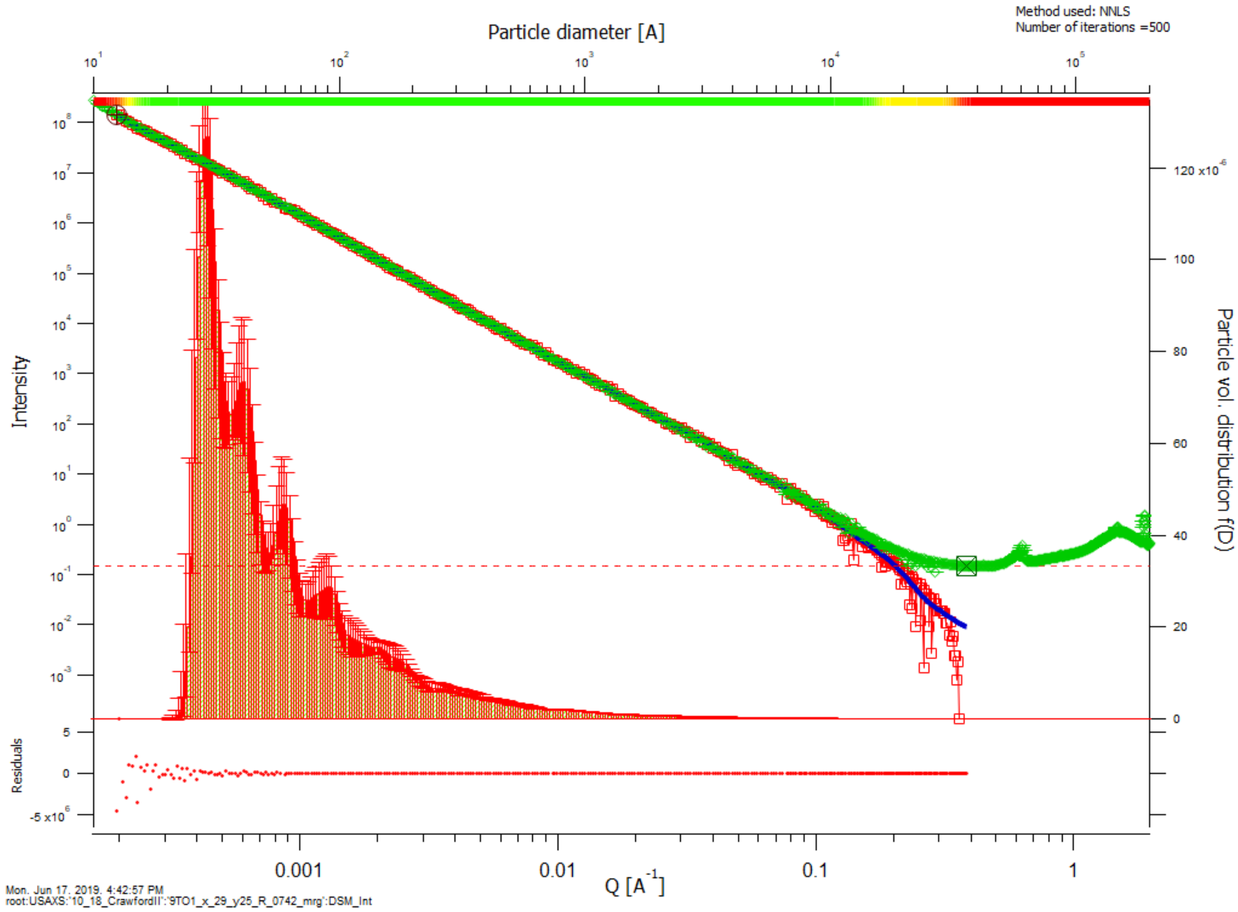

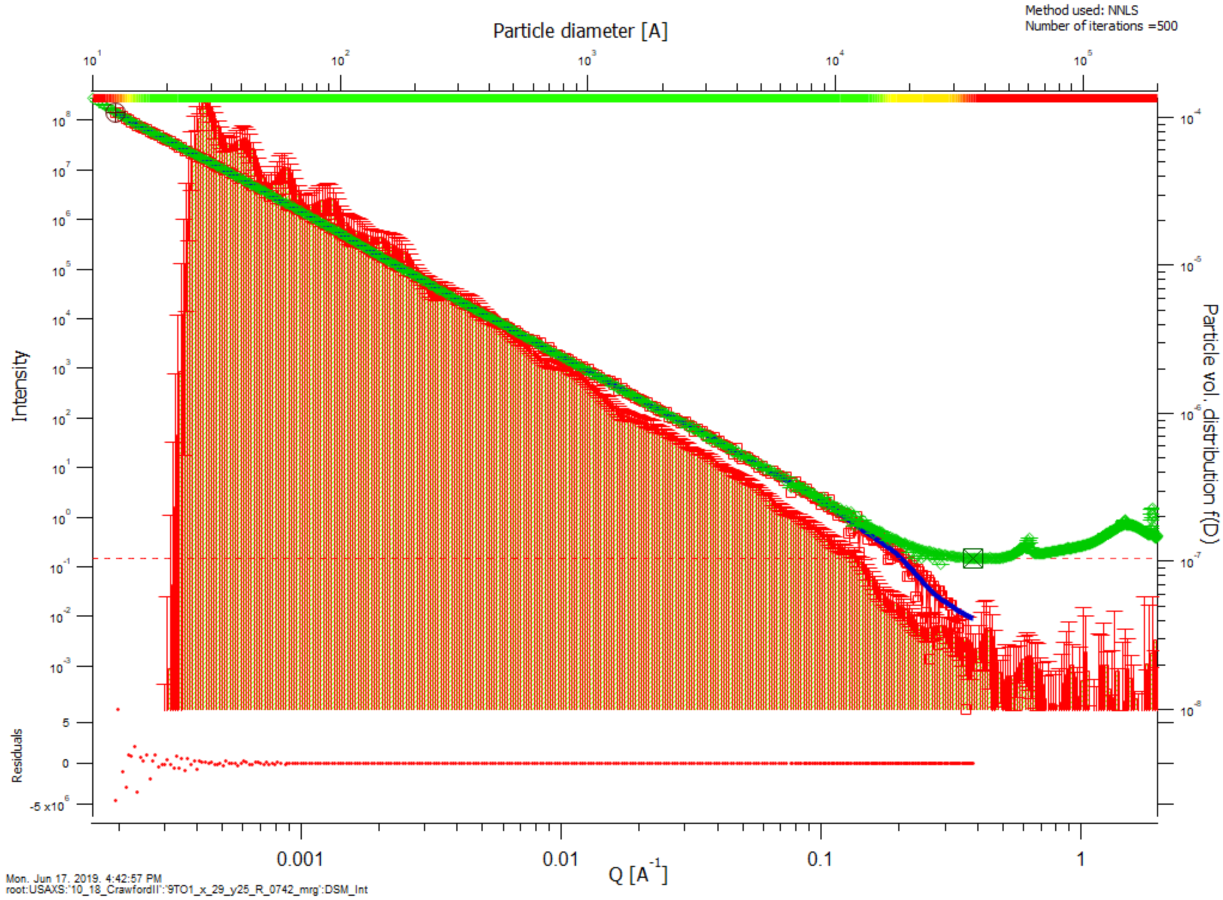
Method used: NNLS
Number of iterations =500
Particle diameter [A]
10^1
10^2
10^3
10^4
10^5
Intensity
10^8
10^7
10^6
10^5
10^4
10^3
10^2
10^1
10^0
10^{-1}
10^{-2}
10^{-3}
Particle vol. distribution f(D)
10^{-4}
10^{-5}
10^{-6}
10^{-7}
10^{-8}
Residuals
5
0
-5×10^6
0.001
0.01
0.1
1
Q [A^{-1}]
Mon. Jun 17. 2019. 4:42:57 PM
root:USAXS:'10_18_CrawfordII':'9TO1_x_29_y25_R_0742_mrg':DSM_Int

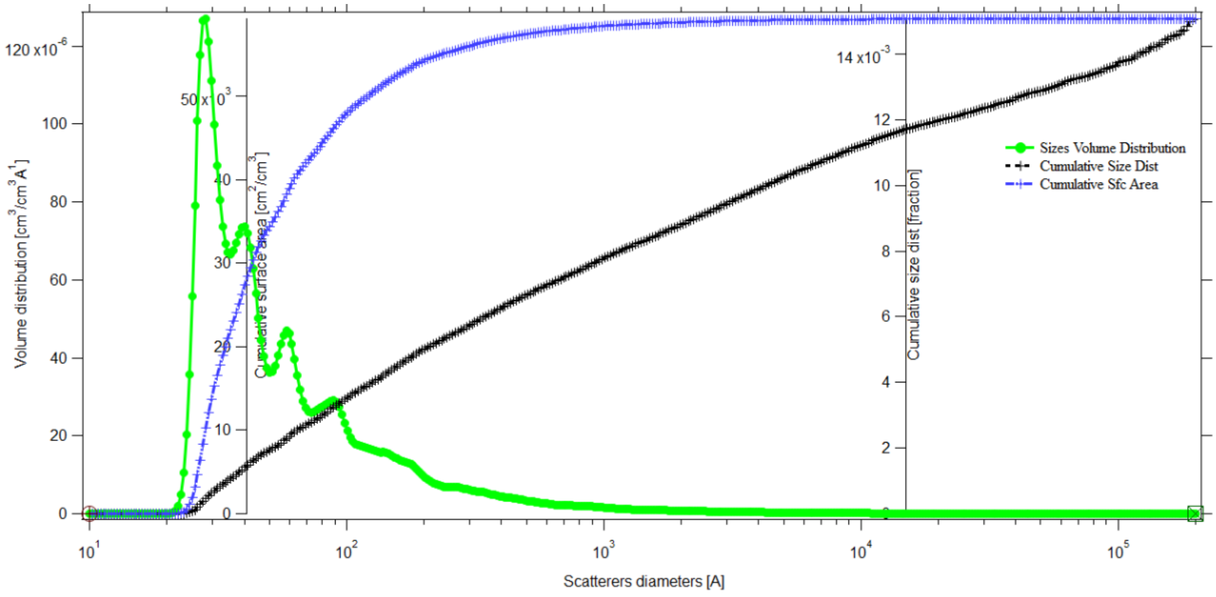
Volume distribution [cm^3/cm^{3}A^1]
120×10^{-6}
100
80
60
40
20
0
Cumulative surface area [cm^2/cm^3]
50×10^3
40
30
20
10
0
Cumulative size dist [fraction]
14×10^{-3}
12
10
8
6
4
2
0
Sizes Volume Distribution
Cumulative Size Dist
Cumulative Sfc Area
10^1
10^2
10^3
10^4
10^5
Scatterers diameters [A]

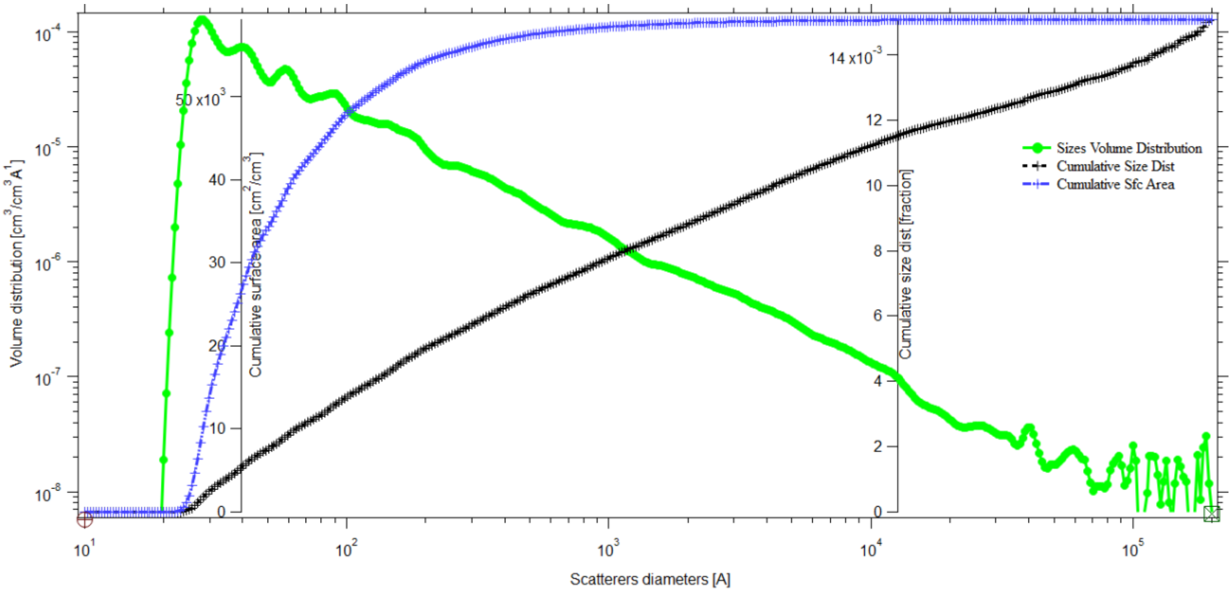

4. 9TO1_x_29_y33_R_0740_

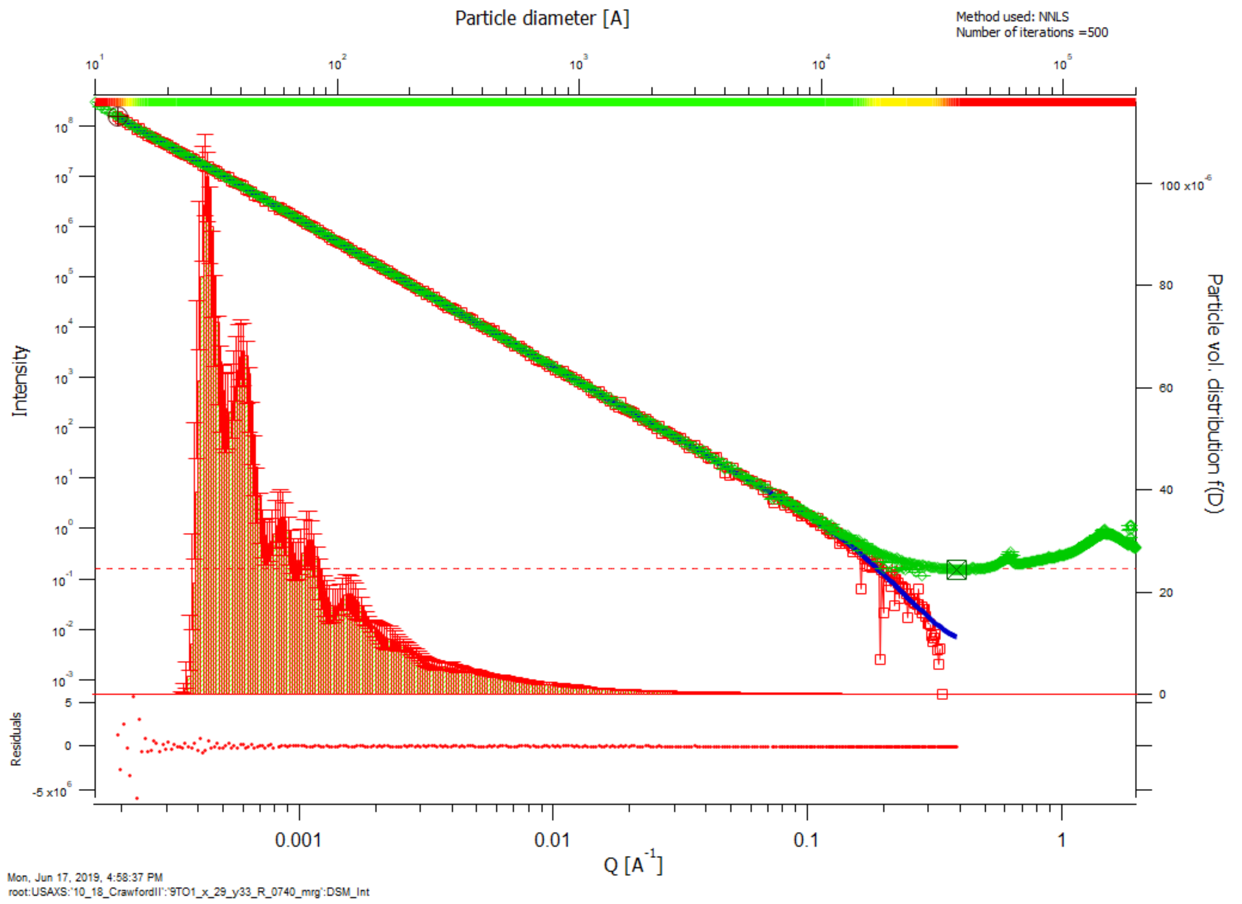

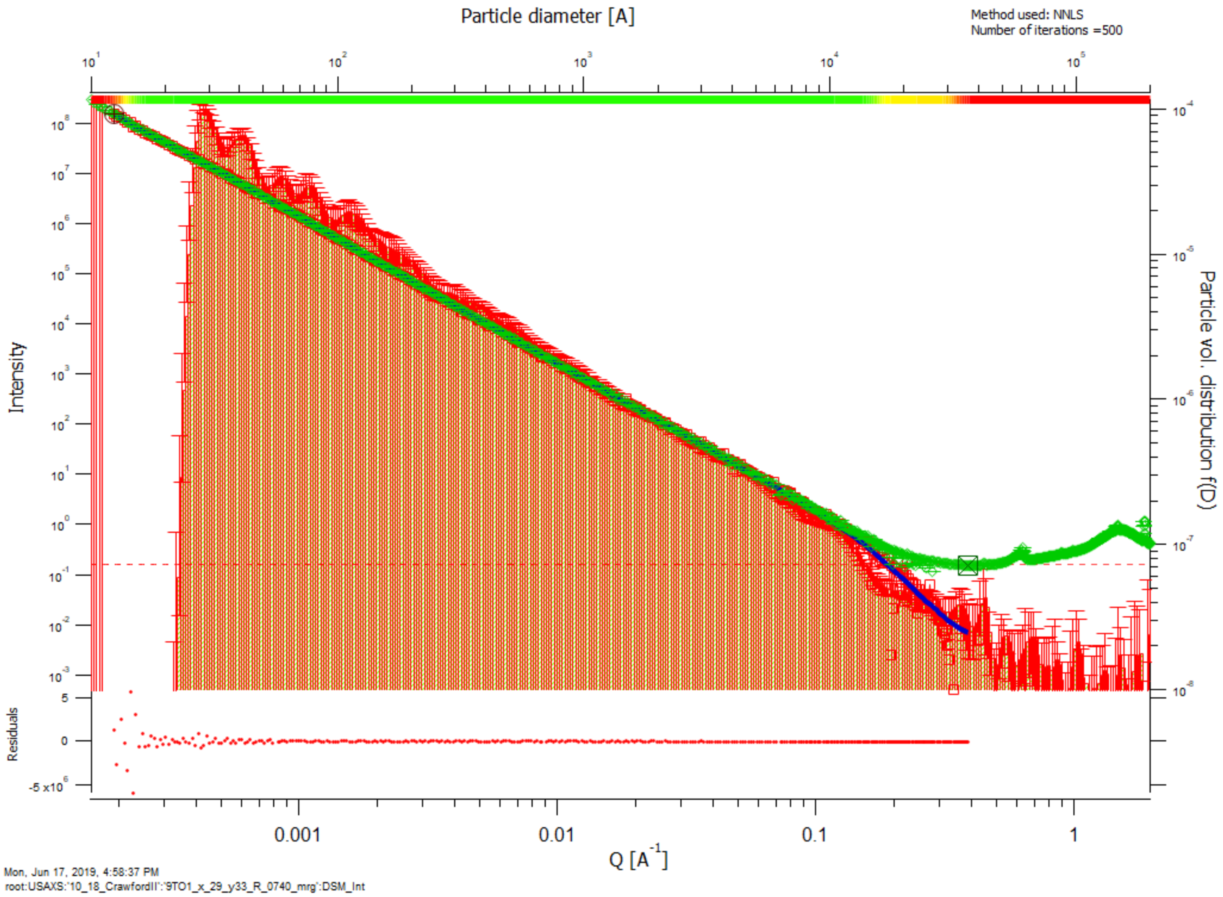
Particle diameter [A]
Method used: NNLS
Number of iterations =500
10^1
10^2
10^3
10^4
10^5
Intensity
10^8
10^7
10^6
10^5
10^4
10^3
10^2
10^1
10^0
10^-1
10^-2
10^-3
Particle vol. distribution f(D)
10^-4
10^-5
10^-6
10^-7
10^-8
Residuals
5
0
-5 x10^6
0.001
0.01
0.1
1
Q [A^-1]
Mon, Jun 17, 2019, 4:58:37 PM
root:USAXS:'10_18_CrawfordII':'9TO1_x_29_y33_R_0740_mrg':DSM_Int

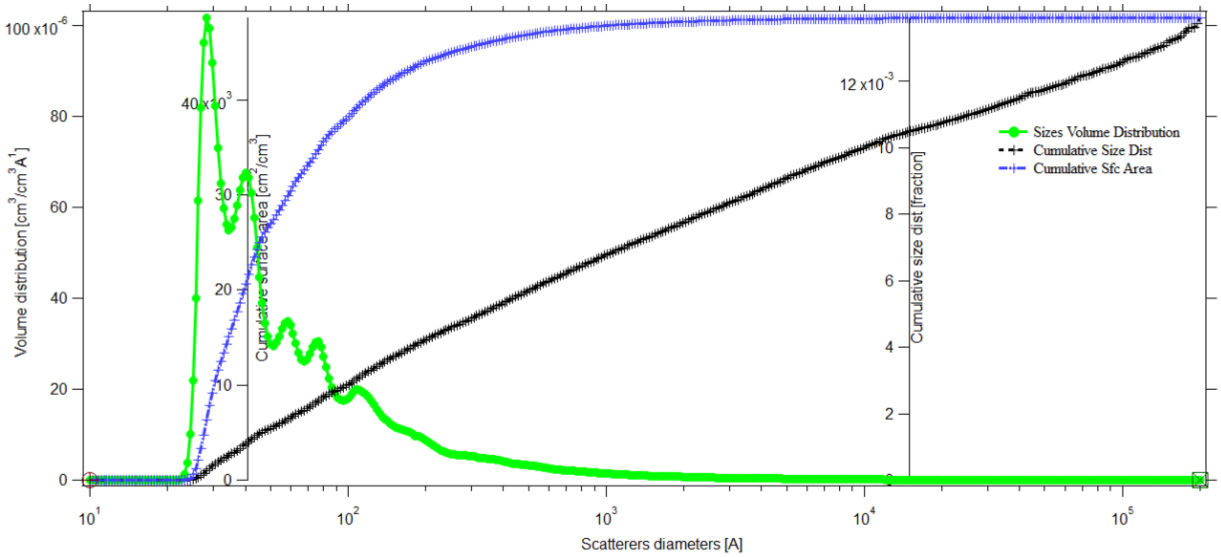
Volume distribution [cm^3/cm^3A^1]
100 x10^-6
80
60
40
20
0
Cumulative surface area [cm^2/cm^3]
40 x10^3
30
20
10
0
Cumulative size dist [fraction]
12 x10^-3
10
8
6
4
2
0
Sizes Volume Distribution
Cumulative Size Dist
Cumulative Sfc Area
10^1
10^2
10^3
10^4
10^5
Scatterers diameters [A]

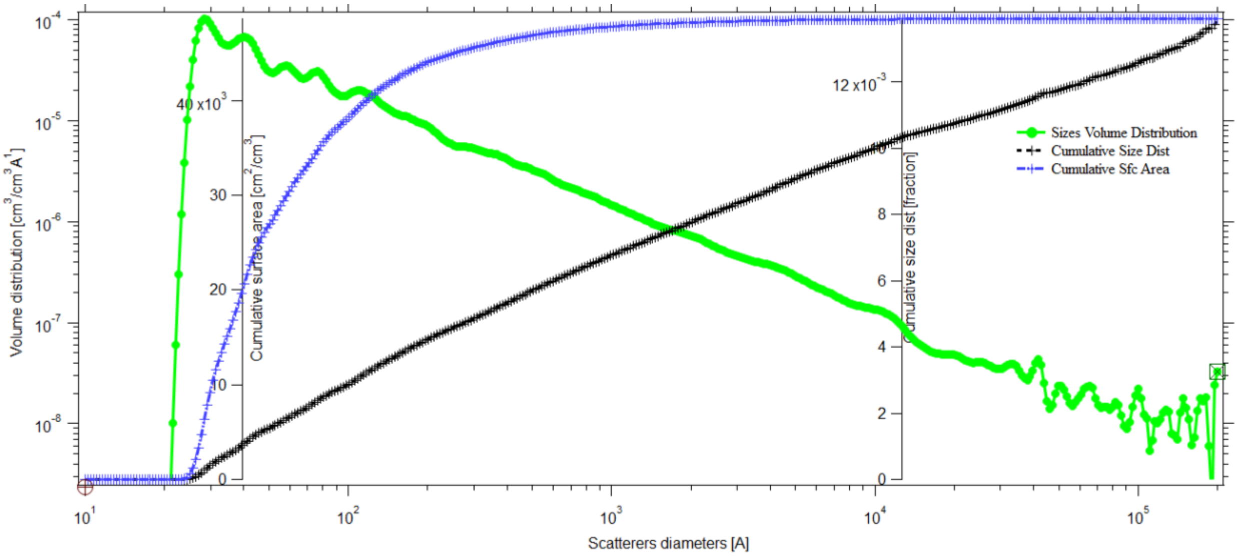

5. 9TO1_x_29_y33_0739

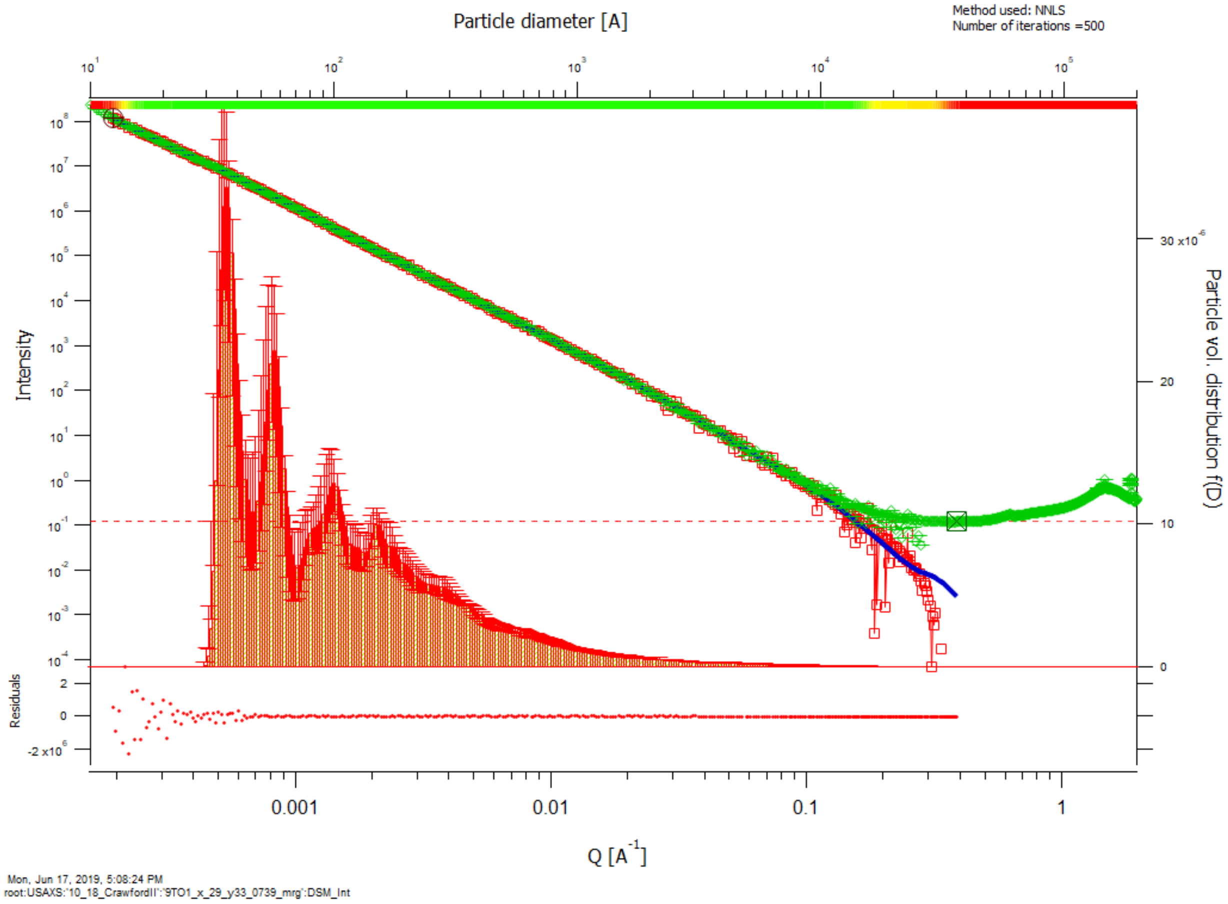

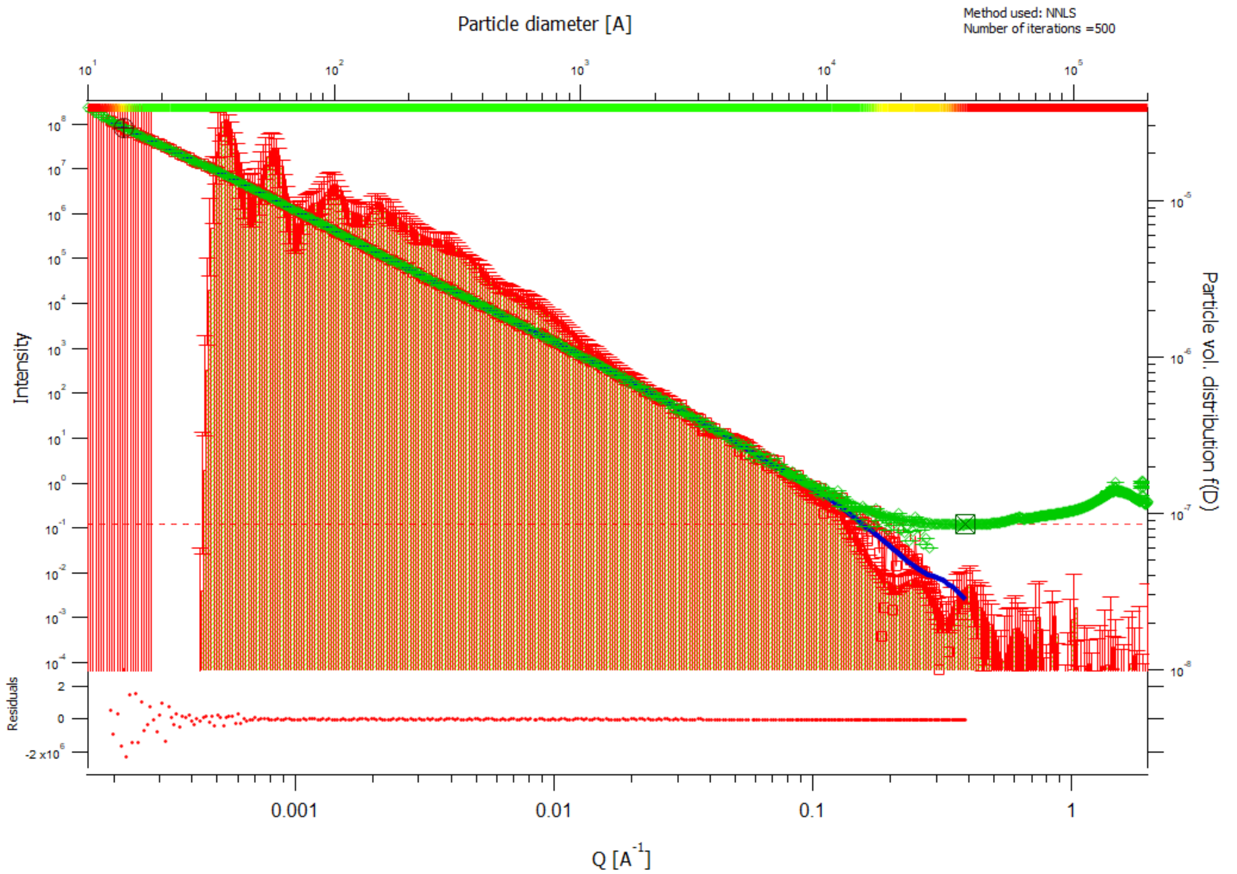

Mon, Jun 17, 2019, 5:08:24 PM
root:USAXS:'10_18_CrawfordII':'9TO1_x_29_y33_0739_mrg':DSM_Int

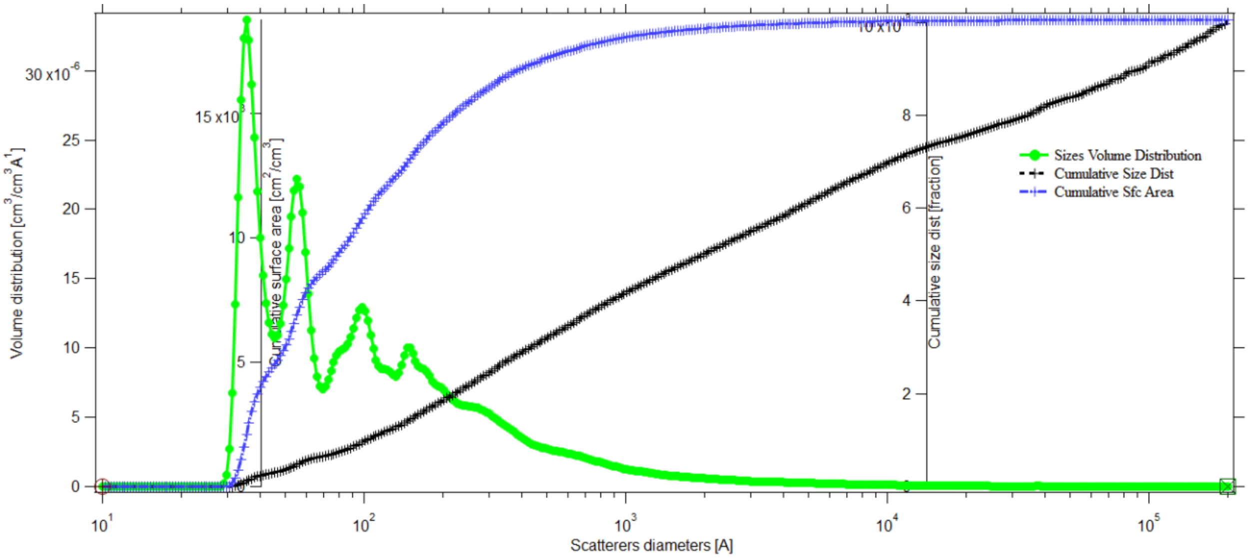

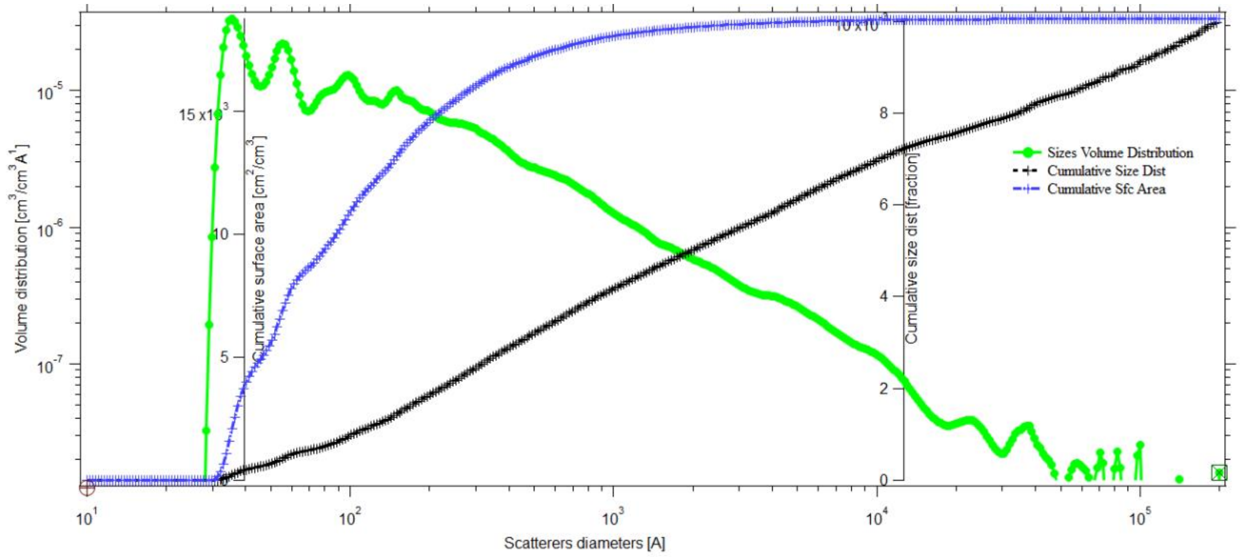

6. 9TO1_x_29_y52_R_0738

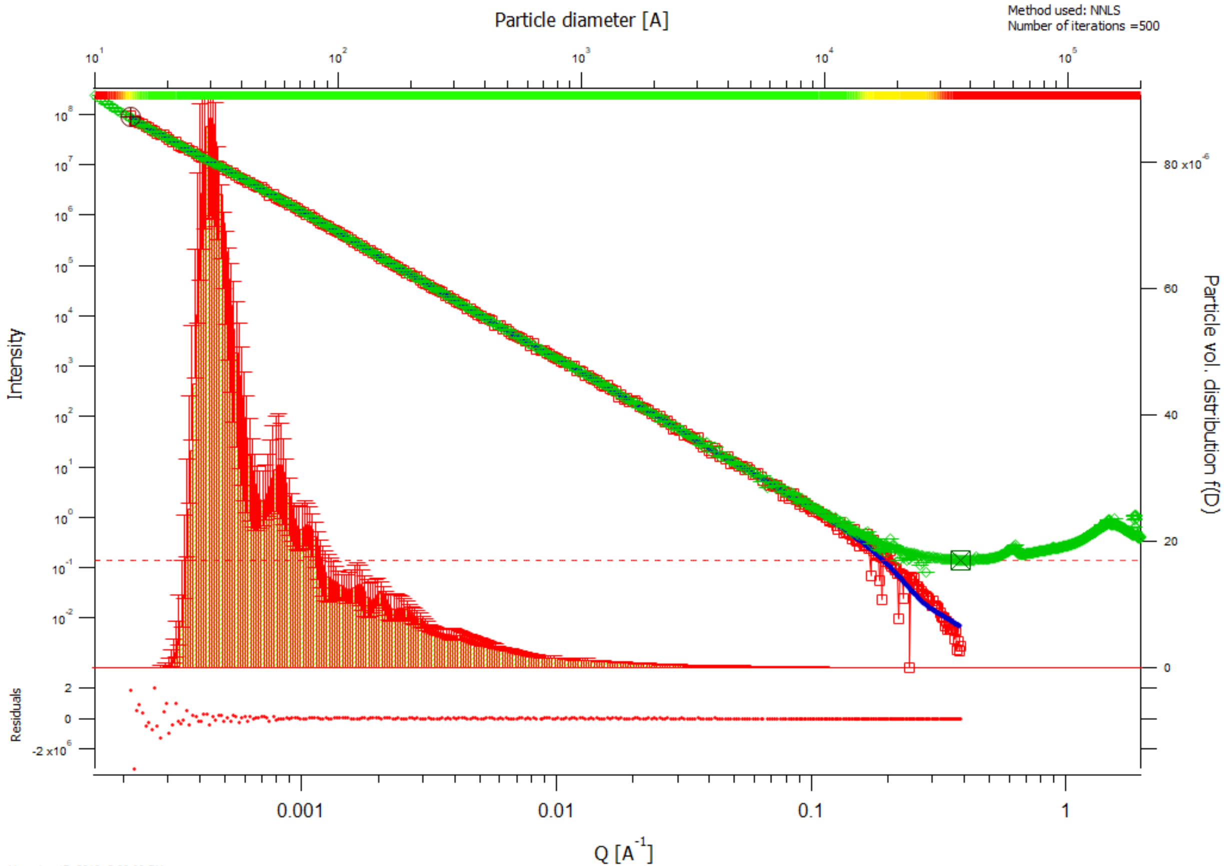

Mon, Jun 17, 2019, 5:20:30 PM
root:USAXS:'10_18_CrawfordII':'9TO1_x_29_y52_R_0738_mrg':DSM_Int

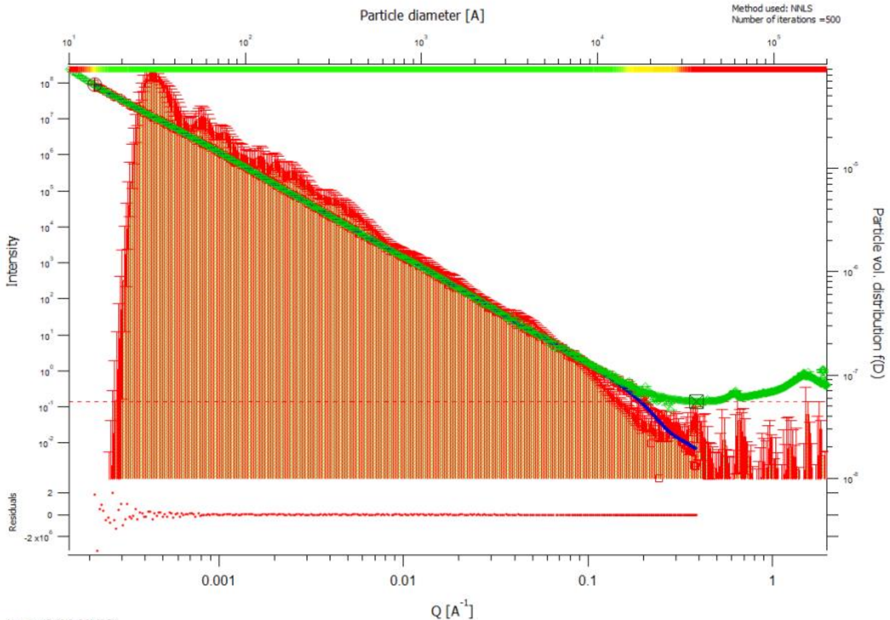

Method used: NNLS
Number of iterations =500

Mon, Jun 17, 2019, 5:20:30 PM
root:USAXS:'10_18_CrawfordII':'9TO1_x_29_y52_R_0738_mrg':DSM_Int

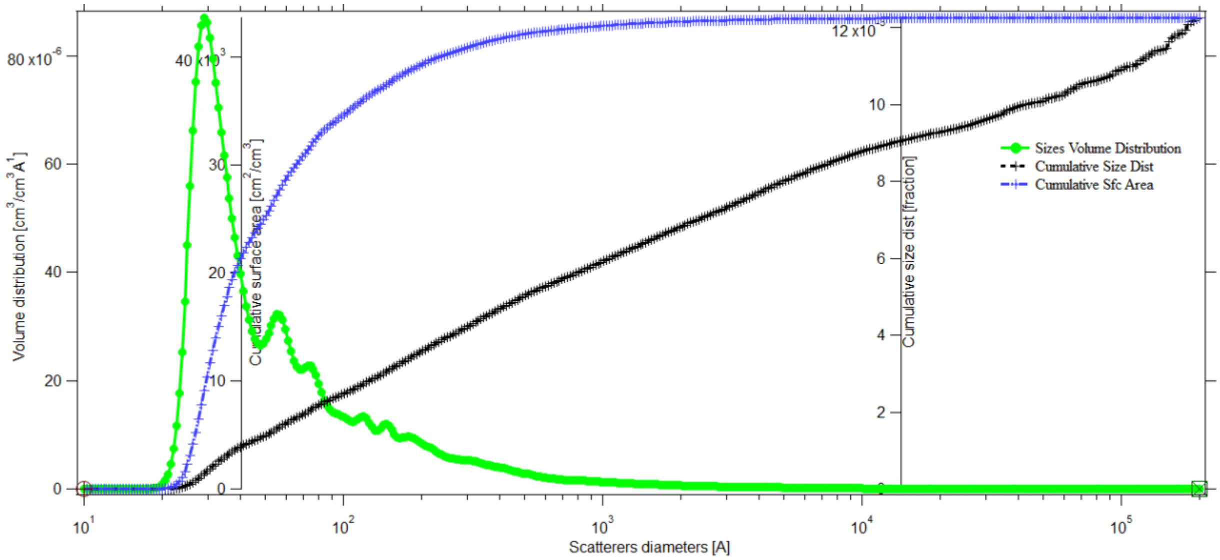

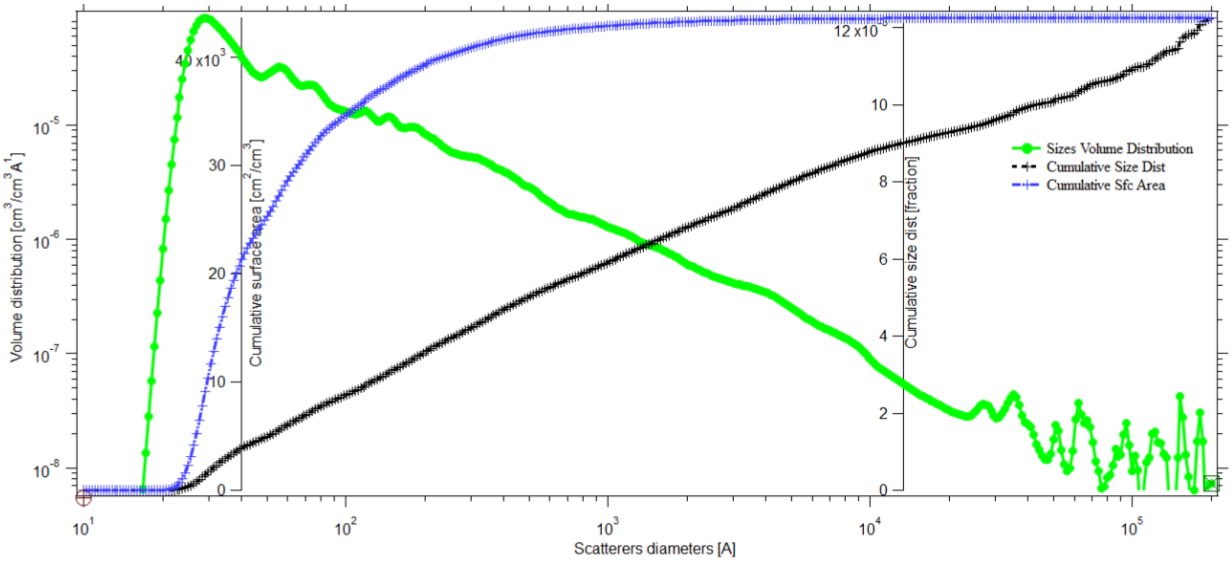

7. 9TO1_X_29_Y52_0737

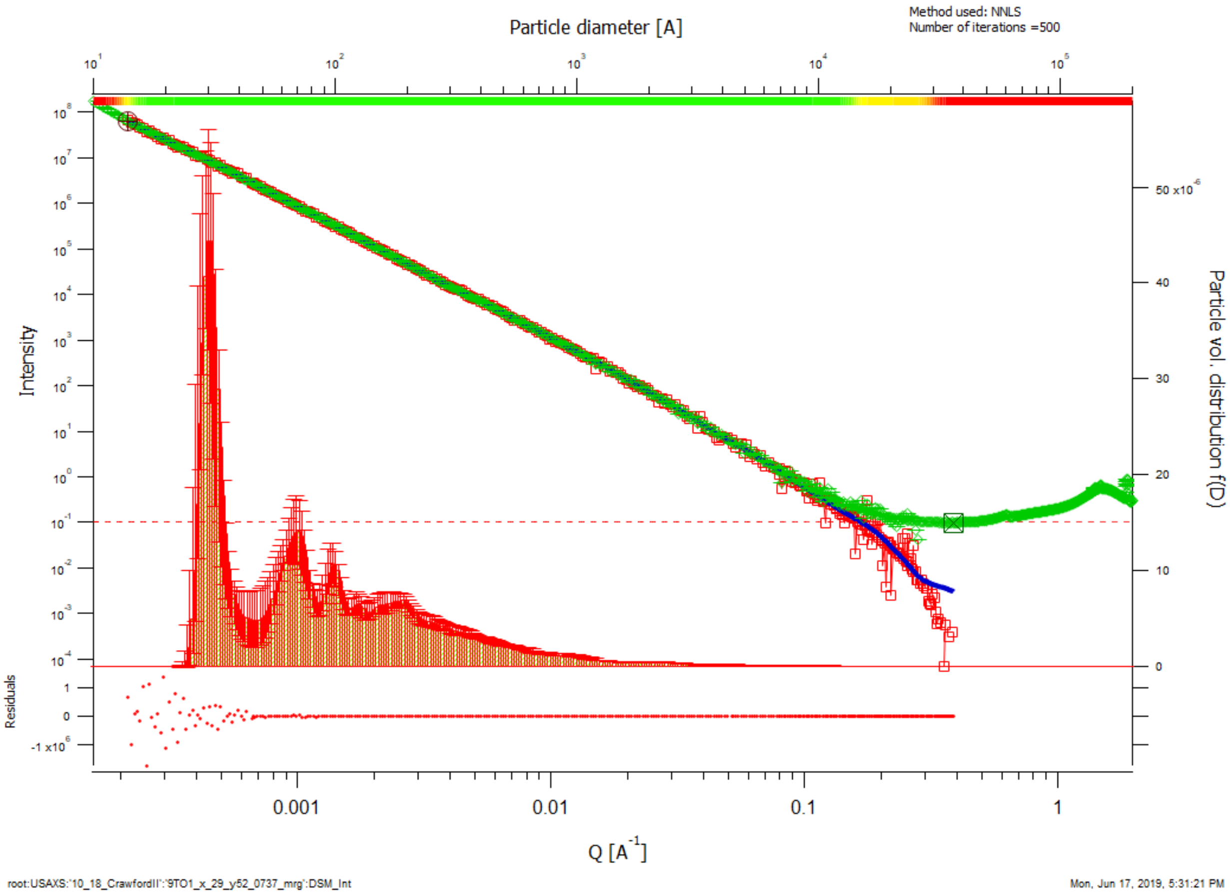

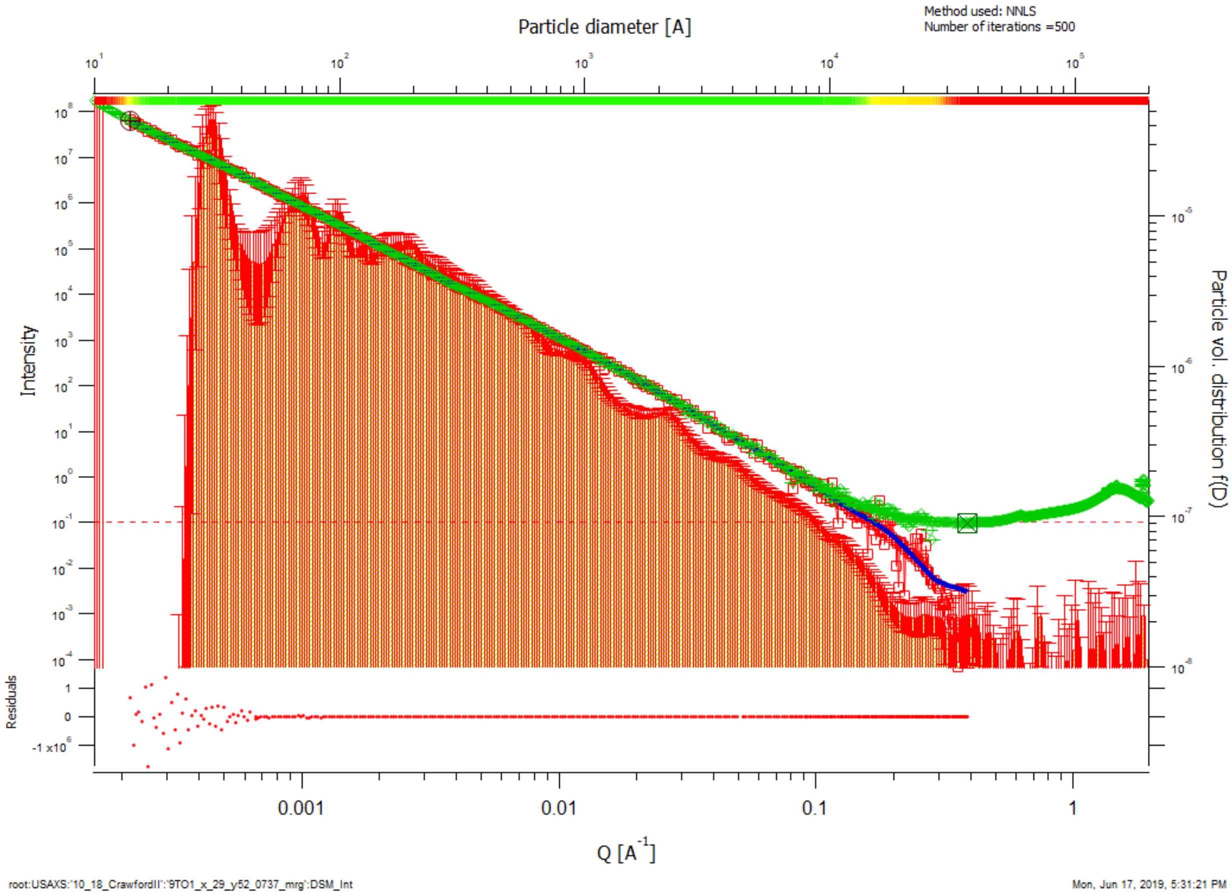
Particle diameter [A]
Method used: NNLS
Number of iterations =500
10^1
10^2
10^3
10^4
10^5
Intensity
10^8
10^7
10^6
10^5
10^4
10^3
10^2
10^1
10^0
10^-1
10^-2
10^-3
10^-4
Particle vol. distribution f(D)
10^-5
10^-6
10^-7
10^-8
Residuals
1
0
-1 x10^6
0.001
0.01
0.1
1
Q [A^-1]
root:USAXS:'10_18_CrawfordII':'9TO1_x_29_y52_0737_mrg':DSM_Int
Mon, Jun 17, 2019, 5:31:21 PM

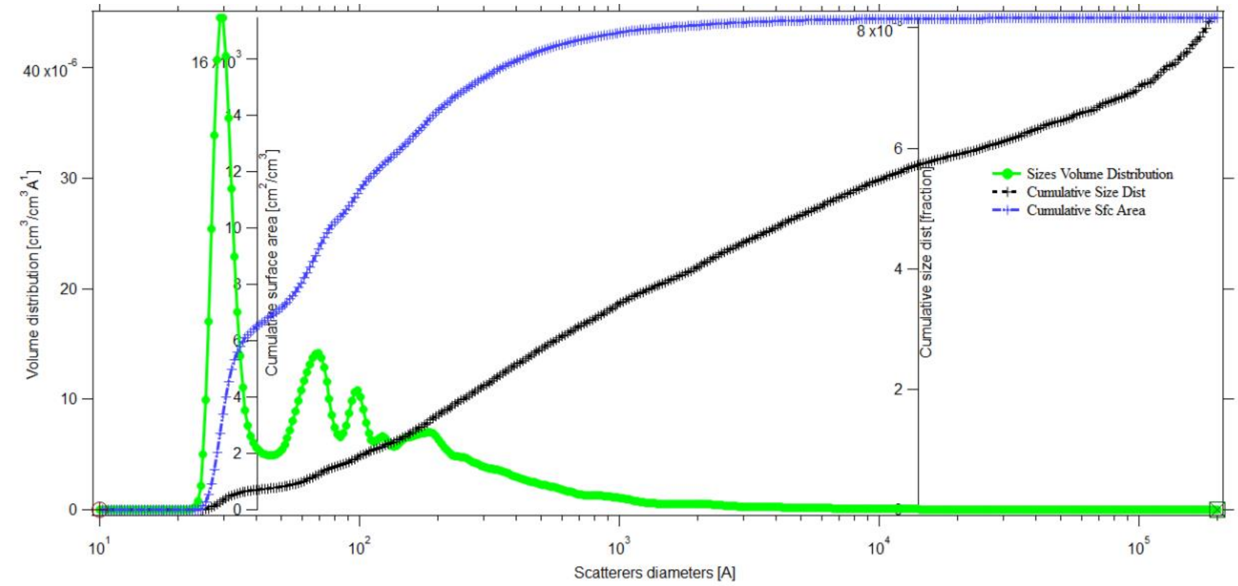
Volume distribution [cm^3/cm^3A^1]
40 x10^-6
30
20
10
0
16 x10^3
14
12
10
8
6
4
2
0
Cumulative surface area [cm^2/cm^3]
8 x10^-3
6
4
2
0
Cumulative size dist [fraction]
Sizes Volume Distribution
Cumulative Size Dist
Cumulative Sfc Area
10^1
10^2
10^3
10^4
10^5
Scatterers diameters [A]

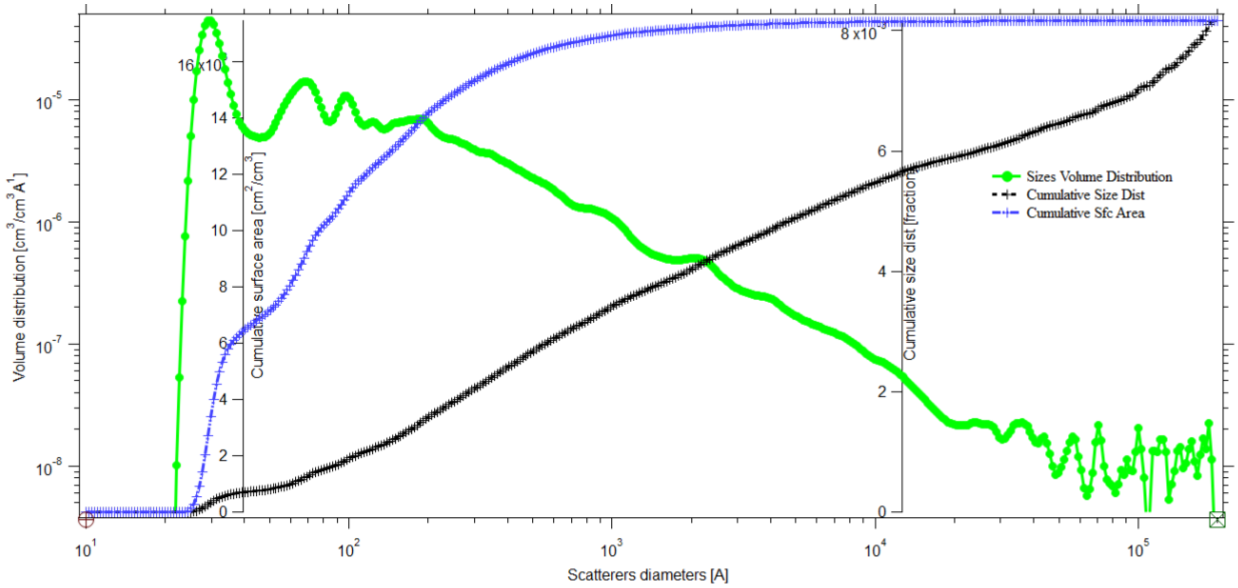

8. 9TO3_x_1_y17_0771

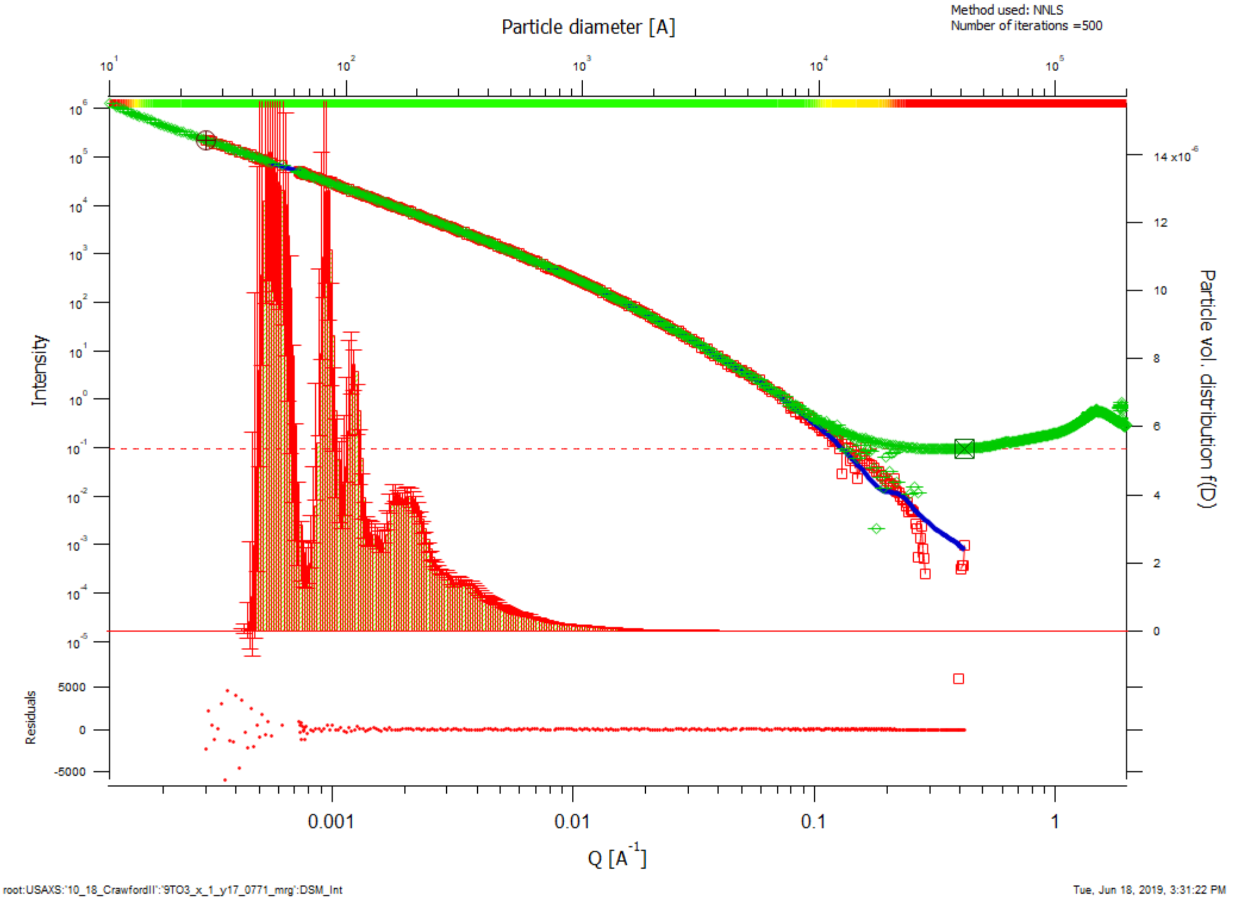

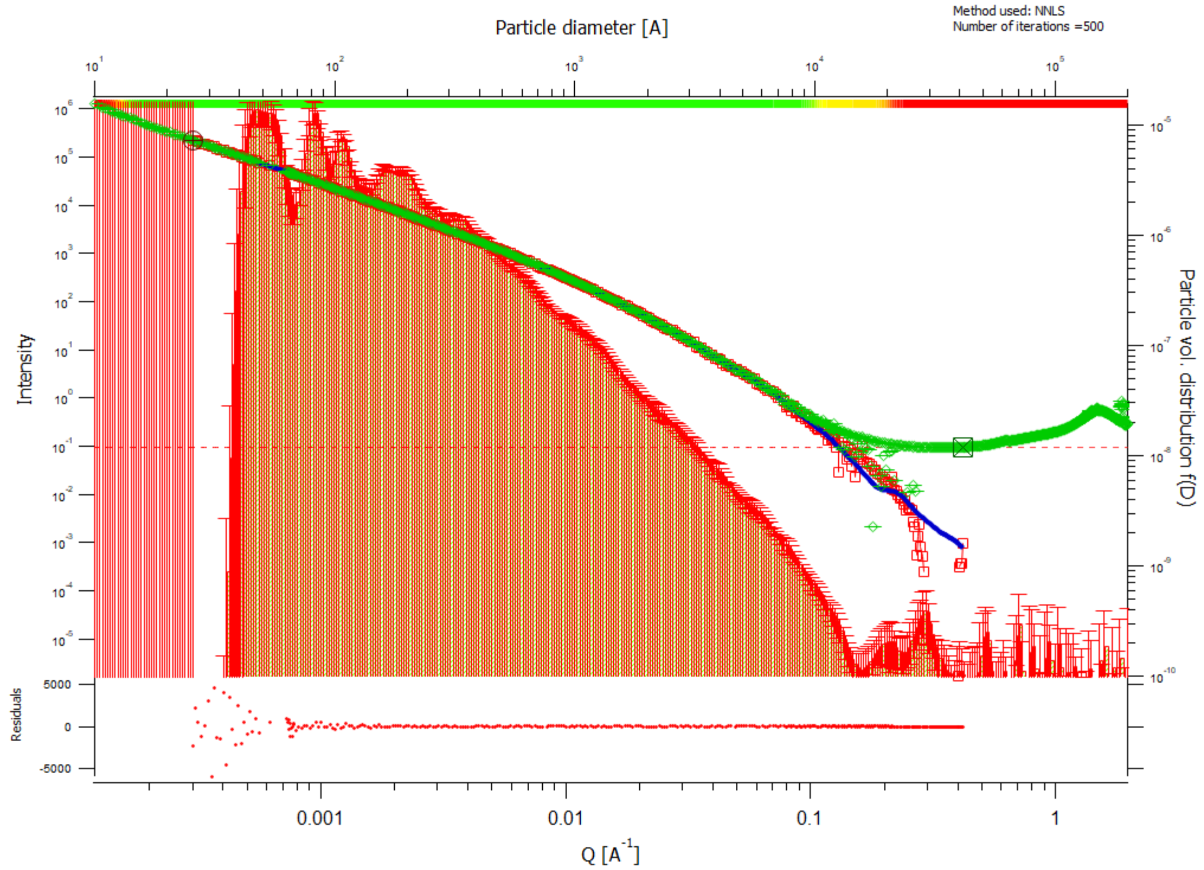

root:USAXS:'10_18_CrawfordII':'9TO3_x_1_y17_0771_mrg':DSM_Int

Tue, Jun 18, 2019, 3:31:22 PM

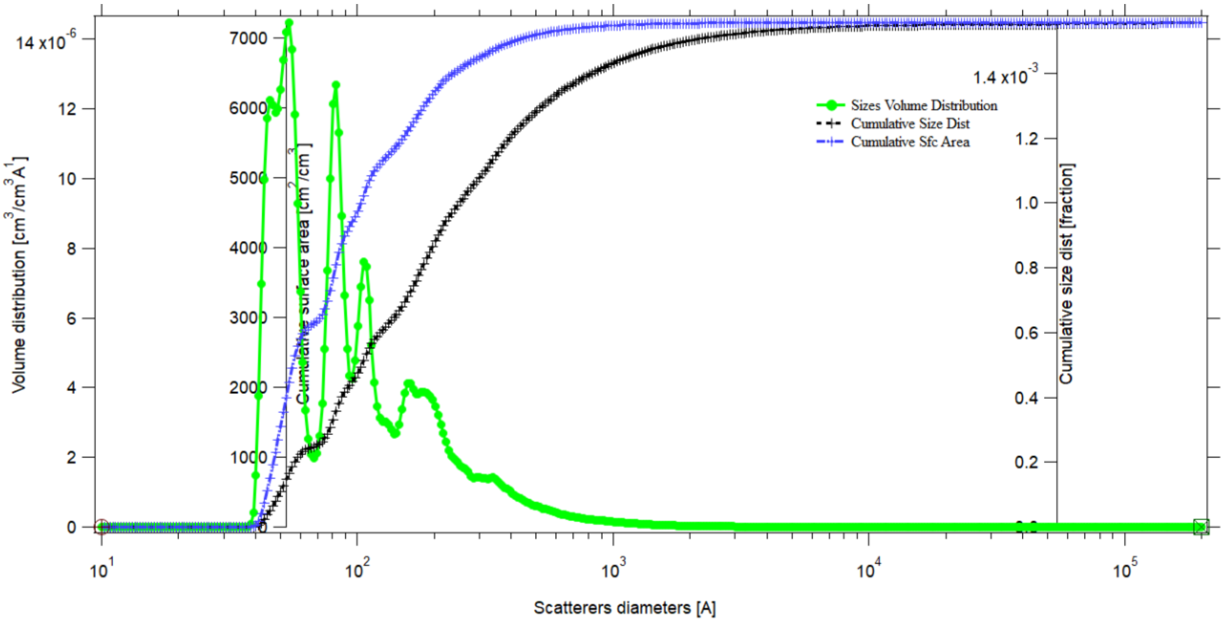

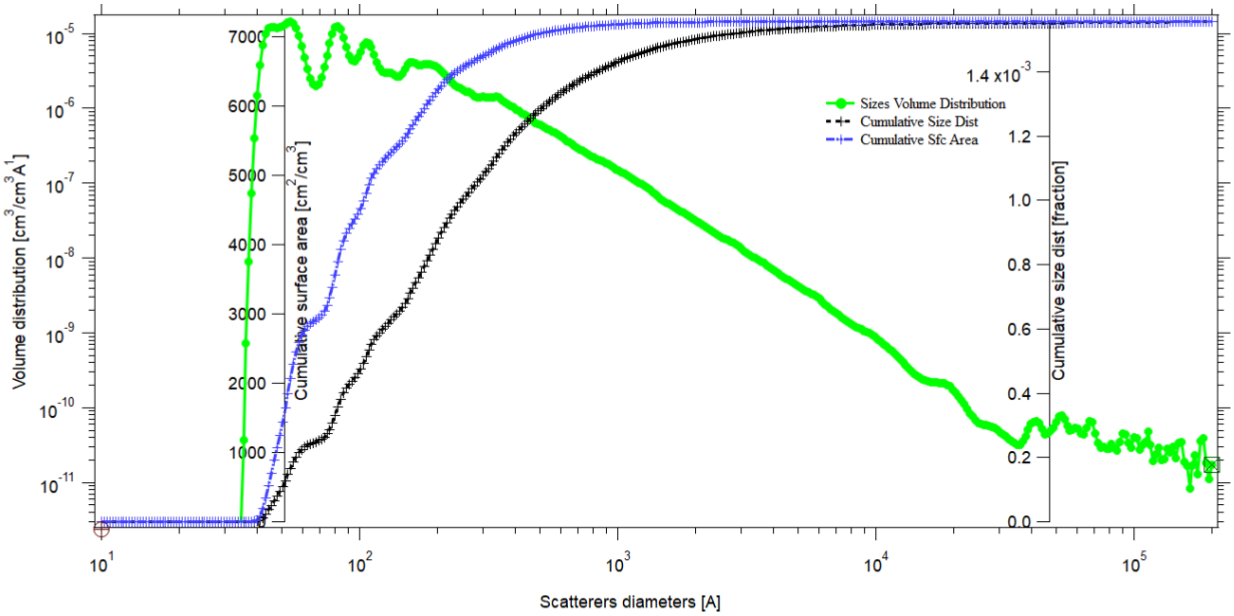

9. 9TO3_x_1_y30_R_0770

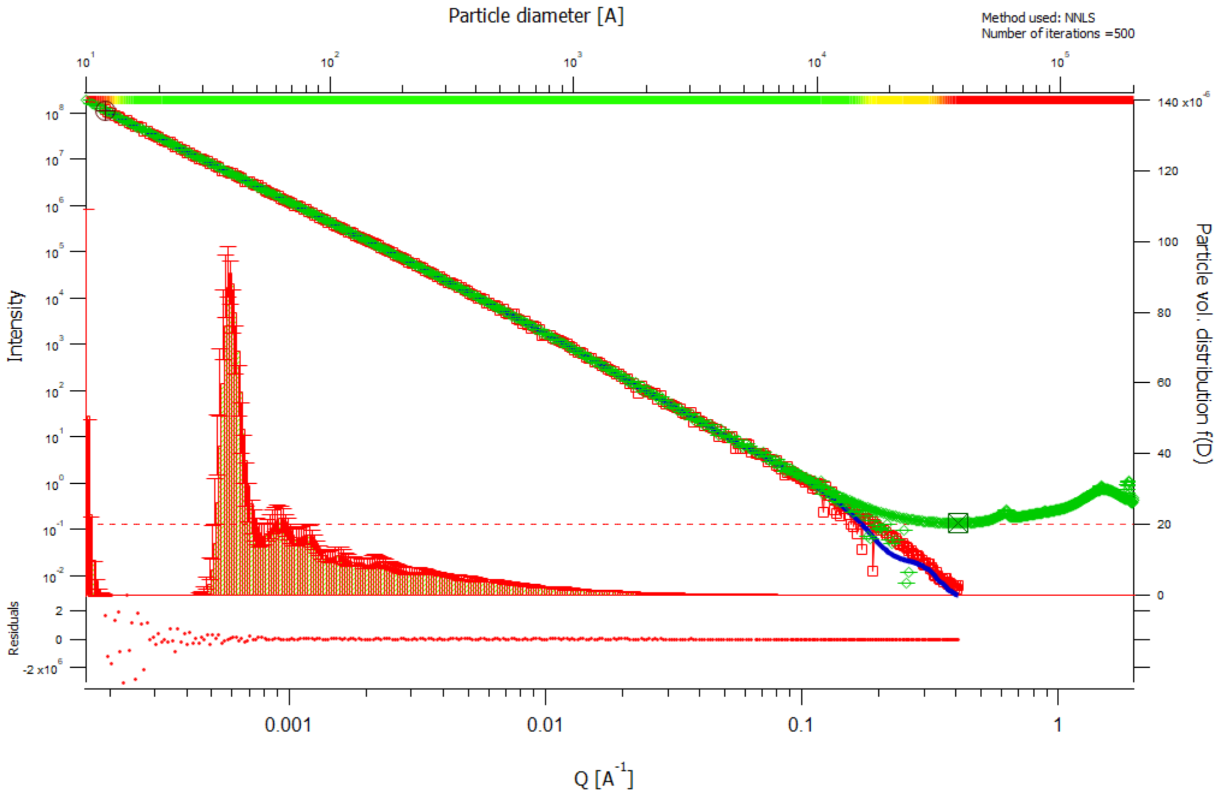

Tue, Jun 18, 2019, 4:04:05 PM
root:USAXS:'10_18_CrawfordII':'9TO3_x_1_y30_R_0770_mrg':DSM_Int

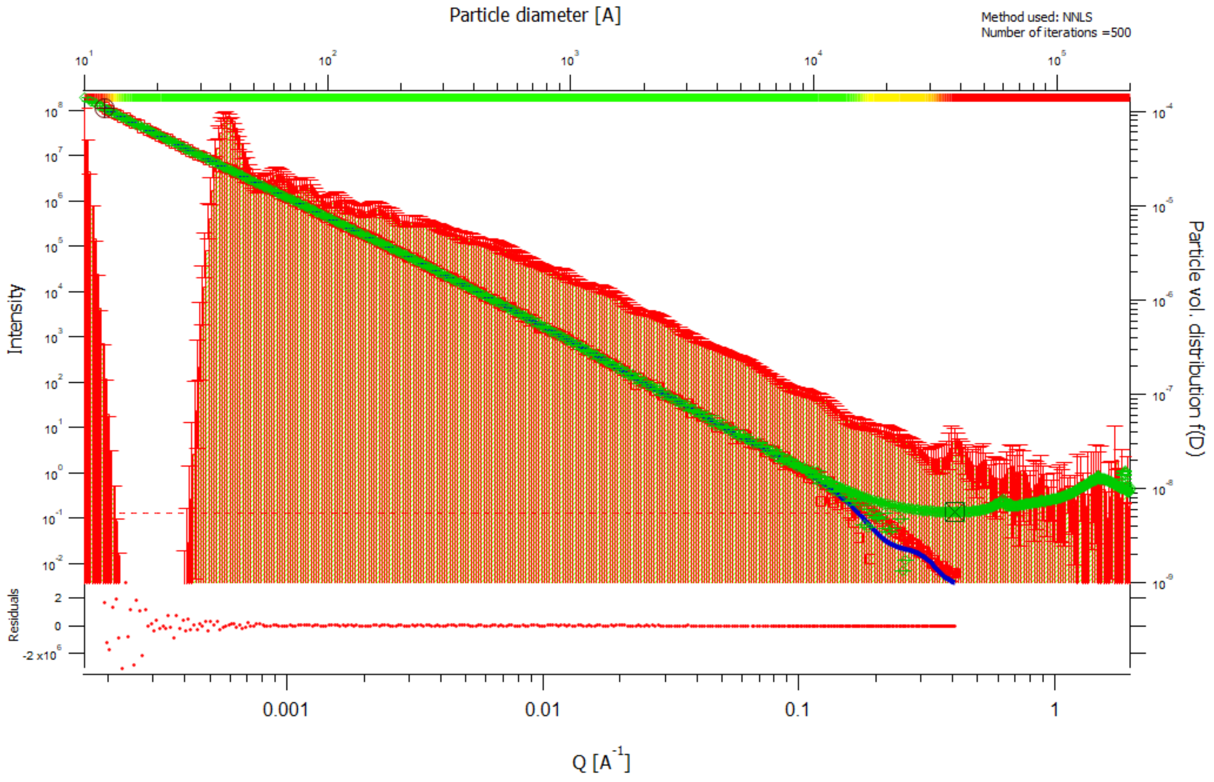

Tue, Jun 18, 2019, 4:04:05 PM
root:USAXS:'10_18_CrawfordII':'9TO3_x_1_y30_R_0770_mrg':DSM_Int

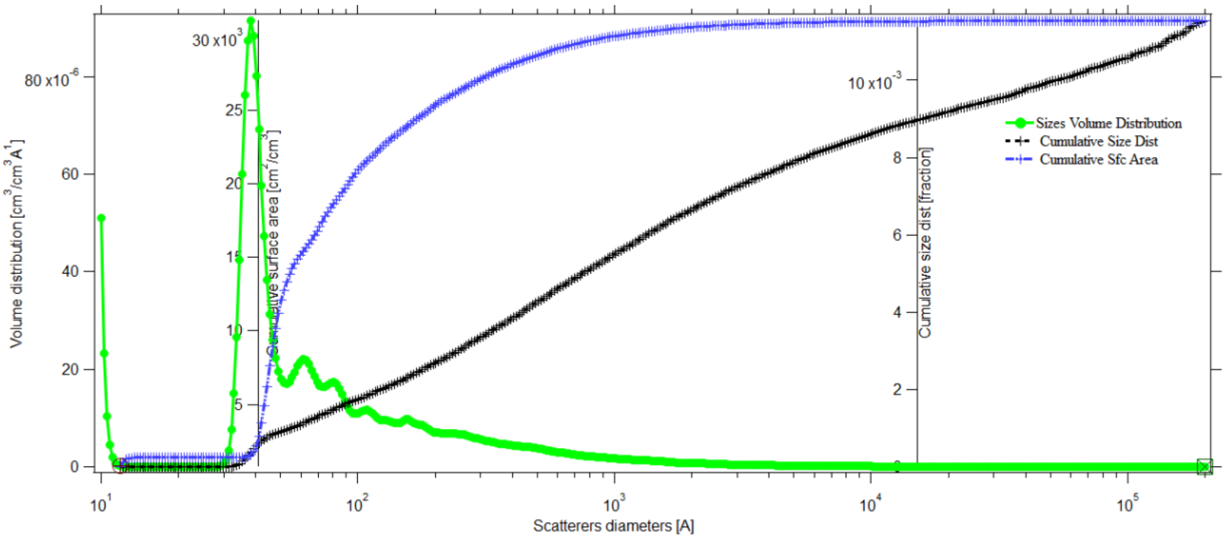
80 x10^{-6}
60
40
20
0
Volume distribution [cm^3/cm^3 A^1]
30 x10^3
25
20
15
10
5
Cumulative surface area [cm^2/cm^3]
10 x10^{-3}
8
6
4
2
0
Cumulative size dist [fraction]
Sizes Volume Distribution
Cumulative Size Dist
Cumulative Sfc Area
10^1
10^2
10^3
10^4
10^5
Scatterers diameters [A]

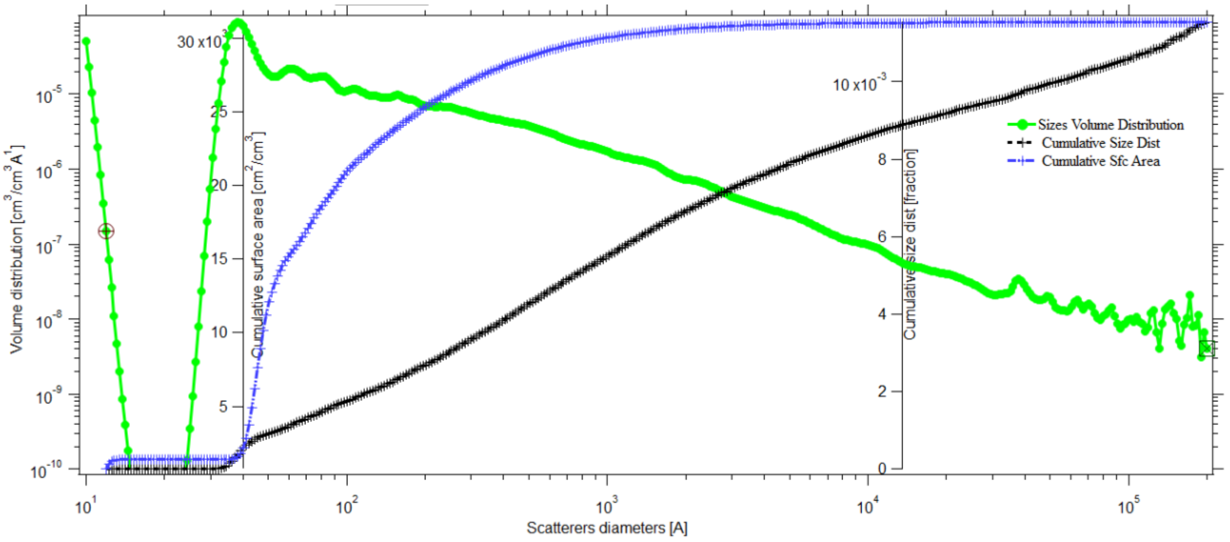
10^{-5}
10^{-6}
10^{-7}
10^{-8}
10^{-9}
10^{-10}
Volume distribution [cm^3/cm^3 A^1]
30 x10^3
25
20
15
10
5
Cumulative surface area [cm^2/cm^3]
10 x10^{-3}
8
6
4
2
0
Cumulative size dist [fraction]
Sizes Volume Distribution
Cumulative Size Dist
Cumulative Sfc Area
10^1
10^2
10^3
10^4
10^5
Scatterers diameters [A]

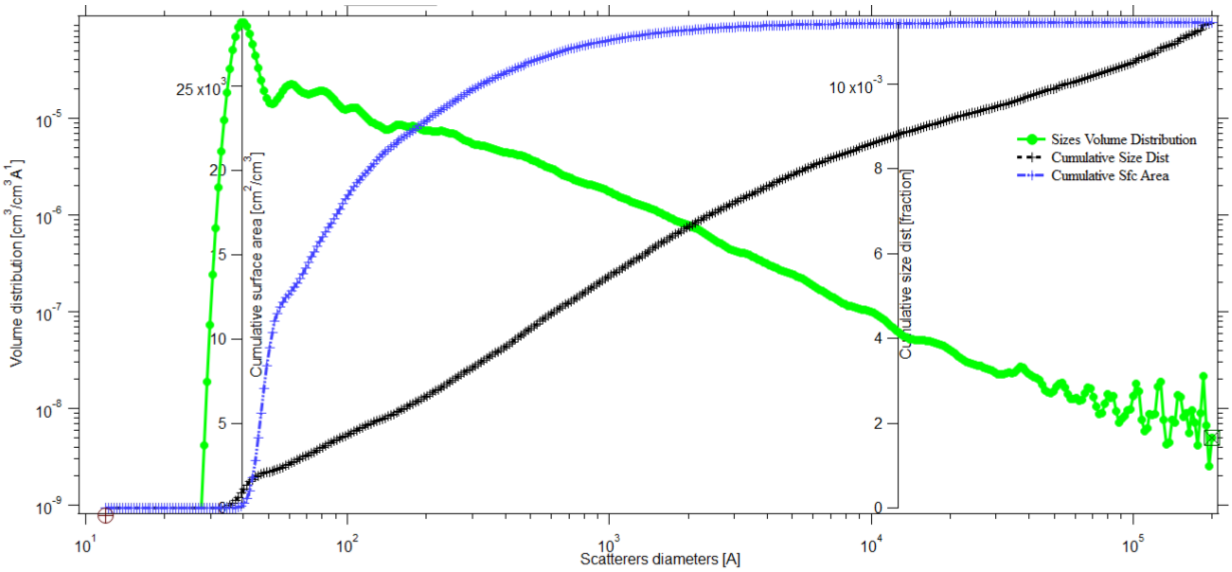

10. 9TO3_x_1_y44_R_0768

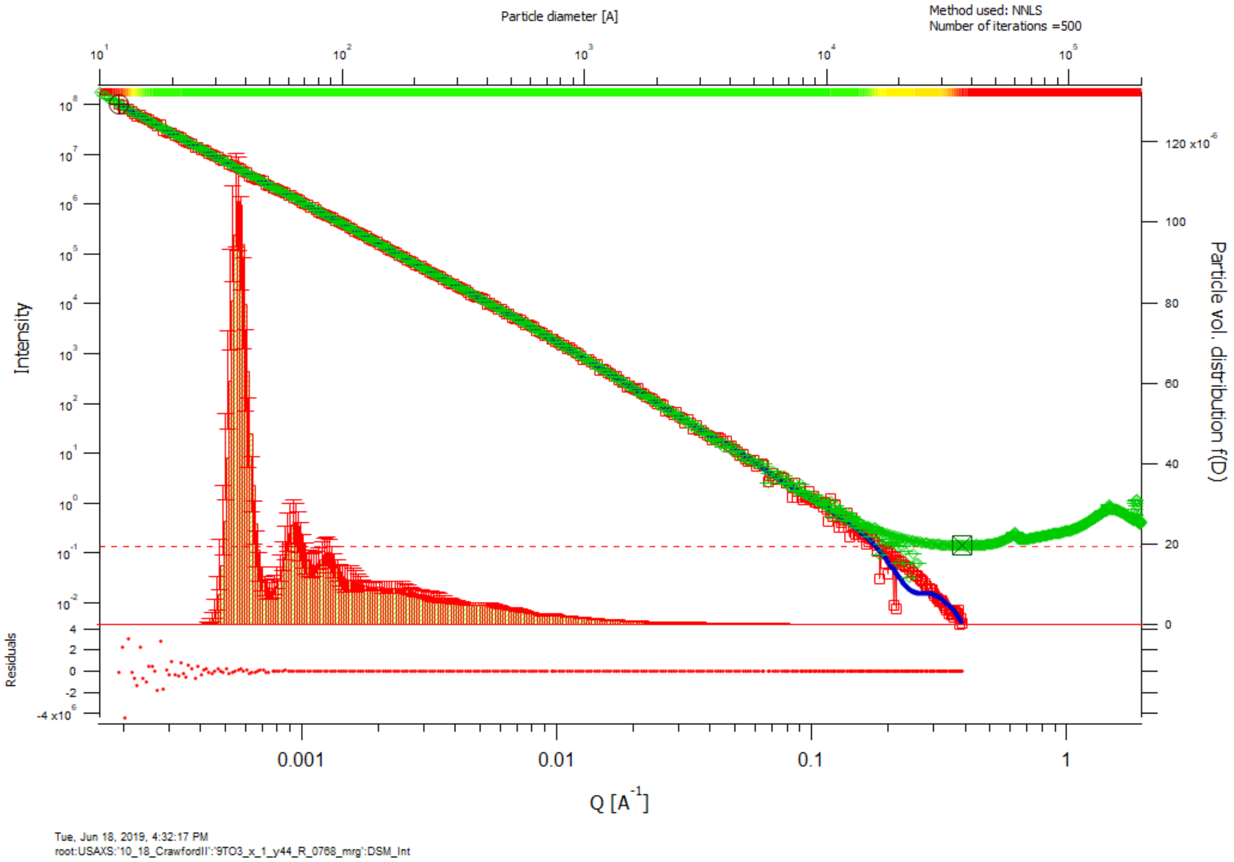

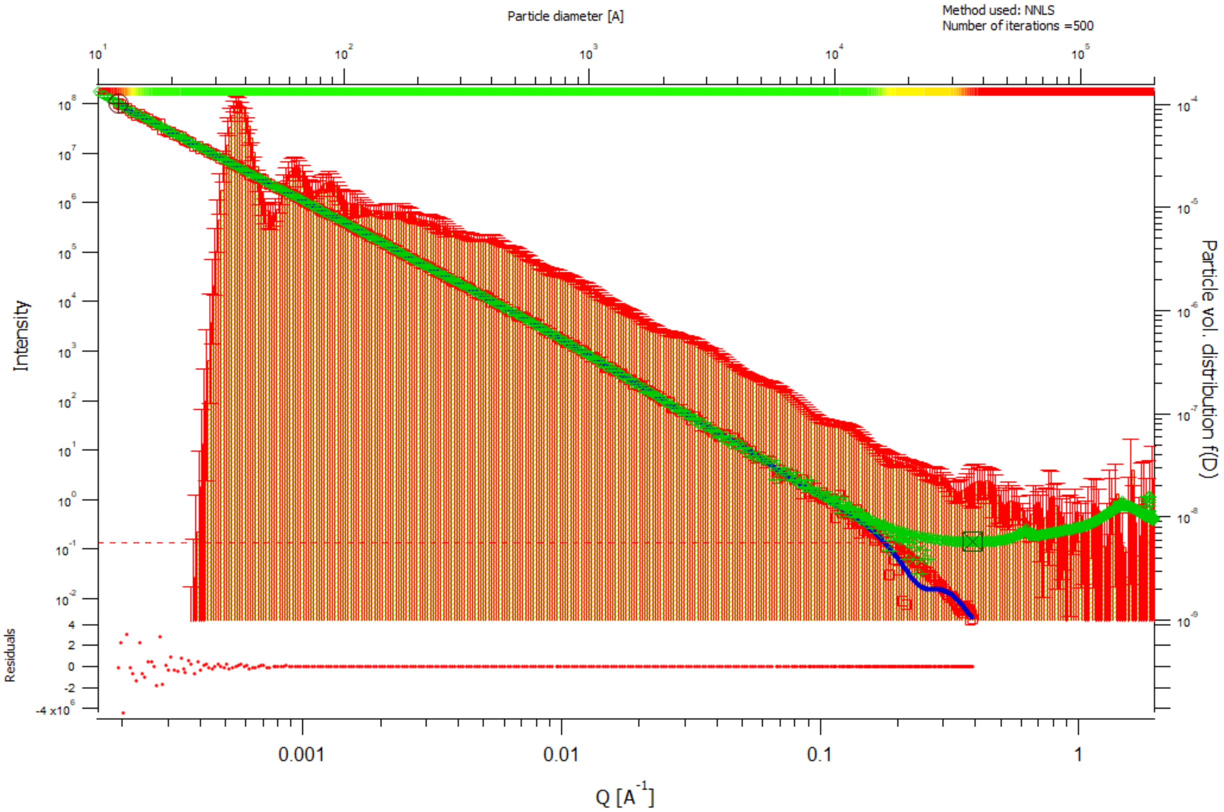

Tue, Jun 18, 2019, 4:32:17 PM
root:USAXS:'10_18_CrawfordII':'9TO3_x_1_y44_R_0768_mrg':DSM_Int

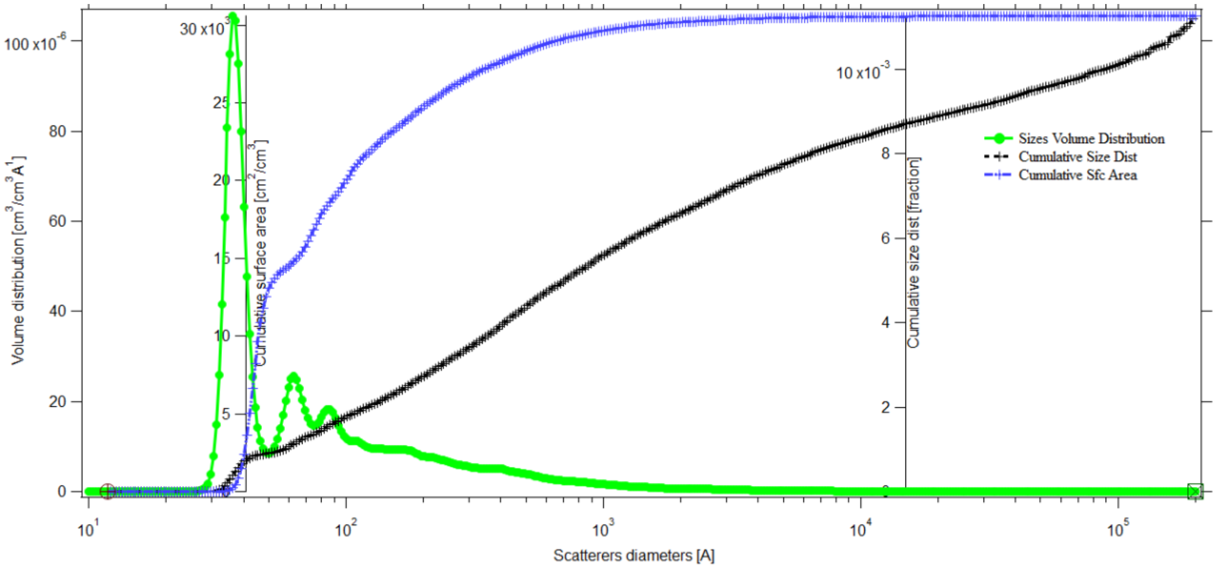

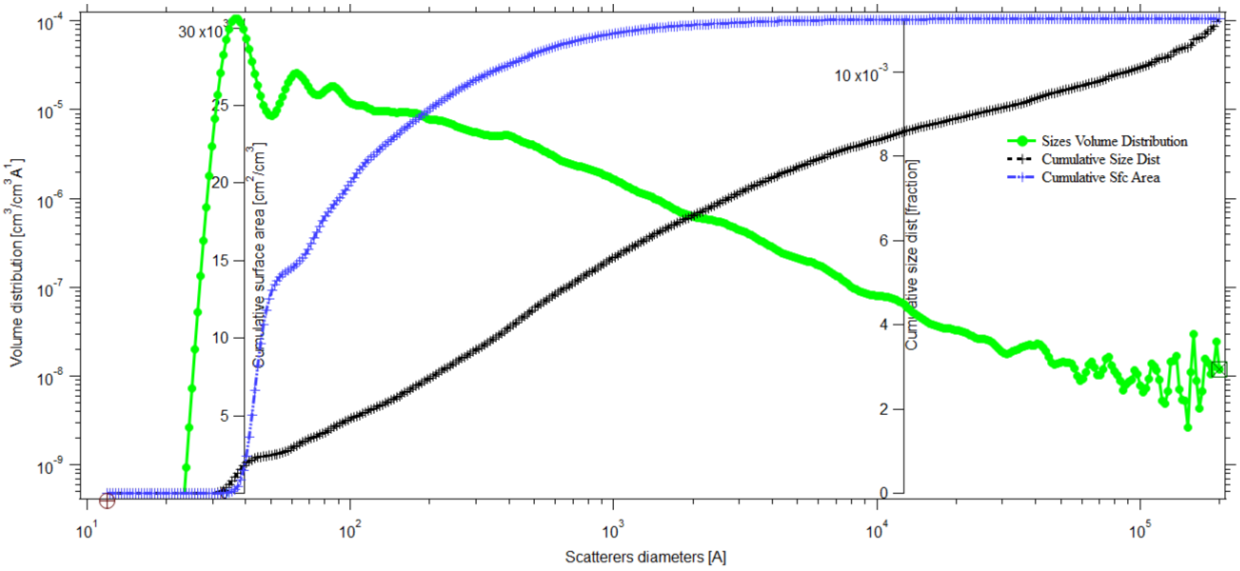

11. 9TO3_x_1_y44_ 0767

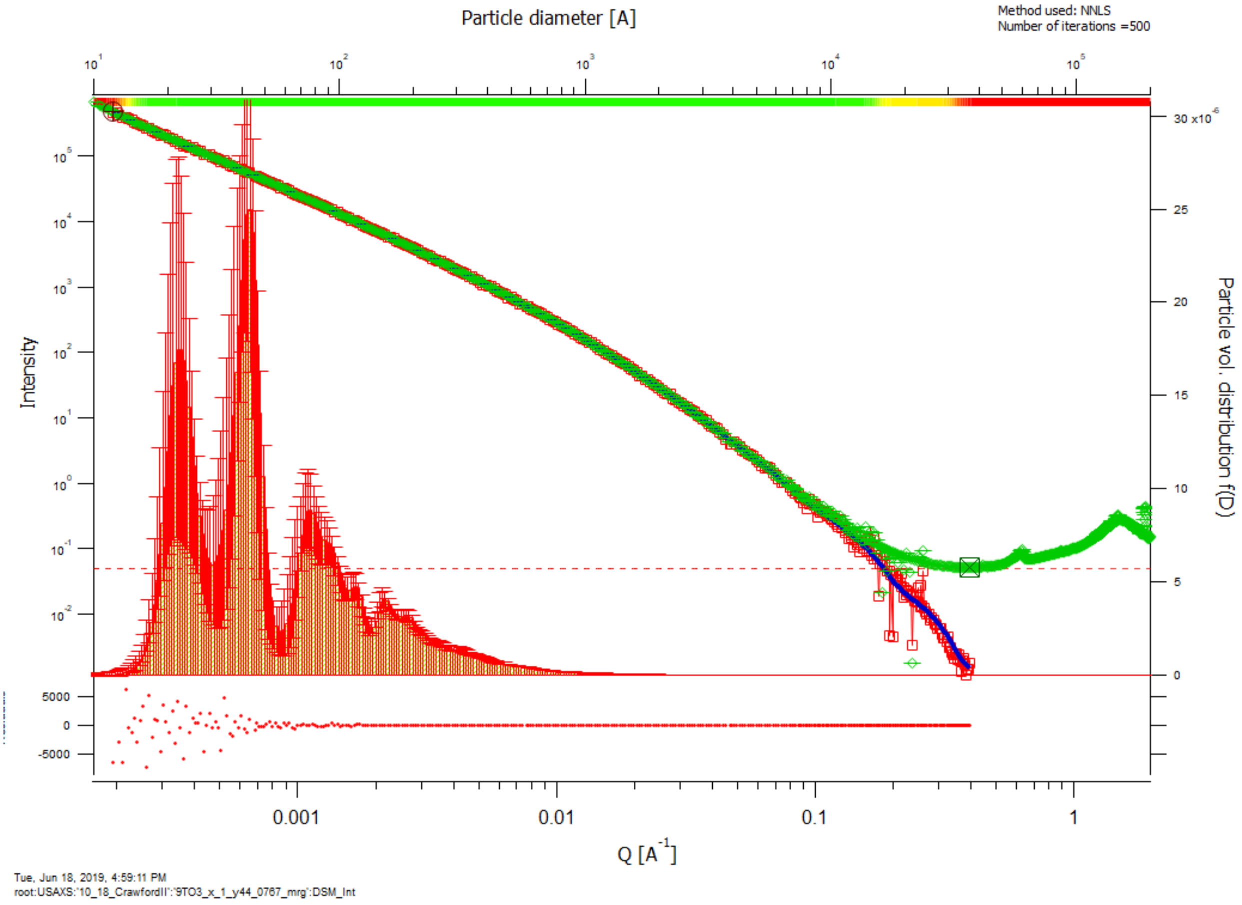

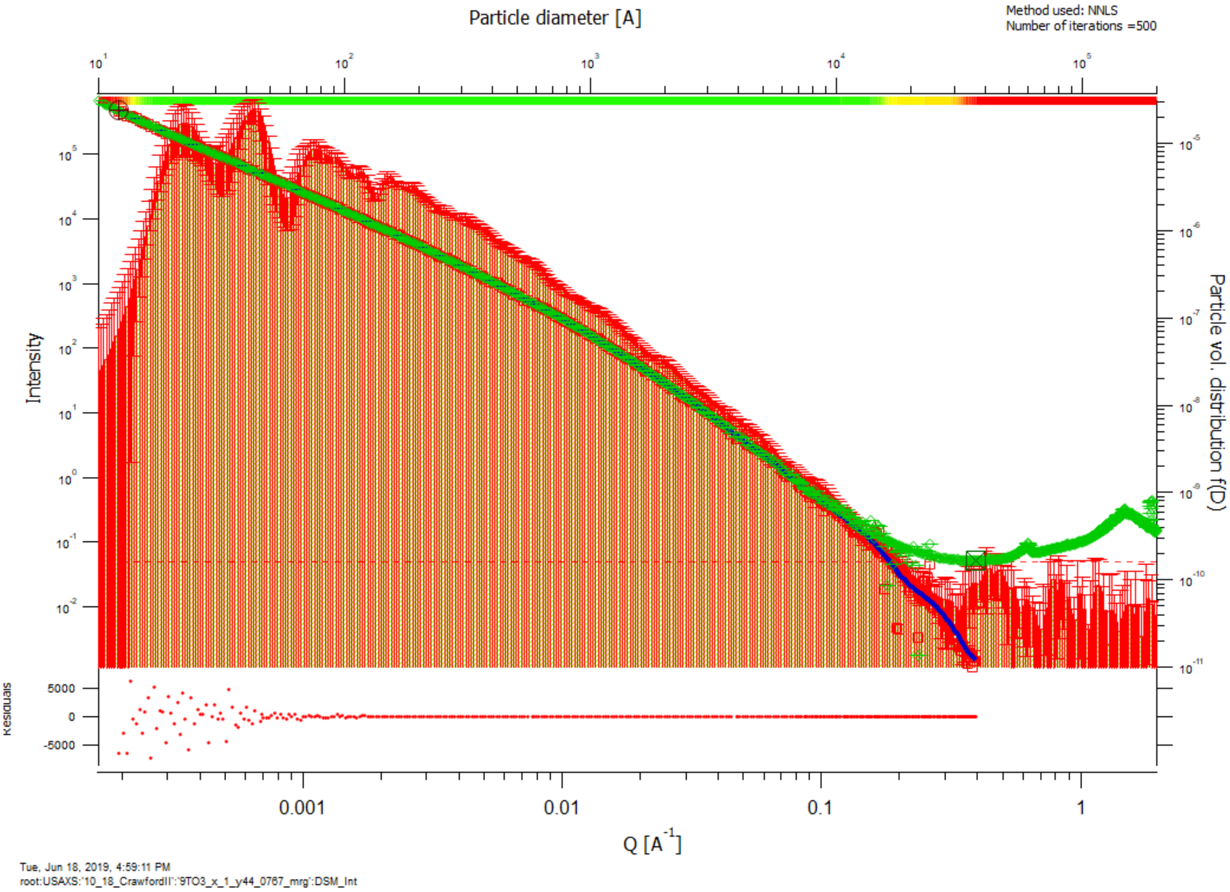

11. 9TO3_x_1_y52_R_0766

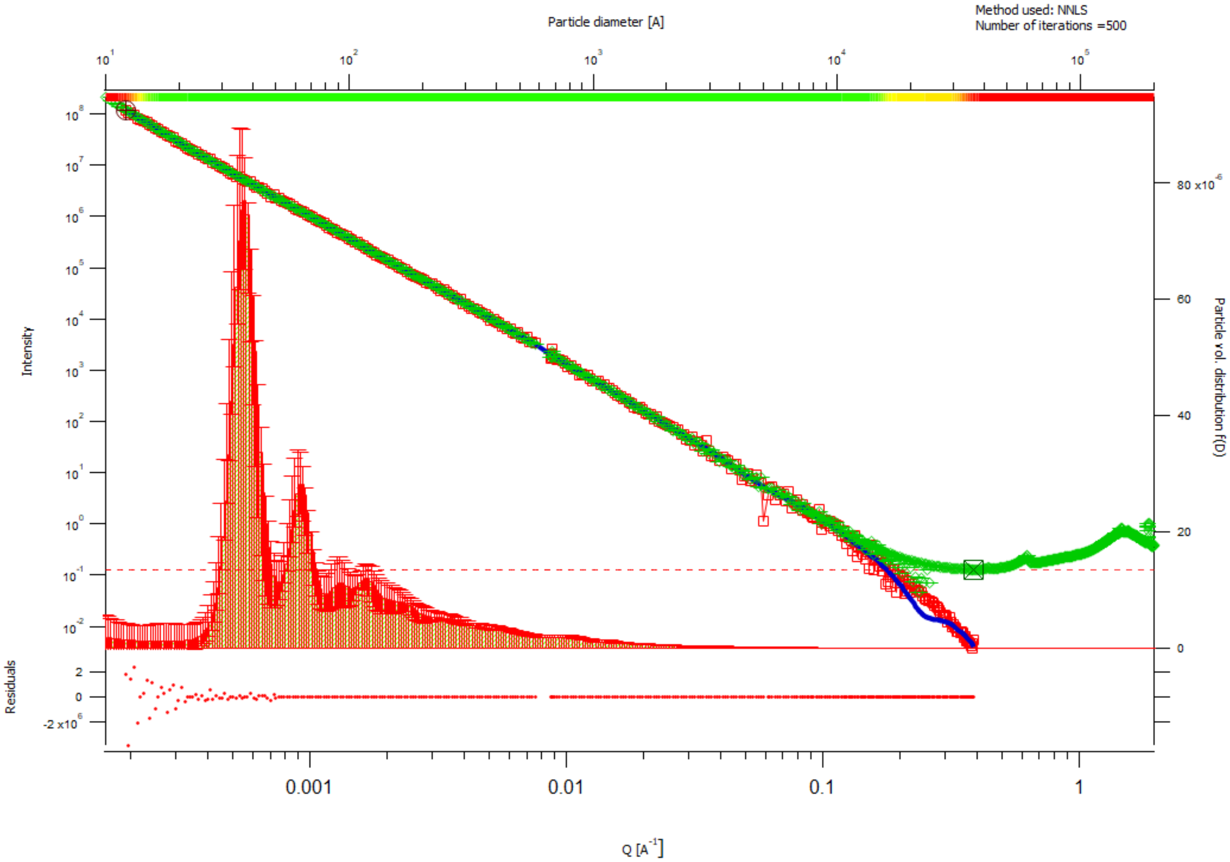

root:USAXS:'10_18_CrawfordII':'9TO3_x_1_y57_R_0766_mrg':DSM_Int

Tue, Jun 18, 2019, 5:28:15 PM

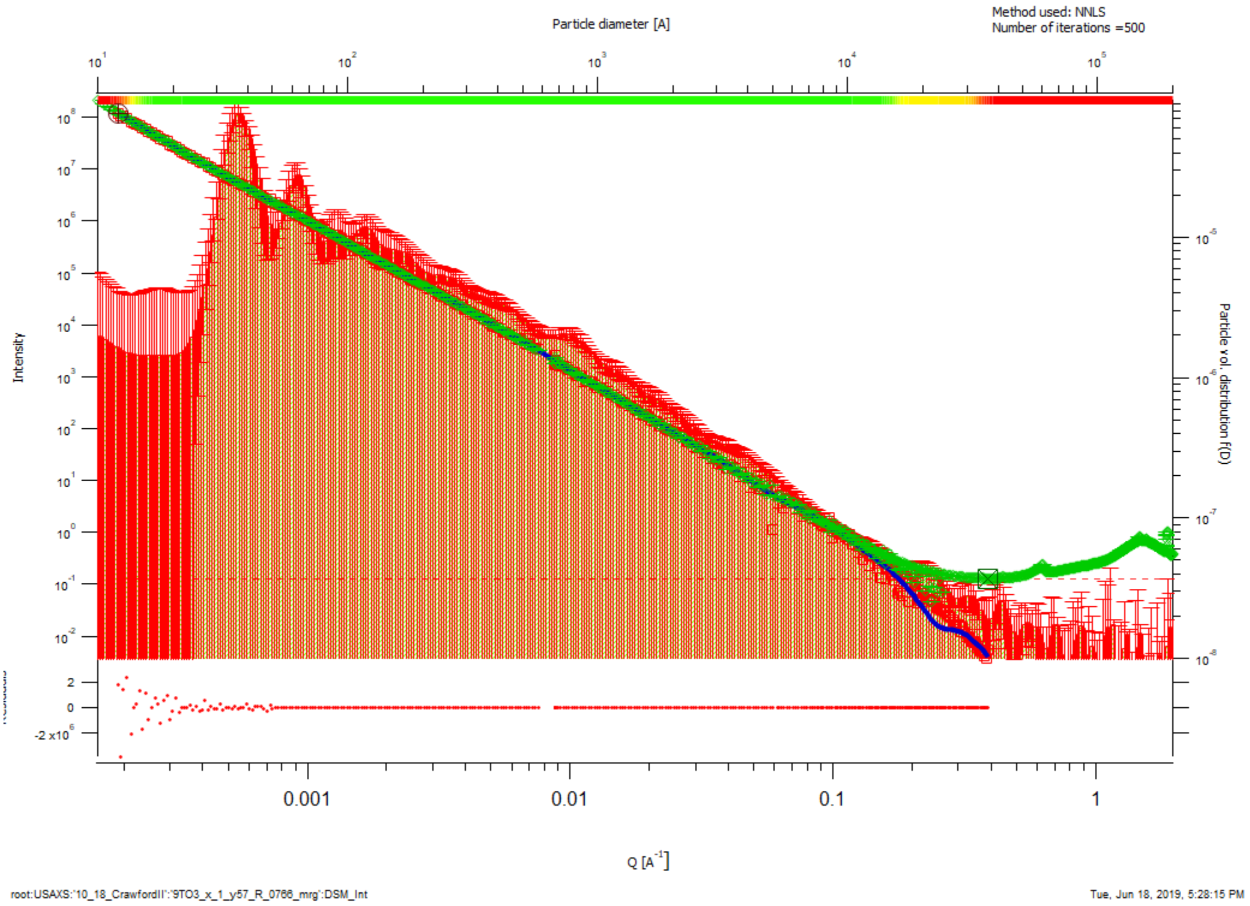

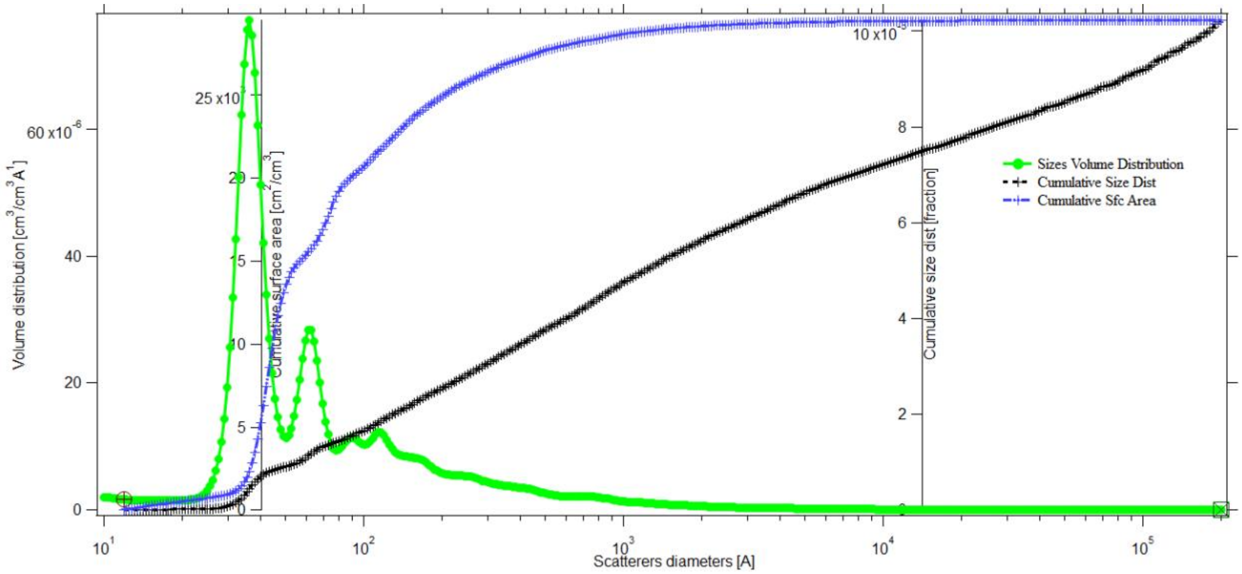

12. 9TO3_x_1_y57_0765

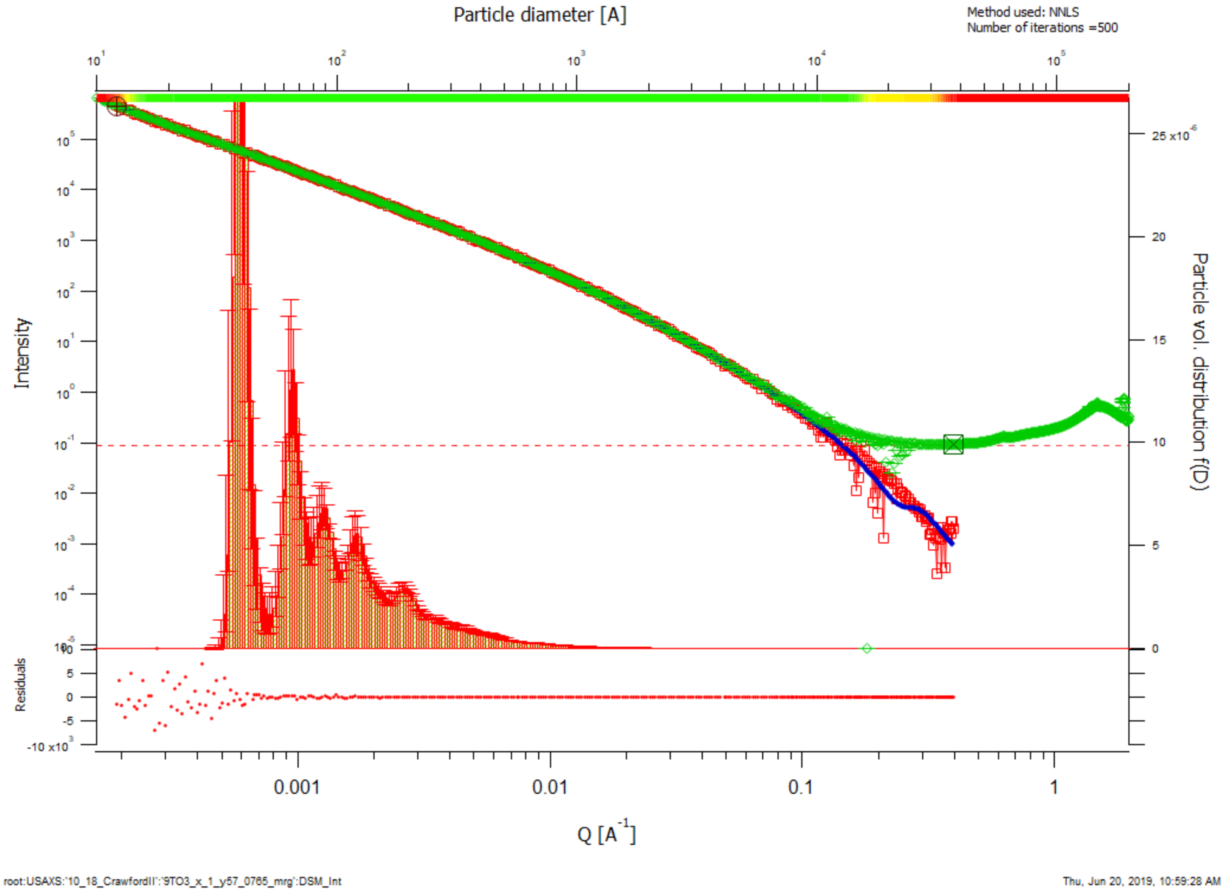
Particle diameter [A]
Method used: NNLS
Number of iterations =500
10^1
10^2
10^3
10^4
10^5
Intensity
10^5
10^4
10^3
10^2
10^1
10^0
10^-1
10^-2
10^-3
10^-4
10^-5
25 x10^-6
20
15
10
5
0
Particle vol. distribution f(D)
Residuals
10
5
0
-5
-10 x10^3
0.001
0.01
0.1
1
Q [A^-1]
root:USAXS:'10_18_CrawfordII':'9TO3_x_1_y57_0765_mrg':DSM_Int
Thu, Jun 20, 2019, 10:59:28 AM

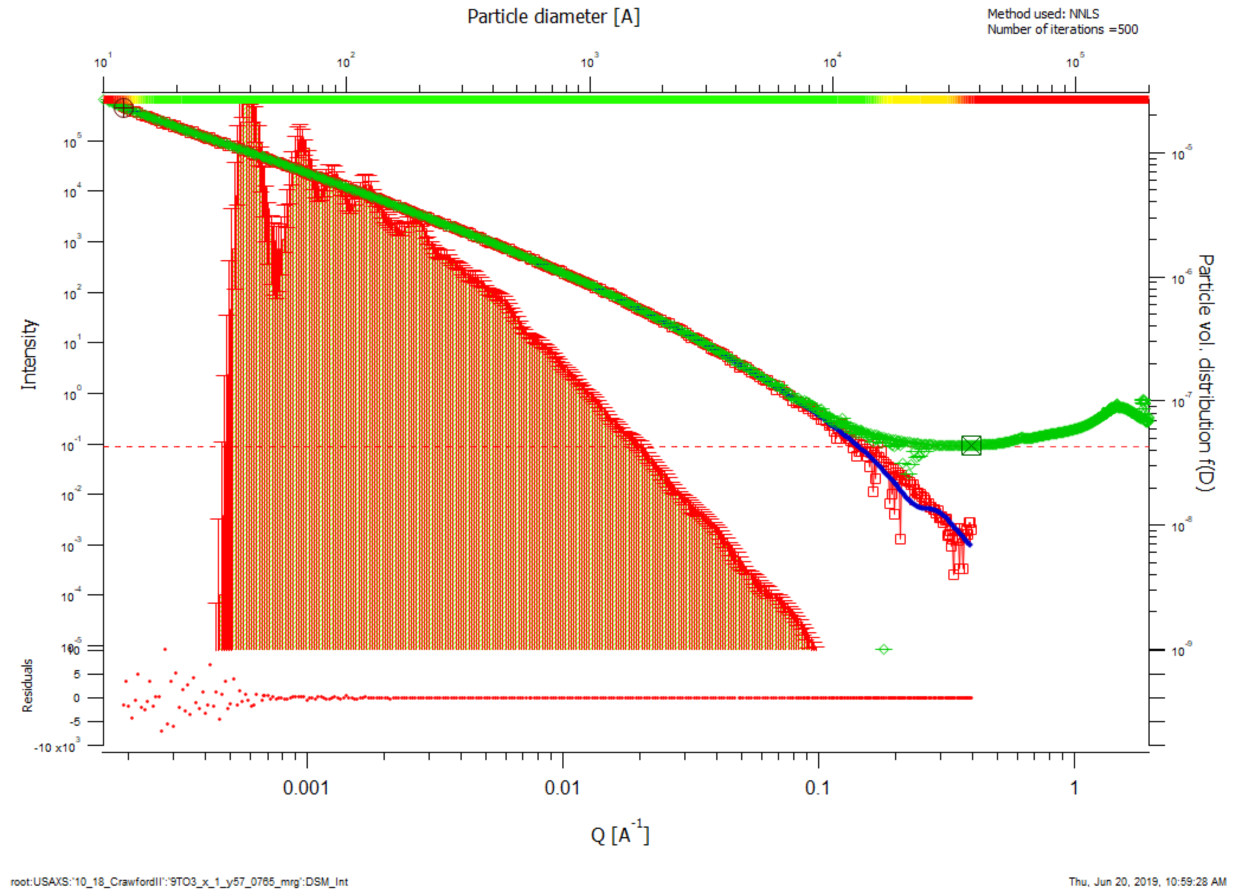
Particle diameter [A]
Method used: NNLS
Number of iterations =500
Intensity
Residuals
Particle vol. distribution f(D)
Q [A^{-1}]
0.001
0.01
0.1
1
root:USAXS:'10_18_CrawfordII':'9TO3_x_1_y57_0765_mrg':DSM_Int
Thu, Jun 20, 2019, 10:59:28 AM

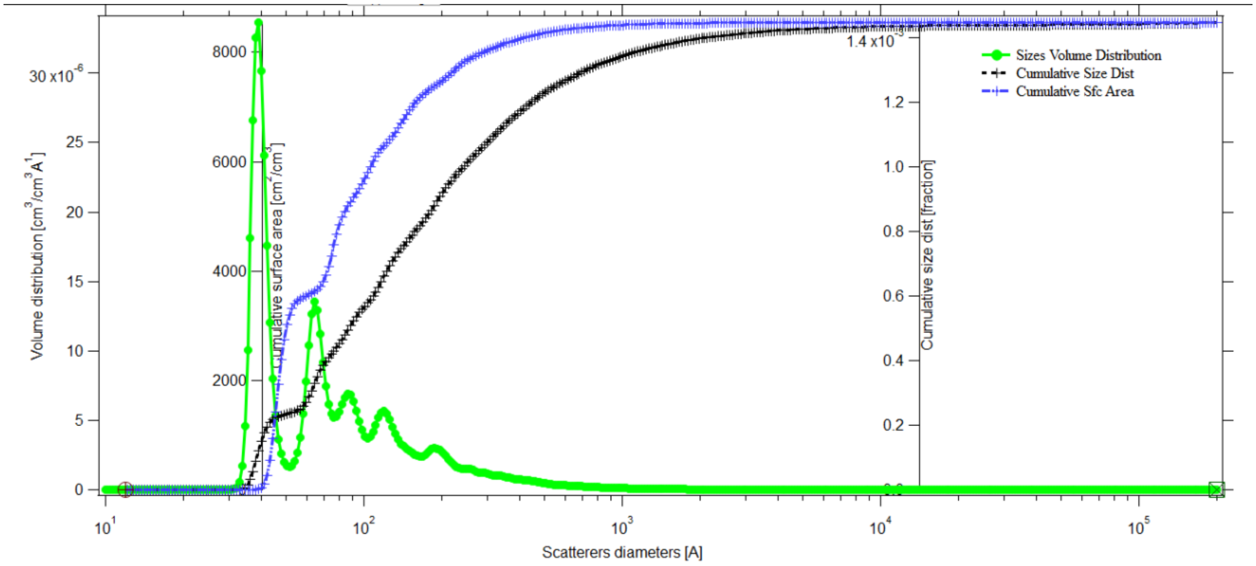
Sizes Volume Distribution
Cumulative Size Dist
Cumulative Sfc Area
Volume distribution [cm^3/cm^{3}A^1]
Cumulative surface area [cm^2/cm^3]
Cumulative size dist [fraction]
30 x10^{-6}
25
20
15
10
5
0
8000
6000
4000
2000
1.4 x10^{-3}
1.2
1.0
0.8
0.6
0.4
0.2
Scatterers diameters [A]

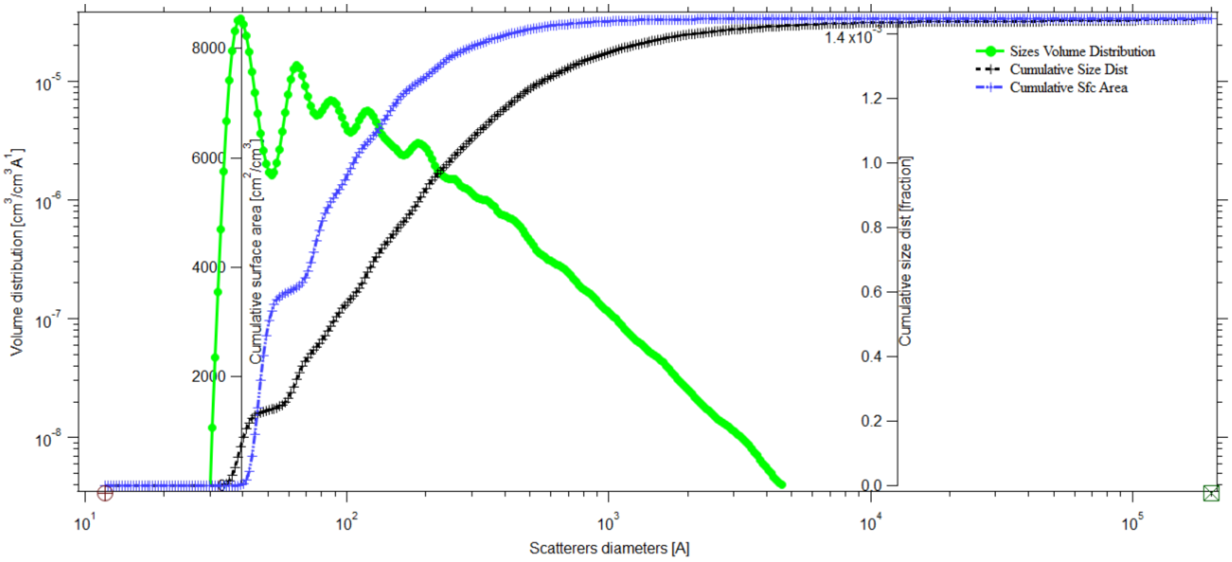

13. 9TO4_x0_y_4_R_0756

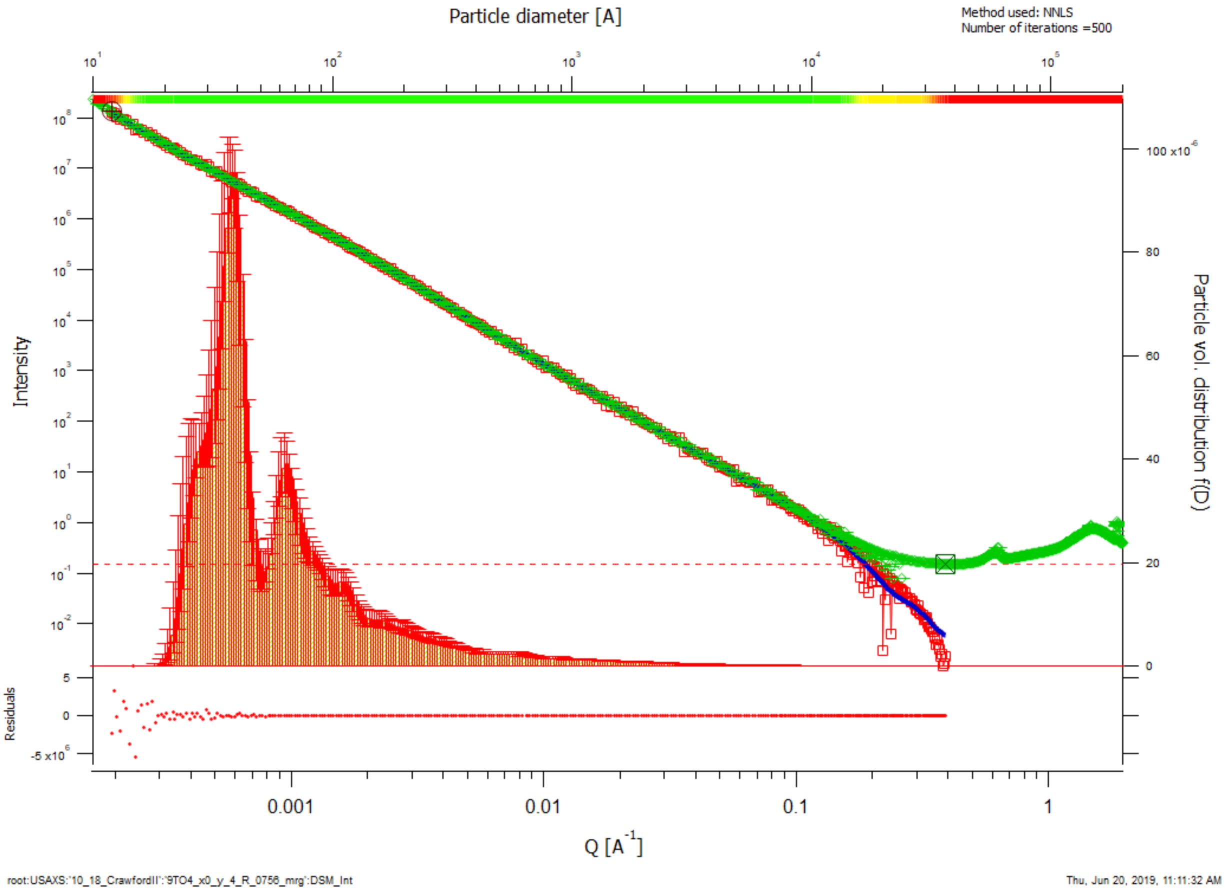

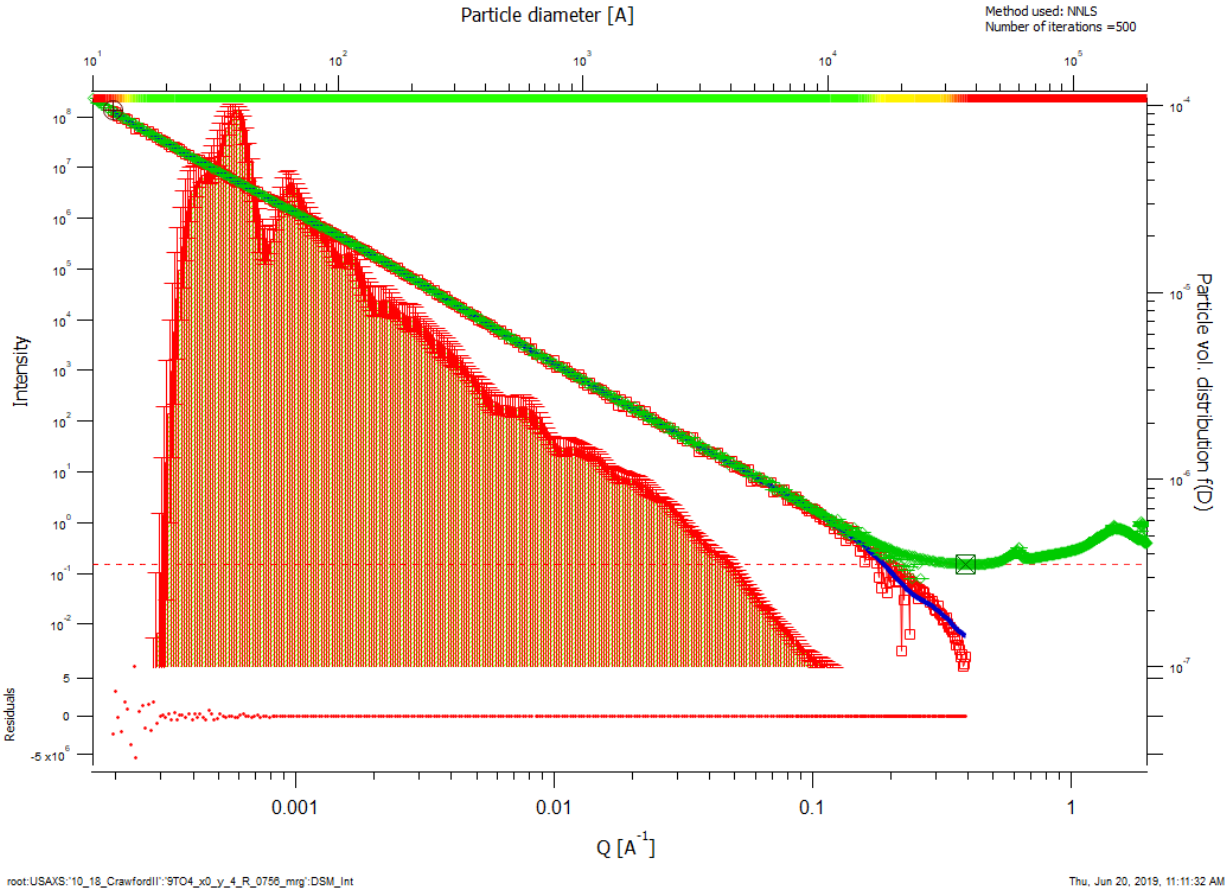
Particle diameter [A]
Method used: NNLS
Number of iterations =500
10^1
10^2
10^3
10^4
10^5
Intensity
10^8
10^7
10^6
10^5
10^4
10^3
10^2
10^1
10^0
10^-1
10^-2
Residuals
5
0
-5 x10^6
Particle vol. distribution f(D)
10^-4
10^-5
10^-6
10^-7
0.001
0.01
0.1
1
Q [A^-1]
root:USAXS:'10_18_CrawfordII':'9TO4_x0_y_4_R_0756_mrg':DSM_Int
Thu, Jun 20, 2019, 11:11:32 AM

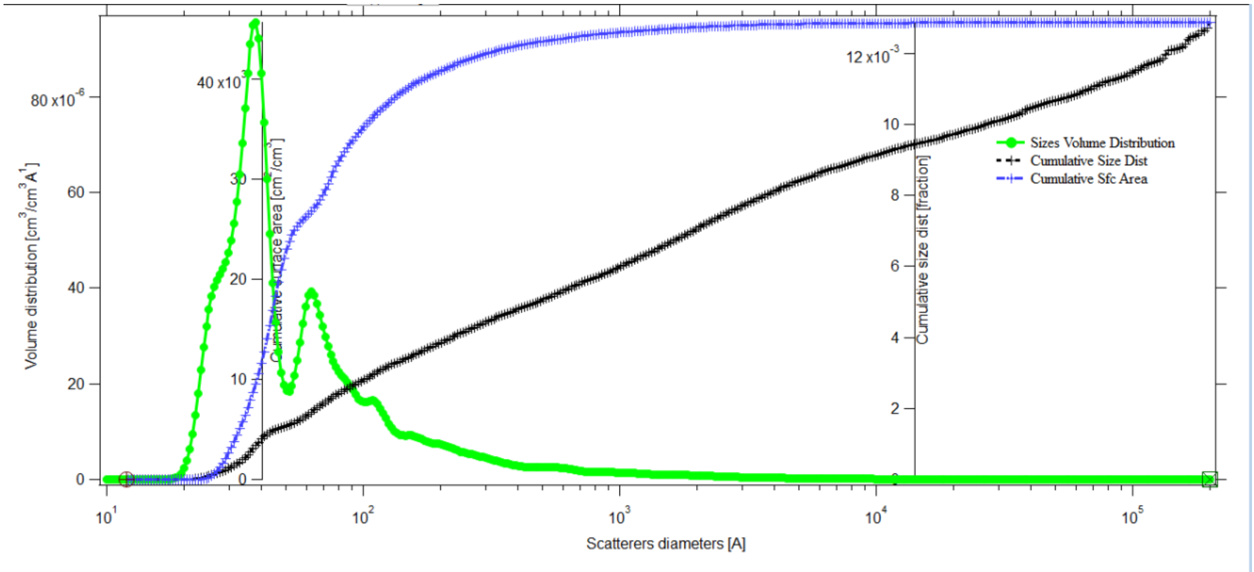
80 x10^-6
60
40
20
0
Volume distribution [cm^3/cm^3A^1]
40 x10^3
30
20
10
0
Cumulative surface area [cm^2/cm^3]
12 x10^-3
10
8
6
4
2
0
Cumulative size dist [fraction]
Sizes Volume Distribution
Cumulative Size Dist
Cumulative Sfc Area
10^1
10^2
10^3
10^4
10^5
Scatterers diameters [A]

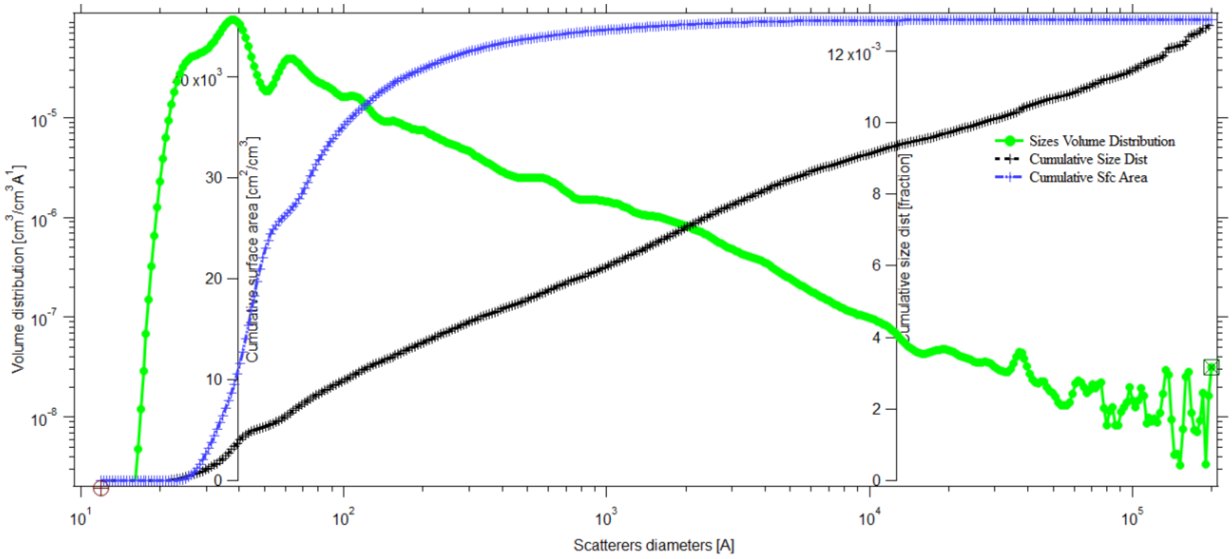

14. 9TO4_x0_y_4_R_0755

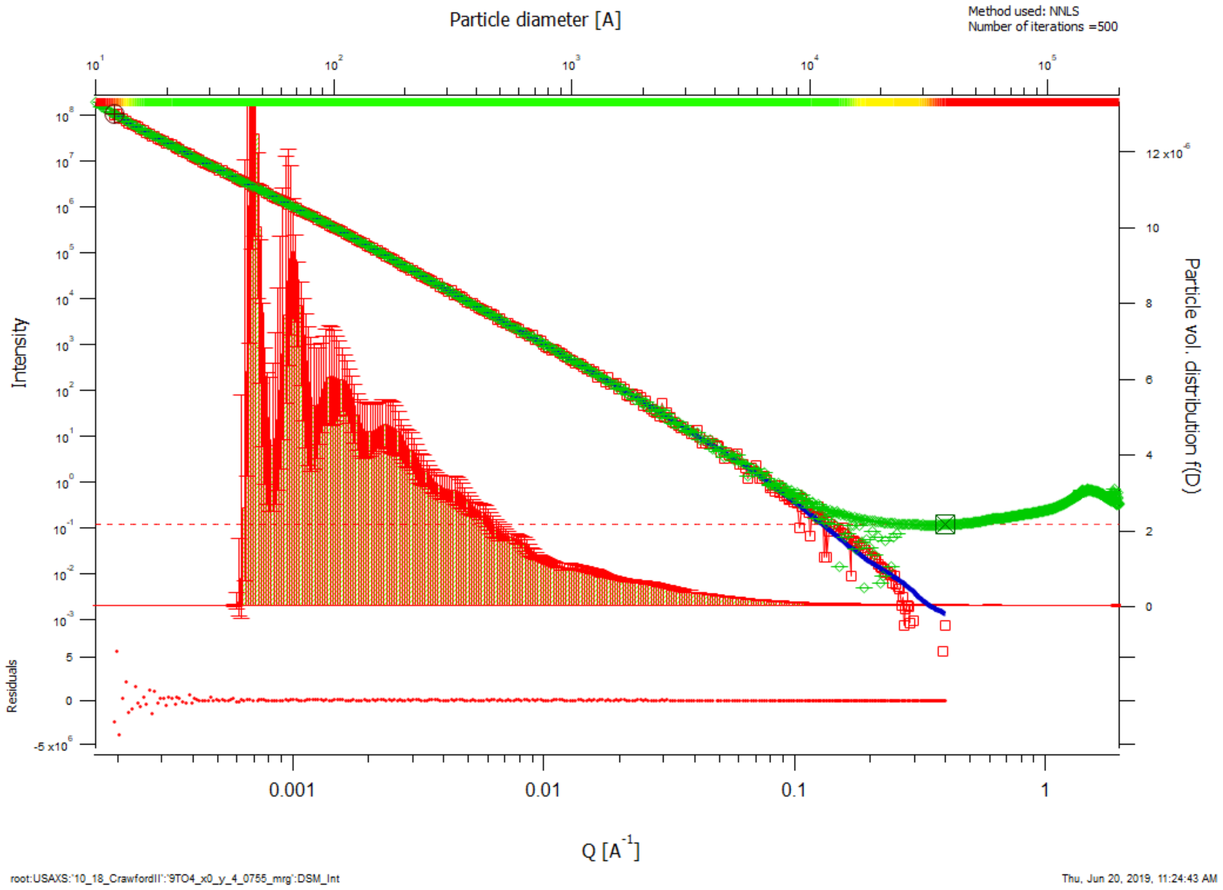

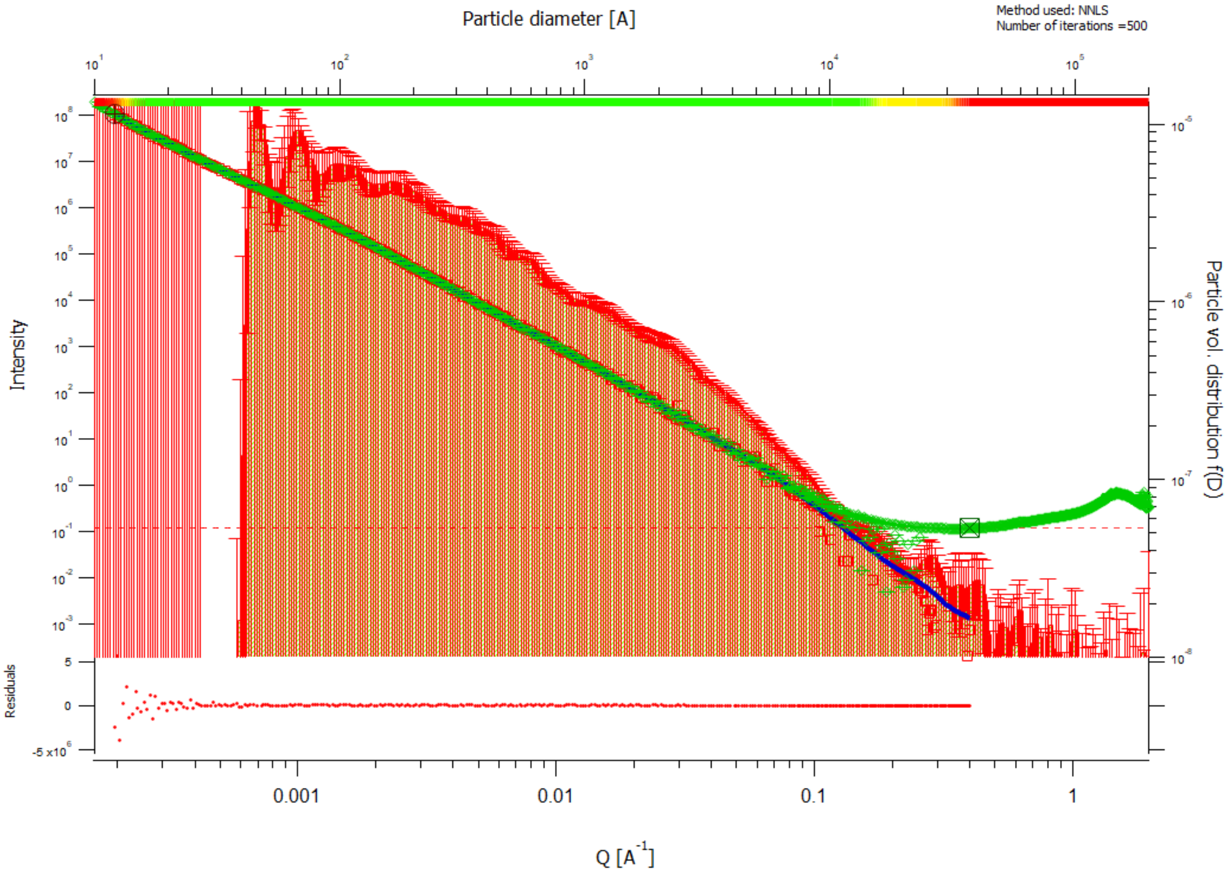
Particle diameter [A]
Method used: NNLS
Number of iterations =500
10^1
10^2
10^3
10^4
10^5
Intensity
10^8
10^7
10^6
10^5
10^4
10^3
10^2
10^1
10^0
10^{-1}
10^{-2}
10^{-3}
Particle vol. distribution f(D)
10^{-5}
10^{-6}
10^{-7}
10^{-8}
Residuals
5
0
-5×10^{6}
0.001
0.01
0.1
1
Q [A^{-1}]

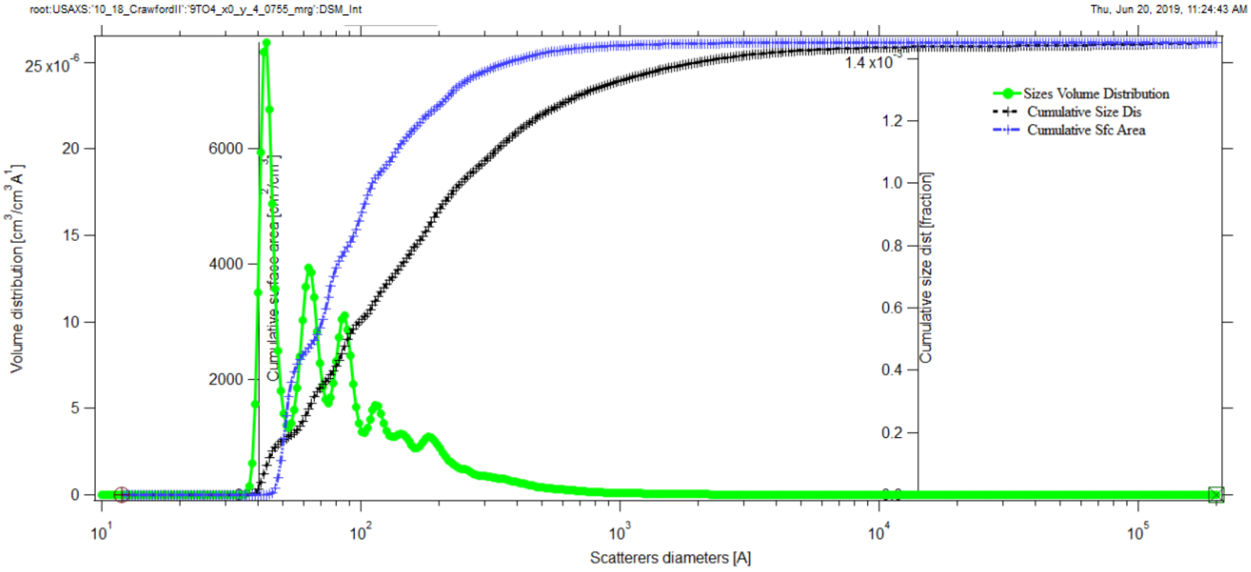
root:USAXS:'10_18_CrawfordII':'9TO4_x0_y_4_0755_mrg':DSM_Int
Thu, Jun 20, 2019, 11:24:43 AM
Volume distribution [$cm^3/cm^3 A^1$]
25×10^{-6}
20
15
10
5
0
Cumulative surface area [cm^2/cm^3]
6000
4000
2000
Cumulative size dist [fraction]
1.4×10^{-3}
1.2
1.0
0.8
0.6
0.4
0.2
0.0
Sizes Volume Distribution
Cumulative Size Dis
Cumulative Sfc Area
10^1
10^2
10^3
10^4
10^5
Scatterers diameters [A]

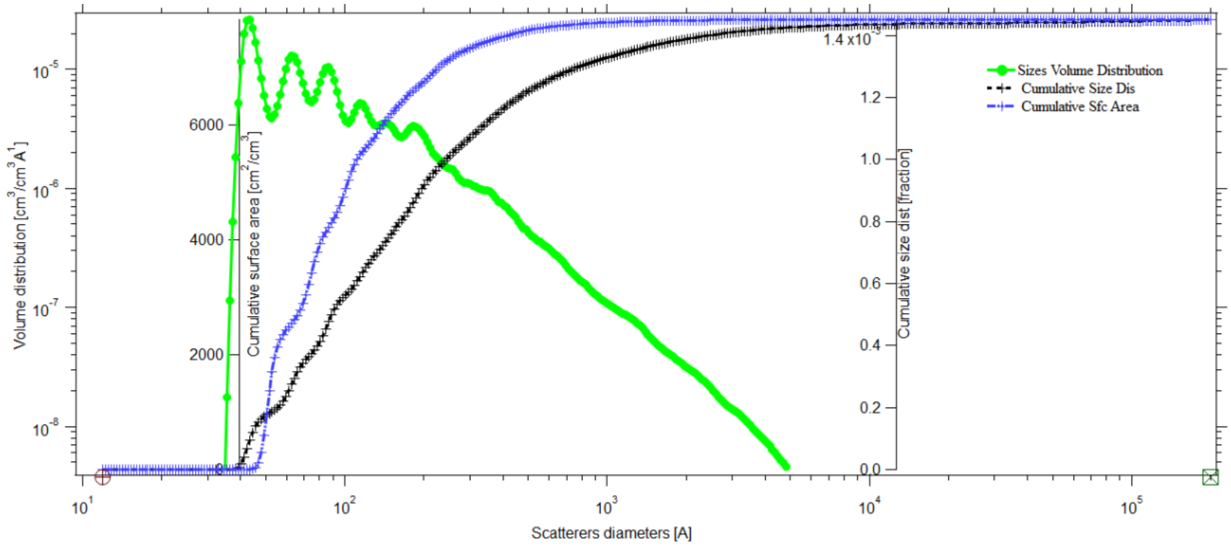

15. 9TO4_x0_y3_0753

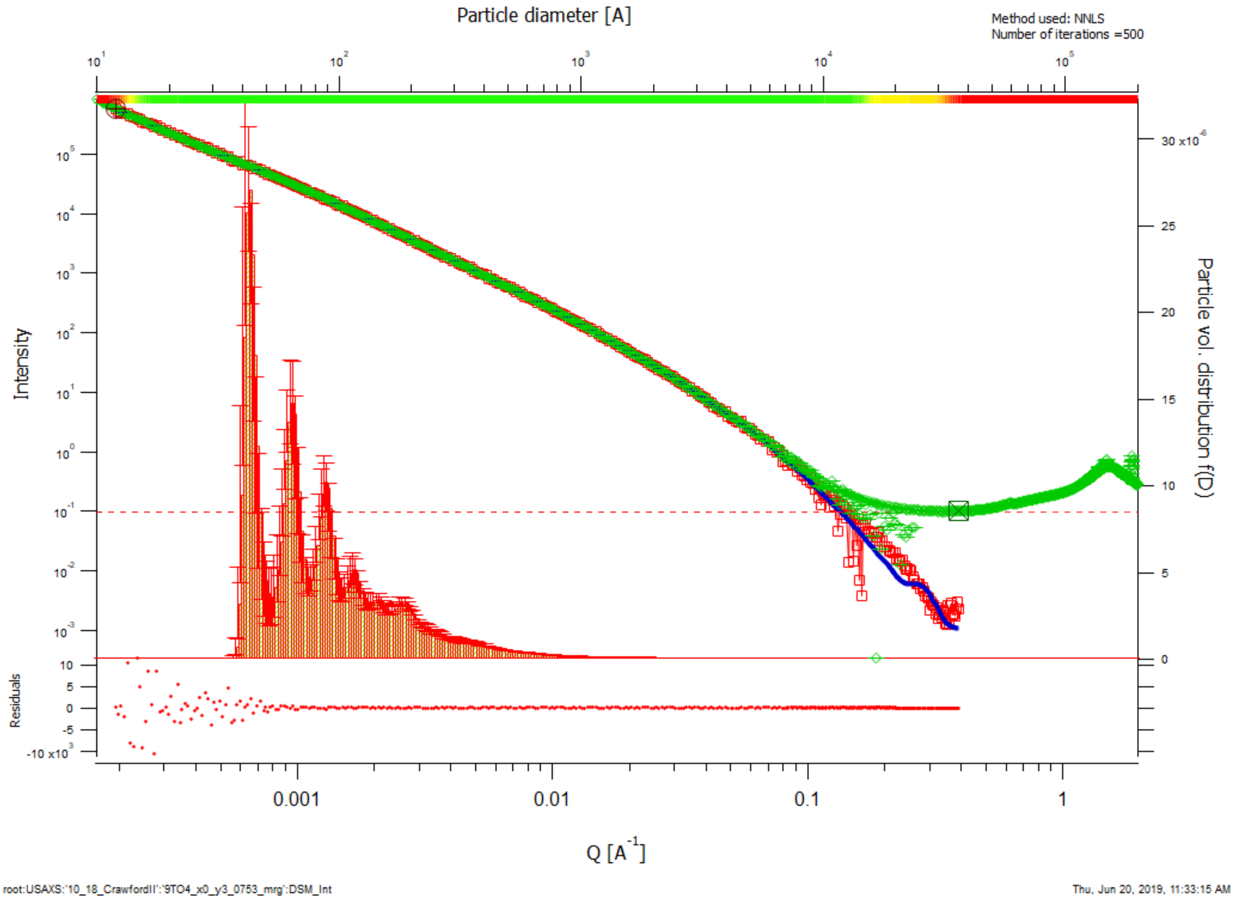

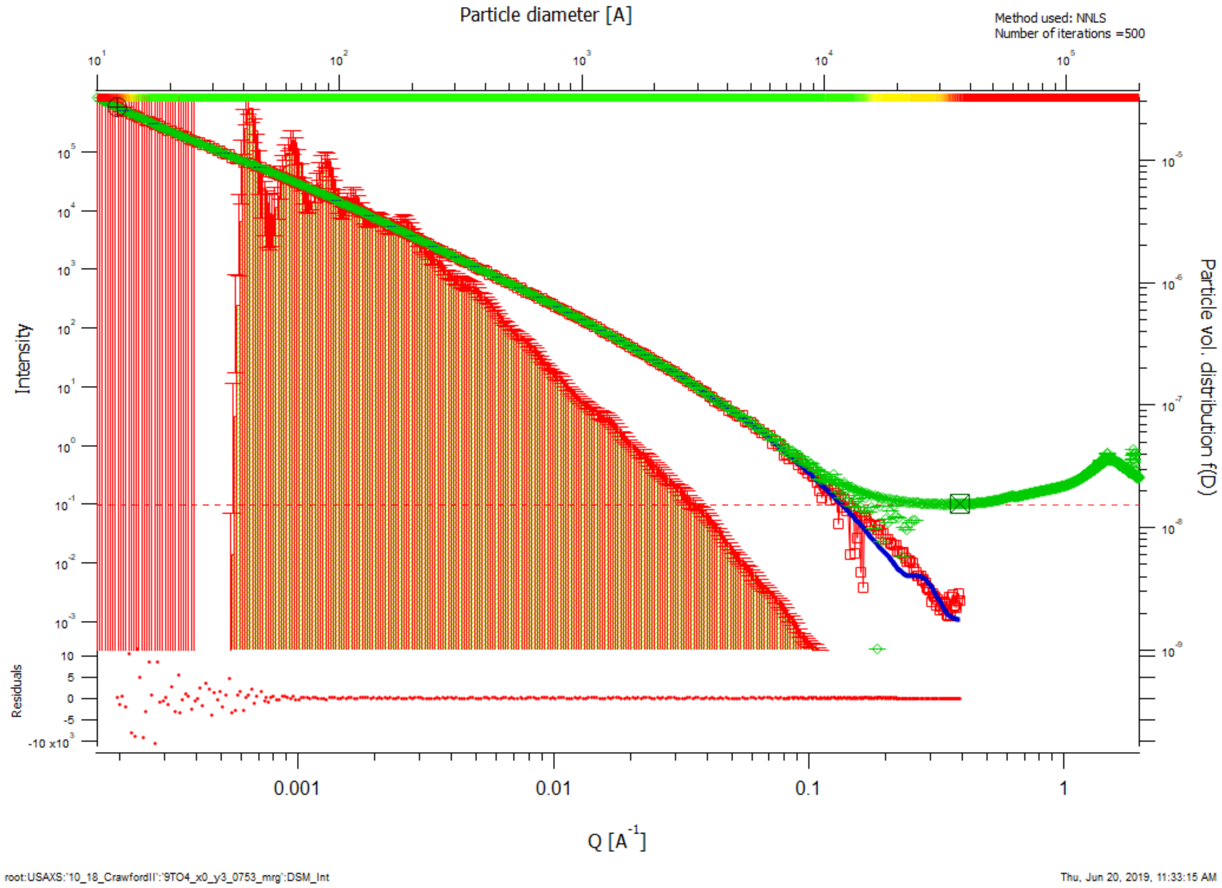
Particle diameter [A]
Method used: NNLS
Number of iterations =500
10^1
10^2
10^3
10^4
10^5
Intensity
10^5
10^4
10^3
10^2
10^1
10^0
10^{-1}
10^{-2}
10^{-3}
Particle vol. distribution f(D)
10^{-5}
10^{-6}
10^{-7}
10^{-8}
10^{-9}
Residuals
10
5
0
-5
-10 x10^3
0.001
0.01
0.1
1
Q [A^{-1}]
root:USAXS:'10_18_CrawfordII':'9TO4_x0_y3_0753_mrg':DSM_Int
Thu, Jun 20, 2019, 11:33:15 AM

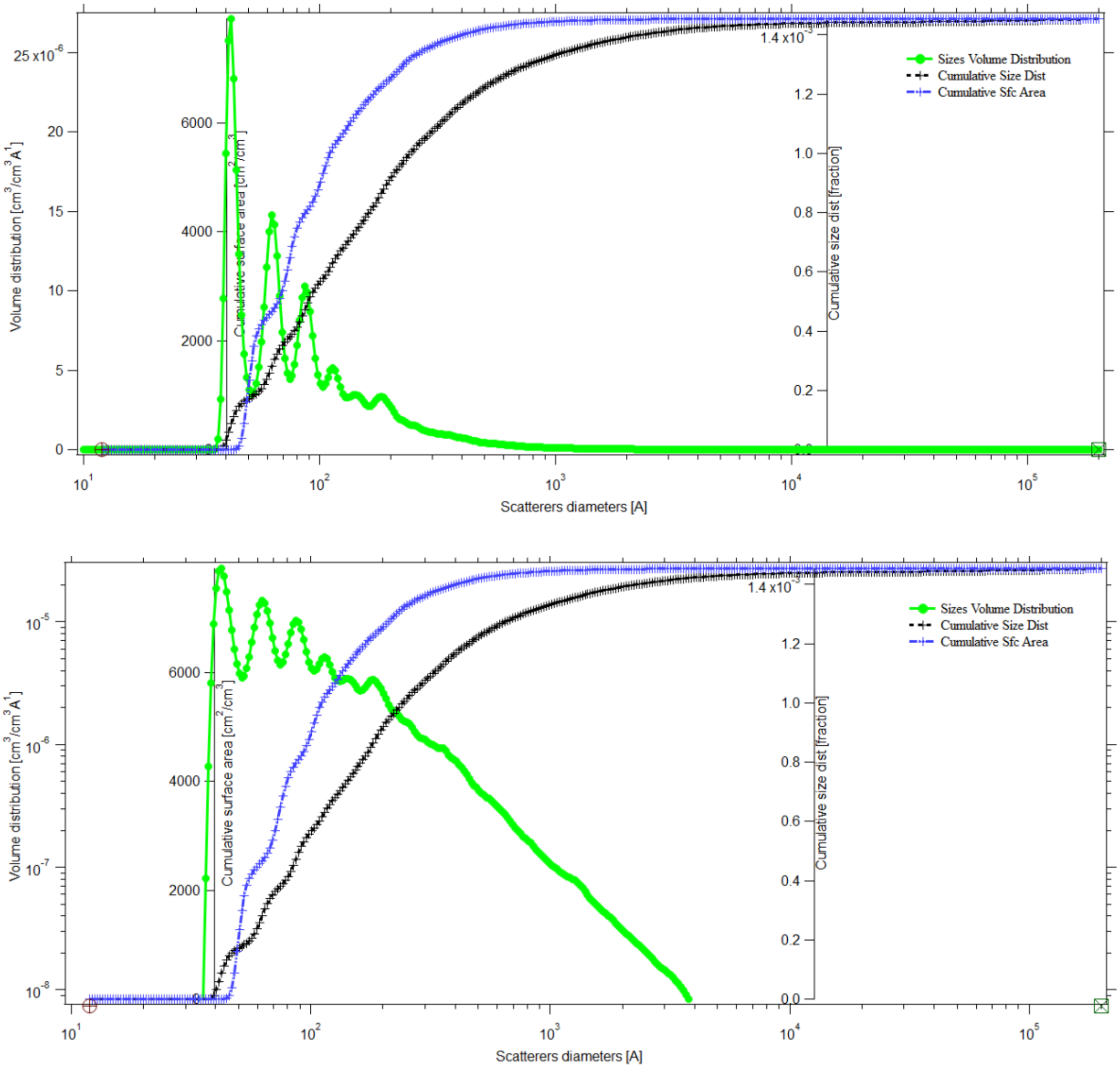

16. 9TO4_x0_y12_R_0752

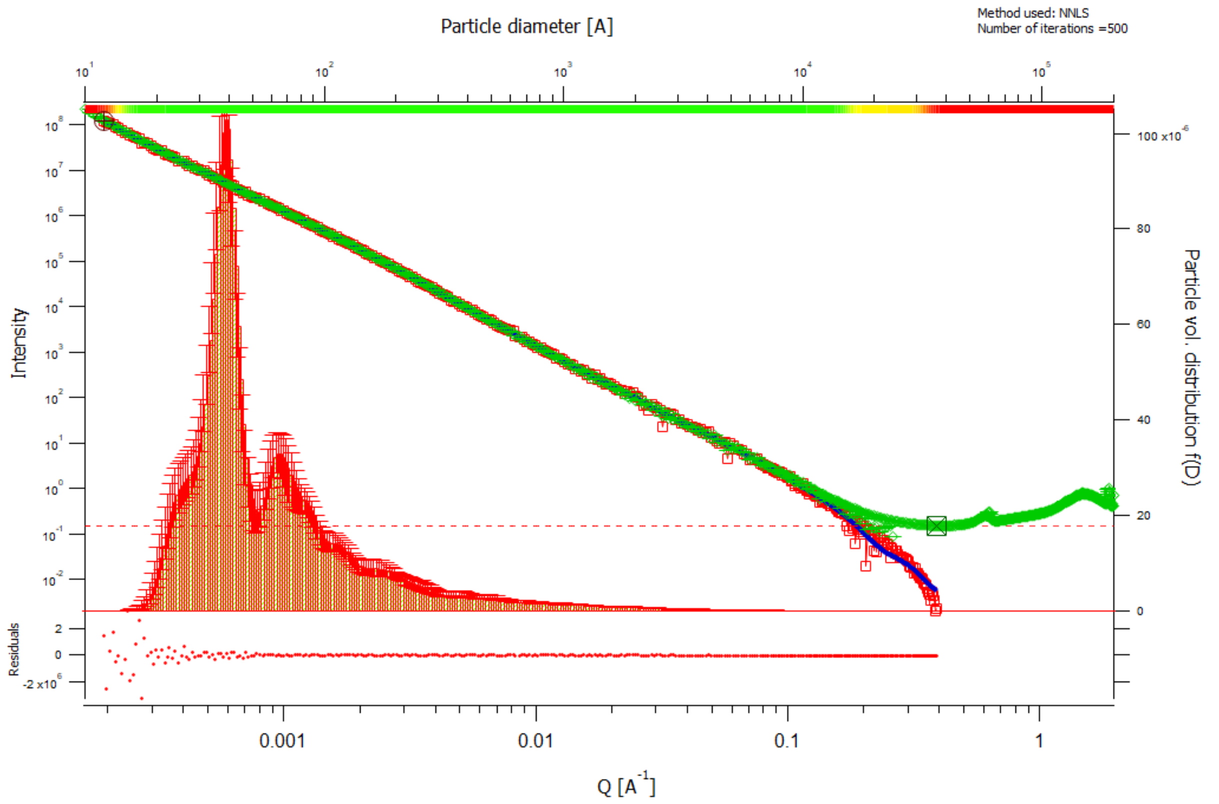

root:USAXS:'10_18_CrawfordII':'9TO4_x0_y12_R_0752_mrg':DSM_Int

Thu, Jun 20, 2019, 11:46:04 AM

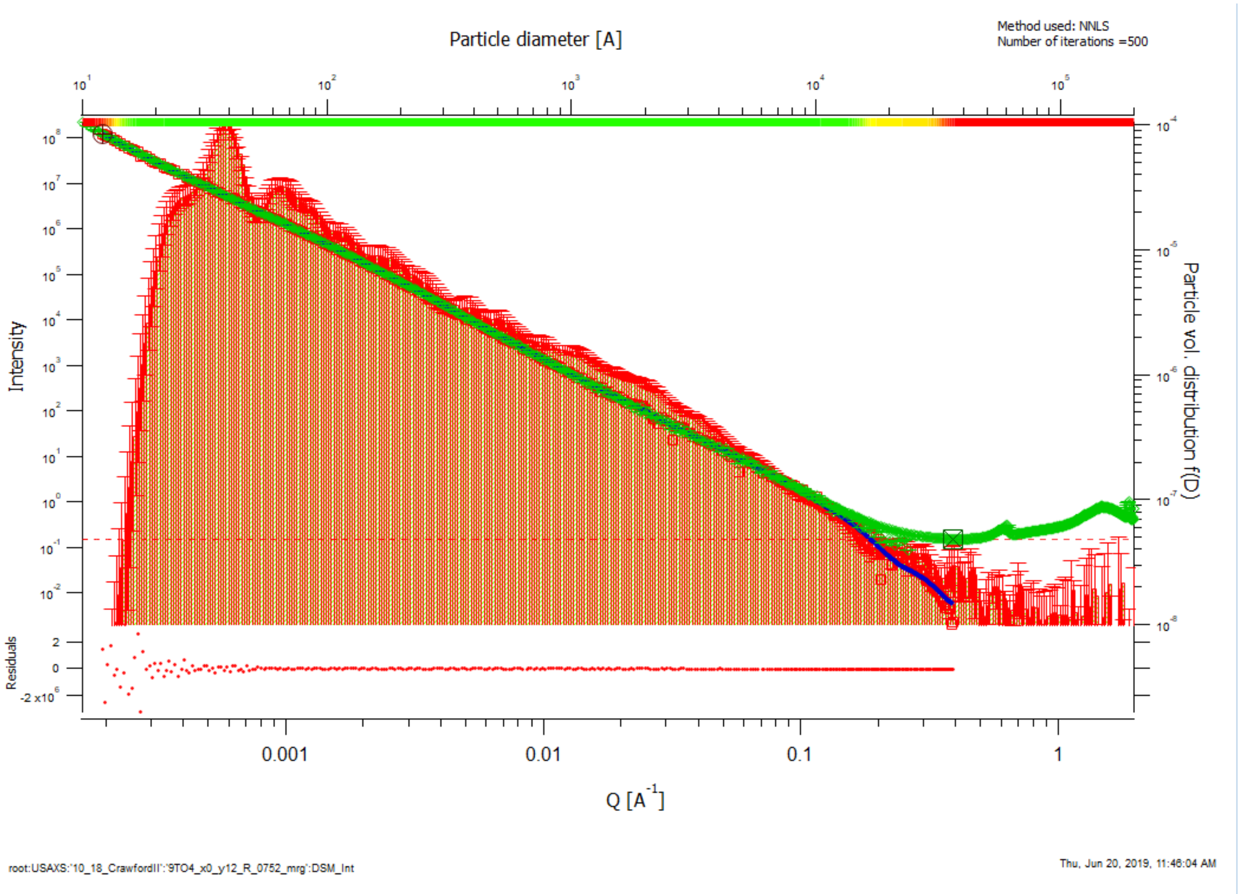
Particle diameter [A]
Method used: NNLS
Number of iterations =500
10^1
10^2
10^3
10^4
10^5
Intensity
10^8
10^7
10^6
10^5
10^4
10^3
10^2
10^1
10^0
10^{-1}
10^{-2}
Particle vol. distribution f(D)
10^{-4}
10^{-5}
10^{-6}
10^{-7}
10^{-8}
Residuals
2
0
-2 x10^{-6}
0.001
0.01
0.1
1
Q [A^{-1}]
root:USAXS:'10_18_CrawfordII':'9TO4_x0_y12_R_0752_mrg':DSM_Int
Thu, Jun 20, 2019, 11:46:04 AM

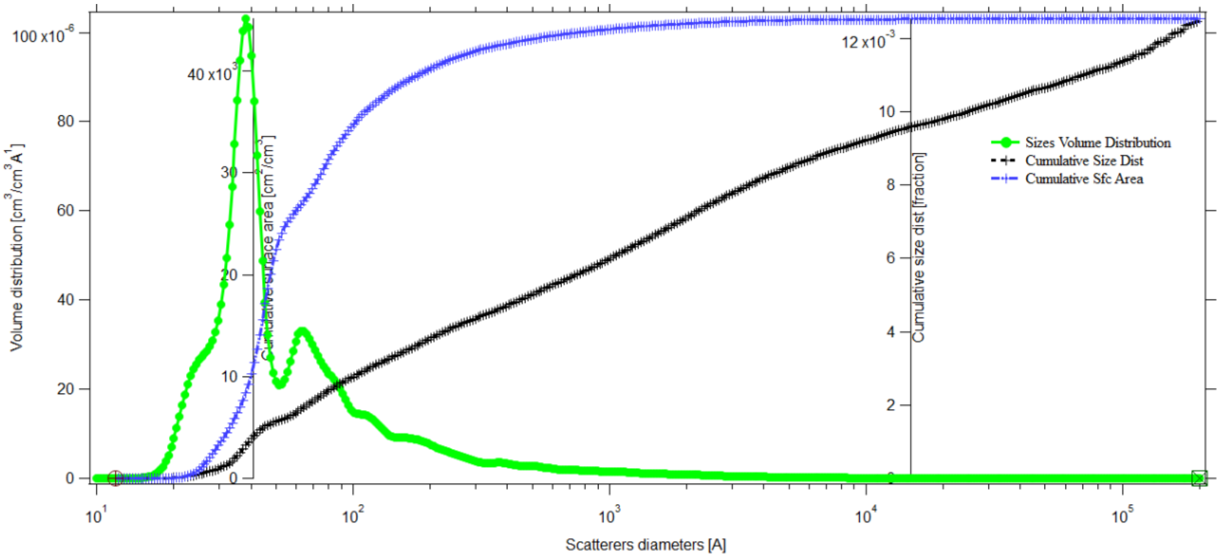
100 x10^{-6}
80
60
40
20
0
Volume distribution [cm^3/cm^{3}A^1]
40 x10^3
30
20
10
0
Cumulative surface area [cm^2/cm^3]
12 x10^{-3}
10
8
6
4
2
0
Cumulative size dist [fraction]
Sizes Volume Distribution
Cumulative Size Dist
Cumulative Sfc Area
10^1
10^2
10^3
10^4
10^5
Scatterers diameters [A]

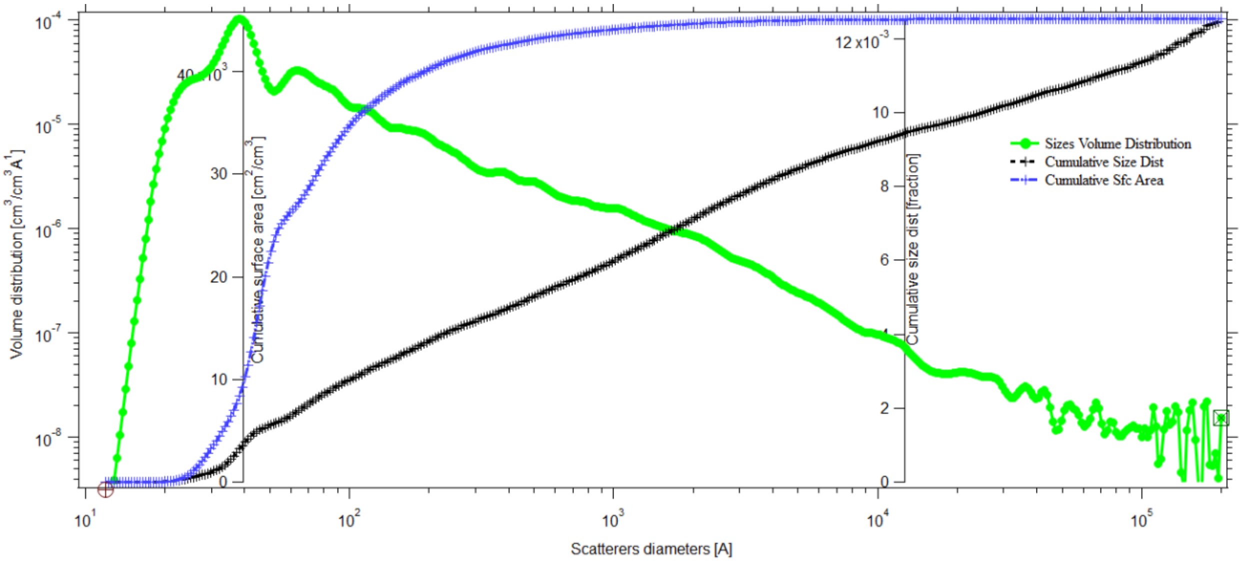

17. 9TO4_x0_y12_0751

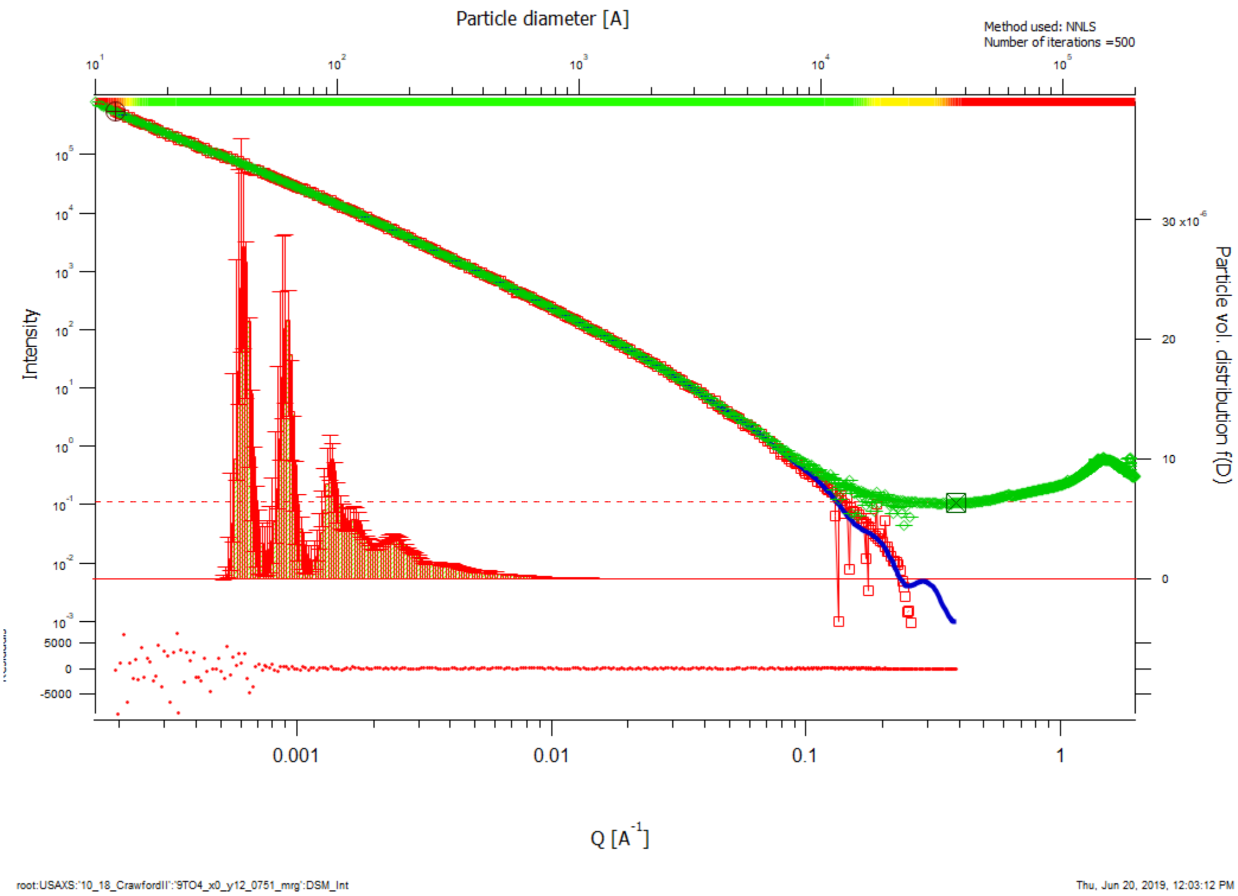

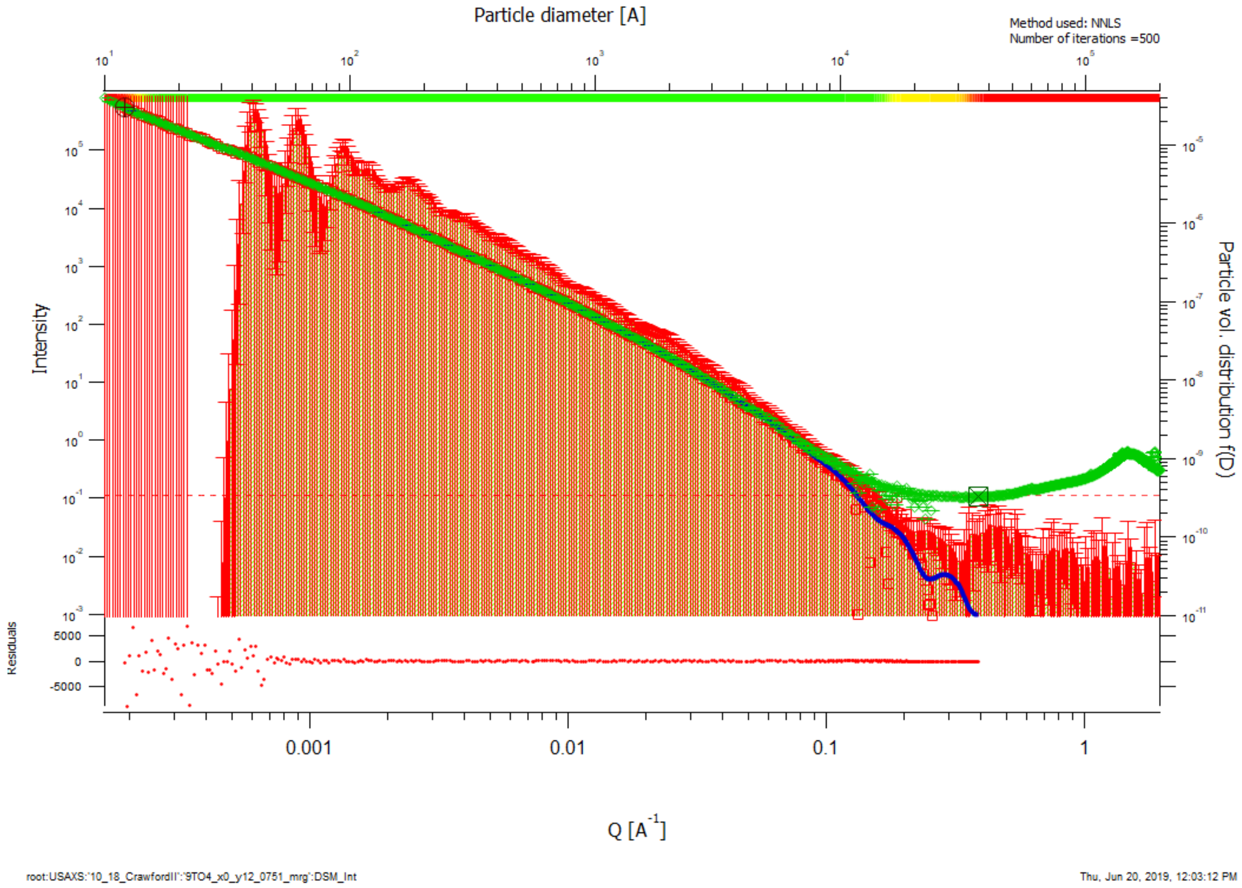
Particle diameter [A]
Method used: NNLS
Number of iterations =500
Intensity
Particle vol. distribution f(D)
Residuals
Q [A^{-1}]
0.001
0.01
0.1
1
root:USAXS:'10_18_CrawfordII':'9TO4_x0_y12_0751_mrg':DSM_Int
Thu, Jun 20, 2019, 12:03:12 PM

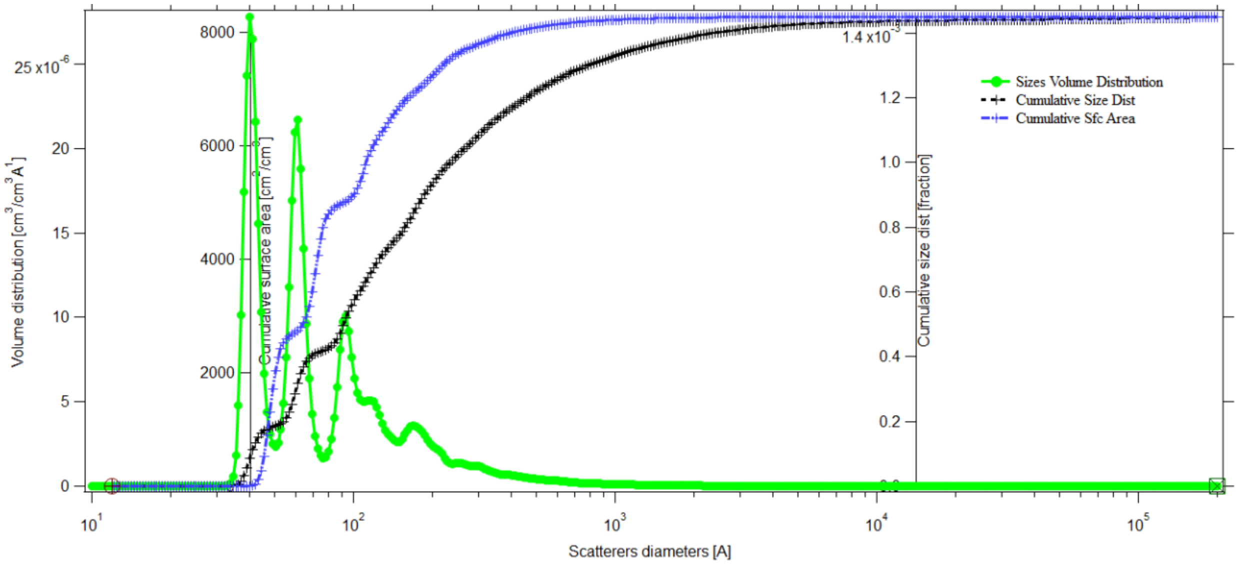
Sizes Volume Distribution
Cumulative Size Dist
Cumulative Sfc Area
Volume distribution [cm^3/cm^{3}A^1]
Cumulative surface area [cm^2/cm^3]
Cumulative size dist [fraction]
Scatterers diameters [A]

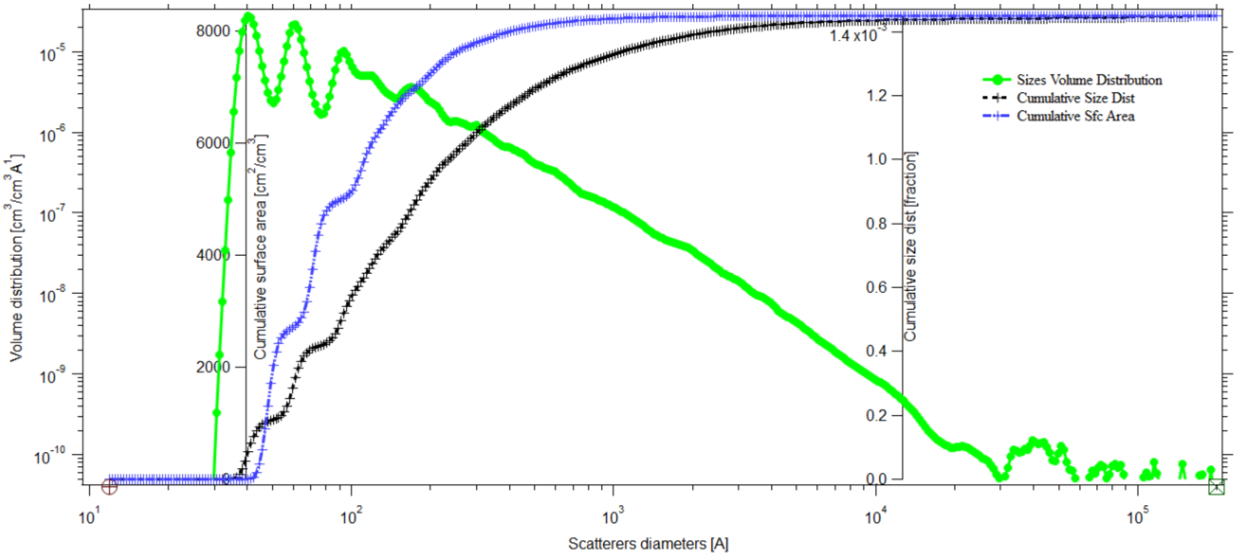

18. 9TO4_x0_y33_R_0750

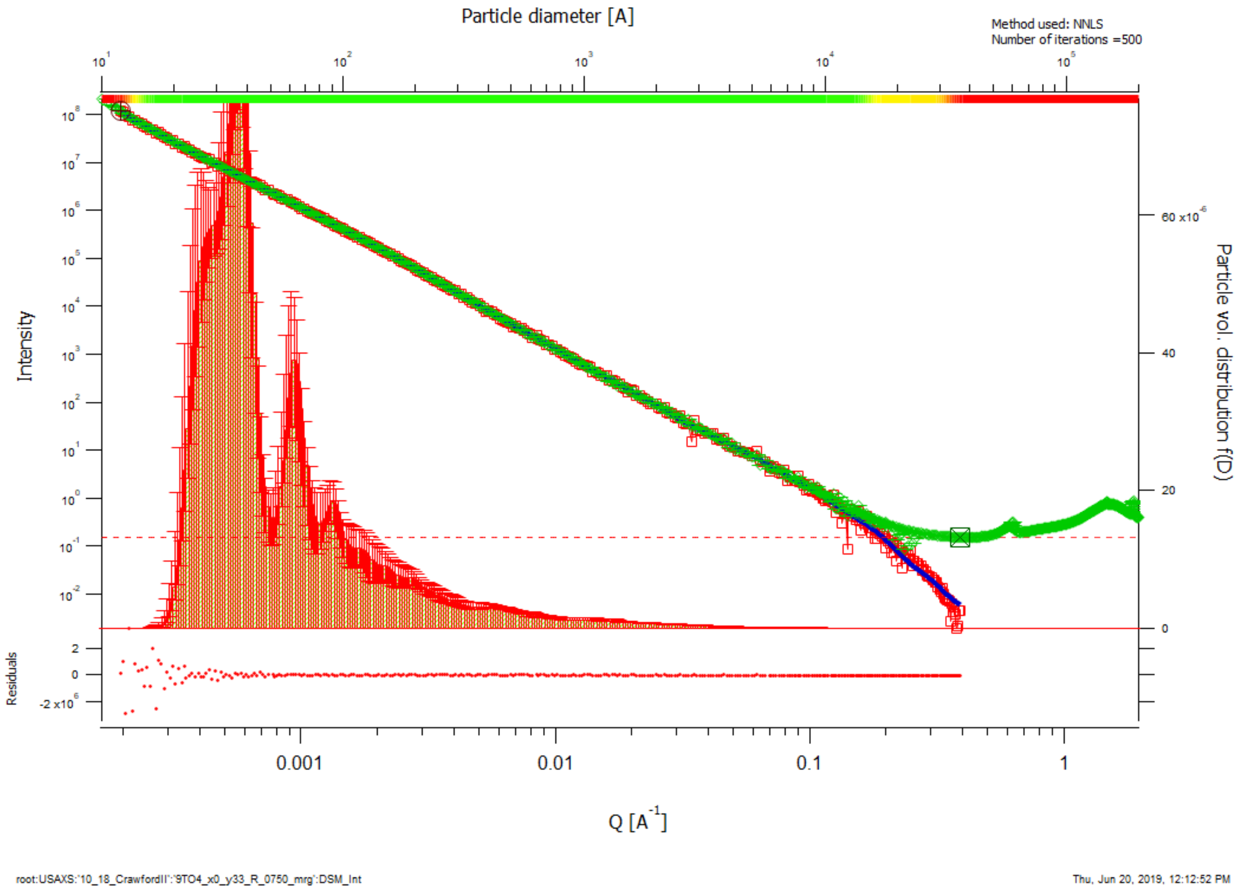

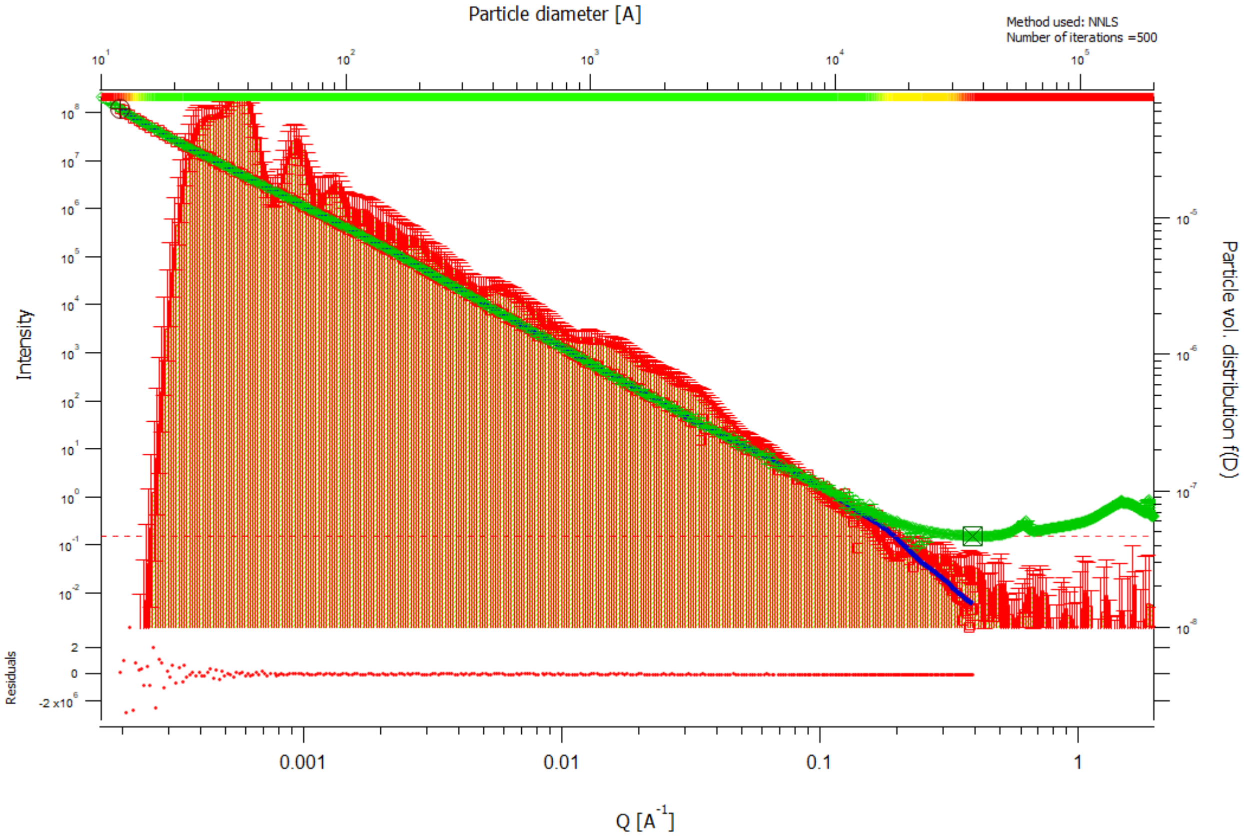

root:USAXS:'10_18_CrawfordII':'9TO4_x0_y33_R_0750_mrg':DSM_Int

Thu, Jun 20, 2019, 12:12:52 PM

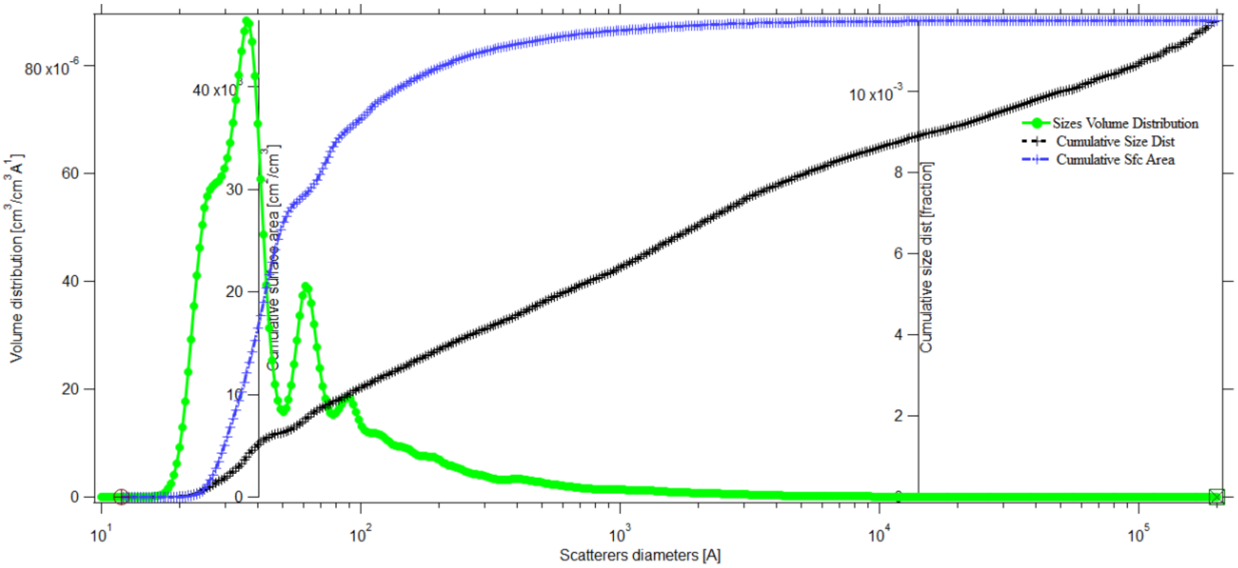

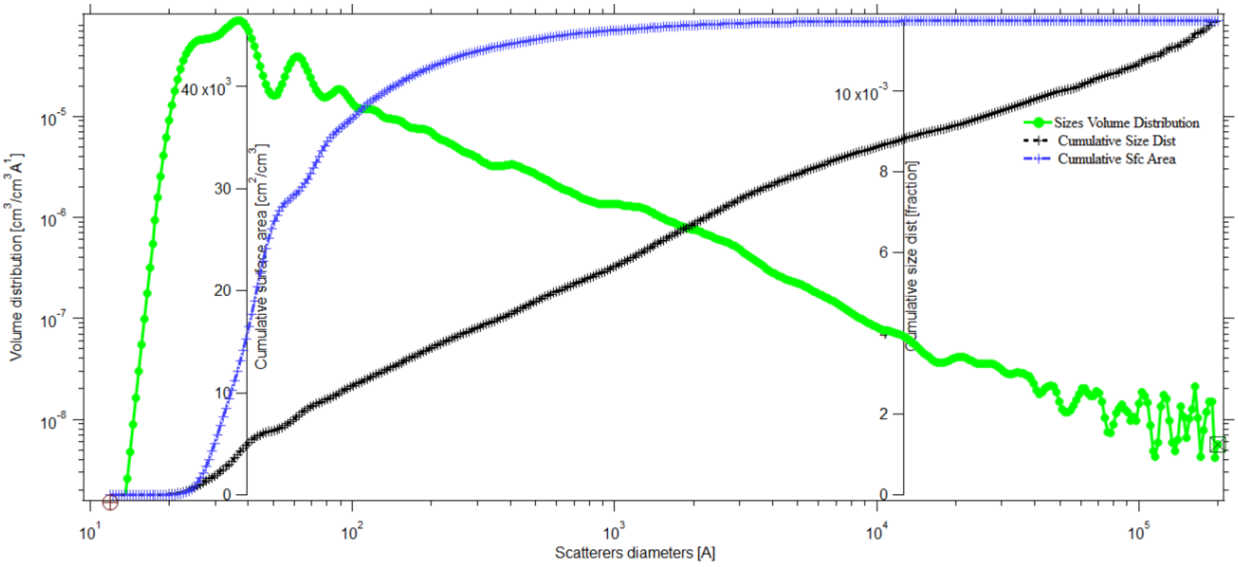

19. 9TO4_x0_y33_0749

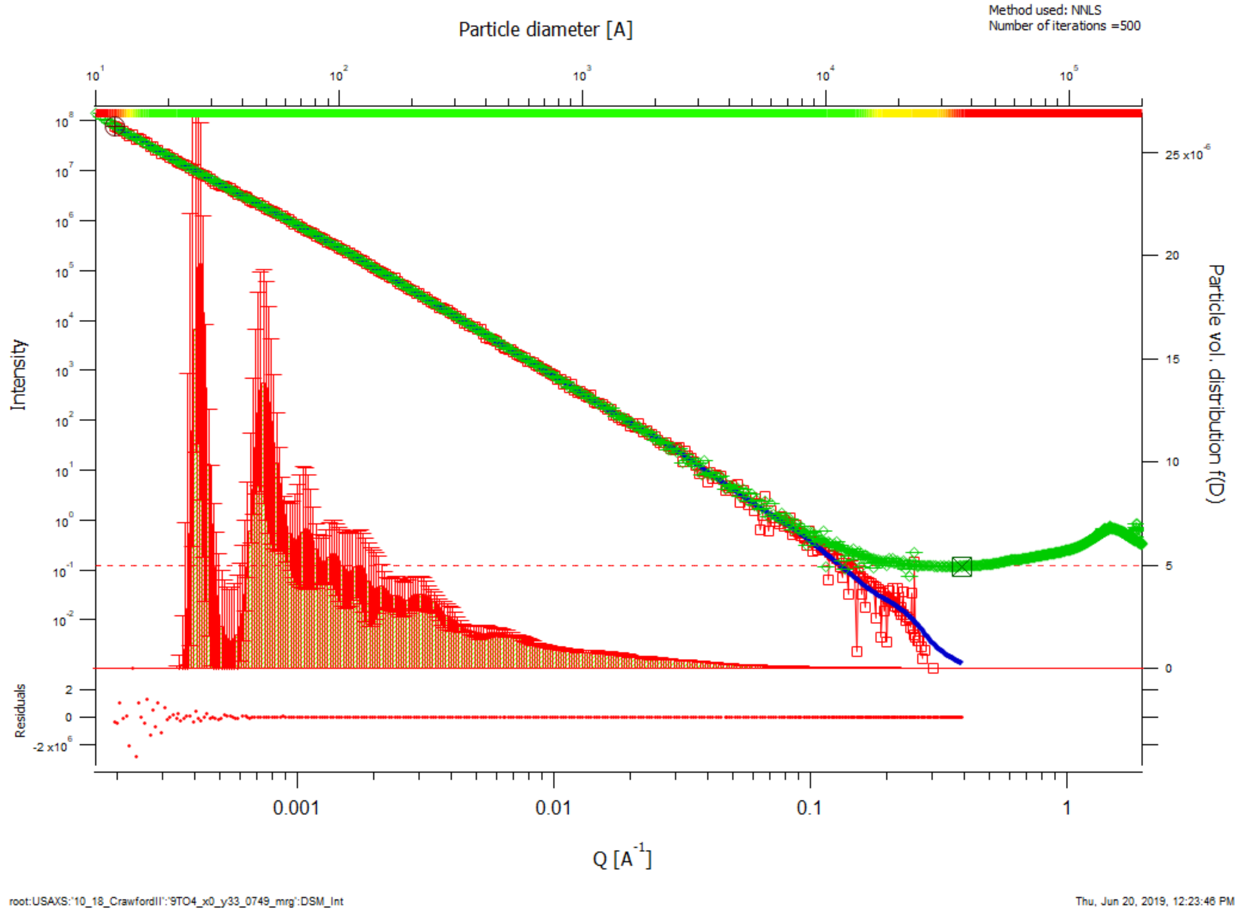

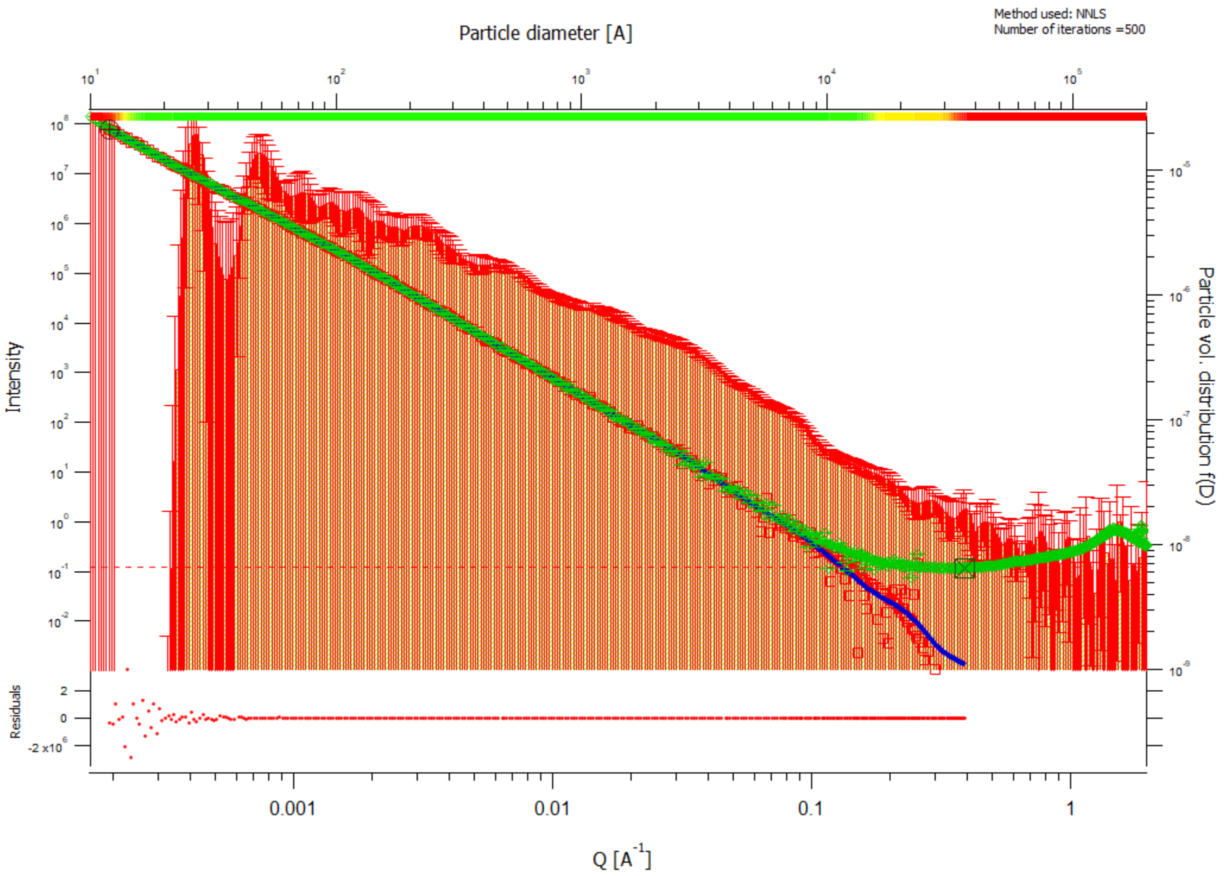

root:USAXS:'10_18_CrawfordII':'9TO4_x0_y33_0749_mrg':DSM_Int

Thu, Jun 20, 2019, 12:23:46 PM

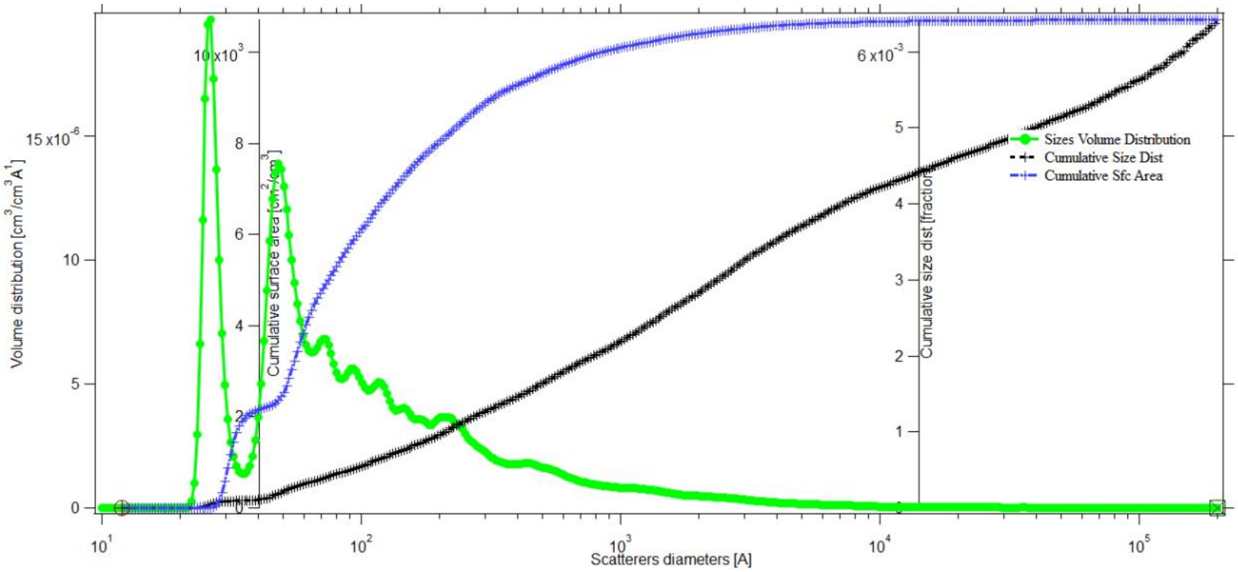

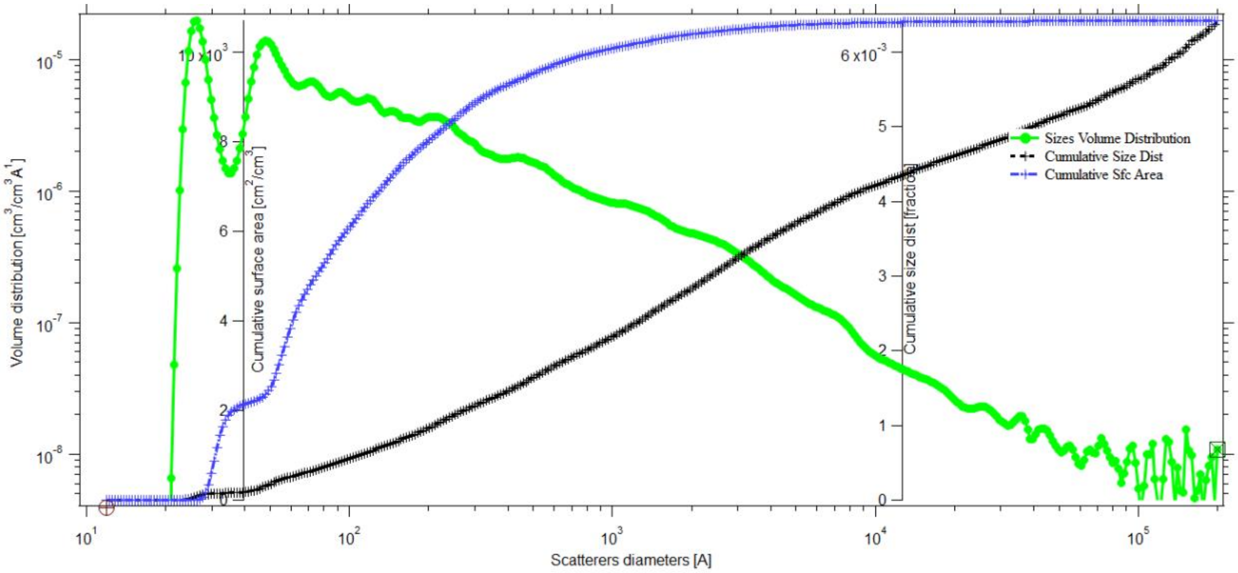

20. 9TO4_x0_y41_R_0748

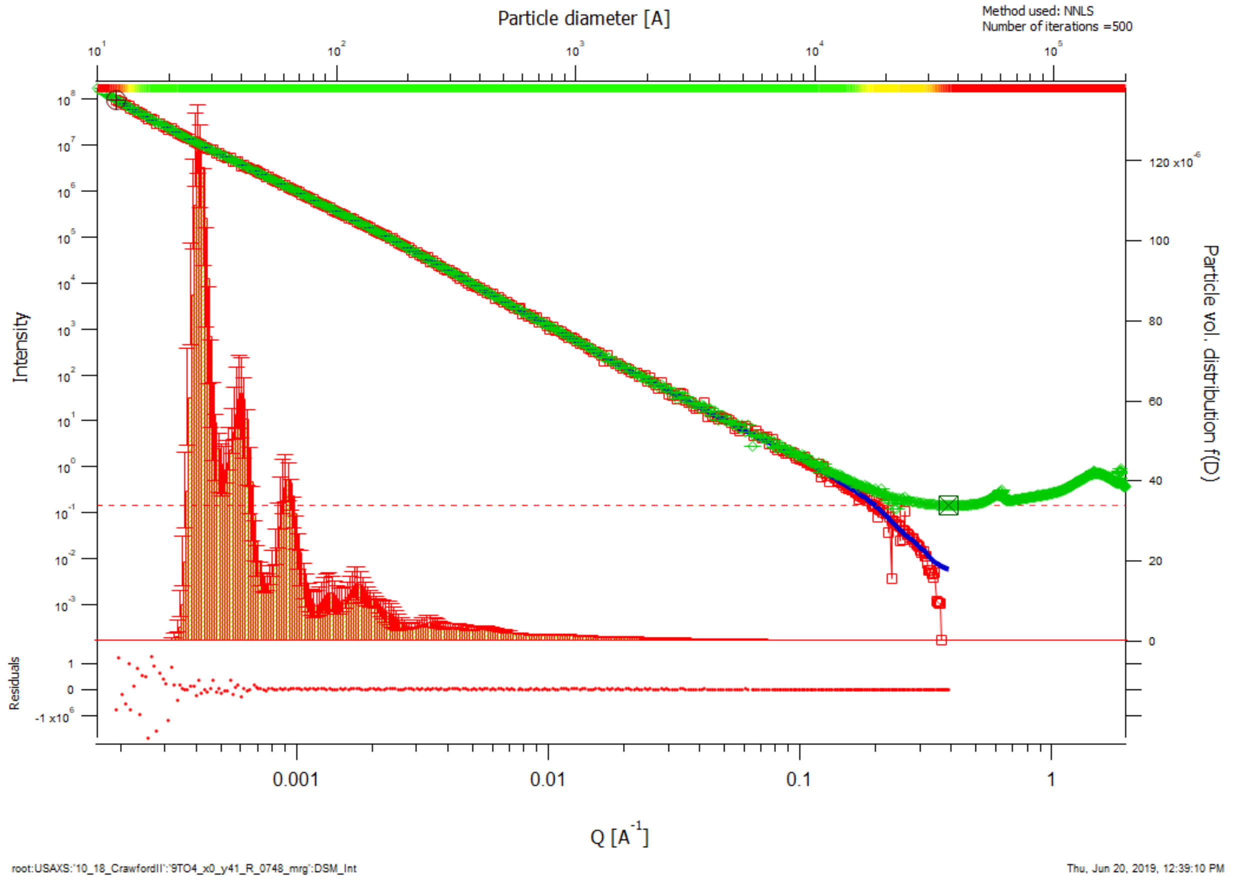

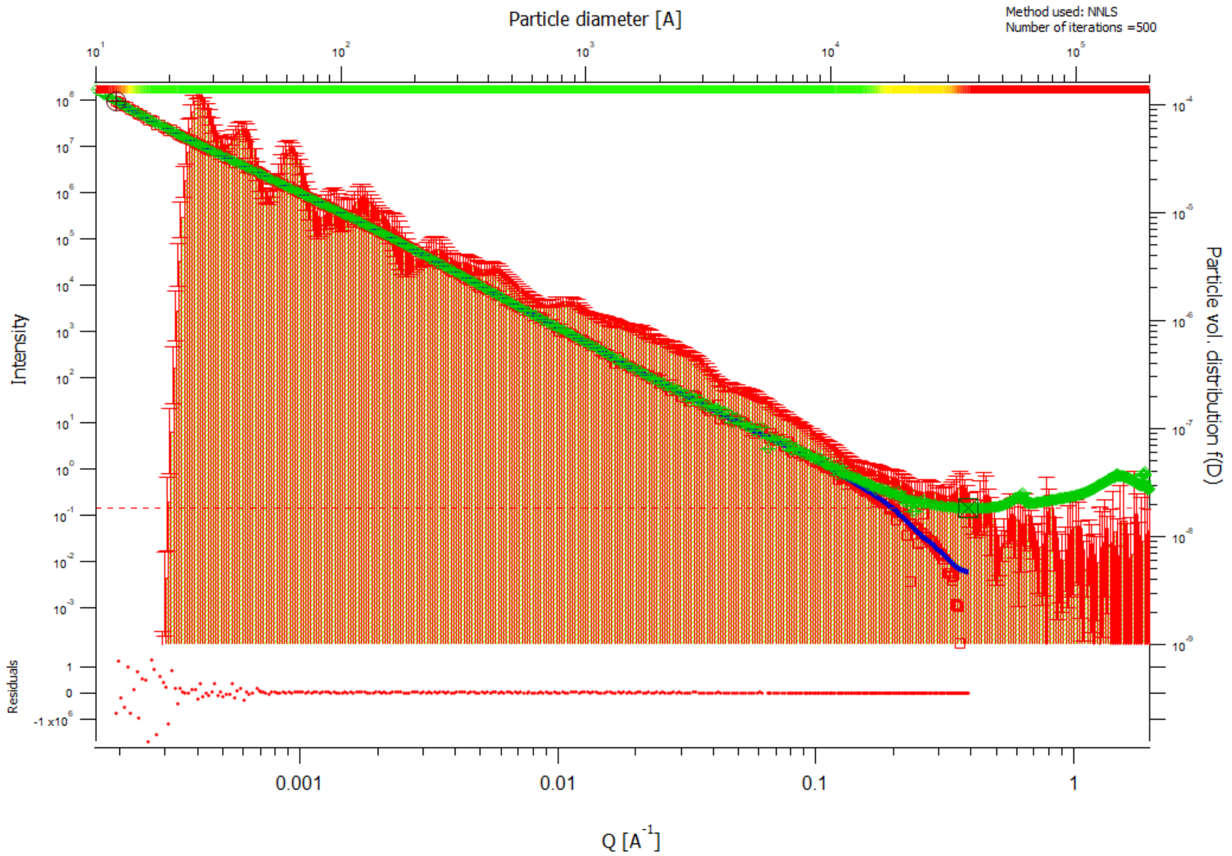

root:USAXS:'10_18_CrawfordII':'9TO4_x0_y41_R_0748_mrg':DSM_Int

Thu, Jun 20, 2019, 12:39:10 PM

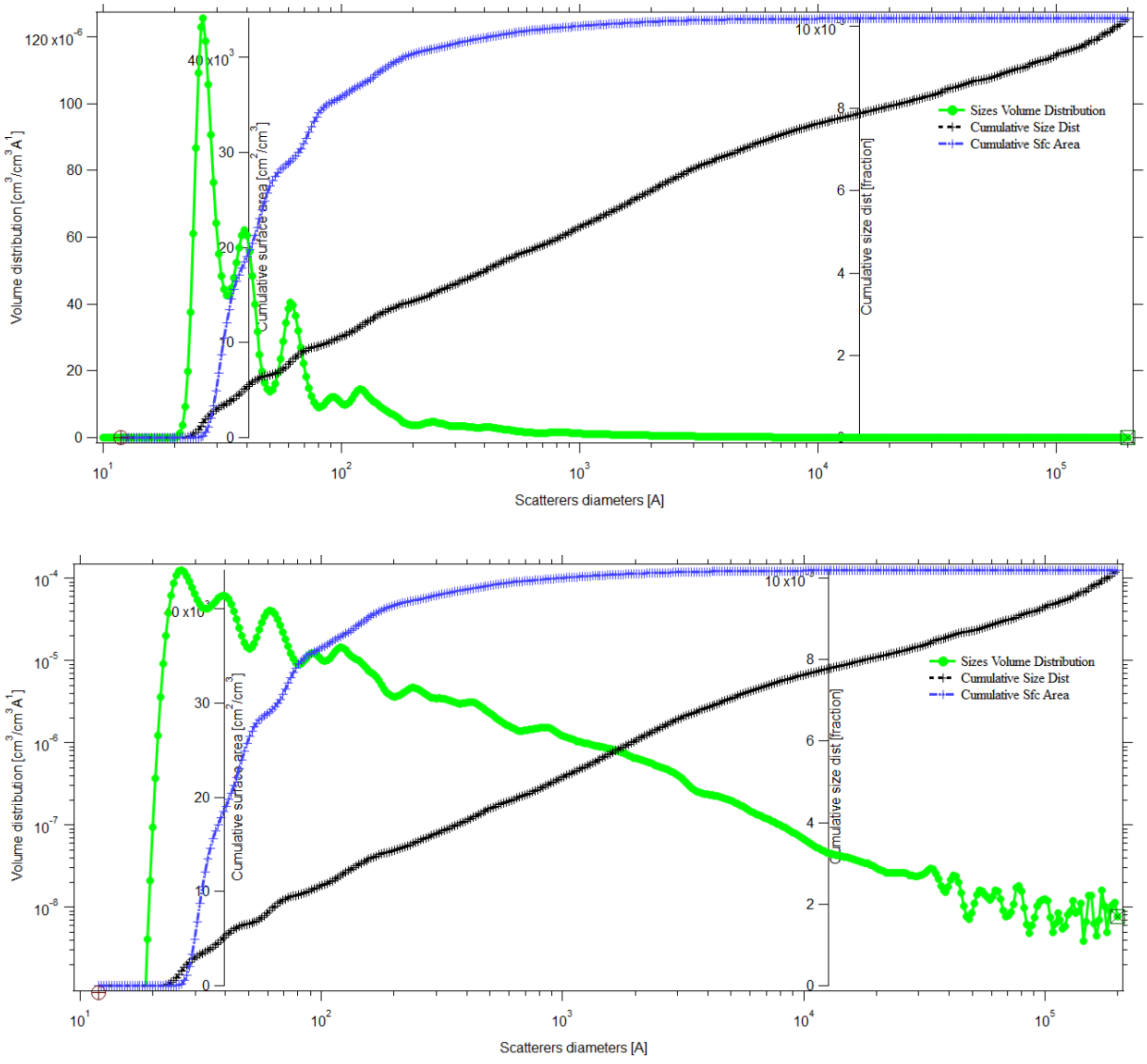

21. 9TO4_x0_y41_0747

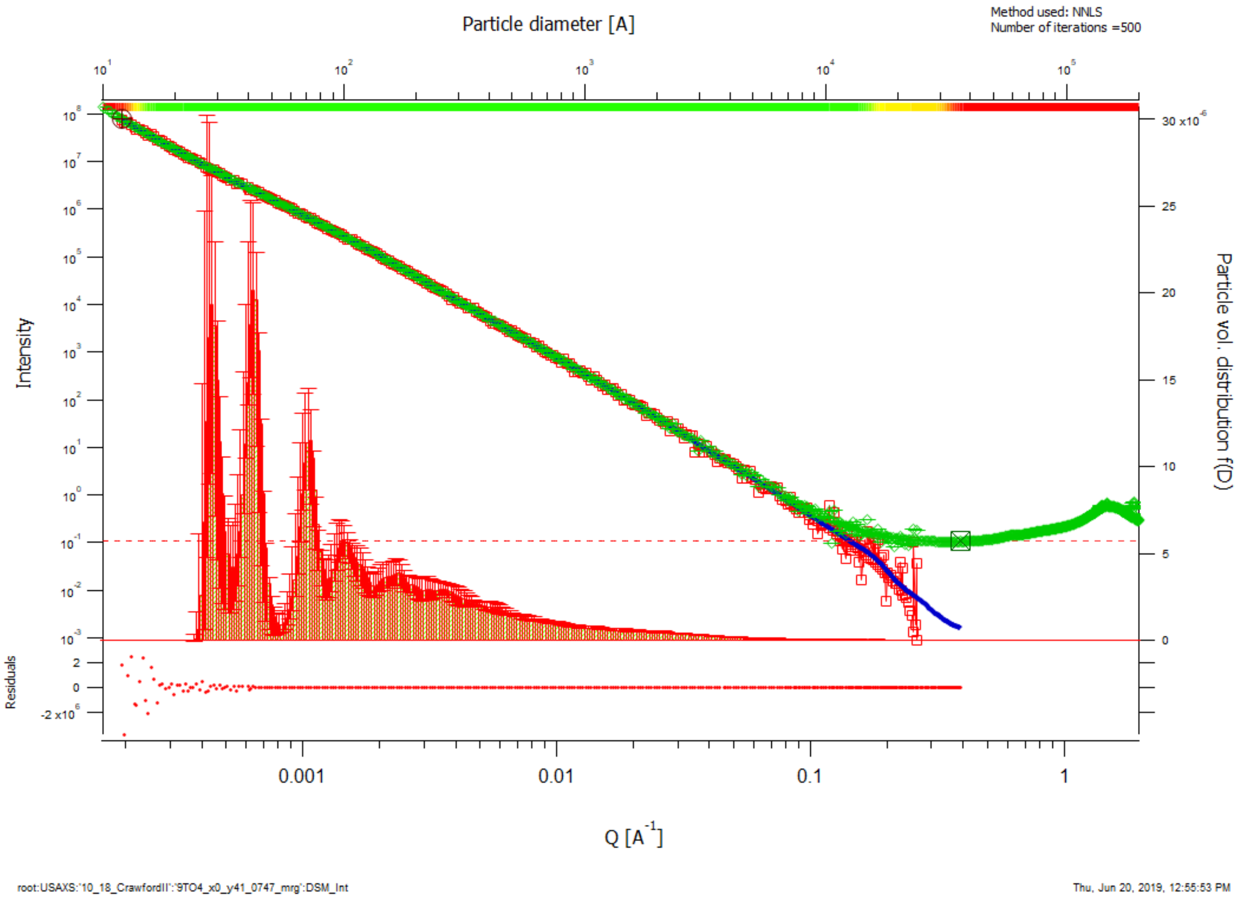
Particle diameter [A]
Method used: NNLS
Number of iterations =500
10^1
10^2
10^3
10^4
10^5
Intensity
10^8
10^7
10^6
10^5
10^4
10^3
10^2
10^1
10^0
10^{-1}
10^{-2}
10^{-3}
Particle vol. distribution f(D)
30×10^{-6}
25
20
15
10
5
0
Residuals
2
0
-2×10^{-6}
0.001
0.01
0.1
1
Q [A^{-1}]
root:USAXS:'10_18_CrawfordII':'9TO4_x0_y41_0747_mrg':DSM_Int
Thu, Jun 20, 2019, 12:55:53 PM

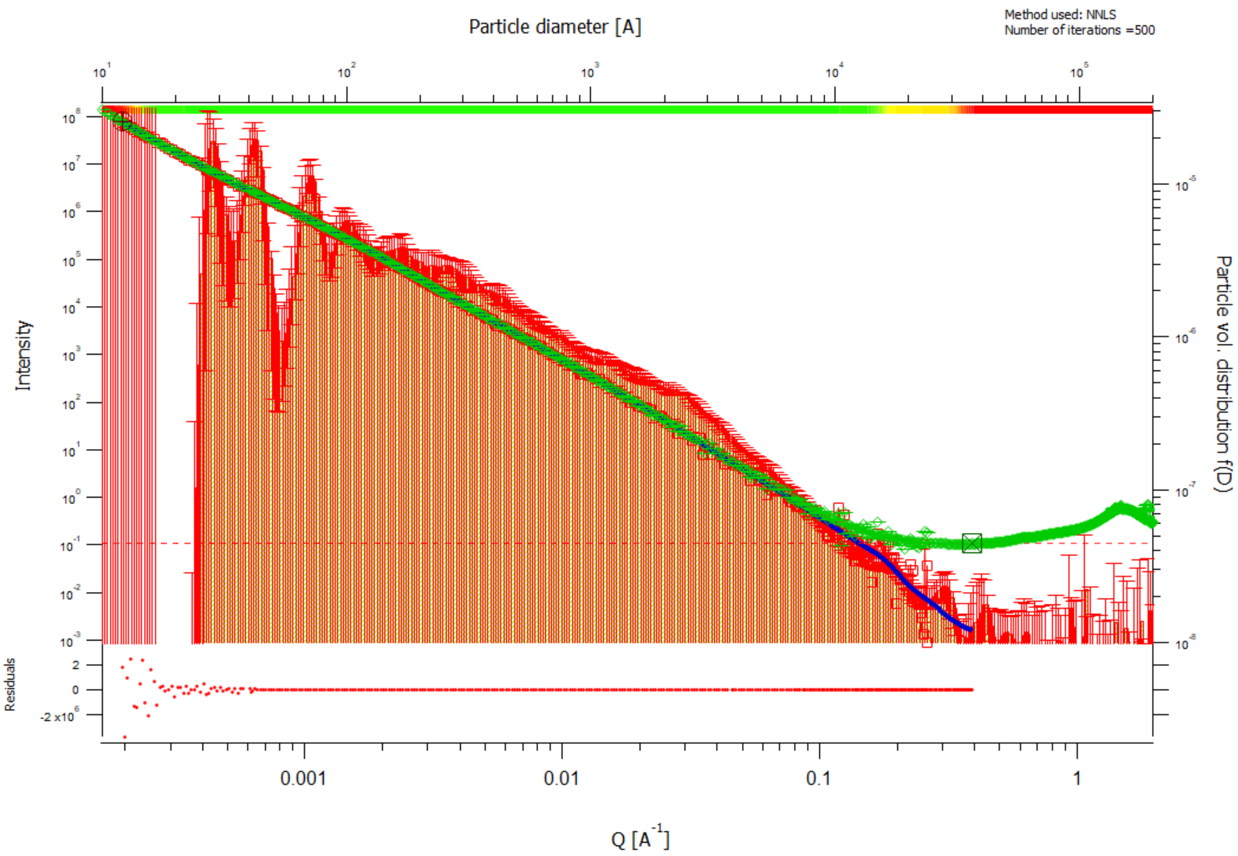

root:USAXS:'10_18_CrawfordII':'9TO4_x0_y41_0747_mrg':DSM_Int

Thu, Jun 20, 2019, 12:55:53 PM

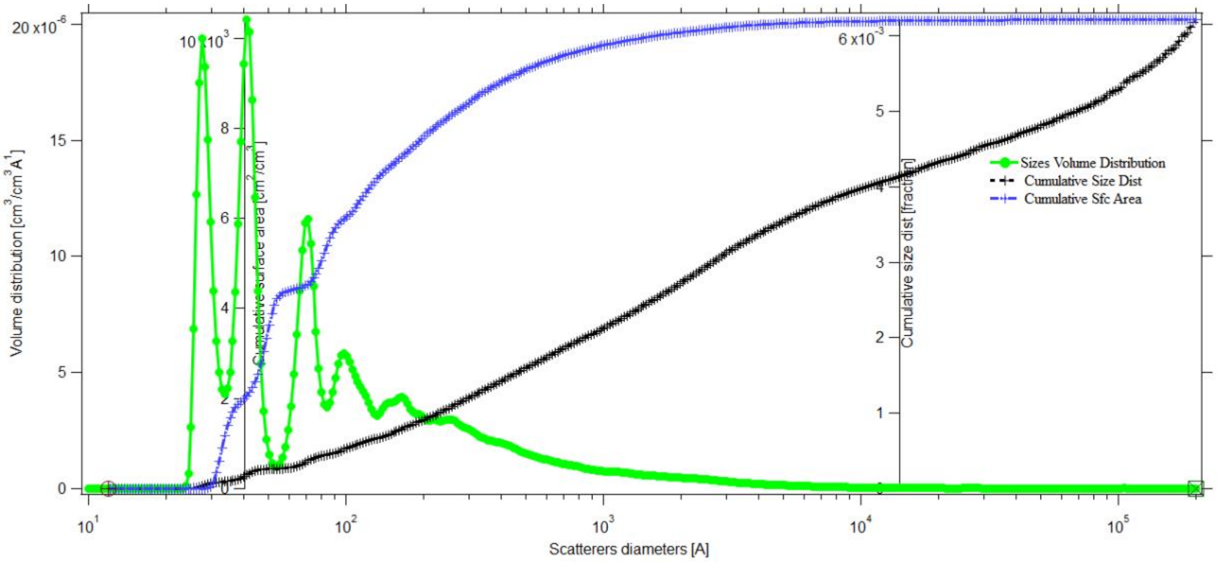

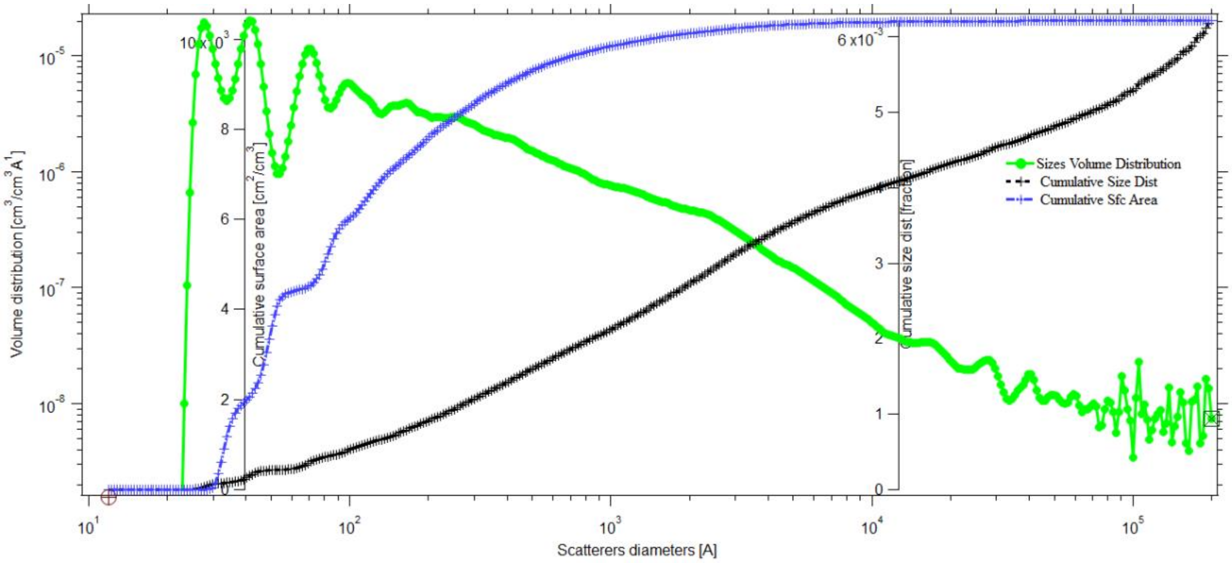

22. 9TO4_x14_y_6_R_0764

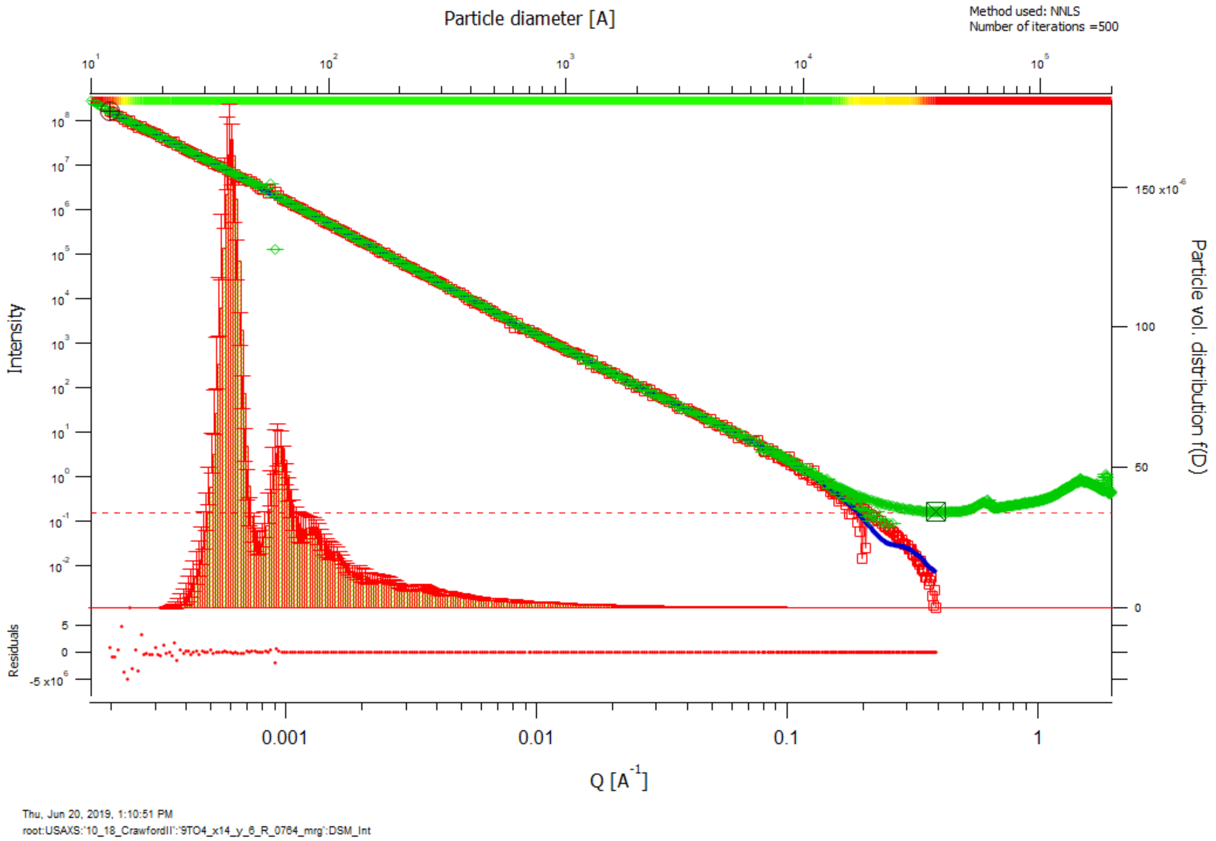

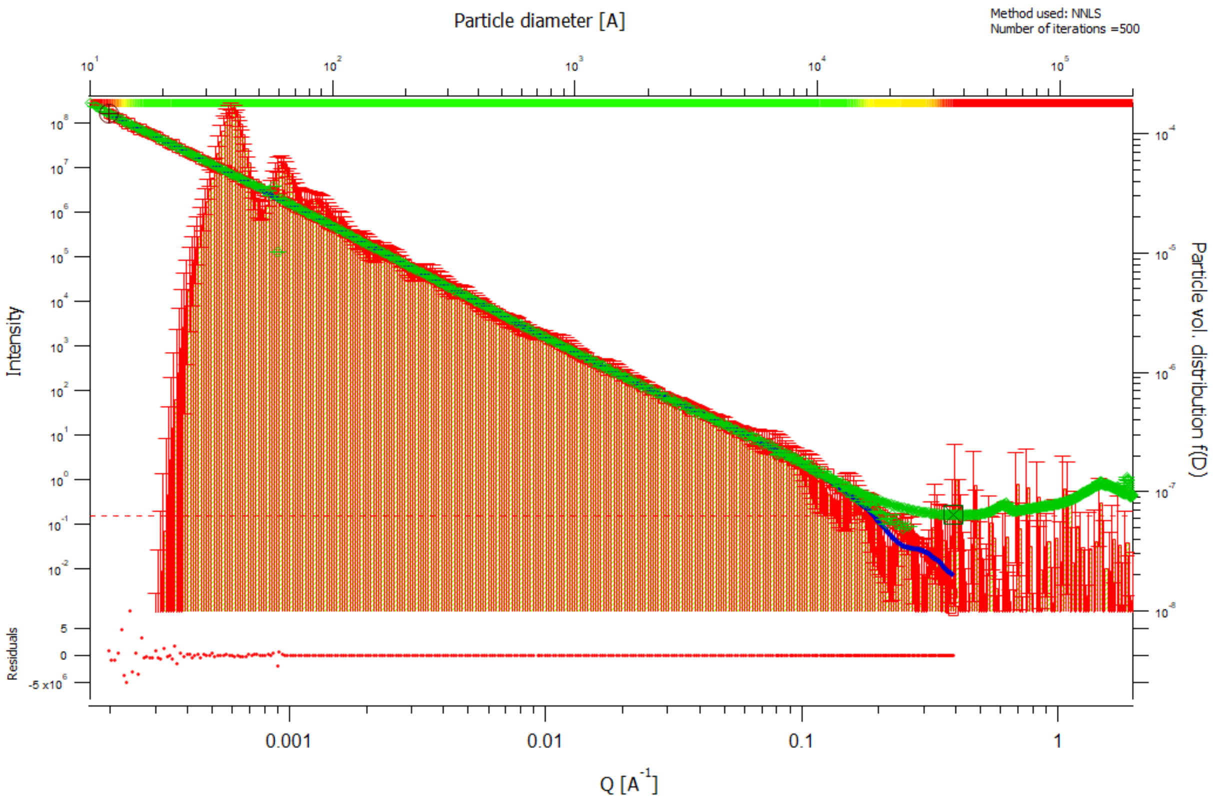

Thu, Jun 20, 2019, 1:10:51 PM
root:USAXS:'10_18_CrawfordII':'9TO4_x14_y_6_R_0764_mrg':DSM_Int

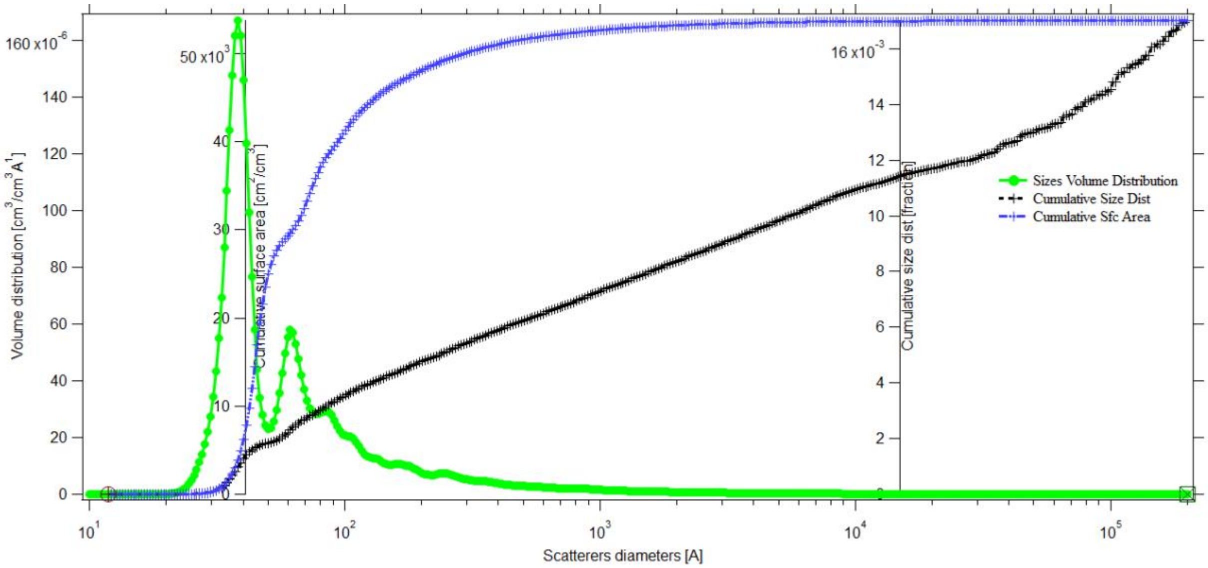

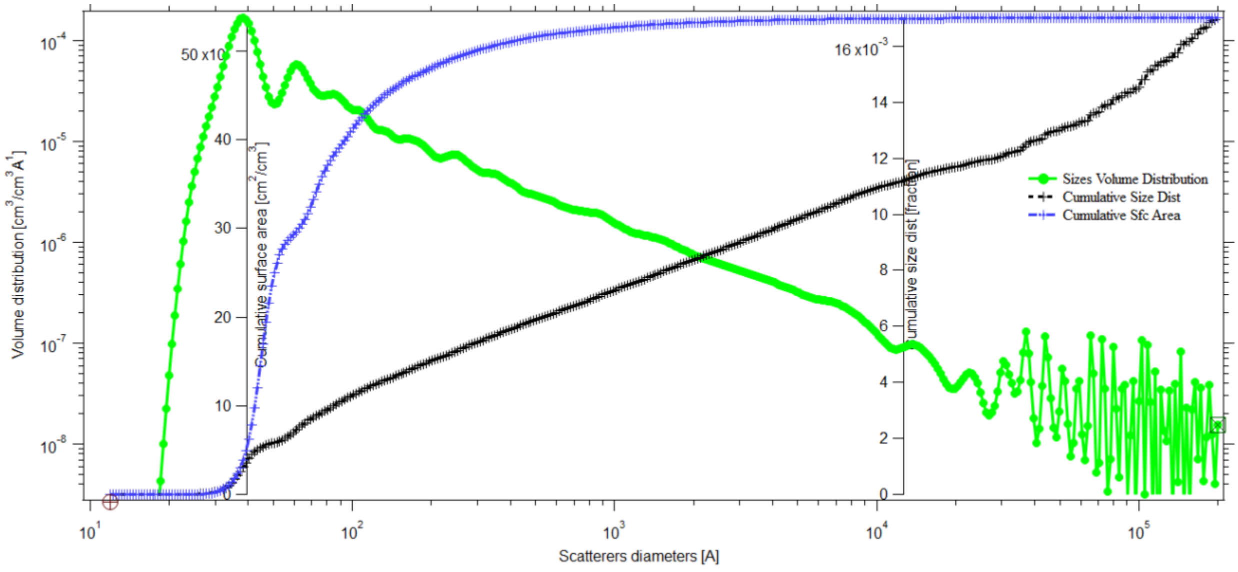

23. 9TO4_x14_y34_0757

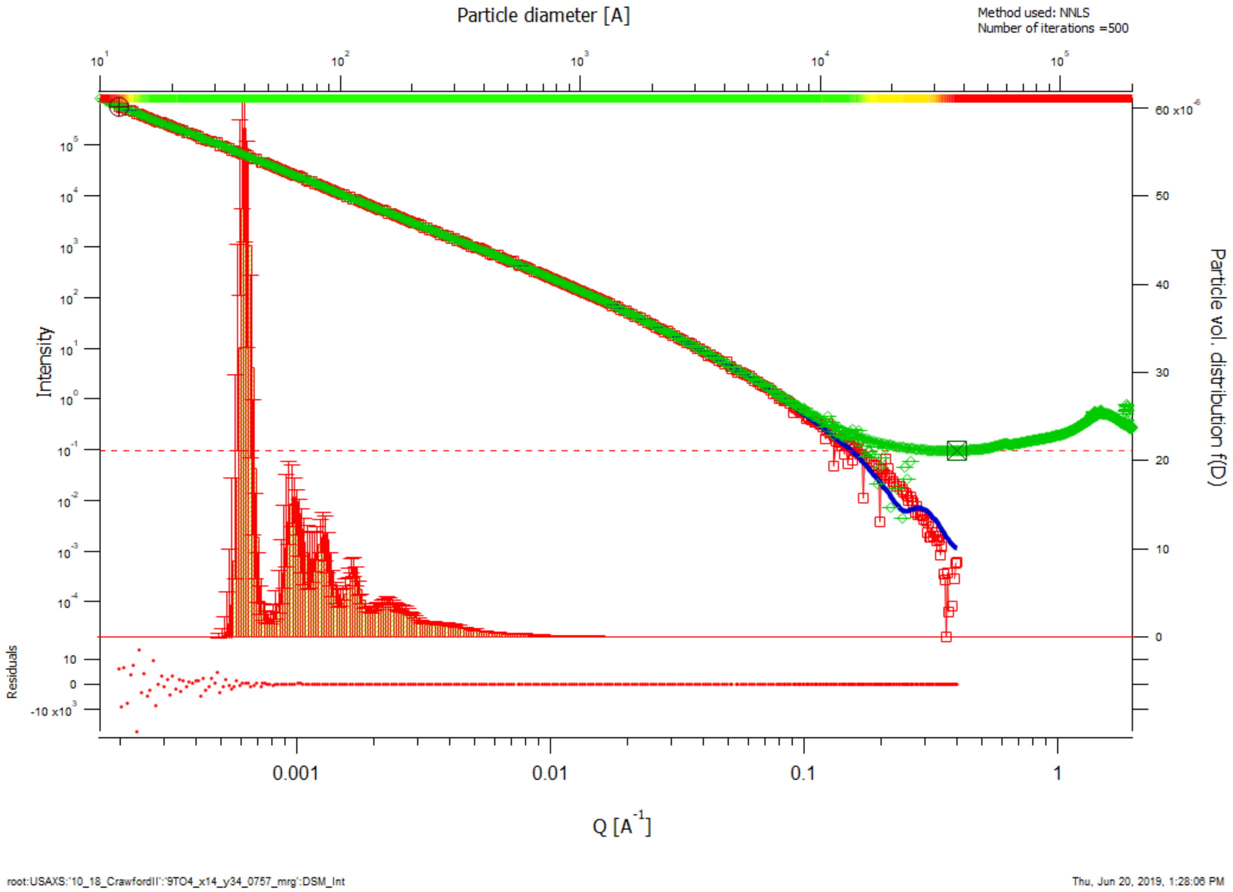

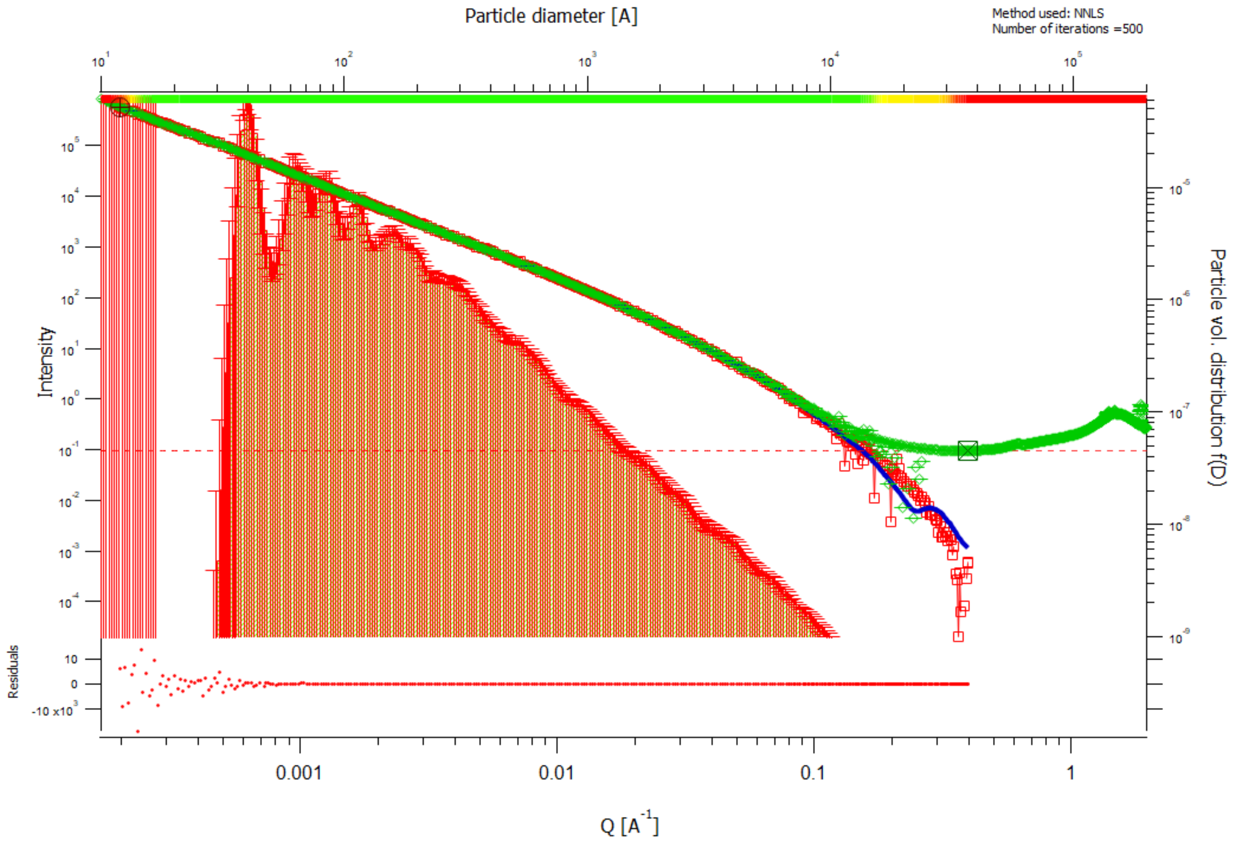

root:USAXS:'10_18_CrawfordII':'9TO4_x14_y34_0757_mrg':DSM_Int

Thu, Jun 20, 2019, 1:28:06 PM

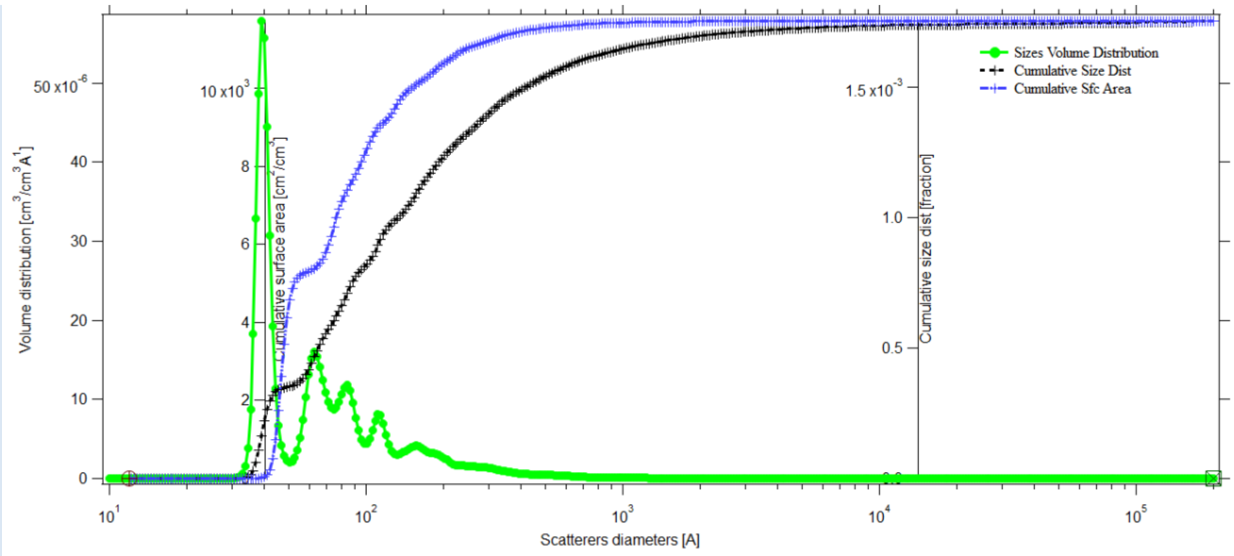

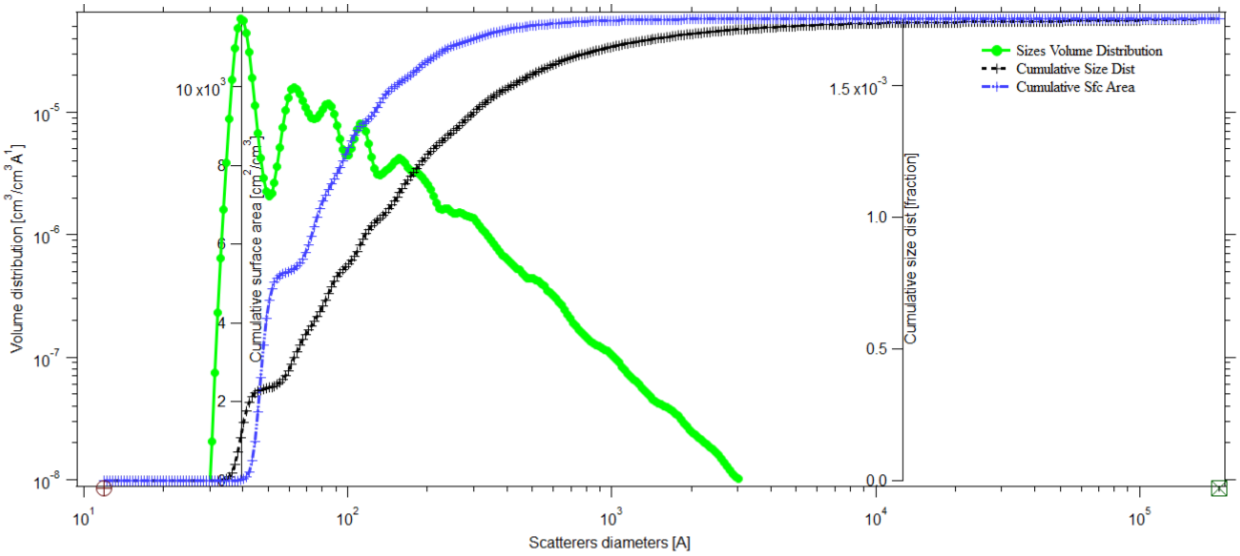

24. 9UL_x42_y_38_R_0734

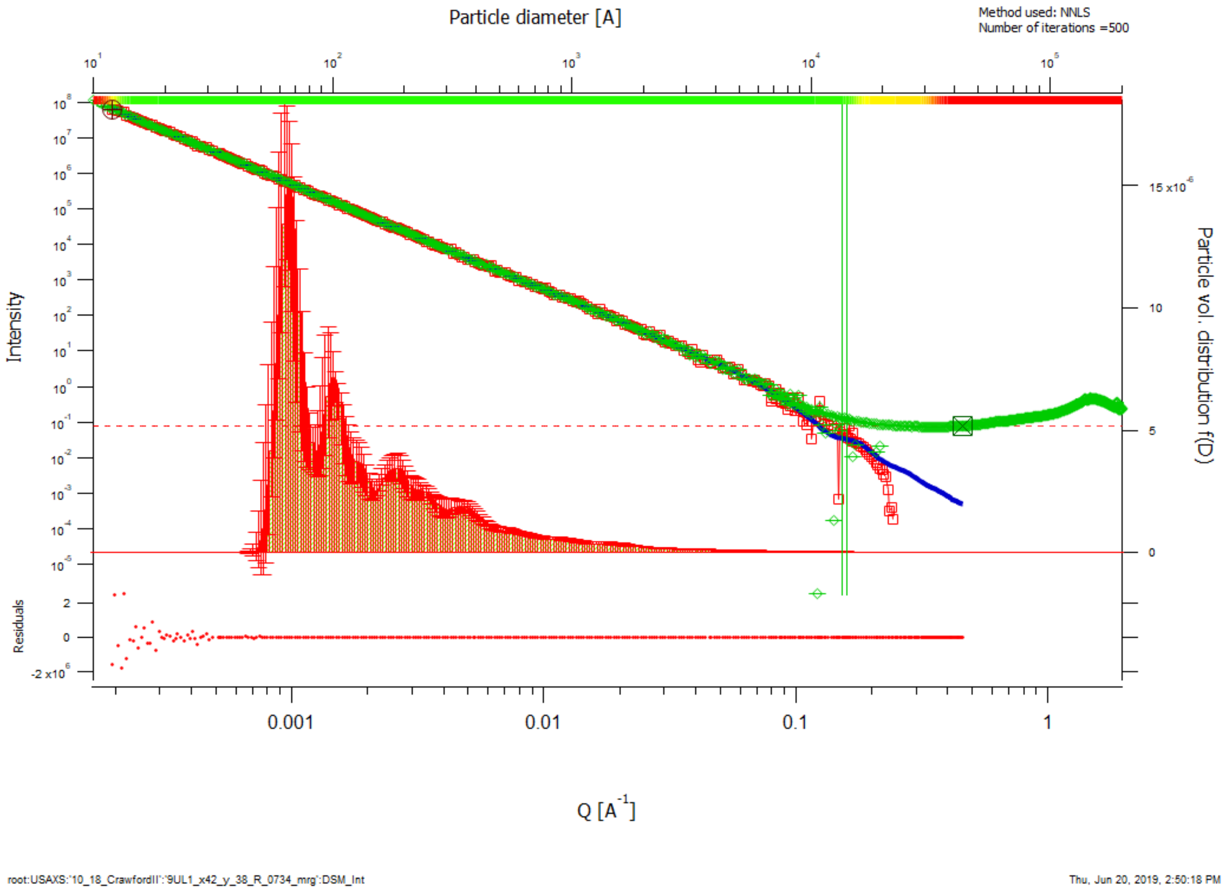

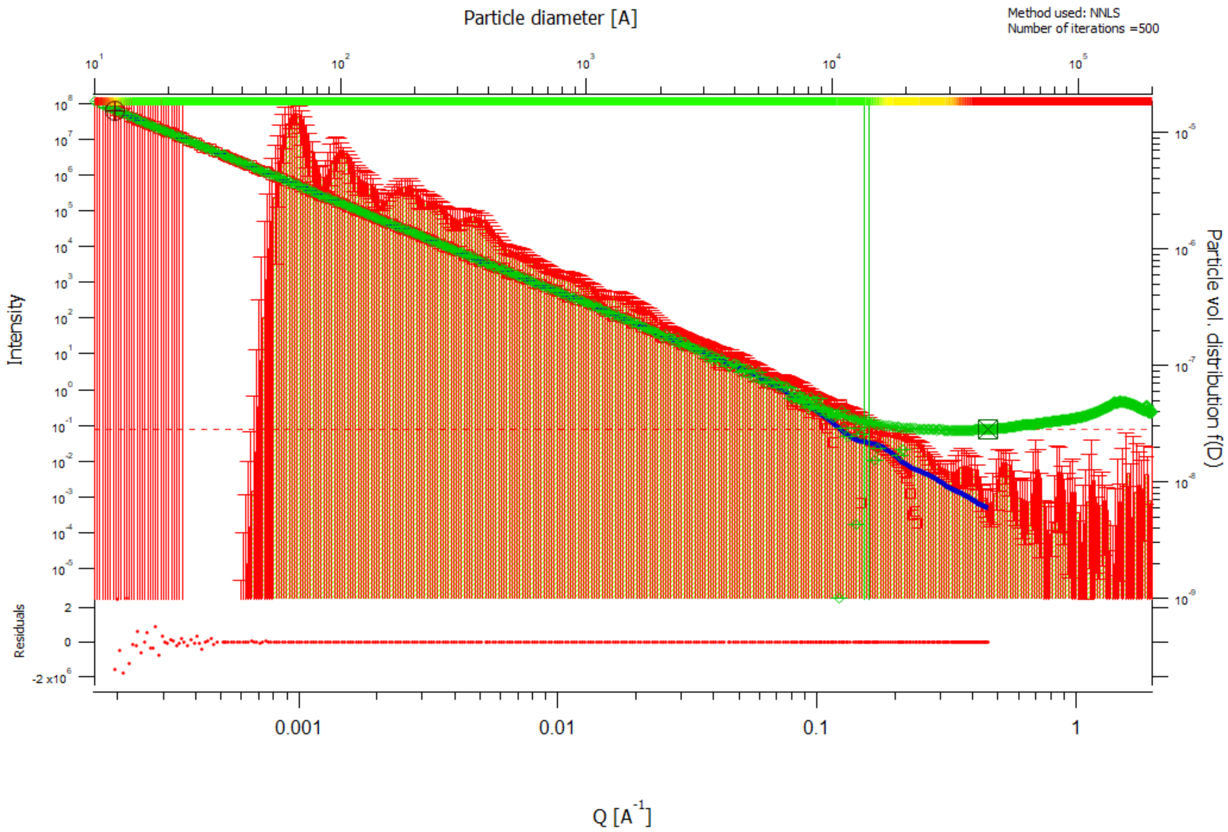

root:USAXS:'10_18_CrawfordII':'9UL1_x42_y_38_R_0734_mrg':DSM_Int

Thu, Jun 20, 2019, 2:50:18 PM

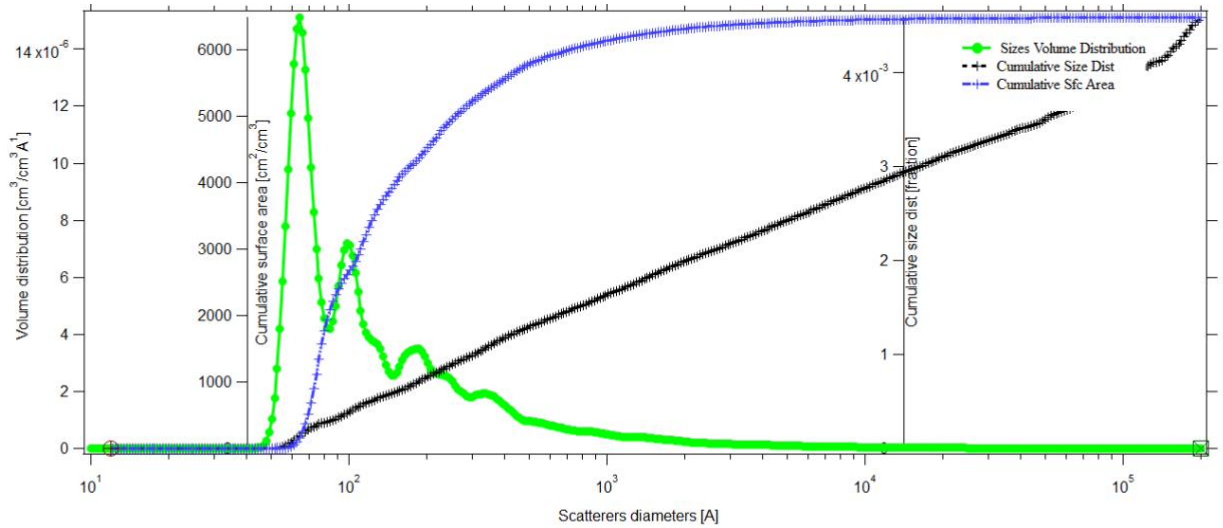

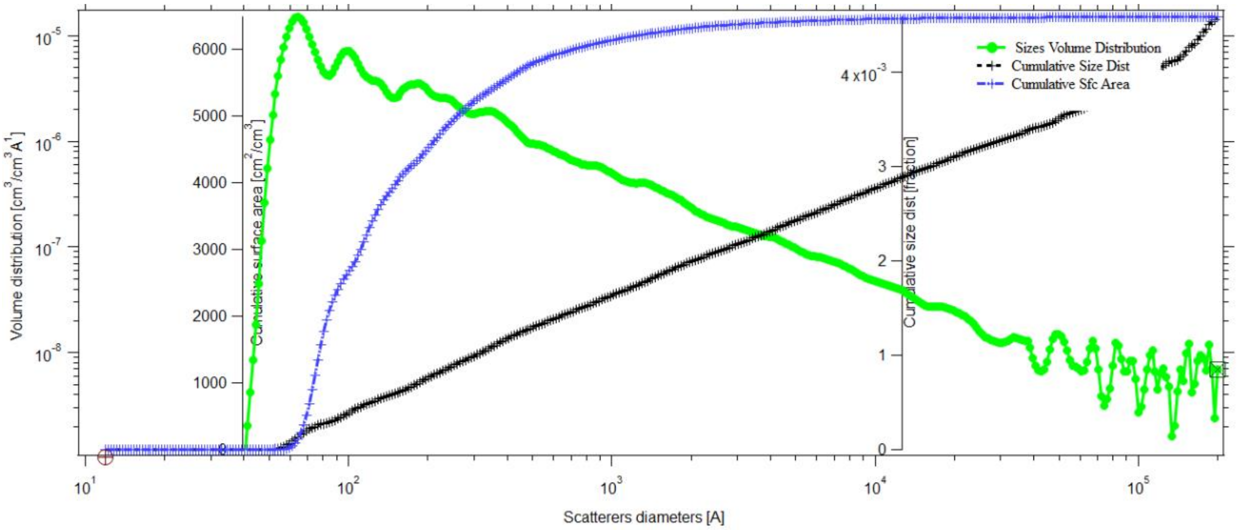

25. 9UL_x42_y0_R_0730

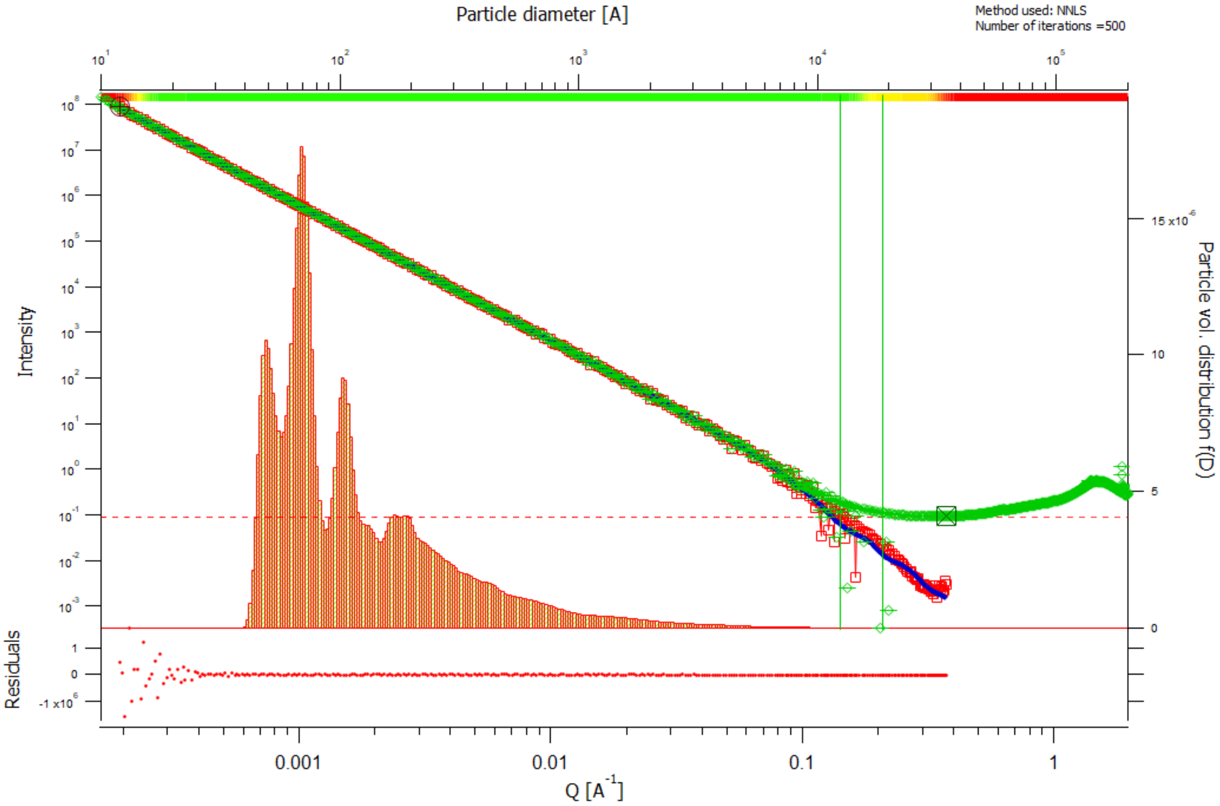

Thu, Jun 20, 2019, 3:14:26 PM
root:USAXS:'10_18_CrawfordII':'9UL1_x42_y0_R_0730_mrg':DSM_Int

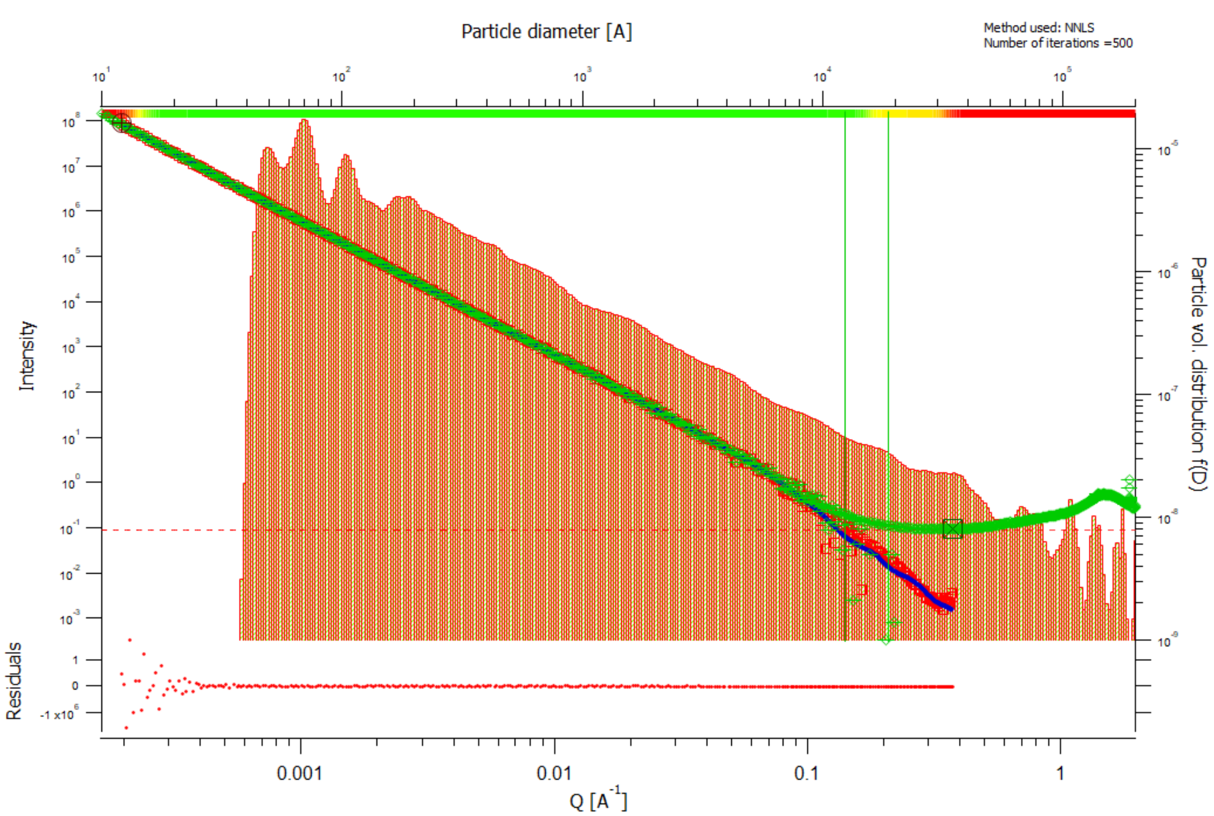

Thu, Jun 20, 2019, 3:14:26 PM
root:USAXS:'10_18_CrawfordII':'9UL1_x42_y0_R_0730_mrg':DSM_Int

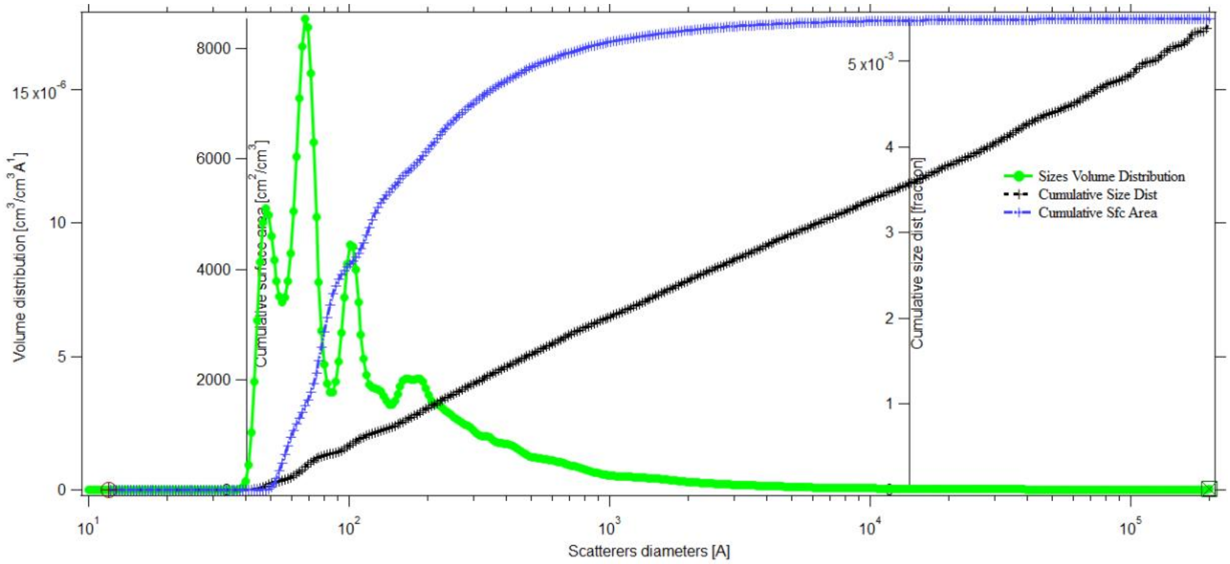

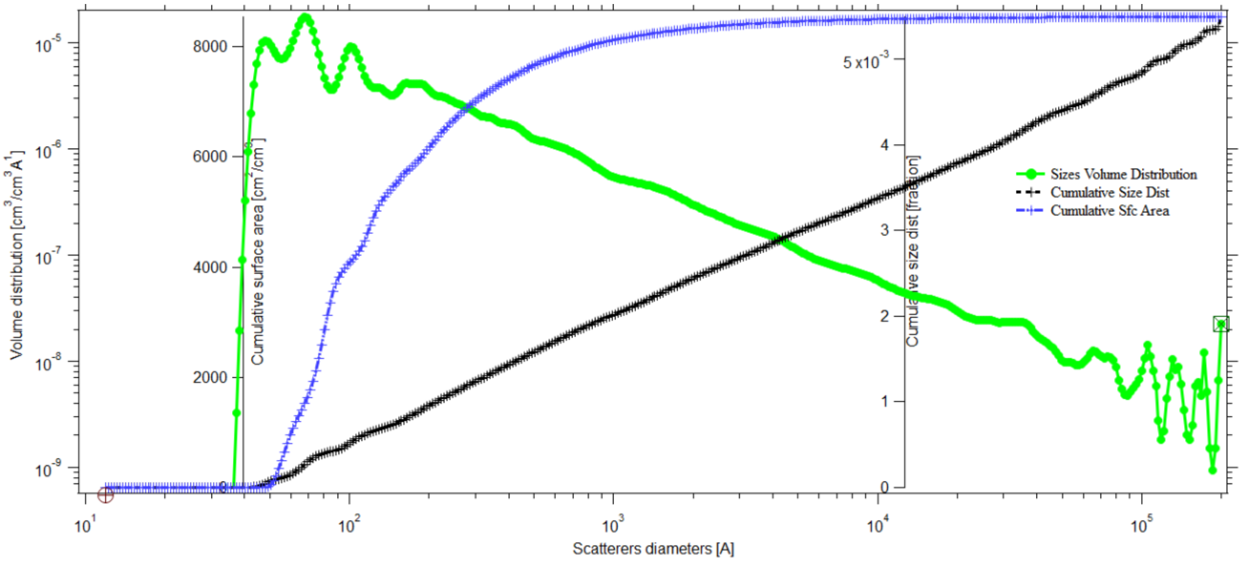

26. 9UL_x62_y38_R_0732

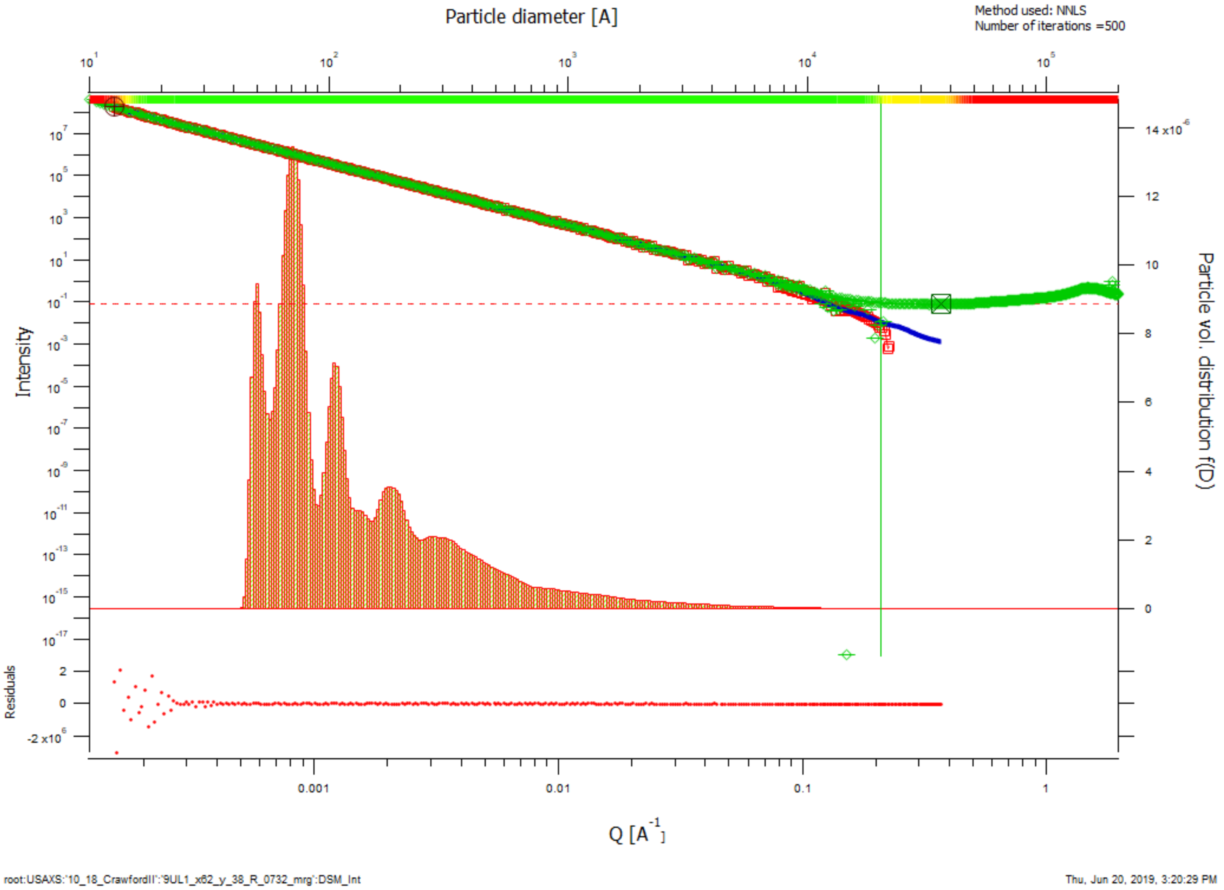

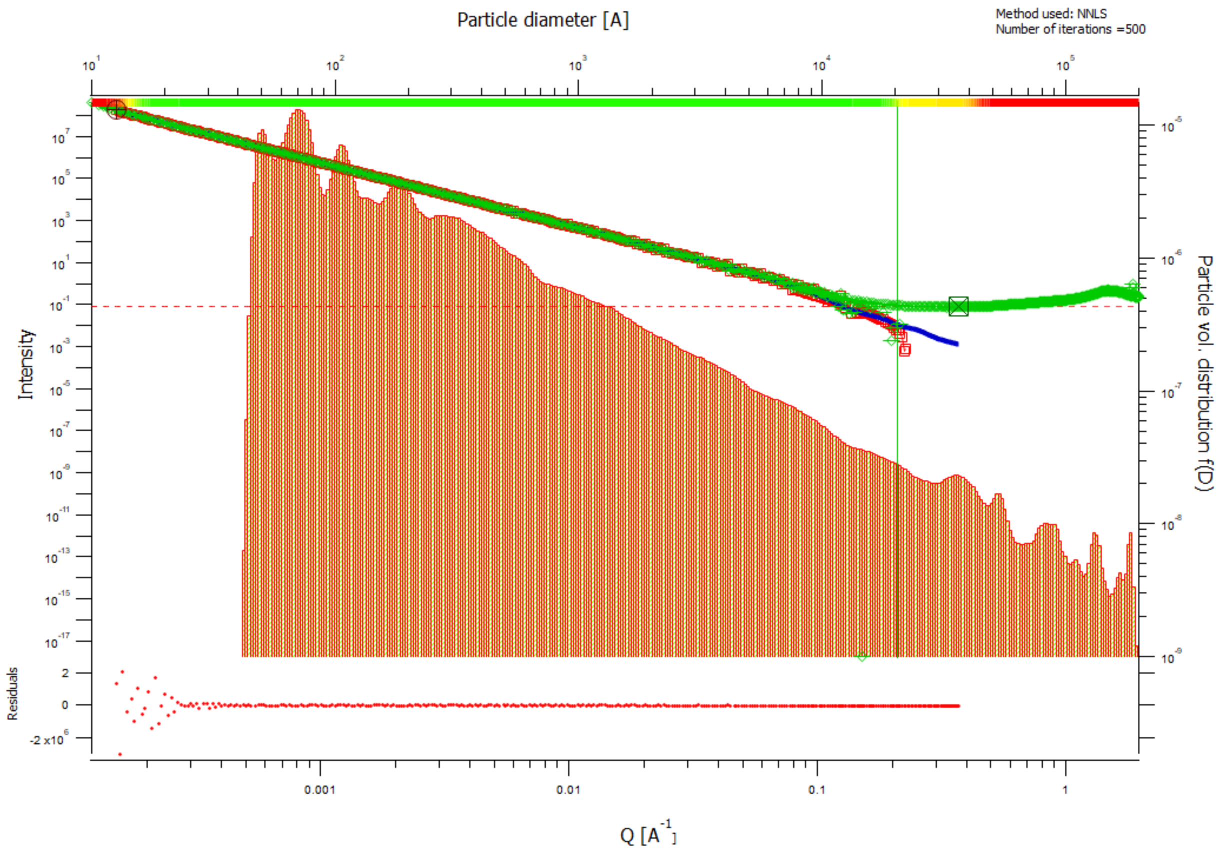

root:USAXS:'10_18_CrawfordII':'9UL1_x62_y_38_R_0732_mrg':DSM_Int

Thu, Jun 20, 2019, 3:20:29 PM

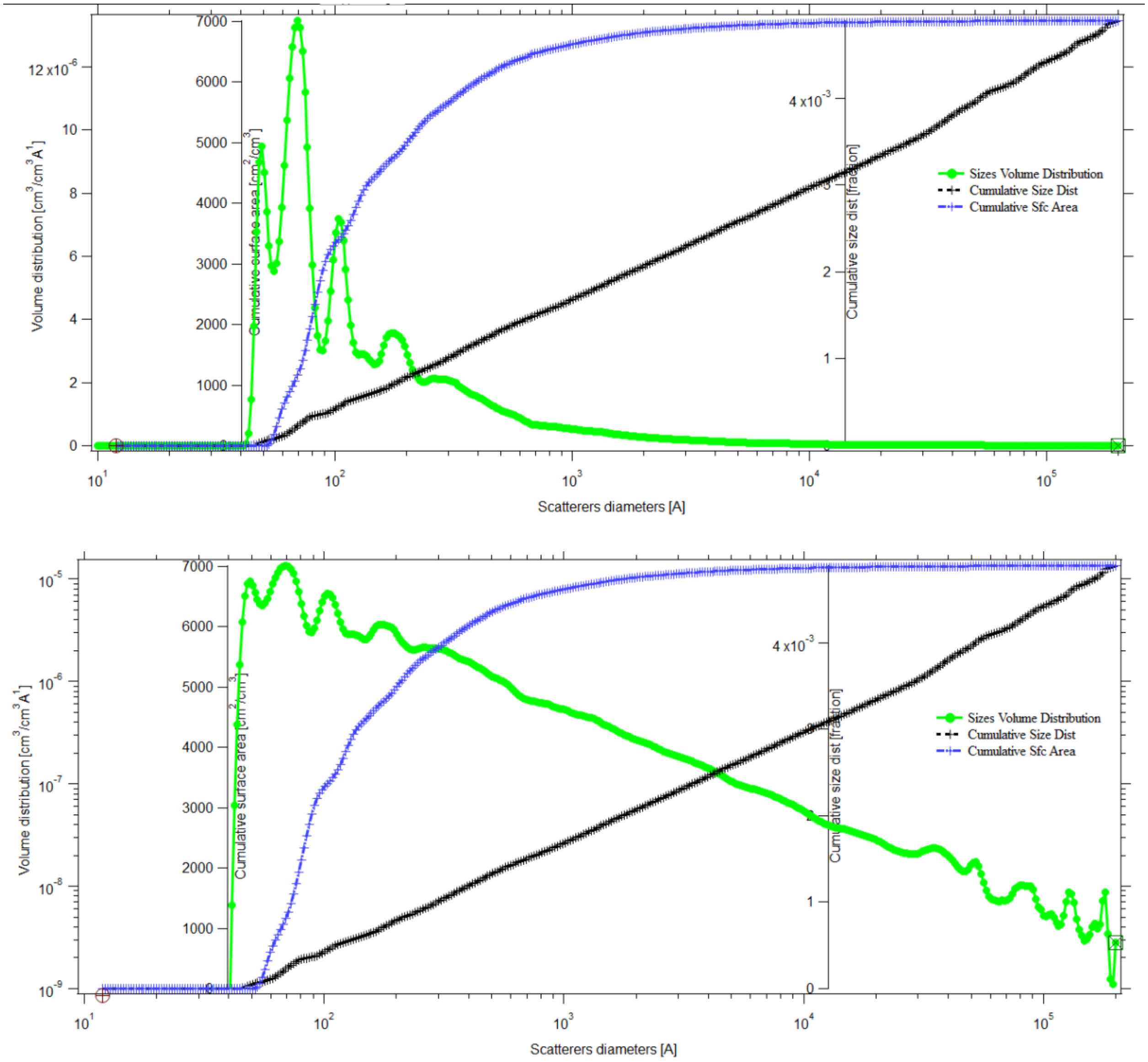

27. 9UL_x62_y0_0727

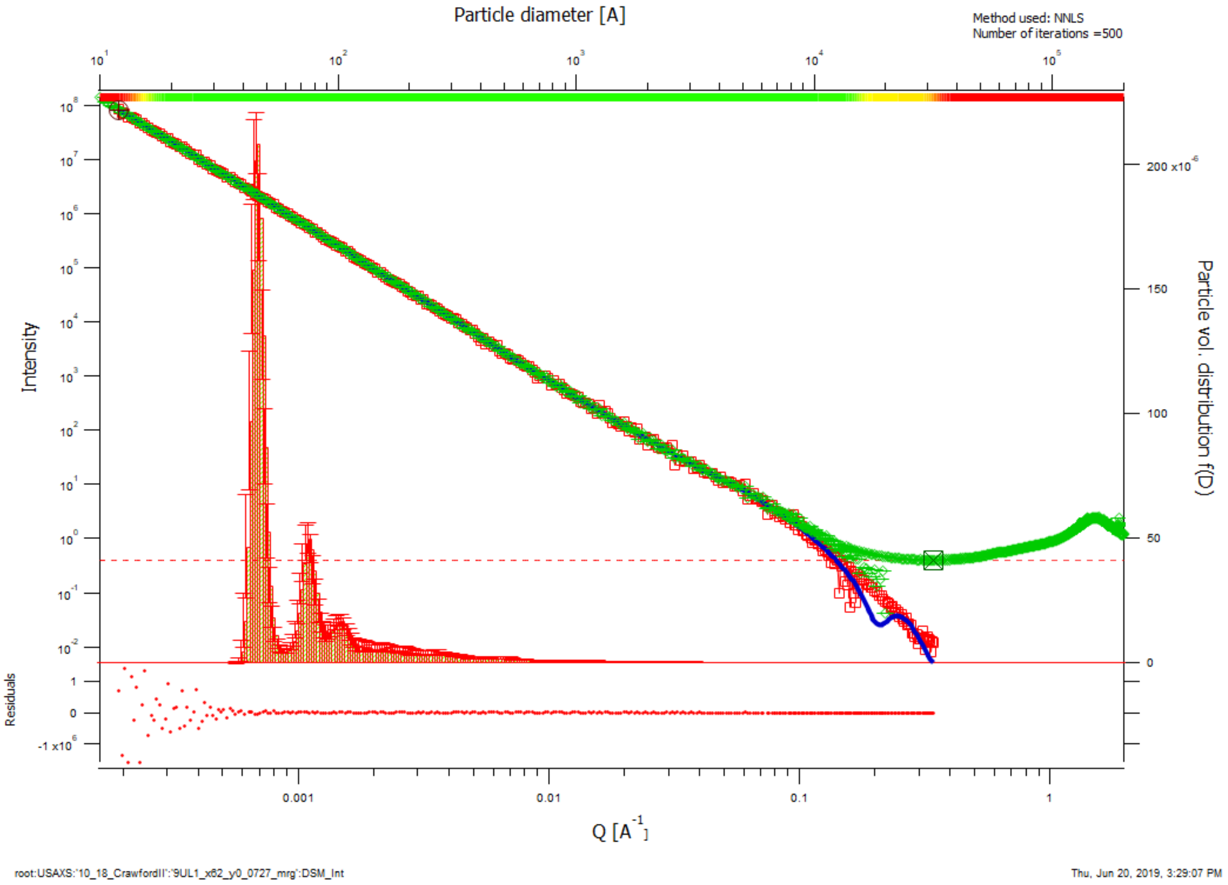
Particle diameter [A]
Method used: NNLS
Number of iterations =500
10^1
10^2
10^3
10^4
10^5
Intensity
10^8
10^7
10^6
10^5
10^4
10^3
10^2
10^1
10^0
10^{-1}
10^{-2}
200 x10^{-6}
150
100
50
0
Particle vol. distribution f(D)
Residuals
1
0
-1 x10^6
0.001
0.01
0.1
1
Q [A^{-1}]
root:USAXS:'10_18_CrawfordII':'9UL1_x62_y0_0727_mrg':DSM_Int
Thu, Jun 20, 2019, 3:29:07 PM

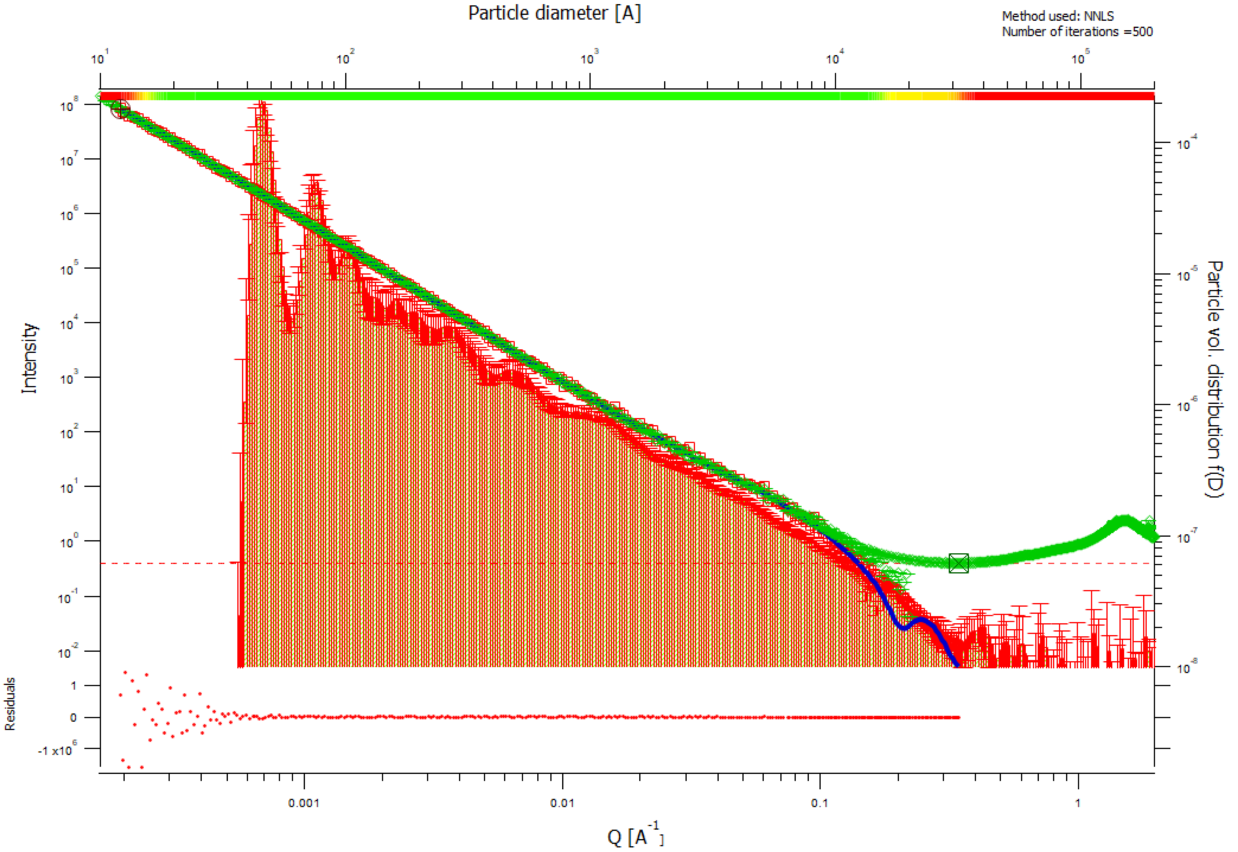

root:USAXS:'10_18_CrawfordII':'9UL1_x62_y0_0727_mrg':DSM_Int

Thu, Jun 20, 2019, 3:29:07 PM

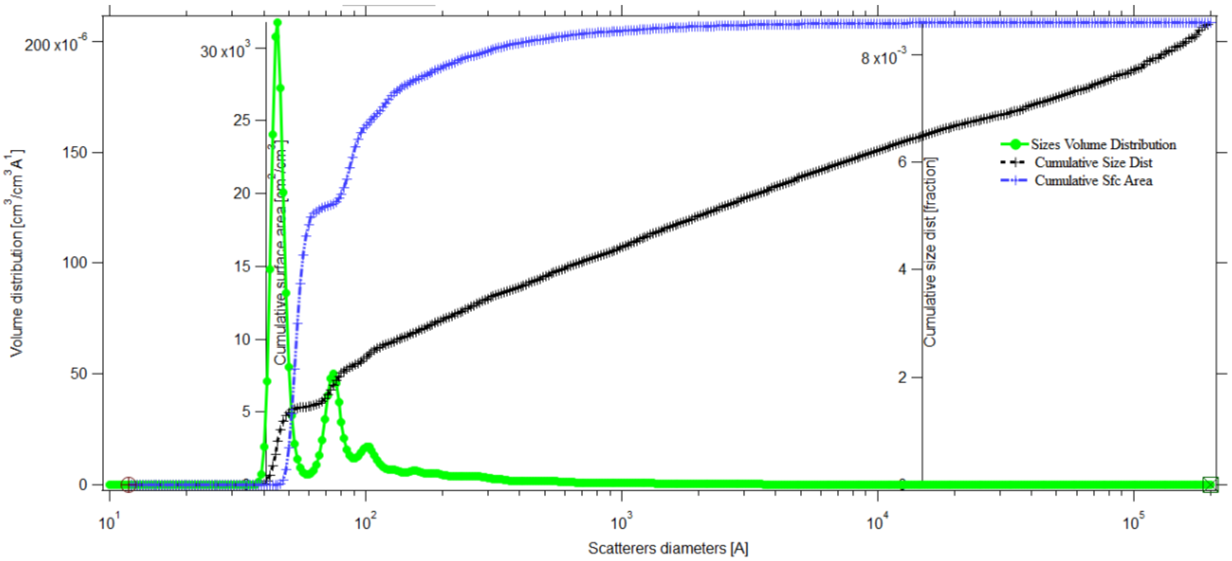

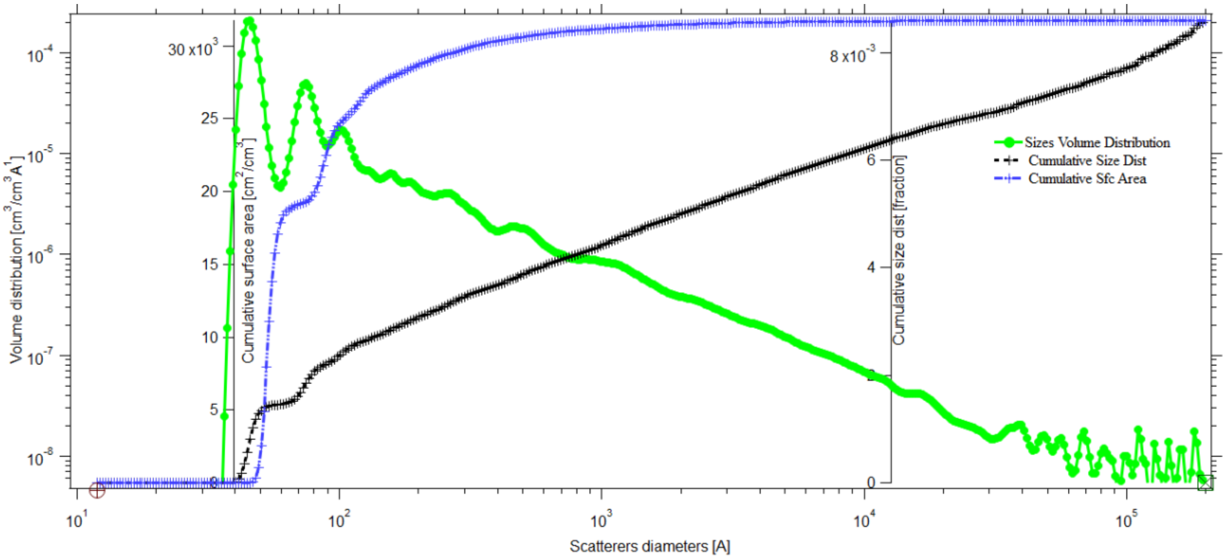

28. 9TO5_x_23_y28_R_0216

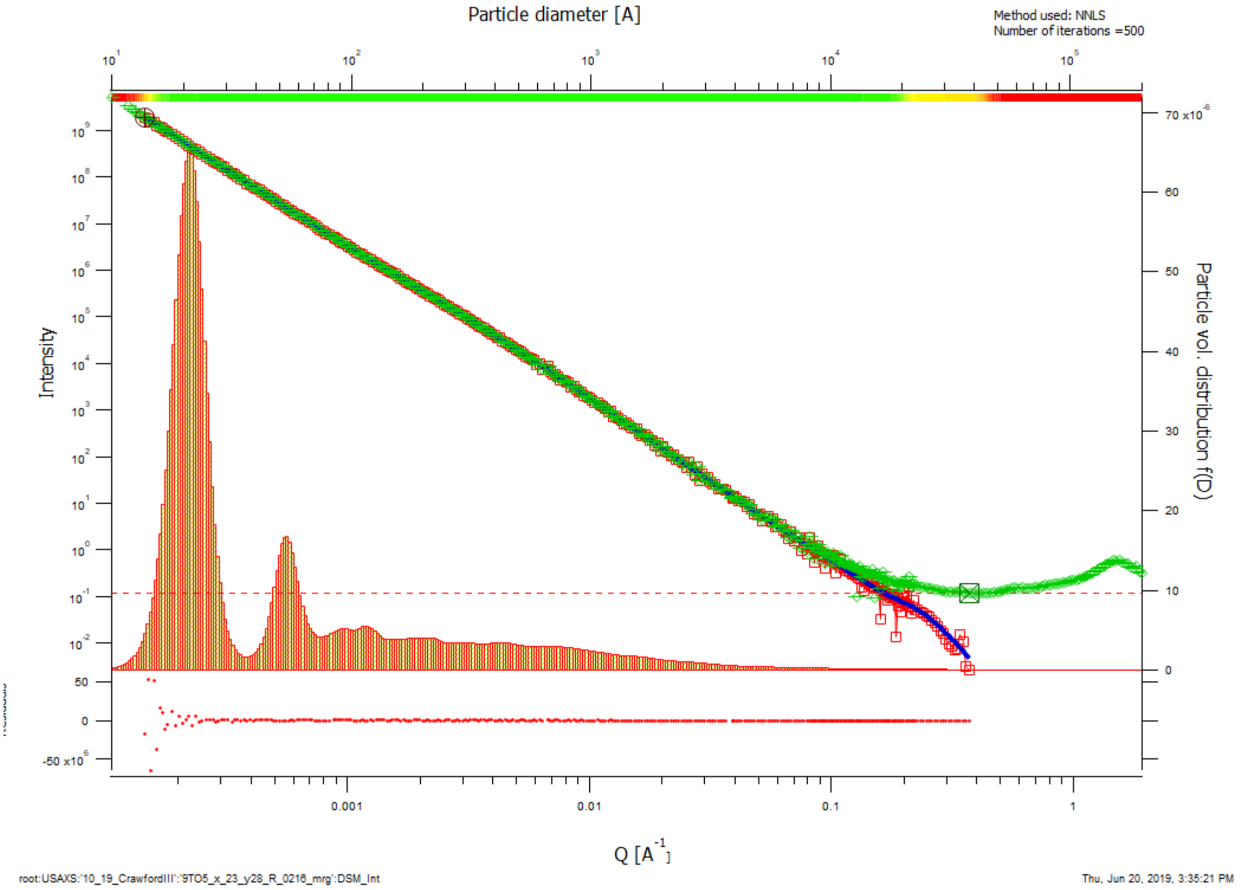

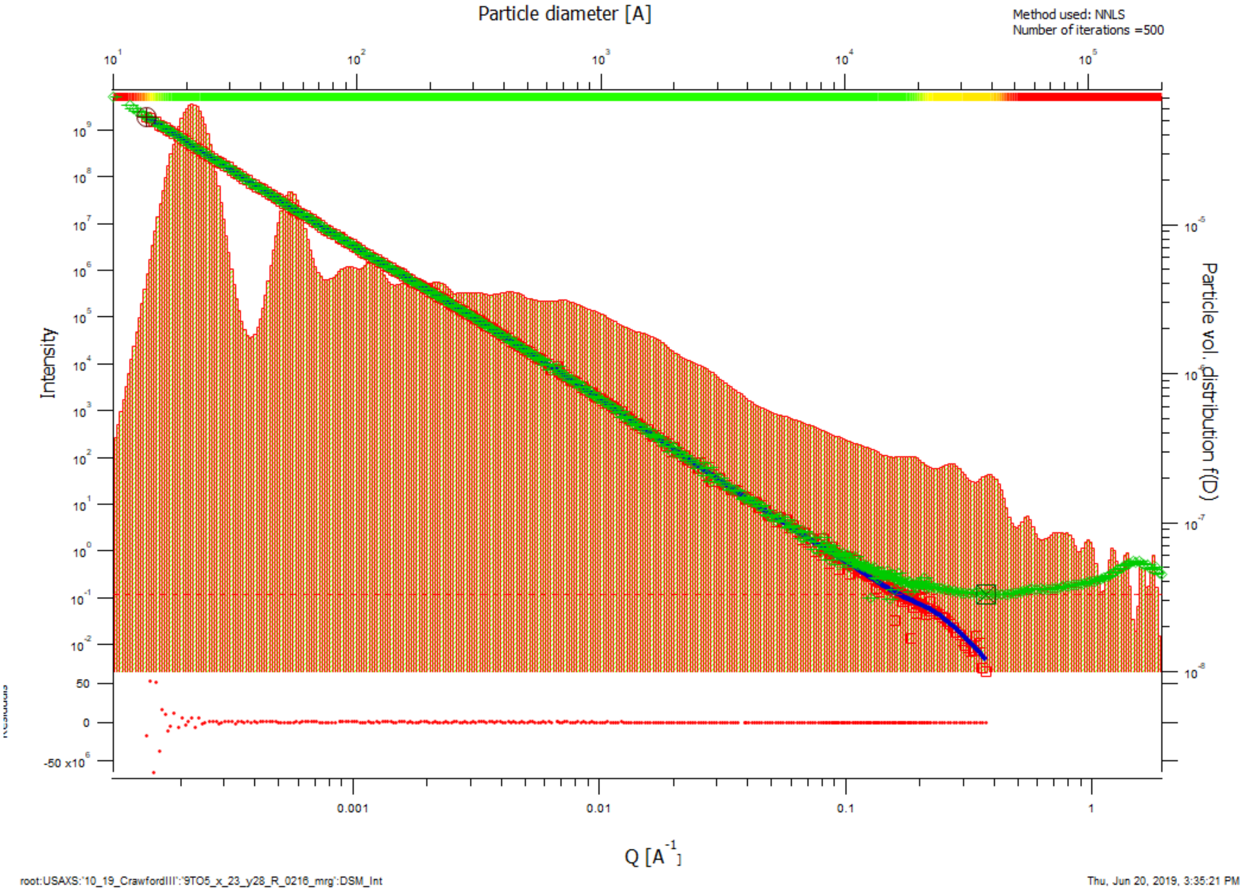
Particle diameter [A]
Method used: NNLS
Number of iterations =500
10^1
10^2
10^3
10^4
10^5
Intensity
10^9
10^8
10^7
10^6
10^5
10^4
10^3
10^2
10^1
10^0
10^-1
10^-2
Particle vol. distribution f(D)
10^-5
10^-6
10^-7
10^-8
50
0
-50 x10^6
0.001
0.01
0.1
1
Q [A^-1]
root:USAXS:'10_19_CrawfordIII':'9TO5_x_23_y28_R_0216_mrg':DSM_Int
Thu, Jun 20, 2019, 3:35:21 PM

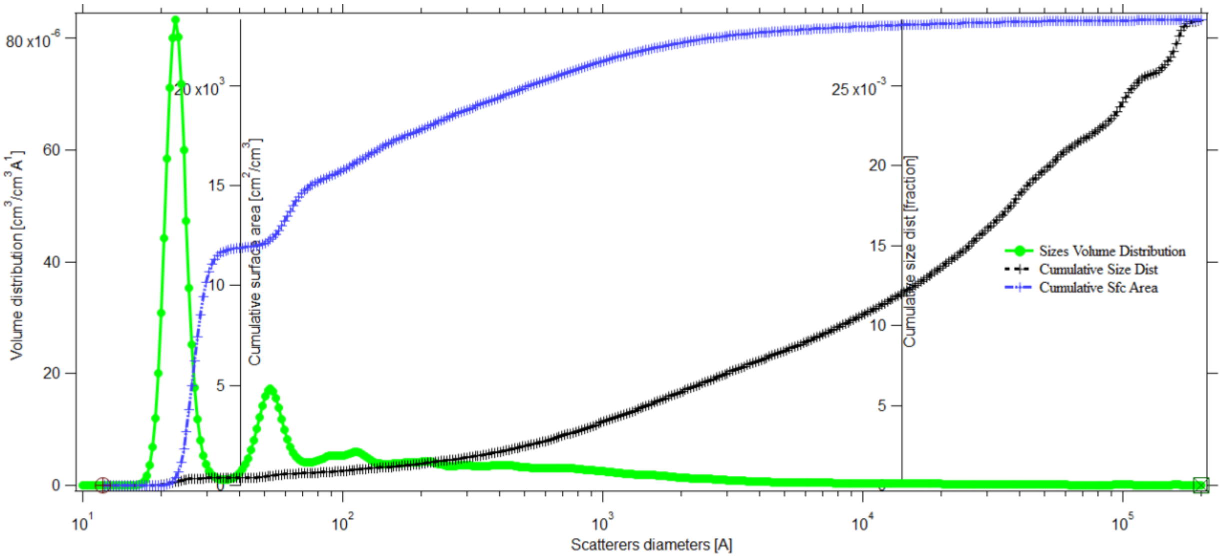

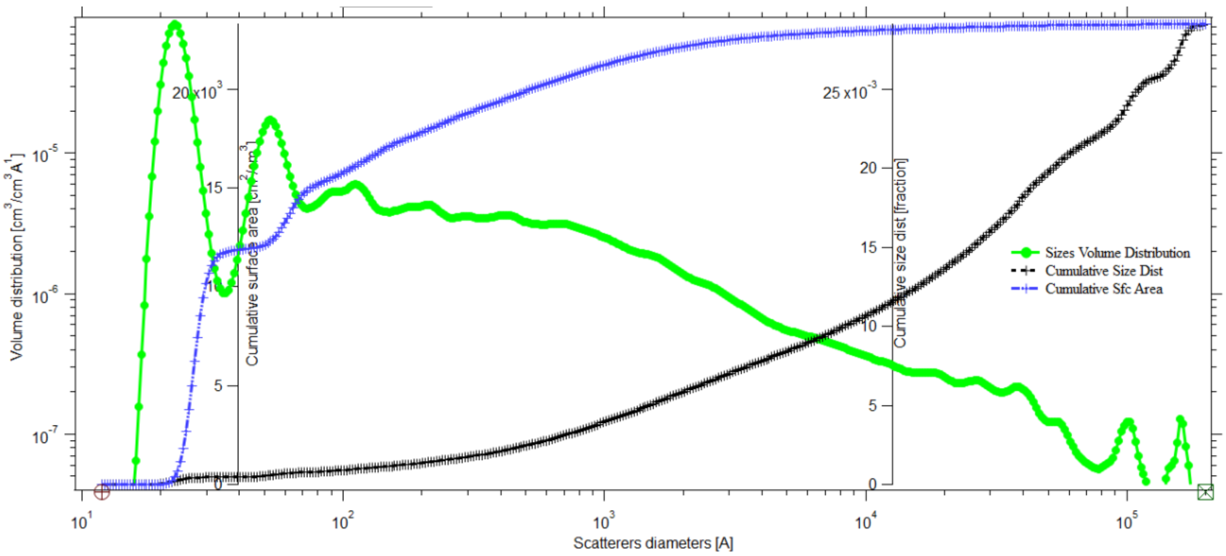

29. 9TO5_x3_y28_R_0220

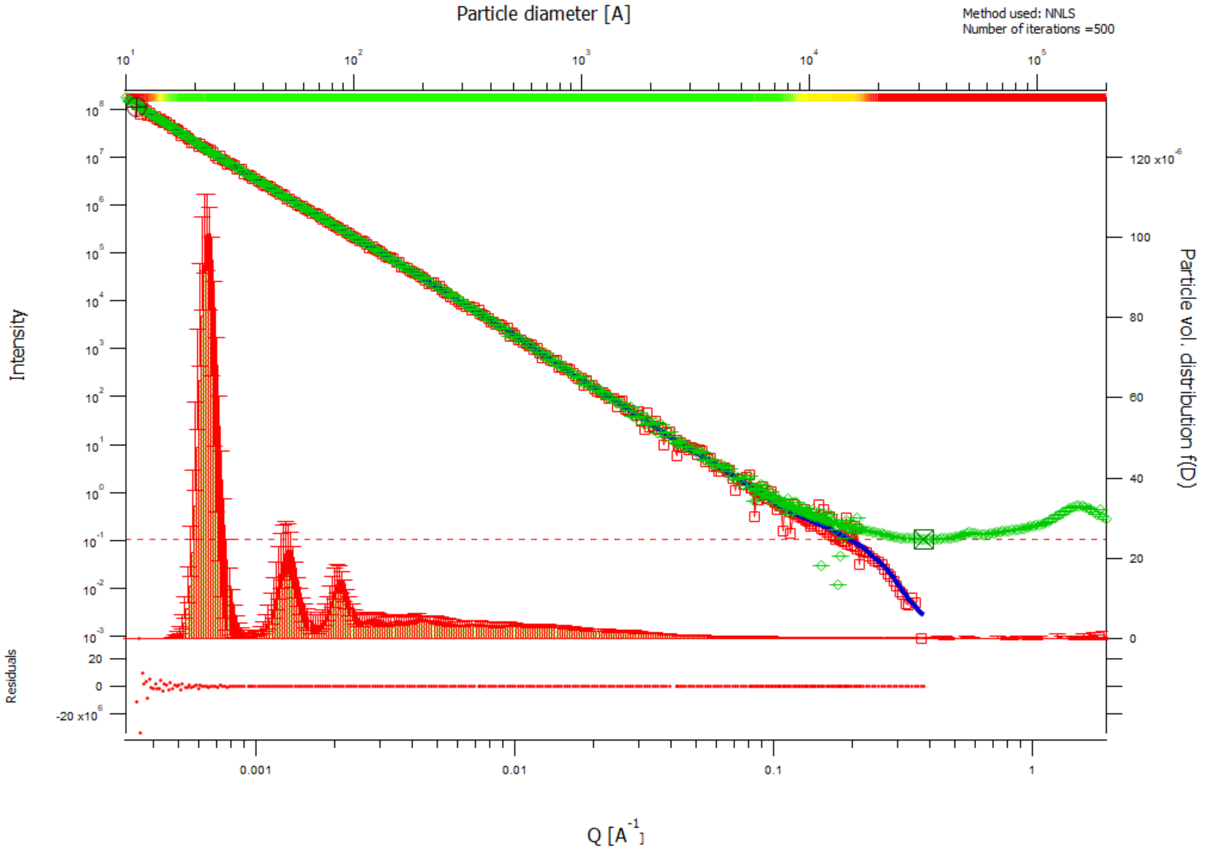

root:USAXS:'10_19_CrawfordIII':'9TO5_x3_y28_R_0220_mrg':DSM_Int

Thu, Jun 20, 2019, 3:47:47 PM

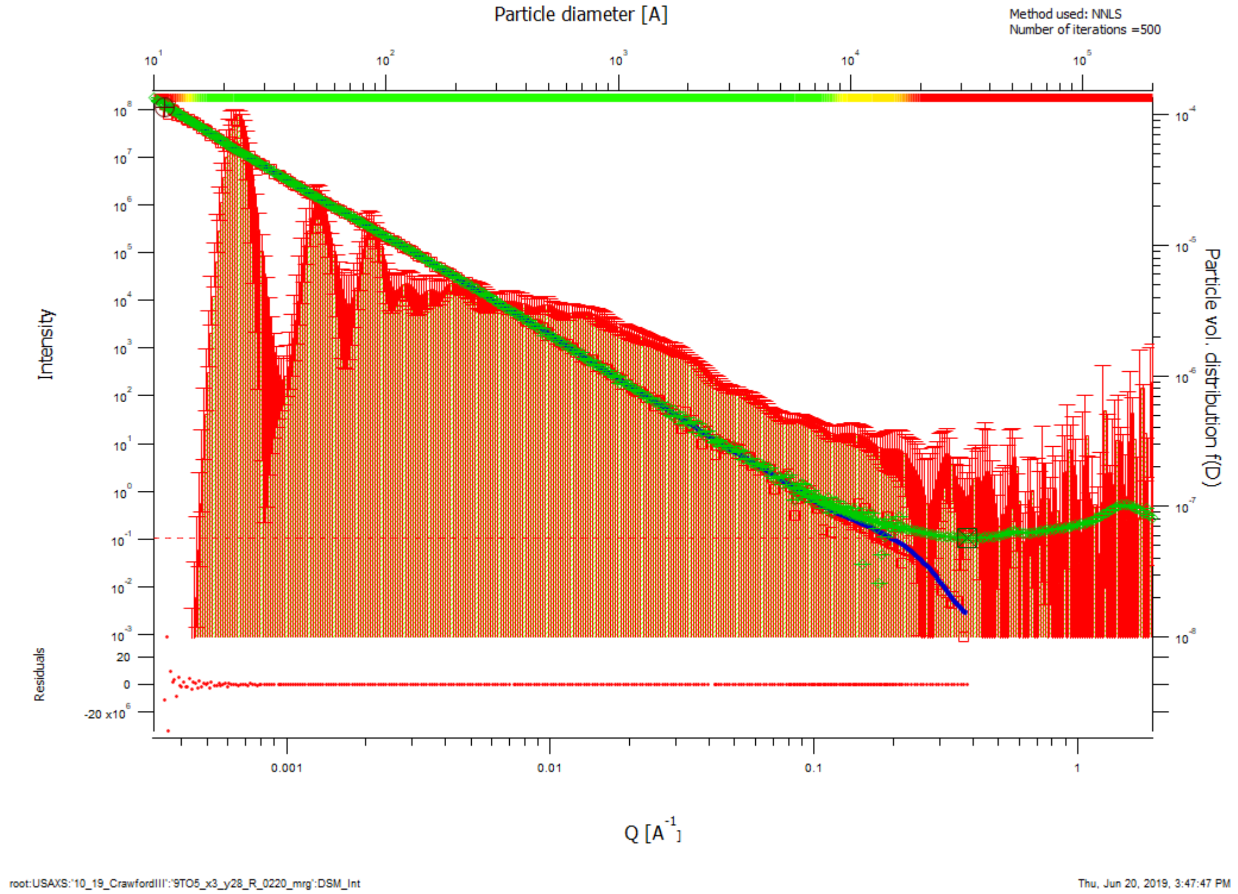
Particle diameter [A]
Method used: NNLS
Number of iterations =500
10^1
10^2
10^3
10^4
10^5
Intensity
10^8
10^7
10^6
10^5
10^4
10^3
10^2
10^1
10^0
10^{-1}
10^{-2}
10^{-3}
Particle vol. distribution f(D)
10^{-4}
10^{-5}
10^{-6}
10^{-7}
10^{-8}
Residuals
20
0
-20 x10^{-6}
0.001
0.01
0.1
1
Q [A^{-1}]
root:USAXS:'10_19_CrawfordIII':'9TO5_x3_y28_R_0220_mrg':DSM_Int
Thu, Jun 20, 2019, 3:47:47 PM

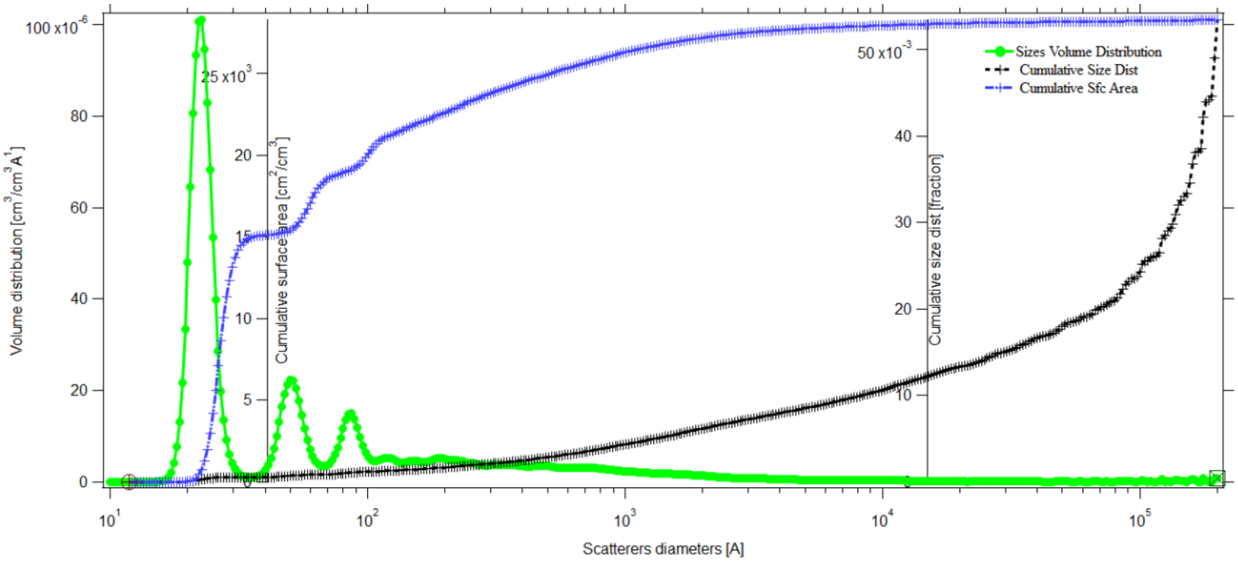
100 x10^{-6}
80
60
40
20
0
Volume distribution [cm^3/cm^3 A^1]
25 x10^3
20
15
10
5
0
Cumulative surface area [cm^2/cm^3]
50 x10^{-3}
40
30
20
10
0
Cumulative size dist [fraction]
Sizes Volume Distribution
Cumulative Size Dist
Cumulative Sfc Area
10^1
10^2
10^3
10^4
10^5
Scatterers diameters [A]

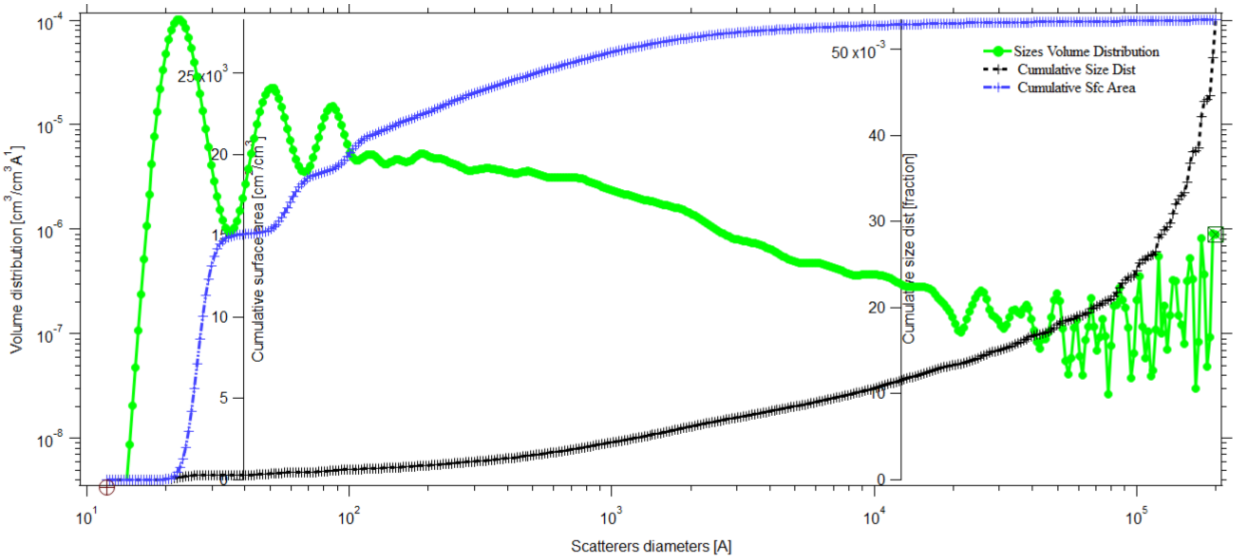

Appendix D

Mineral grains analyzed and photographed during the FE SEM examinations are shown below